CHARACTERIZATION OF THE CATHODOLUMINESCENT DEGRADATION OF
$Y_2O_2S:EU^{3+}$ POWDER CRT PHOSPHOR

By

TROY ANTHONY TROTTIER

A DISSERTATION PRESENTED TO THE GRADUATE SCHOOL
OF THE UNIVERSITY OF FLORIDA IN PARTIAL FULFILLMENT
OF THE REQUIREMENTS FOR THE DEGREE OF
DOCTOR OF PHILOSOPHY

UNIVERSITY OF FLORIDA

1997

ACKNOWLEDGMENTS

Being the last section that I have sat down to write,
all the pages before seem a blur. To me, this section, above
all others, contains the essence of the work which is
contained within. In a few short pages, I am required to
acknowledge all those who have aided and supported me in
this effort. I cannot. For each person mentioned will have
contributed far more than I can hope to express my gratitude
for in one or two sentences. Moreover, their contributions
to my work are the last thing I would thank them for,
instead I would like to thank them for their contributions
to me. In sharing themselves with me, I have gained insight
and knowledge and grown as a person, and perhaps, if they
think about it, they have too. Each person has added
something of themselves to me, and thus to this work.

Dr. Holloway made it so easy for me to walk in and
start asking questions about any subject, and never did I
walk out thinking that the door was closing behind me. He

has mastered the secrets of the student-teacher relationship and has been a father, a friend, and a confidant to me.

Dr. Masi's early example of what a true scientist is will always remain with me. I cannot thank you enough for introducing me to your friend and colleague, Paul Holloway.

Mom and Dad and Todd, through every part of my life, you have stood by me and supported me (albeit at the time I may have been too blind to notice!). Above all others, you are the reason that my dreams have come to fruition. I love you.

Jon Hack, the very definition of what a friend should be, your friendship and presence made the trials of daily life seem manageable. No matter what the signs say, swimming cannot be bad for you.

Wish, it seems to me that for the past 3 years, I have been asking favors of you and never have you hesitated. I give you that in return. Your friendship and devils-advocate attitude towards my research will be sorely missed. Don't ever forget, there will always be a glass of wine waiting for you.

Tall Joe and Little Billie, I must formally apologize in advance for any future breakdowns of Humpty Dumpty (the

new nickname for the Auger, ask Wish!). Besides that, I must

say you both have worked harder on that system than any

others during my time here, I leave it in very capable

hands.

I am indebted to Ron Petersen and Motorola Inc. for

their continued support of my research and my future.

TABLE OF CONTENTS

Abstract of Dissertation Presented to the Graduate School
of the University of Florida in Partial Fulfillment of the
Requirements for the Degree of Doctor of Philosophy

CHARACTERIZATION OF THE CATHODOLUMINESCENT DEGRADATION OF
$Y_2O_2S:Eu^{3+}$ POWDER CRT PHOSPHOR

By

TROY ANTHONY TROTTIER

DECEMBER, 1997

Chairperson: Dr. Paul H. Holloway
Major Department: Materials Science and Engineering

Cathodoluminescent degradation of $Y_2O_2S:Eu^{3+}$ powder

phosphors has been studied by Auger electron spectroscopy

(AES) and cathodoluminescent spectroscopy (CL). The

dependance of CL degradation on pressure, ambient gas and

electron beam energy have been examined.

CL degradation occurred slowly at $1x10^{-8}$ Torr and the

combination of AES and CL spectroscopy indicated the loss of

S and C from the surface of the phosphor. Volatilization

reactions involving O containing gases, the electron beam

and the surface C and S caused a conversion of $Y_2O_2S:Eu^{3+}$ to

a non-luminescent layer, possibly $Y_2O_2SO_4:Eu^{3+}$. This layers growth decreased the total brightness of the phosphor.

The conversion of $Y_2O_2S:Eu^{3+}$ to $Y_2O_2SO_4:Eu^{3+}$ requires O, so CL degradation was studied at $1x10^{-6}$ Torr backfilled from $1x10^{-8}$ Torr with O gas. The CL degradation rate was much higher in the presence of O gas. The conversion of $Y_2O_2S:Eu^{3+}$ to $Y_2O_2SO_4:Eu^{3+}$ was not detected, but in the presence of O, a near surface layer of luminescent $Y_2O_3:Eu^{3+}$ was formed and confirmed by CL spectroscopy.

Makhov's Law was used to predict the brightness loss of the $Y_2O_2S:Eu^{3+}$. Very good correlation was found between all experiments and the brightness loss predictions of the model. The amount of ionized gas at the surface was modeled using a modified ionization efficiency for electrons. Based on these models, protective surface coatings were applied to the phosphor particles in an attempt to slow the CL degradation.

Coatings of TaSi and Ag were deposited by a pulsed laser ablation and were found to reduce the CL degradation. The TaSi coating was tenacious and may have slowed the diffusion of S to the surface formation where it was present on the surface. The Ag coating delayed the CL degradation

but either migrated during bombardment or was desorbed (Ag_2S), slowly exposing the $Y_2O_2S:Eu^{3+}$ phosphor.

Wet chemistry coatings of SiO_2 and phosphate were applied as well, and were found not to affect the CL degradation rate.

CHAPTER 1
INTRODUCTION

Motivation and Objectives

The degradation of phosphor materials in

cathodoluminescent displays is one of the major concerns for

the recently developed FED (field emission display). In

order for FED's to compete with other flat panel display

technologies (EL, LCD, VFD), the luminescent lifetimes of

the currently available phosphors must be extended. The

physical phenomena that cause degradation are related to

surface volatilization and corrosion reactions induced by

residual gases in vacuum and electron beam dissociation of

these gases [Swa96].

Most manufacturers of prototype FED displays are

currently using sulfur based phosphors that have been used

in CRTs for many years. The sulfur-based phosphors (namely

$ZnS:Ag$, $ZnS:Cu$ and $Y_2O_2S:Eu^{3+}$) used in CRTs exhibit the

highest luminous efficiencies of all the currently available

1

industrial phosphors. Unfortunately, it has been demonstrated that the cathodoluminescent (CL) brightness of these phosphors is sensitive to gas pressure and gas ambient. Thus, the initial gains of high luminous efficiency are lost too soon due to CL degradation.

In order to realize the use of sulfur based CRT phosphors in FEDs, a basic understanding of the CL degradation phenomena is required. The objectives of this research therefor is the understanding of this degradation in one phosphor: $Y_2O_2S:Eu^{3+}$ Once the mechanisms of CL degradation are properly defined, methods of slowing or stopping the CL degradation may become apparent.

<u>Scope of the Present Work</u>

A review of the literature (Chap.2) shows that very few basic studies have been reported on the degradation phenomena found in sulfur based phosphors. Evidence of electron beam stimulated reactions causing CL degradation in the ZnS family of phosphors has been reported [Swa96, Ito89]. A comparison of the CL degradation rates of three CRT phosphors has been reported and it was shown that

$Y_2O_2S:Eu^{3+}$ is the least sensitive to electron beam stimulated reactions causing CL degradation [Tro96], but detailed studies of the reasons have not been reported.

One objective of this study was to examine the effects of gas pressure and type of gas on the CL degradation of $Y_2O_2S:Eu^{3+}$. CL spectroscopy and Auger electron spectroscopy (AES) were used in conjunction to correlate surface changes on the phosphor with luminescent changes observed under electron beam bombardment. The experimental procedure for these types of studies are discussed in Chapter 3. The results showed a correlation between sulfur loss from the surface, the presence of oxygen gas and CL degradation. The results of these experiments will be discussed in Chapter 4 and Chapter 5.

Another objective of this study was to examine the effects of electron beam energy on the CL degradation rates of $Y_2O_2S:Eu^{3+}$ and to attempt to model this dependance. A beam energy dependance was observed and modeled. Good correlation was found between the model and the experimental results of Chapter 4 and 5. The results of the beam energy dependance of the CL degradation rate of $Y_2O_2S:Eu^{3+}$ are reported in

Chapter 6. The model used to approximate the CL degradation of $Y_2O_2S:Eu^{3+}$ is developed in Chapter 7.

Finally, it was determined that surface coatings applied to the $Y_2O_2S:Eu^{3+}$ phosphor could be used to slow the CL degradation phenomena. The methods used to coat the phosphor and the types of coating materials studied are discussed in Chapter 3. Many of the coatings that were examined did show improved CL degradation characteristics and the results of these studies are discussed in Chapter 8. The conclusions from this study are given in Chapter 9.

CHAPTER 2
LITERATURE REVIEW

Introduction

For nearly 40 years, cathode ray tubes (CRT's) have dominated the color display industry. A superior quality picture, coupled with long lifetime, and large viewing angle have solidified the CRT's place in the display industry. As with all industries, the need for increased portability and efficiency is now being demanded of the CRT. The basic design of the CRT severely limits its ability to be reduced in size as can be seen in Figure 2-1 [Tan85]. A certain distance is required between the anode and cathode to ensure proper focus and raster capability. The CRT's crisp visual clarity and brightness are dependent upon the power levels used (20-30kV, 1-10nA), thus a reduction in power (increase in efficiency) compromises the visual characteristics of the display. This interdependence of picture quality and power level limits the CRT's ability to

5

become more portable and more efficient without sacrificing the most important qualities of the display.

Field Emission Displays

Field emission displays (FEDs) are one solution to the size reduction and efficiency improvement problems associated with CRT's. Instead of using 3 electron sources (respectively known as red, green and blue guns) and rastering over the entire screen as in the case of the CRT, each pixel is fitted with its own electron source. As shown in Figure 2-2 [Sch96], the placement of an emission source in proximity to the pixel alleviates the need for a relatively long electron path for focus and raster. The distance from the electron source to the phosphor screen can now be 1 mm or less.

One of the major hurdles that the FEDs face is the world-wide acceptance of the CRT as a standard by which fledgling display technologies are measured. The world has become accustomed to the chromaticity, brightness, and overall picture quality of the CRT, and requires that any new display technology be comparable if not better than the

CRT. The CRT and FED modes of operation (cathodoluminescence) are very similar and this ensures the equivalency of chromaticity, picture quality and viewing angle when compared with passive methods of display generation such as is found in the LCD and AMLCD. Both use a directed, accelerated beam of electrons to induce cathodoluminescence from a phosphor screen [Tro96]. Due to this commonality, the FED industry has adopted the standard CRT phosphors as starting materials for the FED display technology. These phosphors have met with limited success in FED's due to complications associated with the large differences in operating parameters of the FED as compared with the CRT. The electrons in a CRT typically strike the phosphor screen with 20 kV or higher kinetic energies. The FED cannot sustain such large potentials between the anode and cathode gap because the distance is much smaller and dielectric breakdown (arcing) can occur [Lev91]. FED's are currently being manufactured with anode to cathode potentials of 5 kV or less. The manufacturers are happy with this intrinsic breakdown limitation because it reduces the voltage requirements of the display package drivers. The trade off becomes apparent in the brightness of the display.

In order to match the brightness of the CRT, the power delivered to the phosphor must be the same. Thus a reduction in voltage from 25 kV to 5 kV necessitates a fivefold increase in screen current to obtain equivalent screen brightness. The increased current requirements of the field emission display are not a problem for the field emitter tips, since they are capable of sustaining currents in excess of 100ma/mm^2 [Der94]. However, the cathodoluminescent lifetime of the phosphor materials is directly related to the total charge density (C/cm^2) impressed upon them [Pfa61]. Thus, the higher the current density applied to the phosphor material, the shorter the useful lifetime of the phosphor [Pet97].

Introduction to Cathodoluminescence

Luminescence has been described by many authors as the conversion of energy into electromagnetic radiation over and above black body radiation [Bla94]. The type of excitation energy defines the luminescent phenomena. For instance, photoluminescence is luminescence stimulated by an UV light source. Triboluminescence defines the luminescent phenomena

caused by friction or fracture, as in the light generated by rubbing two quartz crystals together. Cathodoluminescence, naturally, is luminescence generated by cathode ray excitation of a material.

Only very rarely does a material luminesce efficiently in the visible region of the electromagnetic spectrum. Most materials that are efficient emitters in the visible spectrum have been specifically designed. Ordinarily, a starting material is chosen which has a band gap which would produce luminescence in or above the ultraviolet (uV) (>4.2eV) region. This material is called the host. It serves two purposes, as an optical window for the visible luminescence, and as the container for the optically active luminescent center known as the activator. The activators' visible light emission is affected by its interaction with the host material. The activator is intentionally introduced into the host as a defect. Typically less than a few mole percent of the activator is required to obtain efficient luminescence. An example of luminescence phenomena is depicted in Figure 2-3 [Lum78] for the case of Cr^{3+} in Al_2O_3. The figure displays the absorption and emission spectra as a function of energy in eV. For this case, only one of the

transitions (^2E-$^4A_2$) is observed as visible luminescence. Other transitions occur, as in the absorption spectra, but the energies of these transitions produce emission in the infrared, thus they are not shown in the luminescence spectrum.

Due to the probablistic nature of the interaction between an electron and the material, cathodoluminescence has staunchly resisted theoretical descriptions. Yet by far, it is one of the easiest luminescent mechanisms to create, control and study experimentally. Cathode rays interact with the phosphor system as a whole. Interactions occur with the host, activator, surface atoms and molecules within the penetration limits of the electron beam. The interaction is not limited to the primary beam electrons and their effect on the phosphor. Each primary electron creates many secondary electrons in cascade as it is inelastically scattered within the phosphor. This secondary cascade is one of the major differences between cathodoluminescence and photoluminescence. Photoluminescence primarily excites the activator, whereas cathodoluminescence excites with gain, the host as well as the activator. Gain is possible in cathodoluminescence because a single primary electron can

generate thousands of secondary electrons which can produce photons. In contrast, in photoluminescence a single incident photon typically only produces a single emission photon.

Theoretical Aspects of Cathodoluminescence

At the most basic level, cathodoluminescence is defined by the interaction of electrons with a solid. Two types of interactions are possible between a nearly free electron and a solid. Elastic collisions, which are collisions between an electron and a nuclei [Yac90], produce high energy back scattered electrons. Inelastic collisions, composed of electron-electron and electron-plasmon interactions, provide all the information obtainable in electron beam instruments. These include Auger electrons, X-rays, secondary electrons, and most importantly (for this work), cathodoluminescence.

Figure 2-4 [Hud92] depicts the number of electrons produced as a function of energy. The right-most peak which is denoted by V_p are those electrons which have undergone purely elastic collisions and exhibit no energy loss. All electrons below V_p have undergone inelastic collisions with

the surface or bulk atoms or electrons. The large peak at low energy are the electrons known as true secondaries. These are electrons which have originated in the solid and escape by gaining enough energy to exceed the work function of the solid and leaving into vacuum.

The true secondaries which escape into vacuum are not the electrons responsible for cathodoluminescence. Instead it is the secondaries generated within the solid which do not escape to vacuum which provide the energy to the luminescent center within the phosphors. Comprehension of this concept is vital to understanding the nature of cathodoluminescence. A single primary electron will undergo tens or hundreds of inelastic collisions within a solid. Each collision can produce secondary electrons which may be absorbed by an activator and recombine to produce visible luminescence. Thus, in order to understand cathodoluminescence, knowledge of inelastic scattering and electron-solid interactions is necessary.

Inelastic scattering of primary electrons has been described empirically by Bethe [Bet53]. The continuous power loss of primary electrons in a material has been described by the following simple relationship:

$$\frac{de}{ds} \approx \frac{-785\rho Z}{Ae} \ln\left(\frac{1.166e}{j}\right) \qquad (2.1)$$

where **de** is the incremental energy loss in a unit depth **ds**

in eV/Å, **A** is the atomic weight in g/mol, **Z** the atomic

number, **e** the electron energy, ρ the material density in

g/cm^3 and **j** is the mean ionization potential in eV, given by

the following relation for **Z**>13:

$$j = 9.76 * Z + \frac{58.5}{Z^{0.19}} \qquad (2.2)$$

For high energy electrons (5-100keV), Bethe's stopping power

equation has been shown to closely match experimental data

[Myk76, New76]. As can be seen in Figure 2-5, at low

energies (<0.5keV) the slope of Bethe's stopping power

equation becomes negative. This would imply that the primary

electron is gaining energy from the solid, which is

physically impossible. The most popular solution to this

problem has been the low energy adjustment suggested by

Rao-Sahib and Wittry [Rao74]. Their alteration used a

modified equation below the inflection point of Bethe's

original equation, while keeping the original Bethe equation

intact for energies greater then this inflection point. The
modified equation used by Rao-Sahib is given by:

$$\frac{de}{ds} = \frac{-785*\rho*Z}{\sqrt{A*e*j}} .$$
(2.3)

This model extends the low energy limit to
approximately 500 volts at which point the slope of energy
loss curve continues to increase and the slope of the
experimental data of Tung et al. decreases. Figure 2-5
[Joy89] is a comparison of the original Bethe equation and
the modification proposed by Rao-Sahib and Wittry to the
experimental data found by Tung et al. As can be seen,
neither the original Bethe equation, nor the modification
applied by Rao-Sahib are good approximations for electron
energies below approximately 0.5 keV.

Joy and Luo [Joy89], in an attempt to extend the
capabilities of the original Bethe model to energies down to
50eV, rewrote the ionization potential with an energy
dependent term where j' replaces j (the average energy to
create an electron-hole pair) in the original equation and
is given by:

$$j' = \frac{j}{1 + k * \dfrac{j}{e}}$$

(2.4)

where **k** is a fitting constant which varies from 0.7 to 0.9

depending upon the material system. It has a suggested value

of 0.85 for most materials which produces no more than a 10%

variance from experimental stopping powers. The dependence

of j' on energy has two effects. At high energies, **j'**

approaches **j**, reducing the modified Bethe equation to the

original Bethe equation where its accuracy is well

established. At low energies where **e<j**, the energy

dependance causes **j'** to vary linearly with **e**. Although the

variation of **j'** with **e** is empirically derived, some

experimental evidence for such a variation has been reported

[Lav85]. These alterations allow the modified Bethe equation

to be accurate down to approximately 50 eV. Figure 2-6

compares the theoretical stopping powers obtained by the

modified Bethe (MB) equation to experimental values for Cu

and C reported by Tung and Akkerman [Joy89]. As can be seen,

the predictions of the modified Bethe model proposed by Joy and Luo closely match the experimentally determined stopping power values found for Cu and C by Tung and Akkerman for electron energies from 100 eV to 10,000 eV. The electron energies used to induce cathodoluminescence range from 1 to 3 keV, thus the modified Bethe equation will be used to approximate the power dissipation in the phosphors.

Since the Bethe equation and the modified Bethe equation describe the continuous energy loss of a primary electron, the total range (defined as the total travel distance of an electron in a solid) can be determined by the following integration:

$$R = RR_{50ev} + \int_{50ev}^{PEeV} \frac{1}{(\frac{de}{ds})} de \qquad (2.5)$$

where RR_{50ev} is the residual range of a 50eV electron in Angstroms. The residual range (RR_{50ev}) has been estimated using the results of Nieminen [Nie88] which demonstrates that the stopping power for any material varies as $E^{5/2}$ below 50 eV. The range predicted by Joy and Luo can be used to determine the interaction volume of the primary electrons in

a solid, as well as the amount of energy lost to the solid at a given depth.

Kanaya and Okayama [Kan71] have derived an expression for the total range of electrons in a solid which includes the penetration depth of primary electrons plus a sphere located at the maximum energy dissipation depth with a radius equal to the diffusion length of a secondary electron generated in the material. From Figure 2-7, it can be seen that the range derived from the modified Bethe equation is approximately equal to the Kanaya and Okayama range except at extremely low primary electron voltages (<100eV).

In order for these models of primary electron energy loss to be useful, their validity must be determined for the specific case of cathodoluminescence. As stated earlier, the generation of a cathodoluminescent signal is dependent upon secondary electron generation in a phosphor. Since the number of secondaries greatly exceeds the primary electron density, most of the cathodoluminescent signal can be attributed to secondary electron recombination. Donolato [Don78], using the universal depth dose function proposed by Everhart and Hoff [Eve71] which denotes the local generation rate of carriers in a material, found that the

secondary electron-hole pair generation density was highest inside a volume of the same order of magnitude as the electron generation range. Figure 2-8 [Yac90] is a plot of the excess carrier concentration (solid lines) superimposed upon the secondary electron generation volume(dashed circle). The solid lines depict levels of equal carrier concentrations. The highest carrier densities are contained within the generation volume as denoted by the relatively large numbers within the circles. Outside of the generation volume, the carrier density drops at an exponential rate.

It seems plausible to assume that since the primary electrons generate the cascade of secondary electron-hole pairs, that the electron-hole pair generation volume may be approximated by the same volume which defines the primary electron range, and that the secondary generation rate may be related to the primary electron power density. These assumptions, along with the conclusions based on the data of Figure 2-7, that the highest density of electron hole pairs is found within the generation range allows a first order approximation of cathodoluminescent brightness versus depth to be drawn qualitatively as being parallel to the power loss curve of the primary electrons.

Makhov [Mak60], using similar assumptions, suggested that the brightness produced at any depth in a phosphor must be proportional to the power dissipated by the electron beam at a given depth in the absence of carrier diffusion processes:

$$\frac{dB}{dx} = \rho(x) * \frac{dP}{dx} \qquad (2.6)$$

where dB/dx is the variation in brightness as a function of depth x from the surface of the phosphor. dP/dx is the power dissipated by an electron beam as a function of depth and $\rho(x)$ is the cathodoluminescent efficiency at depth x. Typically, $\rho(x)$ is assumed to be constant for all depths.

It is possible to obtain an approximation to the power dissipated by the electron beam as a function of depth by using the modified Bethe equation. Since average power is equivalent to average energy dissipated per unit time, it is possible to obtain the average power knowing the initial kinetic energy of the electron, the distance it has traveled and its velocity. These three quantities can all be obtained from the modified Bethe equation.

Kingsley and Prener [Kin72] showed very good agreement between theoretical and experimental brightnesses of ZnS:Cu with known thicknesses of non-luminescent ZnS deposited on the particles using the above assumptions by Makhov. Theoretical and experimental brightnesses as a function of primary electron energy shown in Figure 2-9 [Kin72] were in very good agreement. The conclusion was that when non-luminescent surface layers were comparable in thickness (0.08μm to 0.4μm) to the carrier diffusion lengths in ZnS:Cu, the cathodoluminescent brightness was dependant on the power loss of the primary beam in the phosphors and in the non-luminescent surface coatings [Kin72].

<u>CL Degradation</u>

Many phosphors [Han52, Rot54] have been shown experimentally to decrease in brightness under prolonged electron beam excitation. The degradation of cathodoluminescence in phosphors has been studied in many different materials systems, with an equal number of proposed mechanisms for the phenomena. Introduction or diffusion of defects in crystals, increases in optical

absorption, and the desorption of surface species leading to increased surface losses have all been proposed as possible mechanisms for CL degradation. In general, the mechanism for cathodoluminescent degradation appears to be dependent upon the phosphor material studied.

Rhonda et al. [Ron94] found that for high columbic loads (>400 C/cm^2), as would be typical in projection television tubes, that LaOBr:Tb^{3+} excited by low energy(1-4keV) electrons exhibited increases in optical absorption coefficients. Coupled with absorption spectroscopy, ion desorption rates were measured and it was found that the desorption rates of bromine was three orders of magnitude higher than that of oxygen.

By considering the experimental data, three possible mechanisms for phosphor degradation were proposed by the authors [Ron94]: (1) Urbach Tail absorption (broad absorption below the band edge), (2) the formation of color centers (mainly F-centers, where an anion vacancy is occupied by an electron for charge neutrality) producing weak absorption in the visible, or (3) absorption increases caused by chemical modification of the phosphor surface as

indicated by ion desorption of O and Br from the surface were suggested.

The decrease in cathodoluminescence and corresponding increase in absorption coefficient were found to be reversible by heat treatment in a reducing atmosphere. It was suggested by the authors that the reversibility of CL loss by heat treatment indicated a recrystallization of the phosphor material with a decrease in the total number of non-radiative recombination centers [Ron94].

Klaassen and deLeeuw examined the cathodoluminescence degradation of three different phosphors, $Zn_2SiO_4:Mn^{2+}$, $Y_2SiO_3:Ce^{3+}$ and $Sr_2Al_6O_{11}:Eu^{2+}$ as well as the degradation characteristics of Tb^{3+} doped borate glass. For $ZnSiO_4:Mn^{2+}$, the degradation effects were attributed to a thickening of the dead layer by a factor of two [Kla87]. Further experiments showed that the dead layer losses were mainly due to an increasingly oxygen deficient layer on the surface of the phosphor particles.

$Y_2SiO_3:Ce^{3+}$ showed changes in relative radiant efficiency with increased saturation which was interpreted as decreased energy flow to the luminescence center Ce^{3+}. Degradation, in this case, was attributed to a decrease in

the active Ce^{3+} concentration [Kla87]. $Sr_2Al_6O_{11}:Eu^{2+}$ exhibited a characteristic browning in the electron beam exposed area. Decreased external radiant efficiency, coupled with lower reflection values, led the investigators to speculate that the degradation was caused by a decreased photon escape probability [Kla87]. This self absorption was further thought to be due to color centers in the aluminate host. Borate glass doped with Tb^{3+} was found to exhibit decreased non-radiative lifetime for the excited states of Tb^{3+}. The authors suggested that energy transfer to killer centers created in the glass under prolonged electron beam excitation was responsible for the decrease in decay time [Kla87].

Some of the earliest work attempting to categorize degradation phenomena for a large number of phosphors was reported by Pfanhl at Bell Labs [Pfa61]. Pfanhl found that the degradation rate of phosphors followed a simple formula:

$$I(N) = \frac{I_0}{(1 + C*N)} \tag{2.7}$$

where **I** is the cathodoluminescence intensity at any electron dose **N** (#e's/cm^2), I_0 is the initial cathodoluminescent intensity and **C** is the burn parameter (cm^2). Recent work by Bechtel and associates [Bec96] has reconfirmed the validity of this formula for anode voltages as low as 2keV, and high current loads for the CRT phosphors of $Y_2O_2S:Eu^{3+}$, $ZnS:Ag,Cl$, and $ZnS:Cu,Au,Al$.

Pfanhl studied cathodoluminescent degradation in a large number of phosphor systems and found that the physical phenomena leading to cathodoluminescent degradation was attributable to one of two mechanisms. In many phosphors studied, new non-radiative recombination sites were believed to be created by prolonged electron beam bombardment [Pfa61], although no experimental method of proving the existence of these non-radiative sites was discussed or presented. In other phosphors, deactivation of the luminescent center (activator) by charge compensation was believed to be the primary CL loss mechanism. For non-activated crystals such as ZnO and $CaWO_4$ where the lattice ions cause luminescence, the creation of new non-radiative recombination centers was determined to be the

cause of cathodoluminescent degradation. This would be the only possible conclusion since deactivation of intentionally doped activators is not possible.

It was also suggested that activated phosphors (eg. ZnS:Ag,Cl and ZnS:Cu,Au,Al) exhibited higher degradation rates due to the added requirement that carriers must travel many atomic distances before a radiative recombination occurred, unlike the non-activated phosphors mentioned above where all sites can radiatively recombine. Many Ce^{3+} activated phosphors were found to be extremely sensitive to electron beam degradation, and the author concluded that the luminescent center was being directly affected by the electron beam bombardment. The extremely high rate of degradation was attributed to both increasing non-radiative recombination and the loss of luminescent sites by charge compensation (Ce^{3+} to Ce^{2+}) [Pfa61].

In an experiment on zinc oxide, a correlation between degradation rate and phosphor preparation and vacuum conditions was found. The zinc oxide phosphor was prepared in three different ways: an uncoated powder degraded in a de-mountable vacuum test stand operating at $3x10^{-5}$ Torr, an aluminum coated powder degraded in the same test stand, and

an aluminum coated powder degraded in a sealed off CRT tube

operating at $1x10^{-7}$ Torr. The rate of coulomb aging for each

of the zinc oxide samples tested is shown in Figure 2-10

[Pfa61], and there are obvious differences in the rate of

degradation. All three phosphors were tested with a D.C.

beam current density of 5 mA/cm^2 and a primary beam energy

of 10 kV. The uncoated zinc oxide phosphor in poor vacuum

degraded at the highest rate. The aluminum coated phosphor

in a similar vacuum condition degraded at a slower rate, and

the coated zinc oxide in the sealed-off CRT tube (best

vacuum) degraded at the slowest rate of all three phosphors

tested. The author suggested that the vacuum conditions and

the ability to conduct heat away from the phosphor, by

aluminum coating, were vital to slowing the aging process.

Data for a large number of phosphors commercially

available to researchers in 1961 are shown in Table 2-1

[Pfa61,Bli57,Gil56,Mar57,Rot55]. The author determined the

total electron dose required to reduce the initial

brightness by 50%. The column containing these values is

labeled "1/C=No. Of Coulombs necessary to reduce I to

$0.5*I_0$". In the table, higher 1/C values are observed for

phosphors which resist degradation, with $ZnSiO_4$ having the largest value of 104.0 C. It is important to note that all the phosphors listed exhibit different CL half lives under the same electron beam conditions. This clearly indicates that degradation is material dependent, and regardless of the chemical makeup, all of the phosphors exhibit CL intensity loss with higher coulomb load.

CL Degradation of Sulfides

More recent studies of CL degradation have centered around sulfur containing phosphors, in particular ZnS:Ag, ZnS:Cu,Au,Al and $Y_2O_2S:Eu^{3+}$. These three phosphors exhibit the highest efficiencies for CL excitation and are the current standard phosphors for blue, green and red, respectively, for the CRT. The energy efficiency is listed in Table 2-2 as a percentage, and is equal to the ratio of emitted luminous energy versus the incident electron energy. The zinc sulfide, green and blue, efficiencies are the highest of all the known phosphors. As shown in Table 2-2 [Oza90], the highest efficiencies are 23% (ZnS:Ag), 21% (ZnS:Cu), and 13% $(Y_2O_2S:Eu^{3+})$.

Itoh et al. [Ito89] studied the mechanism of degradation of zinc sulfide and zinc cadmium sulfide phosphors at low voltages. In-situ mass spectrometric analysis of the gases present and XPS surface chemical analysis were used to show the desorption of sulfur containing species. Residual gas analysis of the various desorbed species was performed with varying anode potentials raised from 20 to 50 V with partial pressures of water between 2×10^{-8} and 1×10^{-5} Torr. Figure 2-11 [Ito89] shows that higher desorption rates (higher ion currents) were found with increasing anode voltages (increasing power densities), and increasing partial pressures of water. The conclusions drawn from these studies were that the gas generation phenomena was related to the power density (or heat) from the electron beam, and to the increased decomposition of water on the surface of the phosphors at increased partial pressures of water.
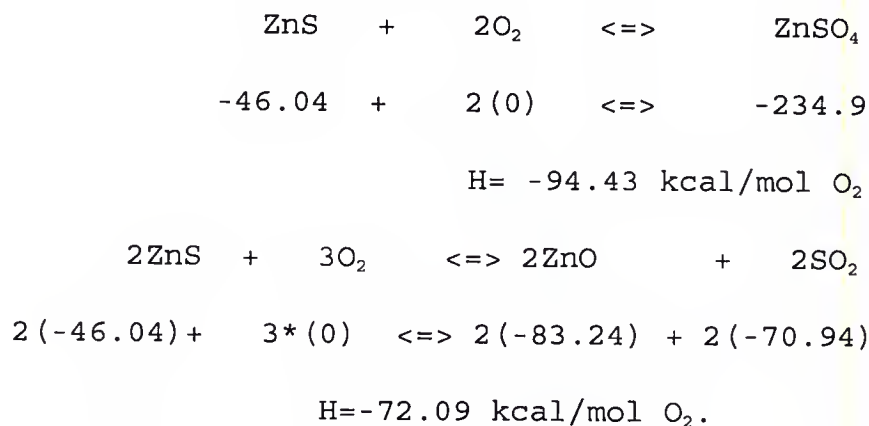
The experiments by Itoh et al., were designed to examine the effects of molecular species desorption on the operation of vacuum fluorescent displays and the consequent decrease in electron emission from oxide coated cathodes. Despite the original intent, the experiments also provide a

tremendous amount of information on the mechanisms involved in the degradation of CL phosphors. One drawback of these experiments was that the power densities used were those of the vacuum fluorescent display, which are generally higher than those found in FEDs.

Similar conclusions about the effects of reactive gas partial pressures were drawn by Swart et al. [Swa96] for ZnS:Cu and ZnS:Ag powder phosphors in simulated FED operating conditions. Degradation of these standard CRT phosphors was studied by Auger electron spectroscopy (AES) and cathodoluminescence (CL) spectroscopy. The background pressures during experimentation were between $1x10^{-8}$ Torr and $1x10^{-6}$ Torr. The higher pressures were obtained by backfilling to the chosen pressure with oxygen gas. The electron beam was operated in the D.C. mode with 1 to 2keV primary beam energies and $2mA/cm^2$ current densities.

Figure 2-12 [Swa96] shows the drastic changes exhibited by the surface of the ZnS phosphor before and after electron beam aging. Both carbon and sulfur were depleted from the near surface region of the phosphor while the O and Zn surface concentrations increased. The authors suggest that the near surface region of the ZnS phosphor was converted

to a sulfur-depleted, oxygen-rich compound, such as ZnO or ZnSO$_4$. Possible chemical reactions and heats of formation were reported and are depicted below [Swa96]:

$$ZnS \quad + \quad 2O_2 \quad <=> \quad ZnSO_4$$

$$-46.04 \quad + \quad 2(0) \quad <=> \quad -234.9$$

$$H= -94.43 \text{ kcal/mol } O_2$$

$$2ZnS \quad + \quad 3O_2 \quad <=> 2ZnO \quad + \quad 2SO_2$$

$$2(-46.04)+ \quad 3*(0) \quad <=> 2(-83.24) + 2(-70.94)$$

$$H=-72.09 \text{ kcal/mol } O_2.$$

Using XPS analysis, Itoh reported that ZnSO$_4$ was formed on the surface of ZnS and ZnCdS degraded by an electron beam, while Swart et al reported the formation of ZnO on the surface [Swa96].

Comparing the AES data with the CL data, Swart et al suggested that a direct correlation existed between the CL intensity decrease and the extent of surface reactions. The formation of a non-luminescent ZnO surface layer was demonstrated by sputter depth profiles taken after total coulomb exposures of 28 C/cm^2 and 38C/cm^2, and found to be 18Å and 30Å, respectively. The oxide thickness was also

calculated from the Zn Auger intensity changes using Seah's

formalism [Sea83, Sea79] and were found to be consistent

with the sputtered thicknesses at 28 C/cm². Both data show

that the thickness of the non-luminescent ZnO layer

increased with increasing coulombic loading. However, the

author concluded that niether optical absorption, nor

electron power dissipation in such a thin oxide layer could

explain the CL brightness loss.

Other authors have examined the influence of the dead

layer on CL by producing non-luminescent layers of known

thickness and studying the changes in efficiency as a

function of accelerating voltage. Figure 2-13 shows results

of Kingsley and Prener [Kin72] who examined the

cathodoluminescent efficiency of ZnS:Cu phosphor particles

on which known thicknesses of non-luminescent ZnS was

deposited. They found that for non-luminescent ZnS coatings

ranging up to $0.4\mu m$ thick, the cathodoluminescent efficiency

was dominated by the power loss of the electron beam in the

non-luminescent layer. Figure 2-13 shows the luminescence

intensity as a function of accelerating voltage for the

ZnS:Cu,Au,Al phosphor with $0.0\mu m$, $0.127\mu m$, $0.254\mu m$, $0.389\mu m$

thick non-luminescent layers. The slope of the intensity versus V_p remains the same, while the V_p at which the response becomes linear increased with increasing dead layer thickness. These results suggest that the intrinsic efficiency of the ZnS phosphor did not change due to the non-luminescent surface layer. The curve simply shifted to the right, due to the required increase in penetration distance of the electron beam resulting from the presence of non-luminescent surface layers. The dependance of efficiency on accelerating voltage is dominated by the power loss of the electron beam in the non-luminescent layer and not by changes in the internal efficiency of the phosphor. If the diffusion length is greater than the dead layer thickness, then both the power loss due to diffusion of electron-hole pairs generated by the primary electrons and the power loss of the primary electrons must be considered in the efficiency calculations [Kin72].

Degradation Resistant Coatings

The sulfide and oxysulfide phosphors are currently the most desirable phosphors available for use in FED's. Yet as

mentioned above, the degradation of these phosphors in an FED environment (low accelerating voltage <5kV, high current density >5mA/cm^2) is unacceptably high. The apparent gains in using the complementary set of RGB CRT phosphors (ZnS:Ag,Cl, ZnS:Cu,Au,Al, Y_2O_2S:Eu^{3+}) is offset by the loss in brightness associated with electron beam stimulated surface reactions.

In order for these phosphors to be useful in an FED, a method of slowing the degradation rate must be found and utilized. Although many different mechanisms have been reported for the degradation of phosphors, many have surface phenomena in common. One method of reducing the amount of electron beam stimulated surface reactions taking place would be to reduce the partial pressure of reactive gas in the flat panel. Another possibility for slowing the degradation rate would be to surface coat the phosphors with a material which inhibits the CL loss. In order to be commercially viable, the coating must not be detrimental to the handling qualities, brightness, and chromaticity of the phosphor.

Wet chemical surface coatings of powder CRT phosphors has been shown to be useful for pigmenting, screening,

increased electrical conductivity, and increasing low voltage efficiency [Sil83, Hay69, Kom96, Jac95]. Very little work to date has examined the potential effects of surface coatings on the degradation characteristics of phosphors. Figure 2-10 shows the results of Pfanhls' work on ZnO and aluminum coated ZnO and it displays a remarkable reduction in the degradation rate of the phosphors which was attributed to increased thermal conductivity and faster removal of heat generated by the electron beam [Pfa61]. Aluminization is a standard CRT processing step designed to reflect light forward toward the viewer and increase the apparent brightness of the screen. Since the lifetime of phosphors in CRT applications was already acceptable, Pfanhl hardly mentioned the 3-4 fold increase in lifetime of the ZnO phosphor with aluminization over the uncoated ZnO standard phosphor.

Summary and Motivation

Cathodoluminescent degradation is one of the major hurdles facing the developing FED industry. The CL degradation is related to the total charge load impressed

upon the phosphor screen. For optimum screen brightness and chromaticity, the phosphors of choice are the RGB CRT phosphors ZnS:Ag,Cl, ZnS:Cu,Au,Al, and $Y_2O_2S:Eu^{3+}$.

Only a few studies have investigated the kinetics of degradation of sulfur-containing phosphors. CL degradation of sulfur-containing phosphors has been found to be dependent on coulomb load and vacuum ambient conditions. The degradation is related to chemical changes on the surface of the phosphor, typically with loss of sulfur from the surface.

No studies have been reported for the kinetics of degradation for $Y_2O_2S:Eu^{3+}$. Such studies, coupled with a model defining the parametric relationship between coulomb load, surface changes, vacuum conditions and CL degradation would be instrumental to finding ways to slow or stop the degradation phenomena. Protective coatings on the phosphors may be one method of slowing the CL degradation and also provide vital information to further develop the kinetic degradation model. This work has addressed these issues.
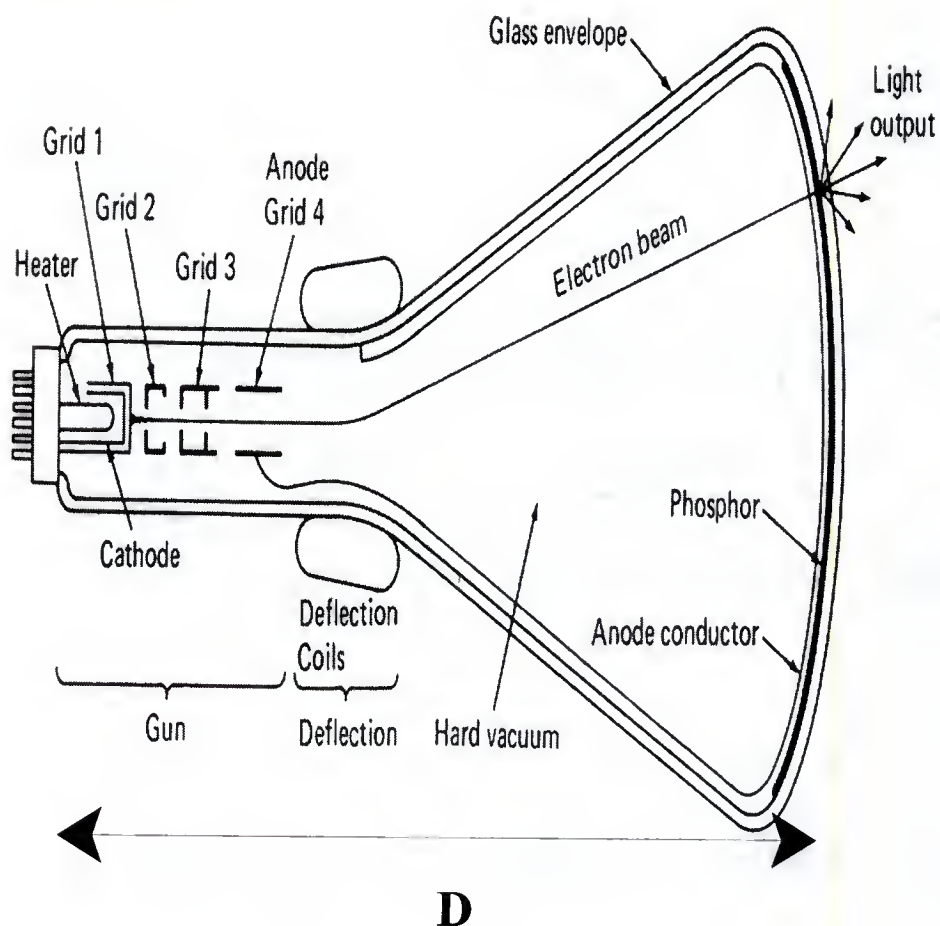
Figure 2-1   A cross section of a CRT tube with arrowed line exhibiting the relatively long working distance (labelled D above) required between the anode and cathode for proper raster and focus [Tan85]. Typical values of D for a CRT range from 25 to 100 cm.
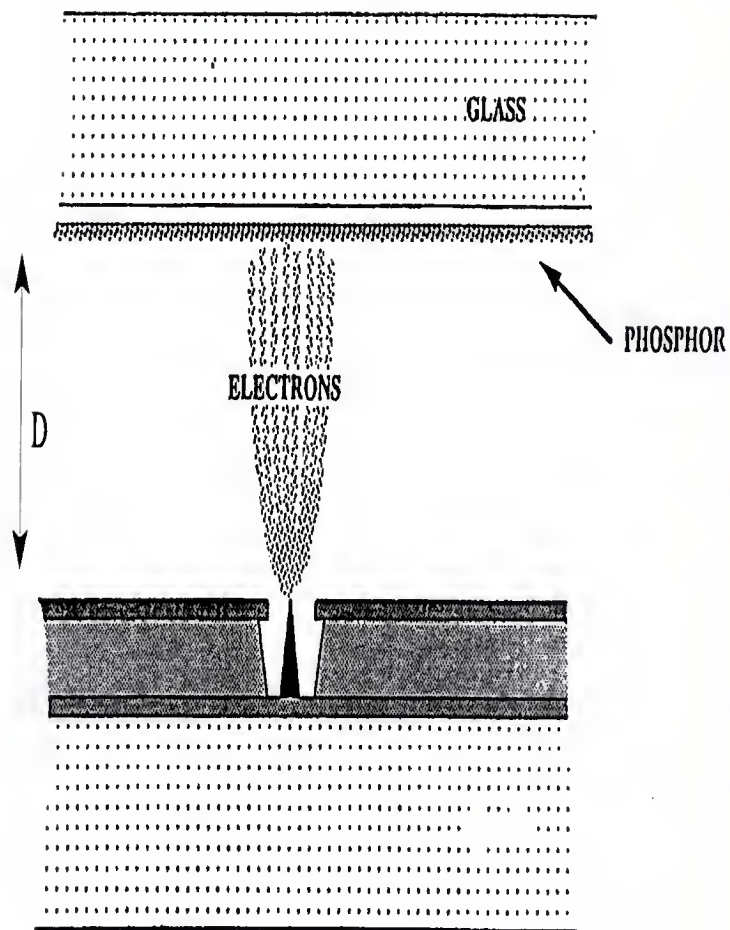
Figure 2-2   A cross section of a Spindt-type Field
Emission Display with vertical line, marked D,
indicating the working distance between the anode
and cathode of a field emission display. Typically D is
approximately 1mm [SCH96].
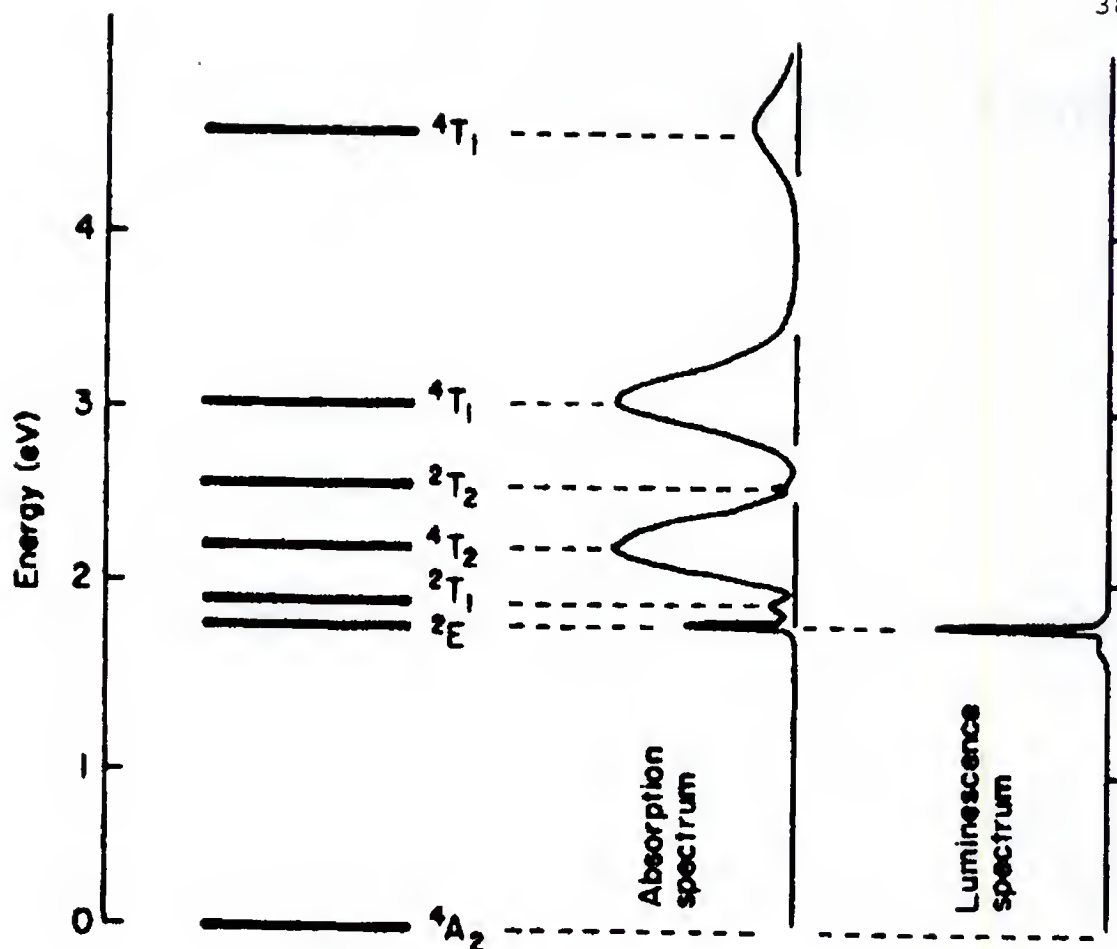
Figure 2-3   Absorption and luminescence spectra for
Cr^{3+} in Al_2O_3, also known as ruby. Absorption bands
exist for all transitions, but a visible luminescence
peak is only observed for the 2_E-$4A_2$ transition, as
this transition has the largest energy change, and
emits characteristic red luminescence. All other
transitions do occur, but are not in the visible region
of the spectrum [LUM78].
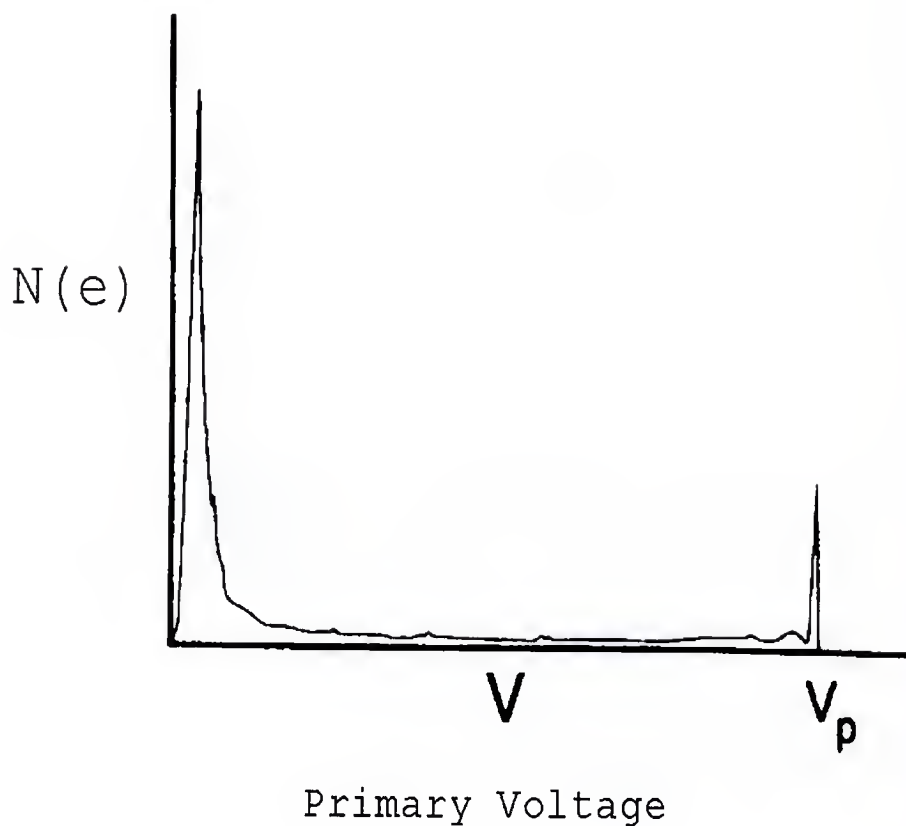
Figure 2-4   Total number of electrons leaving a surface as a function of energy under cathode ray excitation. Incident primary electrons which are elastically scattered are shown at energy V_p. True secondary electrons are depicted by the leftmost peak. Auger and Plasmon electrons are found at energies between the true secondary peak and the elastic peak [HUD92].
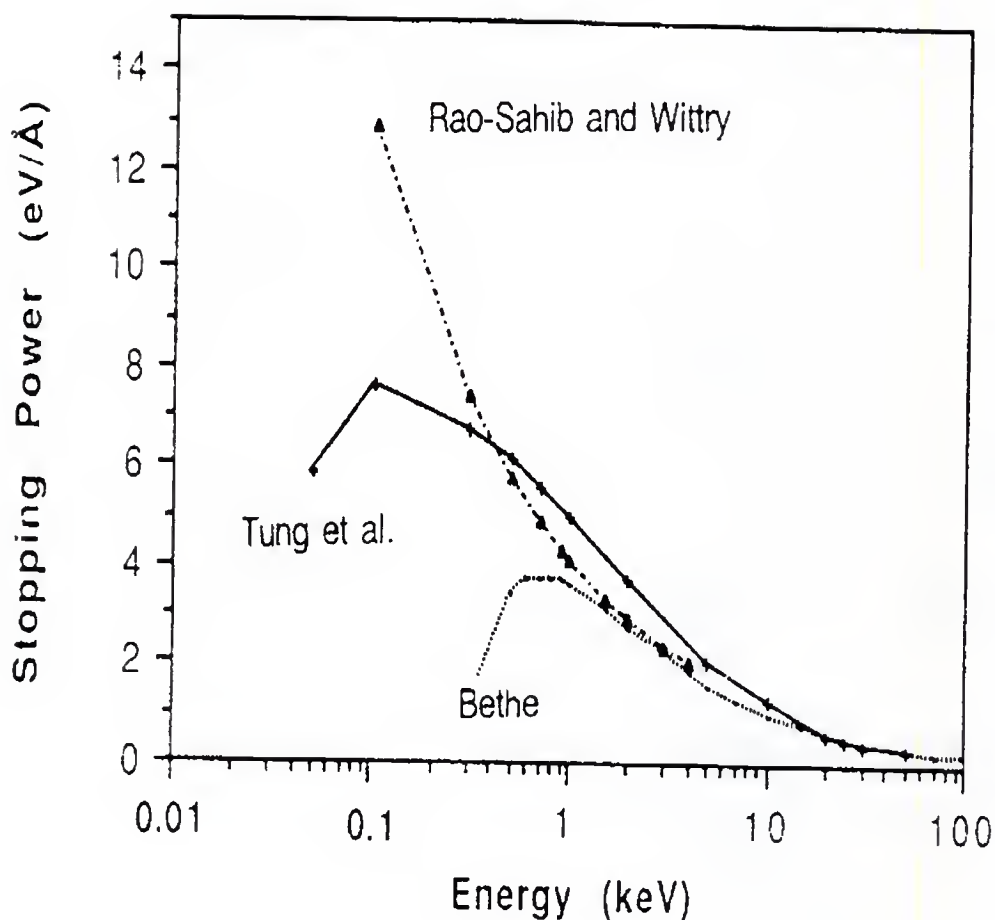
Figure 2-5   A comparison of stopping powers for electron- solid interactions. Dotted line denoted by Bethe depicts the stopping power calculated using Bethe's original stopping power equation. Dash-dot line shows the changes in low energy stopping power predicted with Rao-Sahibs and Wittrys' modification. These are compared to experimetally determined stopping powers by Tung et al. which are shown as a solid line[JOY89].
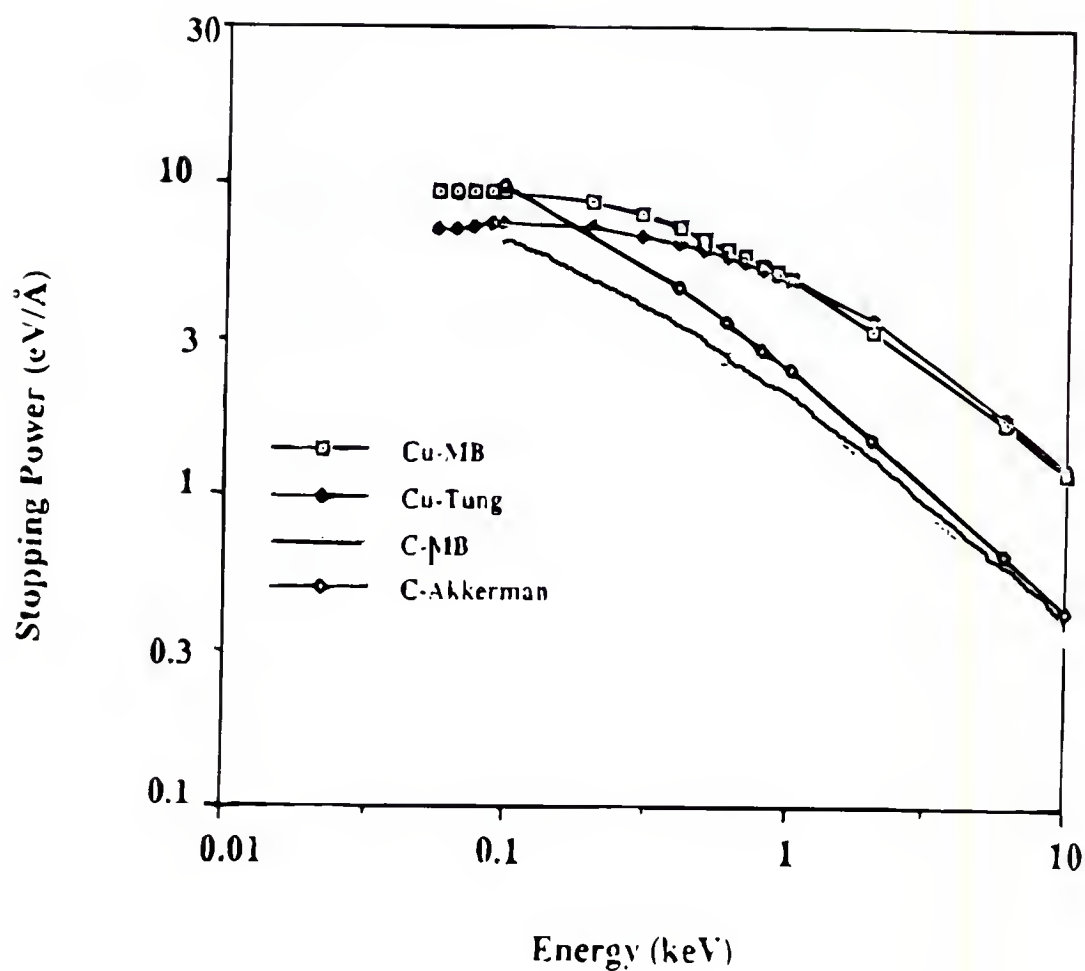
Figure 2-6   A graph comparing the stopping
powers found experimentally in C and Cu by Tung
and Akkerman to the calculated values found by Joy
and Luo using a modified Bethe expression which
allows the ionization potential to vary linearly
(Cu-MB or C-MB) with energy for energies below 1keV
[JOY89,TUN79].
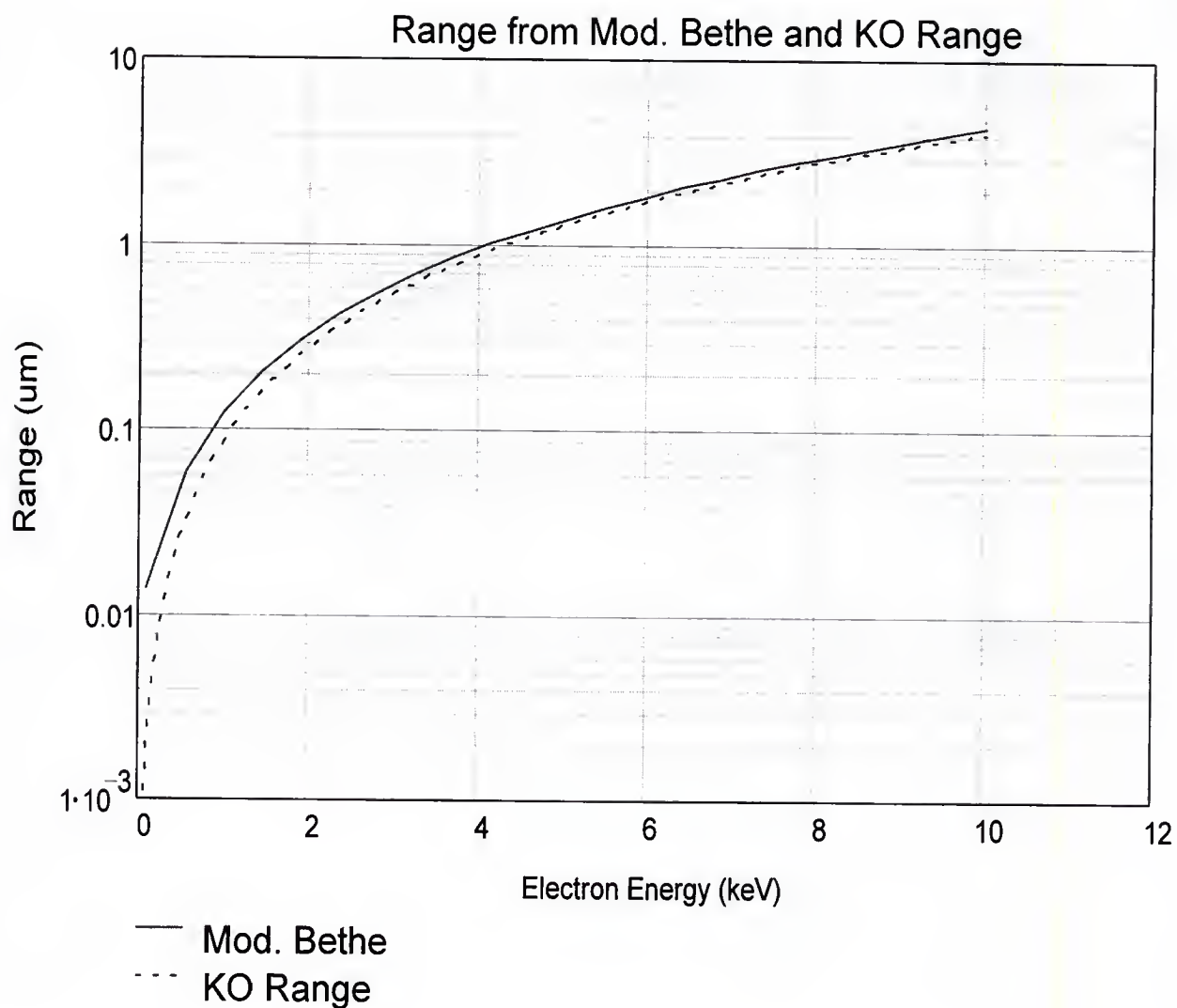
Figure 2-7   A comparison of Kanaya and Okayama range (dashed line), which includes a contribution from secondary electron-hole pair diffusion, to the modified Bethe Range (solid line) obtained by the Joy and Luo adaptation for low energy electrons. Reasonable agreement is found for the models except at very low energies (<500eV) where Joy and Luo approaches the residual range and Kanaya and Okayama range falls to zero.
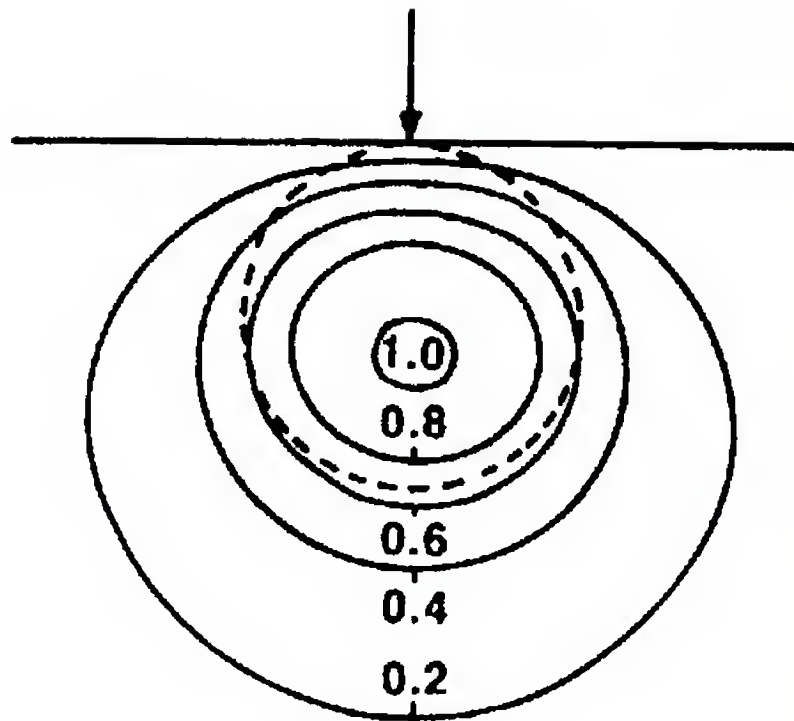
Figure 2-8   The distribution of excess minority carriers(solid lines) and the electron-hole pair generation volume(dashed line) are depicted for the universal depth-dose function. The highest concentration of electron hole pairs is found within the generation volume[YAC90].
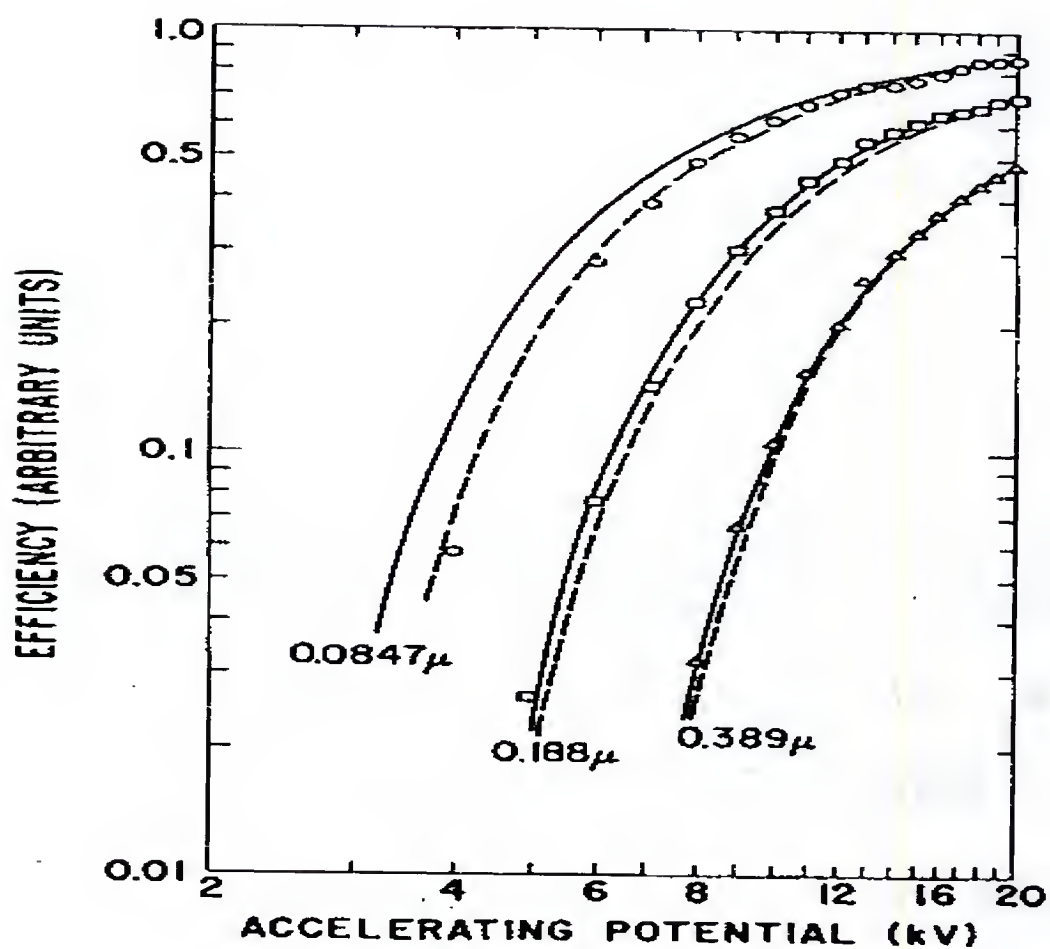
Figure 2-9   The theoretical (solid) and experimentally (dashed) determined CL efficiencies of ZnS:Cu with non-luminescent ZnS coatings of varying thicknesses are depicted and show good agreement over a wide range of accelerating potentials [KIN72].
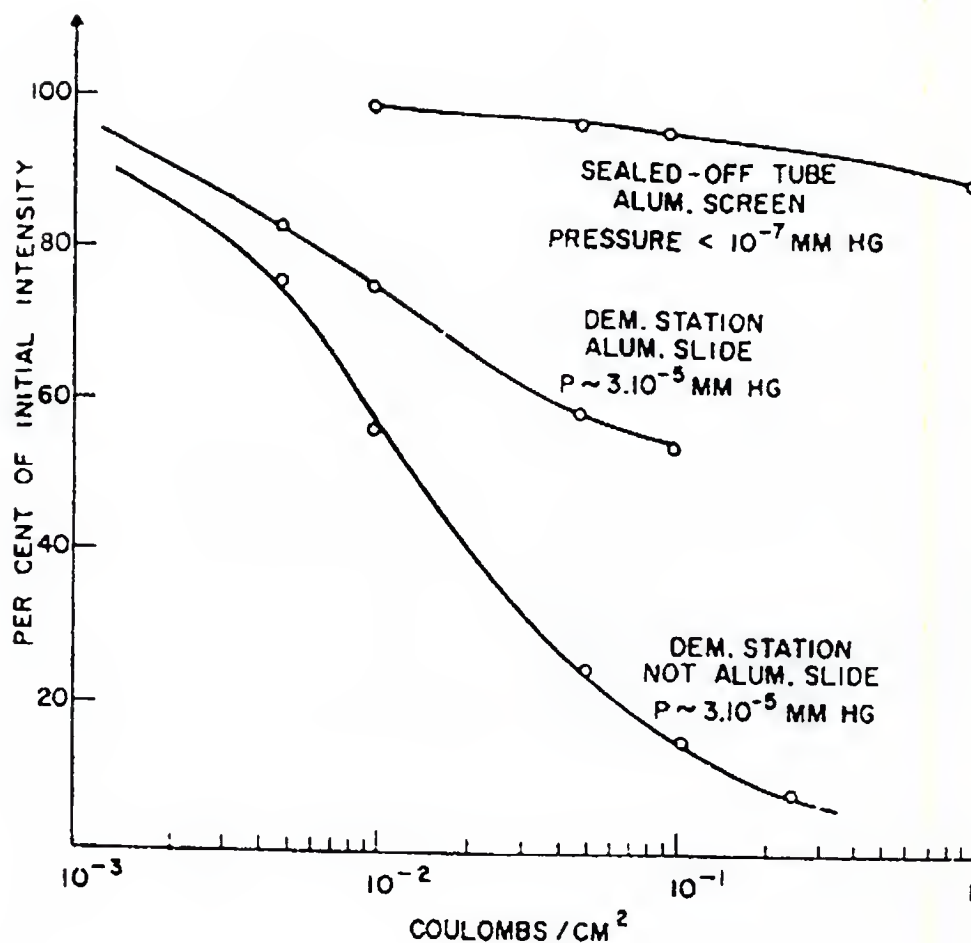
Figure 2-10   Zinc oxide degradation and the
effects of vacuum and aluminization on cathode
ray-induced CL degradation. Longer CL lifetimes
are found for phosphors which have been aluminized
and/or are operated in better vacuum conditions
[PFA61].
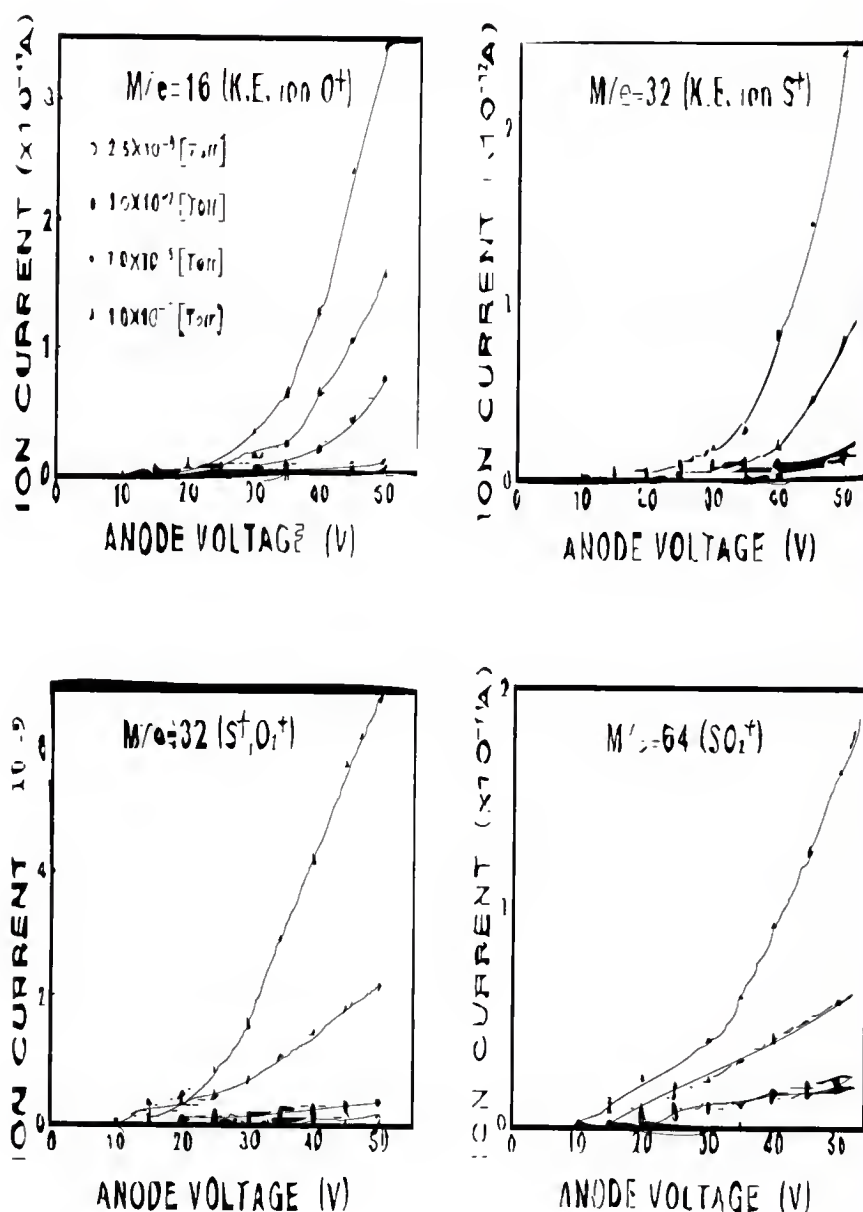
Figure 2-11 RGA (residual gas analysis) ion currents representing the desorption of species from ZnS under cathode ray excitation are shown. Increased desorption rates are found for S^-, SO_2^-, O^-, S^+ and O_2^+ for increasing anode potentials indicating the desorption of surface species under electron bombardment [ITO89].
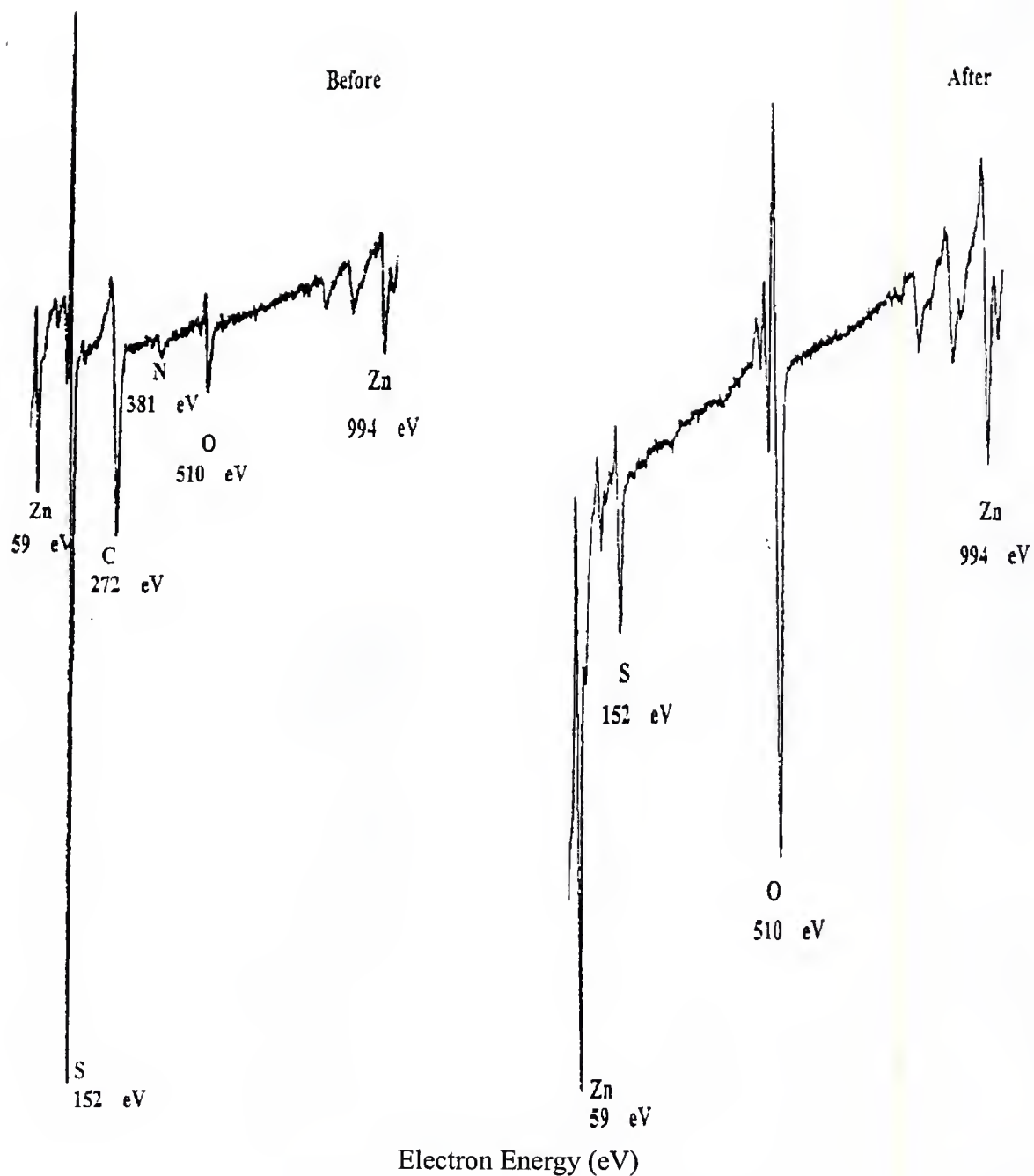
Figure 2-12   AES surface study of ZnS before and after electron beam aging. Note the loss of S (152eV) and C(272eV) with concurrent increases in Zn (59eV, 994eV) and O (510eV). The surface becomes sulfur depleted and oxygen rich[SWA96].
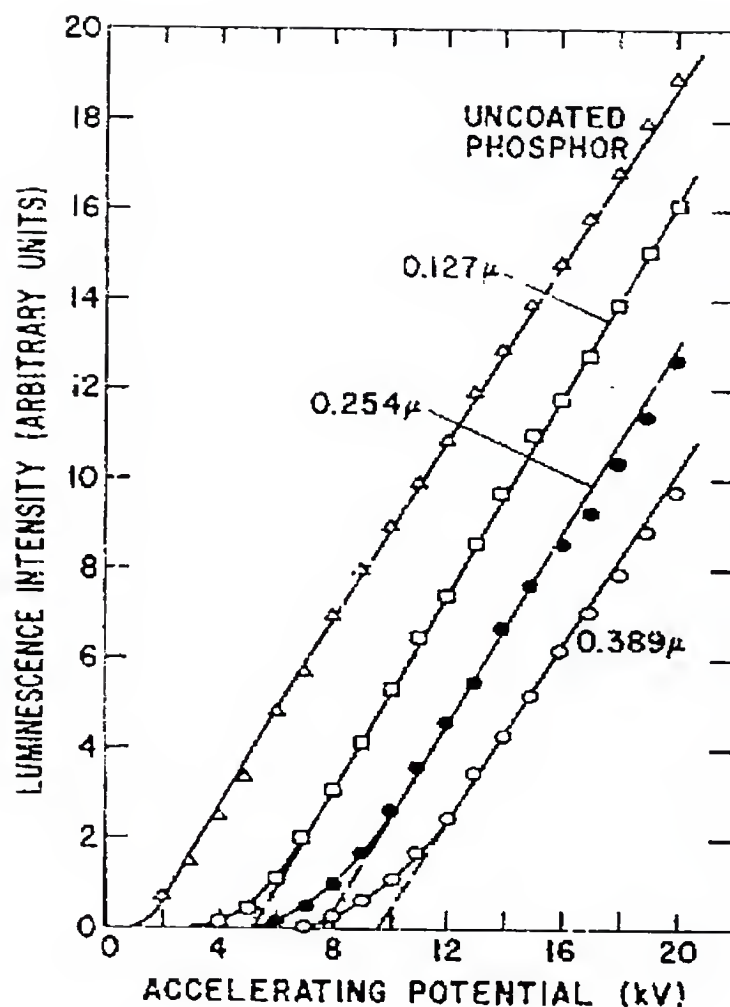
Figure 2-13   Luminescent intensity versus electron accelerating potential for ZnS:Cu with non-luminescent ZnS coatings of varying thicknesses. The linear portions of each curve are parallel, indicating no change in efficiency, only the threshold value is shifted to higher energy values by the increasing thickness of the dead layer which electrons must first pass through to excite cathodoluminescence [KIN72].
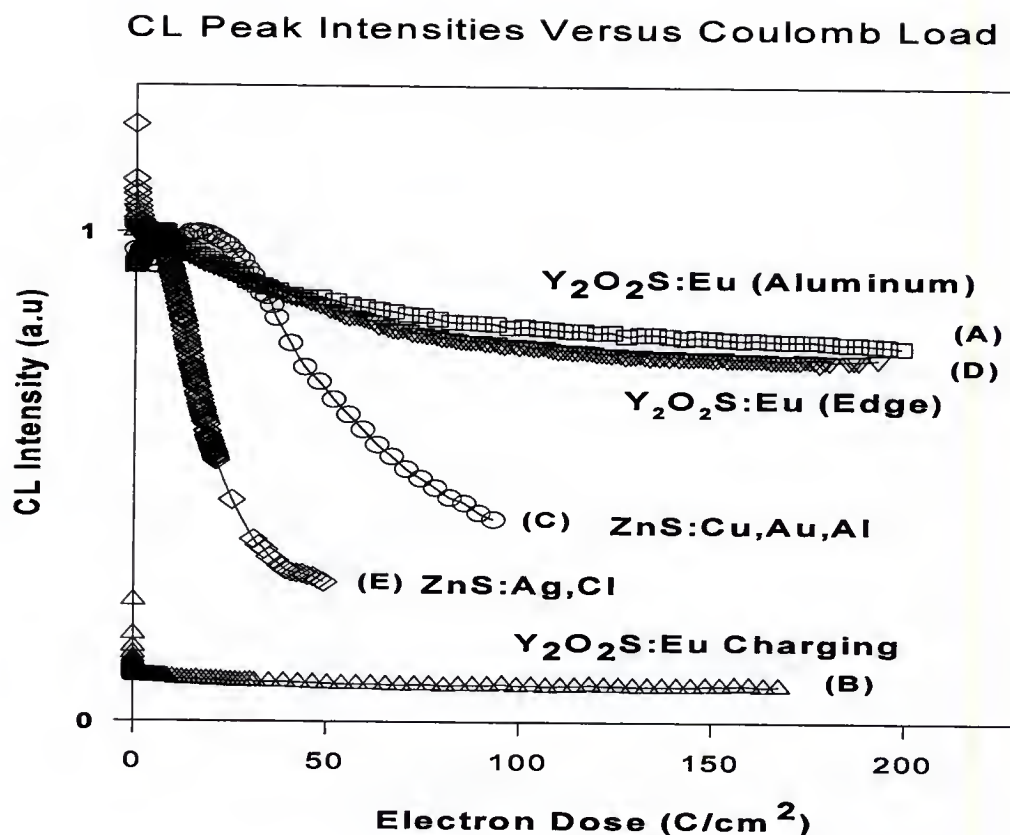
CL Peak Intensities Versus Coulomb Load

Figure 2-14   A comparison of degradation rates of $Y_2O_2S:Eu^{3+}$, ZnS:Ag, and ZnS:Cu cathode ray phosphors. Note that the ZnS:Ag and ZnS:Cu degrade at higher rates than does the $Y_2O_2S:Eu^{3+}$. Three seprate degradation curves are shown for $Y_2O_2S:Eu^{3+}$. Line A shows the degradation of $Y_2O_2S:Eu^{3+}$ with good contact to an aluminum holder. Line D shows the degradation of $Y_2O_2S:Eu^{3+}$ with nominal contact to the aluminum holder and Line B shows the degradation curve for $Y_2O_2S:Eu^{3+}$ with no contact to the aluminum holder. The thermal and electrical conductivity decreases with each successive move away from the aluminum holder, and the effects of this change are easily seen [TRO96].
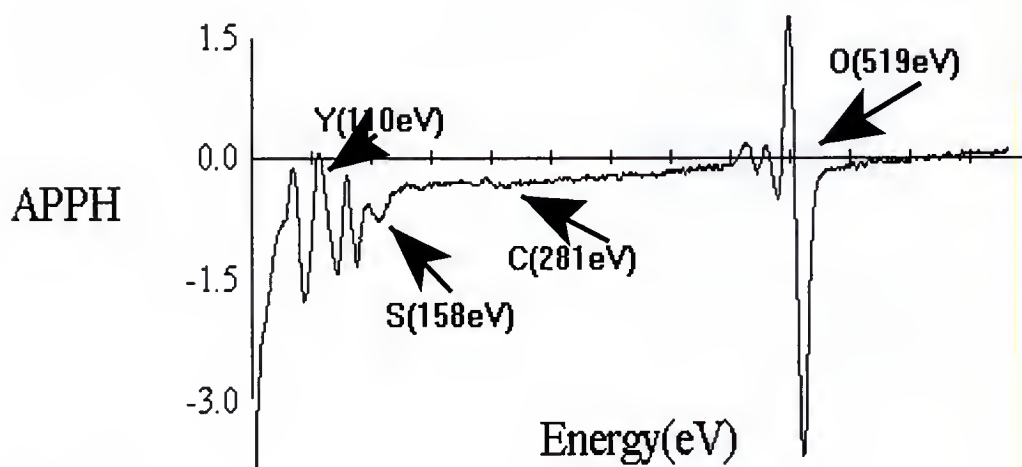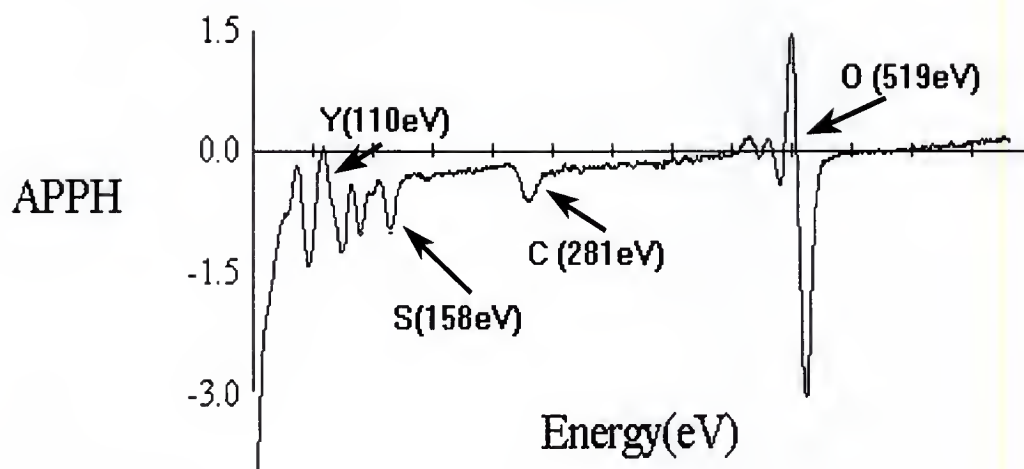
Figure 2-15   Depicts the surface state exhibited by $Y_2O_2S:Eu^{3+}$ before and after electron beam aging. Note the loss of C (281eV) and S (158eV) with concurrent increases in Y (110eV) and O (519eV) after the phosphor has been exposed to prolonged electron beam excitation [TRO96].

TABLE I

Burn Characteristics of P-type Phosphors Excited with 10 kV Electrons

Phosphor	P-No.	Use	Chemical Composition	Activator	$1/C$ = No. of coulombs/cm² Necessary to Reduce I to $\frac{1}{2}I_0$	Electron Burn Constant $C \times 10^{19}$, cm²		H₂⁺ ion Burn Constant, $C \times 10^{12}$ cm²	Reduction in Decay Time	
						These Measurements	Others		%	After coulombs/cm²
Ce⁺⁺⁺ activated Silicates	P16	Flying Spot Scanner	$(CaO)_2.MgO.(SiO_2)_2$	Ce	About 10⁻¹	10			60	10⁻²
	P16	Flying Spot Scanner	$CaO.Al_2O_3.SiO_2$	Ce		10				
Sulfur dominated, Ag and Cu activated	P2	Oscilloscopes	Zn SCdS	Cu	11.9	0.140			15	100
	P4	Direct View TV, (Blend)	ZnS / ZnSCdS/ZnS	Ag	4.5	0.370		0.43[11]	25	112
	P7	Cascade Screens for Oscilloscopes	ZnS	Ag	9.9	0.170			40	130
			ZnCdS	Cu	10.0	0.167			30	150
	P11	Photography	ZnS	Ag	16.6	0.100	0.08 0.13[3]	0.35 - 0.70[4,11,5]	17	150
	P14	Radar	ZnCdS	Cu	16.6	0.100			25	100
	P22	Projection Color TV	ZnS	Ag	20.0	0.083		0.35[4]	30	110
			ZnS	Ag, Al	33.3 —	0.050			23	175
Oxygen and Sulfur dominated, Mn and Ti activated	P1	Scopes Radar	Zn_2SiO_4	Mn	104.0	0.016	0.01[3]	0.02[11,5]	25	65
	P4	Projection TV	$CaO.MgO.SiO_2$	Ti	55.5	0.030				
	P4	black and white	$ZnO.BeO.SiO_2$	Mn	83.5	0.020		0.02[4]		
	P4	Red TV, Projection	$Zn.Mg.Cd.SiO_3$	Mn	16.6	0.100				
	—		ZnS	Mn				0.06[11]		
Oxygen dominated	P15	Flying Spot Scanner	ZnO	—	33.5	0.050			20	100
	P24	Flying Spot Scanner	ZnO	Zn	33.5	0.050		0.02[4]	20	100
	P5	Oscilloscopes	$CaWO_4$	—	16.6	0.100		0.004[6,11]	07	150
Other	—		$BaSO_4$	Pb	About 10⁻¹	10				

Table 2-1   A comparison of degradation costants for a large number of phosphors. 1/C values denote the total coulomb load required to reduce the initial brightness of the phosphor to half of its value. The larger values indicate phosphors which resist degradation [PFA61,BLI57,GIL56,MAR57,ROT55].

Phosphors	Probability S	Efficiencies (%)		First-trapped Carriers	ϵ $(\times E_g)$	E_g (eV)	E_m (eV)
		Calculate	Reported				
ZnS:Ag:Cl	0.66	23	23	hole	2	3.8	2.75
ZnS:Cu:Al	0.66	21	19—21	hole	2	3.8	2.32
Y_2O_2S:Eu	0.66	13	13	electron	2	4.7	1.98
Y_2O_2S:Tb	0.8—1.0	19—24	19	hole	2	4.7	2.29
La_2O_2S:Eu	0.5	10	11	electron	2	4.7	1.98
La_2O_2S:Tb	0.5	13	12	hole	2	4.7	2.29
Y_2O_3:Eu	0.8	7	7	electron	4	5.8	2.03
YVO_4:Eu	0.66	8	8	electron	4	4.0	2.0
Zn_2SiO_4:Mn	0.8	9	8	hole	4	5.5	2.36

Table 2-2   External radiant efficiencies for a number of phosphors including ZnS:Ag,Cl, ZnS:Cu,Au,Al and Y_2O_2S:Eu^{3+} [OZA90].

CHAPTER 3
EXPERIMENTAL APPROACH

Introduction

$Y_2O_2S:Eu^{3+}$ phosphor powders, designated P22R, used in this study were obtained from Osram Sylvania through the Phosphor Technology Center of Excellence. P22R is the standard, red phosphor used in the manufacture of CRT screens. The P22R phosphor was manufactured by the sulfide fusion industrial process [KOT95]. The powder consists of faceted particles with an average diameter of 4.5 μm and a range of sizes from 1 to 10μm. The details of the sulfide fusion formation process is discussed below in greater detail.

Two techniques were used to apply coatings to the base phosphor material. Wet chemistry techniques, and pulsed laser ablation were used to deposit coatings on single particles.

The phosphor particles were characterized by various techniques including cathodoluminescent spectroscopy, Auger electron spectroscopy (AES), and scanning electron microscopy (SEM). The phosphor manufacturing processes, methods of coating the particles, and techniques used for characterization are discussed in the following chapter.

Phosphor Material

Industrially Processed Yttrium Oxysulfide Phosphor

The standard industrial procedure for producing a Eu^{3+} activated Y_2O_2S phosphor is by a sulfide fusion process which involves a solid-melt reaction between the rare-earth sesquioxides (Y_2O_3 and Eu_2O_3) [KOT95]. The general chemical reaction is as follows:

$$(1-y)Y_2O_3 + yEu_2O_3 + S \iff Y_{2(1-y)}Eu_{2y}O_2S + \tfrac{1}{2} O_2.$$

This reaction is assisted by Na_2CO_3 and other fluxes. Depending on the desired Eu content of the product, y can take on values from 0.00 to 0.04.

During this reaction, S reacts with the Na_2CO_3 flux which produces polysulfides [PHA91]:

$$2Na_2CO_3 + 5S <> \frac{1}{2} Na_2SO_4 + 3/2\ Na_2S_3 + 2CO_3 + H_2S + SO_2.$$
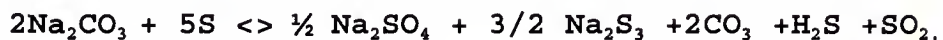
In order to increase the efficiency of the overall reaction, the reactants are initially ball-milled for homogenization. The mixture is placed in an alumina crucible and heated in a flowing nitrogen atmosphere to 1100 C for 4 hours. The solid-melt reaction takes place and an ingot is formed. The ingot is cooled to room temperature by an air quench, then reduced to a fine powder again by ball milling. The final product is washed in hot DI water and 2% HCL several times to remove the flux, residual sulfur, and polysulfides [YOC97].

Methods of Applying Coatings to Phosphors

Wet Chemistry Coatings

A number of coatings were applied by modified wet chemical techniques which were developed for use in the

phosphor screening industry. Silica (SiO_2), thoria (ThO_2), and phosphate (PO_4^{3-}) coatings have been deposited by wet chemical techniques which are described in the literature [SIL83, HAY69, KOM96, JAC95]. Silica, and phosphate coatings have been used for years in the phosphor industry as dispersing agents prior to the application of the phosphor to the screen and the chemistries associated with these types of coatings are well defined.

Prior to the wet chemical coating process, a small quantity (typically 20 grams) of industrially processed $Y_2O_2S:Eu^{3+}$ from Osram Sylvania was suspended in a solution of 0.1M HCL. The powder was slurried for 1 hour using a magnetic stir plate, decanted and filtered (#110 Fine Buckner filter) with two methanol rinses. A final DI water rinse was used to remove any residual impurities. The compacted cake was placed in a 120 C oven overnight (minimum 8 hours) to bake off excess water. The compact was ground by hand using a mortar and pestel. This powder was then used for all wet chemistry coatings that follow.

Phosphate Coating

In order to produce a phosphate (PO_4^{3-}) coating, a 0.1 M solution of phosphoric acid was prepared. The phosphor

powder was slowly added to the acid and the mixture was slurried for various times and temperatures, depending on the desired coating. Slurry times of 30 minutes to 2 hours were used, at temperatures ranging from 25 C to 80 C. Typically, the coatings would cover more particle surface area with longer slurry times and higher temperatures. The chemical reaction proceeded with noticeable evolution of H_2S detected by its odor.

The mixture was removed from the stirrer and decanted through a #110 fine Buckner filter. The powder was then rinsed with methanol twice, and finally rinsed with DI water. The powder compact was air baked for a minimum of 8 hours at 120 C to remove excess water. The dried compact was hand crushed by mortar and pestel. The phosphate coated powders were stored in a desiccator until characterized.

SiO_2 Coating

SiO_2 coatings have been used for many years in vacuum fluorescent displays (VFDs). The coating is applied in order to keep the particles adherent to the anode of the screen. No aluminization of the phosphor screen can be utilized due to the low energy electron penetration limits in VFDs.

The phosphor powder was slurried in DI water for approximately 1 hour by a magnetic stir plate and then transferred to a sonicator. The sonicator was used to break up agglomerates of phosphor particles prior to coating. Typically, the slurry was sonicated for 10 minutes and returned to the coating fume hood.

In the hood, the slurry process was re-initiated and LUDOX was dropper fed into the slurry. LUDOX is the Dow Chemical trade name for a SiO_2 nanoparticle sol. The mixture was slurried at room temperature for 1 hour, then decanted and filtered through #541 fine filter paper. The compact was DI water rinsed and methanol rinsed. Unlike the phosphate coating, which was produced by a chemical reaction, the SiO_2 coating occurs due to the attractive surface potentials associated with the phosphor particle and the SiO_2 nanoparticles.

Once decanted and rinsed, the powder compact was transferred to an oven and air baked at 120 C for 24 hours to remove excess water and methyl alcohol. The completed compact was crushed by mortar and pestel and stored in a desiccator until further characterization was required.

Pulsed Laser Ablation

Recently, pulsed laser ablation has been used to coat particles with diameters ranging from 1 to 1000 μm [FIT97]. The pulsed laser ablation system consisted of a Lamda Physik excimer laser and a vacuum chamber. The beam enters the vacuum chamber through a quartz viewport where it strikes a target material. The energy and power of the laser is sufficient to ablate atomic and molecular species from the target. These ablated particles produce a visible plume of material inside the vacuum chamber. Figure 3-1 shows details of the pulsed laser ablation system used to coat phosphor particles.

The P22R particles were introduced into the plume and agitated by means of a motorized shaker [FIT97]. The ablated target material formed a thin transparent coating on the phosphor particles. Pulsed laser ablation has been used to coat particles with up to 70% surface coverage and thicknesses from 5 to 30 nm in the following systems; TiO_2 on Al_2O_3, Ag on Al_2O_3, $YBa_2Cu_3O_7$ on Al_2O_3, TiO_2 on SiO_2 and Ag on SiO_2 [FIT97]. Pulsed laser ablation was used to produce

thin metal (Ag) and intermetallic TaSi coatings on the surfaces of the P22R particles.

Characterization Techniques

Cathodoluminescent and Auger Electron Spectroscopy

Since both cathodoluminescent spectroscopy (CL) and Auger electron spectroscopy (AES) data were collected concurrently from the same spot on the same sample using the same electron beam, both techniques will be discussed in this section. P22R phosphor was cold pressed into a 1/4 inch diameter dimple in a stainless steel holder, and mounted in the AES chamber. The AES spectrometer is a Physical Electronics model 545 with a cylindrical mirror analyzer and a lock-in amplifier detector. The primary beam energy ranged from 1 to 3 keV with currents between $1\mu A$ and $15\mu A$. Data was collected in the dN/dE mode using a 4eV peak-to-peak modulation voltage. Auger peaks from Y (77eV-MNN), S (152eV-LMM), C (272 eV-KLL), and O (502 eV-KLL) were recorded. The chamber was rough pumped to $1*10^{-3}$ Torr by two cryo-sorption pumps. Cross over to the high vacuum ion pump, a Perkin

Elmer Ultek DI 800 l/s, was accomplished by closing the roughing valve and opening the poppet valve to the ion pump. The entire system was then wrapped in aluminum foil and baked to 200 C by heater tapes wrapped around the system for 8 hours. The bake-out is used for desorbing gases, mainly H_2O, from the chamber walls and allowing those gases to be removed from the system by the ion pump.

The system was cooled after bake-out. Vacuum pressures were measured by a Granville Phillips ionization gauge and controller. Base system pressures varied from $9X10^{-9}$ Torr to $2X10^{-8}$ Torr.

Typical AES operating parameters were 1, 2, or 3 kV primary beam energies, with sample current densities of 200 to 300 $\mu A/cm^2$. The AES spectra, Auger peak-to-peak heights (APPHs) and cylindrical mirror analyzer (CMA) pass energy, were sampled and stored on an PC compatible computer by an analog to digital converter and software developed by the author. Sampling delay was 0.2 seconds per point with two channels of data being recorded simultaneously. CL data was collected by an Oriel Instaspec IV CCD spectrometer. Maximum CL peak height, integrated CL area (550-750nm), and spectral

distribution (intensity as a function of wavelength) were acquired.

To determine the effects of the type and pressure of gas in the system on phosphor degradation, the steady state pressure was increased. For typical residual gas with no specific composition, the poppet valve was partially closed and the pressure rose in the chamber. The steady state pressure could be varied or maintained by adjusting the closure of the poppet valve. System pressures during AES and CL analysis ranged from $2x10^{-8}$ to $1x10^{-6}$ Torr.

For high partial pressures of oxygen, a gas bottle was attached to the system through vacuum compatible seals. The poppet valve was slowly closed until a small pressure rise in the system was observed. A leak valve attached between the system and the oxygen bottle was slowly opened until the desired pressure was achieved. This method allowed known partial pressures of oxygen gas ($2x10^{-8}$ to $1x10^{-6}$ Torr) to be introduced into the system.

Degradation Experiment

The phosphors were cold pressed without binder into an stainless steel dimple and mounted onto the carousel which was placed in the ultra high vacuum AES system. After a base

pressure of better than 2×10^{-8} Torr was reached, the oxysulfide phosphors were subjected to electron beam bombardment at pressures from 1×10^{-8} Torr to 1×10^{-6} Torr background or backfilled gas. Figure 3-2 shows a diagram of the experimental setup.

AES was used to characterize the surface composition and any changes in it. Primary beam energies of 1, 2, or 3 keV with a continuous current density of 200-300 $\mu A/cm^2$ was used. Auger spectra were repetitively recorded and monitored from 30 eV to 700 eV over the duration of the experiments (typically 24 hours).

Cathodoluminescent data were also recorded simultaneously by an Oriel Instaspec IV CCD camera and monochromator. The monochromator used a 600 line/mm grating which allowed a 200 nm scan width with 0.7nm resolution. The spectral distribution and total area under the emission peaks were recorded from the phosphor. CL intensity as a function of wavelength, along with peak intensities and total integrated area (from 550nm to 750nm) were recorded concurrently with the AES data. The CL software was programmed to take one 25ms exposure per minute for 24 hours.

Upon completion of a 24 hour experiment, the AES and CL data were reduced and compared. Reduction of the AES data typically required software measurements of APPHs for carbon, oxygen, sulfur, yttrium, and any other elements contained within the coatings.

Conversion of Time and Current Density to Coulomb Load

Typically, due to the wide variations in spot size, beam current, sample current and time of electron beam exposure, CL degradation experiments have used total coulomb load (or dose) as the dependant variable for comparison. Total coulomb load is a direct measure of the number of electrons passing through a surface due to an electron beam. The total coulomb load is calculable knowing the beam spot size, the sample current (measurement of which specified above in C/s), and the time for electron beam exposure.

$$CoulombLoad(\frac{C}{cm^2}) = Current(\frac{Coulomb}{Sec}) * \frac{1}{Area}(cm^2) * Time(Sec)$$

By measuring the sample current with the picoammeter as shown in Figure 3-3, and knowing the area of the spot size by optical measurements, the time of exposure can be calculated from the time for a repetitive auger scan or from software settings on the CL spectrometer and the total

coulomb load can be calculated. The phosphate coated phosphor exhibited a distinct surface darkening during electron beam bombardment. This spot was used to estimate the beam spot size. This size was assumed for all other experiments.

Turn-On Voltage Experiment

The primary beam voltage of the AES was set to 7 kV, and the sample current was set at 0.2 $\mu A/cm^2$. Low current densities were chosen in order to avoid phosphor saturation (the point at which the brightness no longer increases as the accelerating voltage is increased at constant current) issues at all beam voltages. Figure 3-3 shows the method used to measure sample current by placing a 90 Volt battery and a picoammeter in series with the sample while the electron beam to strikes the stainless steel holder. The battery is used to return low energy secondary electrons which are emitted from the surface to the sample holder. This is necessary because the sample current is the sum of the secondary emitted electrons and the ground current. Without the use of the battery, the sample current measured would be only 10% of the actual sample current. After setting the sample current, the accelerating voltage was

turned off and the sample carousel was turned to align the phosphor with the electron beam. With the initial alignment completed, the system was sealed so that no external light could enter. The pressure in the system was recorded and the ionization gauge filament was turned off. To reduce internal shot noise, the CCD array was cooled to 27 C by an internal thermo-electric cooler.

The CL spectrum from a 25 millisecond background exposure was recorded and used to remove spurious signals from the phosphor cathodoluminescent signal. The electron beam was turned on and a single CL spectra was recorded with a 25 millisecond exposure. The spectrometer software calculated the area under the curve of the CL signal from 550 to 750 nm, and both the integrated area and CL spectra were saved in a manipulable file format. The electron beam was turned off and the accelerating voltage was adjusted to 6.5 kV and the process was repeated from 7 kV down to as low as 0.2 kV. Each reduction in accelerating voltage required a verification of the sample current to insure constant current during the entire experiment. Random data points in the specified range were sometimes recorded to determine the actual phosphor turn-on voltage more accurately.

A graph of the normalized CL area (total brightness), as a function of accelerating voltage was used to extrapolate the turn-on voltage of the phosphor. The turn-On voltage was identified as the Y = 0 intercept on the voltage axis before saturation. Figure 3-4 shows a typical extrapolation to determine a phosphor's turn-on voltage.

Scanning Electron Microscopy

Scanning electron microscopy (SEM), was used to examine the surface morphology of the phosphor particles. A JEOL 35C operating at 15kV and a working distance of 39 millimeters was used. The sample was normally tilted at 30 degrees to increase the signal from the surface and produce a better image. To prepare a sample for SEM, a thin layer of particles was applied to one side of double sided sticky tape. The other side of the tape was then attached to a standard SEM holder. Due to the highly insulating nature of the phosphor particles and tape, a thin Au-Pd coating was sputter deposited using a Technics D.C sputter system to decrease charging phenomena in the SEM. The coatings were 100 to 150nm thick.
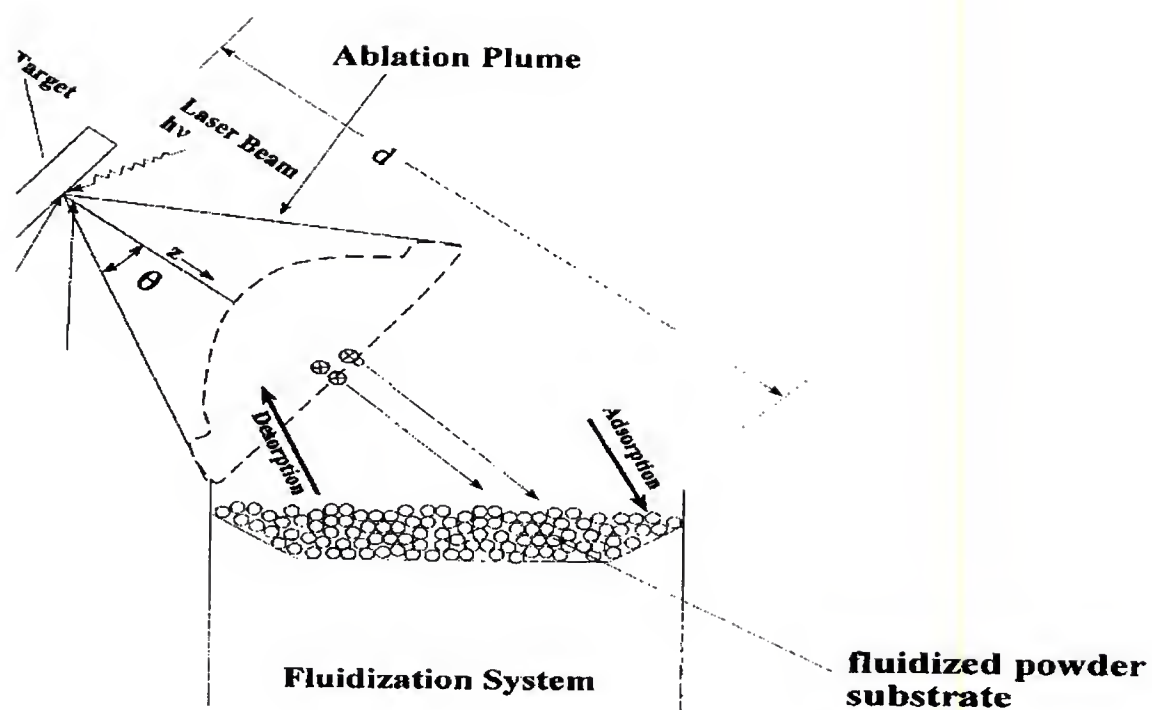
Figure 3-1   Depiction of Pulsed Laser ablation system showing the laser, target, ablation plume, motorized shaker and phosphor bed (bottom center) [FIT97]. This apparatus was used to produce nano-particle coatings of TaSi and Ag on the P22R phosphor particles.

AES/CL Experimental Setup
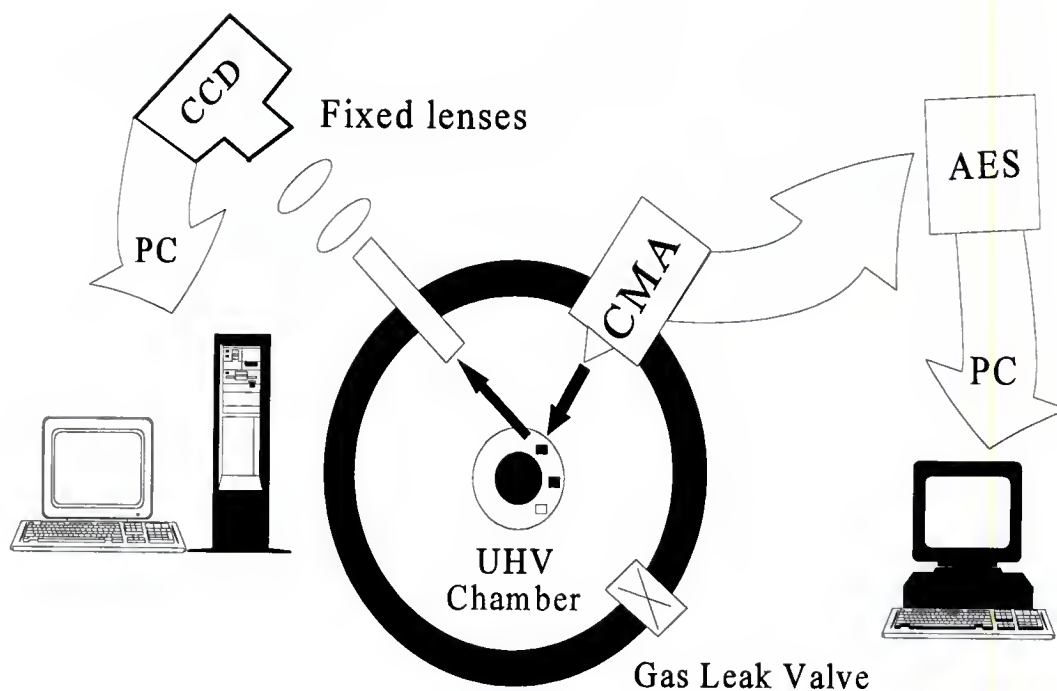
Figure 3-2   Auger electron spectrometer and cathodoluminescent system setup. The system was designed to be able to operate both measurement systems concurrently. The electron beam of the Auger system induced cathodoluminescence in the phosphor which was measured by the CL spectrometer.
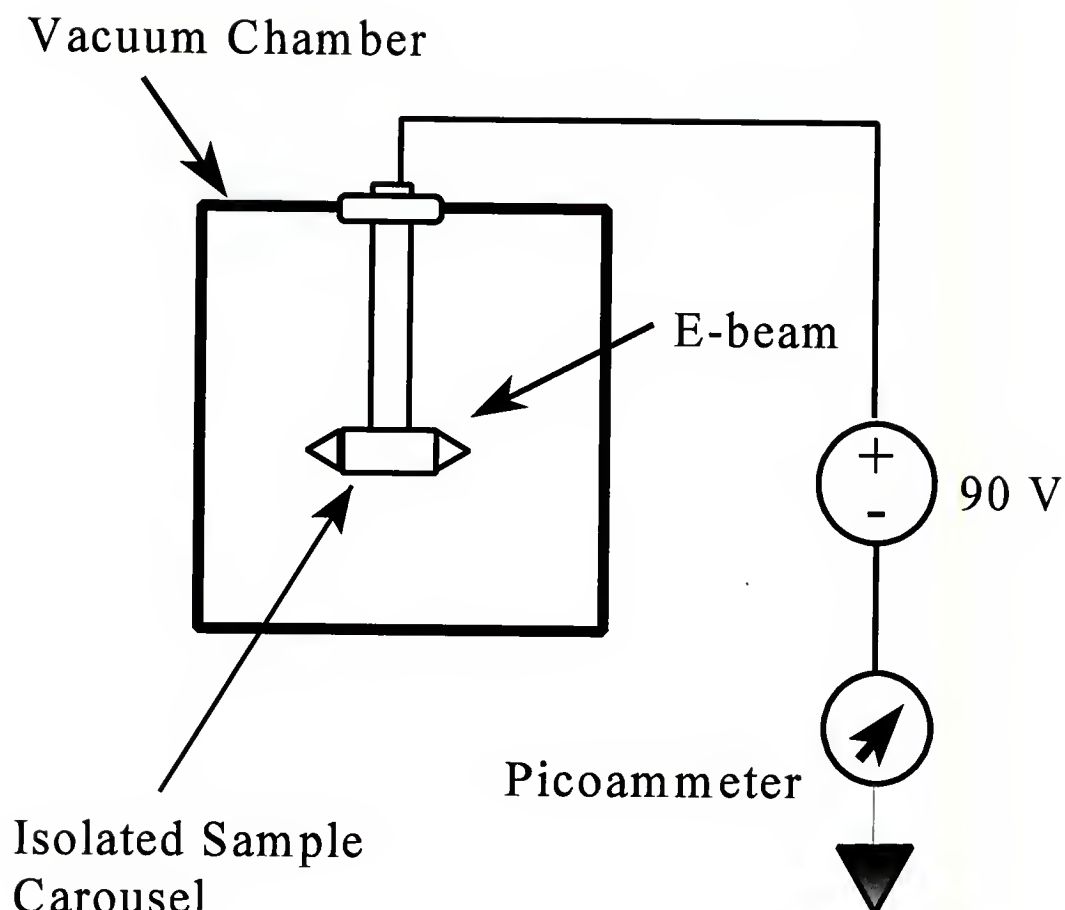
Figure 3-3   Sample current measurement is
accomplished by connecting a 90 volt battery and
picoammeter in series with the isolated sample
carousel. The current measured is the sum of the
primary current and the secondary electron current
which has been re-attracted to the sample by the field
of the battery.
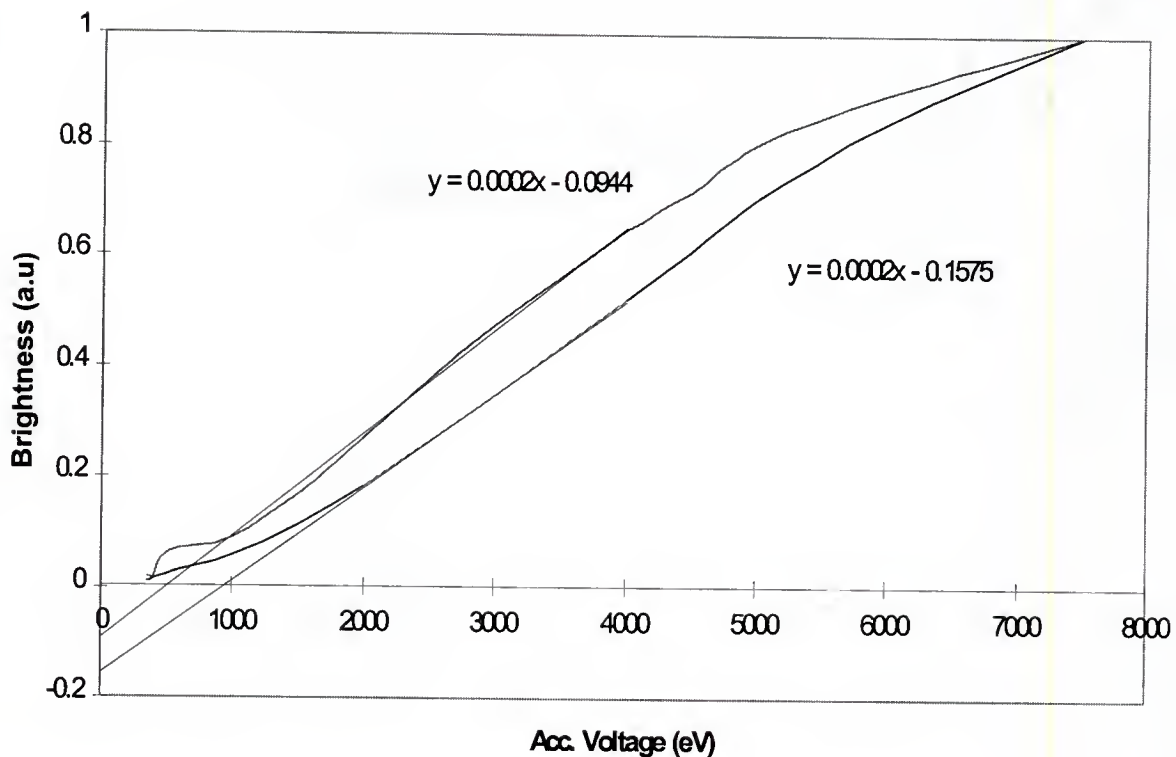
Figure 3-4   Example of turn-on voltage determination
from brightness versus accelerating voltage data. A
straight line is drawn from the linear portion of
the curves and extrapolated to the intersection of y=0
on the x-axis. This voltage value is known as the
turn-on voltage and is a measure of the energy at which
the phosphor cathodoluminescence becomes measurable.
The linear equations displayed are fits of the straight
line approximations and can be used to determine the
turn-on voltages.

CHAPTER 4

BASELINE STUDIES OF $Y_2O_2S:EU^{3+}$

Introduction

This chapter will discuss the results of CL degradation

experiments conducted on $Y_2O_2S:Eu^{3+}$ (P22R) powder phosphor.

AES and CL spectroscopy were used to study the degradation

phenomena. AES surface spectra were measured at various

coulomb doses up to ~ 20 C/cm² using a 2keV electron beam

and a current density of 272 $\mu A/cm^2$. The experiment was

conducted in the best vacuum available (typically ~1x10⁻⁸

Torr) in the AES spectrometer and Auger peak-to-peak heights

(APPH) as well as Auger peak energies for Y, C, S and O were

recorded during electron bombardment. The initial and final

CL spectra were recorded along with the total brightness,

and the wavelength for maximum emission. Threshold voltage experiments (see Chapter 2) were conducted prior to and after electron beam aging of the sample to examine the relative changes in brightness at constant current as well as to determine the change in threshold voltage due to CL degradation.

Physical and Luminescent Properties of $Y_2O_2S:Eu^{3+}$

In order to better understand CL degradation, the basic physical and luminescent properties of $Y_2O_2S:Eu^{3+}$ phosphor were studied. SEM was used to examine particle size and morphology and x-ray diffraction was used to examine the crystal structure of the phosphor. The CL degradation characteristics of $Y_2O_2S:Eu^{3+}$ were also examined using AES analysis and CL spectroscopy. The degradation of $Y_2O_2S:Eu^{3+}$ was carried out in typical FED operating conditions to obtain a baseline for comparison with other experiments reported in future chapters.

Physical properties of $Y_2O_2S:Eu^{3+}$

SEM images, as shown in figure 4-1, shows that $Y_2O_2S:Eu^{3+}$ particles were faceted with sizes ranging from 1 to 10 μm with an average particle size of 4.5μm. X-ray powder diffraction was used to determine the crystal structure of the $Y_2O_2S:Eu^{3+}$ particles and Figure 4-2 shows the X-ray intensity as a function of 2$\ominus$ angle. The upper portion of Figure 4-2 is the experimental diffraction spectrum obtained from the powder, and the lower portion is the expected peak positions and intensities for a hexagonal Y_2O_2S structure obtained from the JCPDS files (card #:24-1424). The peaks in the X-ray spectrum have been assigned Miller indices as shown in figure 4-2. The excellent correlation between the experimental data and the JCPDS file data suggests that the $Y_2O_2S:Eu^{3+}$ powder has a hexagonal structure with lattice parameters of a=3.284Å and c=6.509Å. Figure 4-3 depicts 1/3 of the aforementioned unit cell. Three such rhombehedral subunits combine to form the hexagonal Y_2O_2S unit cell. Each rhombehedral structure contains one molecule of $Y_2O_2S:Eu^{3+}$.

Luminescent properties of $Y_2O_2S:Eu^{3+}$

The CL intensity spectrum as a function of wavelength from an unaged (as received) $Y_2O_2S:Eu^{3+}$ sample was measured using a 2kV accelerating voltage and $200\mu A/cm^2$ current density. Figure 4-4 shows the relative CL intensity distribution as a function of wavelength. The strongest transition occurs at 626nm which is the $^5D_0-^7F_2$ transition of the Eu^{3+} ion [KAD91]. Secondary emission peaks, corresponding to other transitions of the Eu^{3+} ion, can be seen at 616nm and 702nm. The CL spectrum matches the published spectra for $Y_2O_2S:Eu^{3+}$ powder phosphors. A very small peak is found at 611nm which corresponds with the main emission peak in $Y_2O_3:Eu^{3+}$. The luminescent transitions found in $Y_2O_2S:Eu^{3+}$ are extremely narrow line emissions. This is due to the transitions being localized on the europium ion.

The relative brightness of the starting material has been studied as a function of accelerating voltage at a constant current density of $20\mu a/cm^2$. Relative brightness was obtained by determining the area under the CL spectra as a function of wavelength (500nm to 700nm) at a given accelerating voltage. A representative threshold curve is

shown in Figure 4-5 where brightness is plotted as a

function of accelerating voltage. Two important aspects of

the luminescent characteristics of the phosphor are obtained

from the brightness as a function of accelerating voltage

(threshold) data. The first, threshold voltage, is defined

to be the intercept of the extrapolation of the linear

portion of the B-V curve. The dotted line in figure 4-5 is a

fit to the linear region portion of the B-V curve. The x-

intercept at the y=0 crossing for the phosphor is the

threshold voltage. The crossing value is found to be 871 V

for this unaged sample.

Secondly, a qualitative, relative brightness efficiency

for the phosphor can also be determined from the slope of

the linear portion of the curve. In this case the linear

region extends from 2000 volts to ~ 4000 volts. The slope

for this phosphor is found to be 2.3×10^{-4} brightness(a.u)

units per volt.

The luminescent characteristics obtained from the

threshold voltage curve can be used to examine changes in

the phosphor due to coulomb aging. In the literature, the

threshold voltage is attributed to a surface layer with

reduced or no luminescence which an electron must penetrate

before luminescence will occur. In this study, it will be shown that the change in threshold voltage after coulomb aging may indicate one or a combination of several changes including a change in the thickness of any non-luminescent surface layer, a changed secondary electron emission coefficient resulting in a different surface region charging, or a change in radiative efficiency near the surface. A change in radiative efficiency can be determined by a change in the slope of the threshold curve in the linear portion of the curve which would indicate a change in radiative efficiency of the phosphor powder. Probable causes of changed efficiencies are decreased radiative transition probabilities or de-activation of luminescent centers in the phosphor.

Degradation Characteristics of Yttrium Oxysulfide

Previous studies by Swart et al [SWA96] and Itoh [ITO89] showed that the CL degradation of ZnS powder phosphors were sensitive to overall vacuum pressure and types of gas. In considering previous studies on sulfur containing phosphors, it was decided that initial studies on yttrium oxysulfide should be completed under good vacuum

conditions to minimize the degradation effects due to ambient. A 2keV primary electron beam with DC current density of ~ 272 μA/cm^2 was used for the aging studies of the phosphor.

Figure 4-6 shows the loss in CL brightness (integrated area under the CL spectrum) as a function of coulomb dose for a P22R phosphor in a vacuum ambient of 1.4×10^{-8} Torr, as measured by a Bayrd-Alpert hot cathode ionization gauge. The degradation experiment left a dark beam spot which was used to estimate the electron beam spot area (0.011 cm^2) and calculate current densities. The spot was found to be spherically shaped by microscopic analysis. As shown in figure 4-6, a rapid decay in brightness occurs at the beginning of the cathodoluminescent degradation. This decrease is typically attributed to either charge buildup on the surface of the phosphor due to its extremely low electrical conductivity (10^{12}-10^{14} mhos for Y_2O_2S) or to thermal quenching of luminescence due to electron beam heating of the phosphor [Has90]. This rapid loss will not be considered in determining the extent of CL degradation due

to large variations observed in the initial loss from sample to sample.

The initial rapid drop is followed by a slow increase in brightness(from 0.57 to 0.60) until a maximum is reached at ~ 4-5 C/cm^2· and then a slow steady decrease in CL brightness until the end of the experiment at 22 C/cm^2 (from 0.6 to 0.5). The phosphor does not degrade while the electron beam is turned off.

In order to determine if chemical changes in the phosphor were responsible for the changes observed in the CL brightness, AES was conducted concurrently with CL spectroscopy. The AES peak heights and shapes, as well as energy shifts were recorded continuously throughout the experiment. Figure 4-7 shows the AES peak to peak height changes (APPH) which occurred during the experiment for O, C, S and Y. Changes in APPHs are qualitative indicators of the relative amount of an element present which are sampled within the AES probed volume (0.011 cm^2 by ~30Å depth). As can be seen, the signals from oxygen and yttrium increased slightly from 0 to 5-10 C/cm^2 and then remained relatively constant, while the AES signals for carbon and sulfur

dropped dramatically over the first C/cm² (as did the CL brightness in figure 4-6) and then stabilized for the duration of the experiment. Although the S APPH is low, the signal is still present in the final AES spectra. The C APPH, however, has fallen below the detection limit of the AES spectrometer.

It is evident that the chemical changes near the surface of the phosphors, observed by AES analysis, can be correlated with the slight increase in CL brightness to ~ 5 C/cm² in figure 4-7, but this determination could be errant due to the volatility of the species studied (O,C, and S). These species can be removed from the surface by desorption or volatilization reactions. A better way to examine the data would be to normalize the peak intensity of O, C, and S to the Y AES signal. The vapor pressure of yttrium is extremely low (~10^{-18} Torr at room temperature) and therefore it is unlikely that the total amount of Y sampled by the electron beam will change due to the loss of yttrium from the surface of the phosphors. Figure 4-8 shows the APPH ratios for oxygen, carbon and sulfur normalized to the yttrium APPH. The CL brightness as a function of coulomb load is also shown. The APPH ratios for C/Y and S/Y exhibit

a rapid initial decrease over the first C/cm^2 and a subsequent stabilization to nearly constant values beyond ~ 3 C/cm^2, while the O/Y ratio is nearly constant or decreasing slightly from 0 to 22 C/cm^2. The S/Y decrease corresponds to the slow increase in CL brightness observed from 0 to 5 C/cm^2. Apparently the carbon at the surface is rapidly removed during the early stages of degradation. Another possibility to explain the increase in CL up to 5 C/cm^2 is the modification of the phosphor work function due to the chemical modifications associated with the C and S removal, resulting in a change in secondary electron yield which could affect the CL brightness.

Not only did the APPH values for Y,O,C and S change during the aging experiment, but also the peak energies shifted as well. Figure 4-9 illustrates the initial (0.5 C/cm^2) and final (19.9 C/cm^2) AES scan. The spectrum shows the AES peaks for Y, S, C and O as a function of electron energy. The changes in peak height are small for Y, O and S. The C signal is barely detectable at 0.5 C/cm^2 and has fallen below the AES detection limit (~10^{12} atoms/cm^2) by 19.9C/cm^2.

A measurable shift (~1.5 eV) to higher energies of the Auger peaks of Y and O as well as the secondary emission peak (lowest energy peak) is observed from 0.5 C/cm^2 to 19.9 C/cm^2 (Figure 4-9). The Y, O, and S peaks all exhibit positive shifts in energy from the expected AES peak energies 14, 11, and 7 V ,respectively. Since surface charging and/or changes in surface charging during degradation could be significant, the AES energies for Y, O, C and S were measured throughout the experiment to determine if these energy shifts could be correlated with the surface chemical changes. The shifts are small in relation to the energy of each Auger peak, so linear trend lines were fitted to the real data to discern any measurable patterns as shown in figure 4-10, consistent with figure 4-9, Y and O exhibit shifts to higher energies (indicated by a positive slope denoted in trend line equation) while carbon and sulfur exhibit slight decreases (negative slope). The C energy shifts can only be examined until ~ 2 C/cm^2 due to the carbon surface concentration falling below the minimum detectable limit for AES analysis. The positive shift in energies associated with Y and O could be consistent with a charging shift caused by the removal of the conductive C

surface species. The C and S peak energies shift negatively throughout the experiment.

The APPH data shows the loss of surface C and S. It is possible that the electron beam interaction with the surface and with gas species impinging on the surface are volatilizing the weaker bond C and S, leaving a sulfur depleted, oxygen rich surface. A conversion of Y_2O_2S to Y_2O_3 or $Y_2O_2SO_4$ may be occurring. If the conversion of Y_2O_2S to Y_2O_3 or to $Y_2O_2SO_4$ is real, peak shifts or new peaks in the cathodoluminescent spectra may become visible. This postulate assumes that the Eu in the forming phase is still active for luminescence and remains in yttrium sites in the lattice. Figure 4-11 is a graph of the initial and final CL spectra (0.5 C/cm^2 and 19.9C/cm^2) as a function of wavelength in nanometers. The peaks are all known emissions from $Y_2O_2S:Eu^{3+}$ as indexed in figure 4-4. The overall decrease in intensity due to coulomb aging is found on all emission peaks, but no shifts or new peaks are immediately evident.

Since the changes in intensity are small in comparison to the peak intensities, the differences between these spectra can be enhanced by subtraction of the initial from

the final spectrum. Figure 4-12 shows the results of this manipulation. The wavelength scale (x-axis) has been expanded to enhance the differences found between the spectra. Negative changes on the CL difference line indicates a peak in the original $Y_2O_2S:Eu^{3+}$ spectra which has decreased in intensity after the degradation has occurred. These include the 612, 617, 626 and 632 nm peaks. Positive deflections in the CL difference spectra indicate new peaks or peaks which have increased in intensity. It is clear that the lower integrated CL brightness largely results from reduced detected emission from $Y_2O_2S:Eu^{3+}$. Increased emission peaks are found at 618, 629 and 632 nm and the peaks at 618 and 632 nm correspond with known emissions of $Y_2O_2SO_4:Eu^{3+}$ [OZA91], possibly indicating its presence on the surface. The 618, 629, and 632nm peaks could also be caused by spectral broadening of the main emissions of $Y_2O_2S:Eu^{3+}$. The presence of $Y_2O_2SO_4:Eu^{3+}$ would be surprising since the temperature required for oxidation in air of $Y_2O_2S:Eu^{3+}$ to produce $Y_2O_2SO_4:Eu^{3+}$ is about 750-975C [OZA91]. Since these temperatures are clearly not achieved by electron beam heating, the phase conversion of $Y_2O_2S:Eu^{3+}$ to $Y_2O_2SO_4:Eu^{3+}$ or

$Y_2O_3:Eu^{3+}$ by an electron beam assisted reaction is suggested.

Figure 4-13 shows the overall change in brightness as a function of accelerating voltage thrshold voltage data for unaged versus $Y_2O_2S:Eu^{3+}$ aged to 19.9 C/cm^2. The relative brightness for the aged and unaged phosphor are normalized to their maximum value over the voltage range studied (typically maximum brightness is found at maximum voltage), so the slope of the linear region (proportional to luminescent efficiency) and threshold voltage can be compared. The undegraded spot has a threshold of 539 V, whereas the degraded spot has a threshold of 640 V. These data show conclusively that an increase in the threshold voltage (which would be attributable to the growth of the over layer of $Y_2O_2SO_4:Eu^{3+}$, or to increased charging of the surface) directly affects the brightness of the phosphor. In the linear region of the curve, the loss in brightness is ~ 4% at a current density of 20uA/cm^2 and a 2 keV accelerating voltage. The loss in brightness is nearly constant throughout the linear portion of the curves (2keV to 4.5keV). This, along with the linearity (parallel slopes for aged and unaged between 2.5 keV and 5 keV) in the

non-saturated region, suggests that the Eu^{3+} residing in the excited volume of the Y_2O_2S host has not undergone any radiative efficiency losses. At the lower accelerating voltages (0.5 keV to 2.5 keV), the slopes of the aged and unaged spot diverge. The aged spot has a lower slope, indicating a loss in brightness efficiency. Clearly, the surface changes measured by AES and CL spectroscopy indicate an altered near surface region of the phosphor which results in an altered low voltage brightness efficiency.

By considering the increase in range associated with the increase in threshold voltage, figure 2-7 can be used to estimate the increase in dead layer thickness. The range of a 539 eV electron is ~ 0.057μm. The range of a 640 eV electron is 0.07μm. The difference in the range of the electrons can be used as an approximation of the thickness of the dead layer found near the surface of the Y_2O_2S particles and is ~ 130Å.

Summary

Initial experiments in a vacuum of ~1×10^{-8} Torr have shown that CL degradation may occur by the partial surface conversion of $Y_2O_2S:Eu^{3+}$ to $Y_2O_2SO_4:Eu^{3+}$ or $Y_2O_3:Eu^{3+}$. The CL degradation observed is small and may be a combination the new phase formation and surface charging induced by the chemical changes. A possible surface reaction driving the CL degradation is:

$$Y_2O_2S + 2O_2 \Leftrightarrow Y_2O_2SO_4.$$
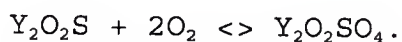
This reaction occurs in the presence of oxygen or oxygen-containing species and only takes place under electron beam stimulation.

The CL degradation proceeds by the initial removal of C. Once the carbon is removed by surface reaction, the detrimental surface reaction (loss of S) takes place and CL degradation occurs. AES peak energy shifts to higher energies for Y and O, and to lower energies for C and S. The CL degradation is marked by an increase in threshold voltage.
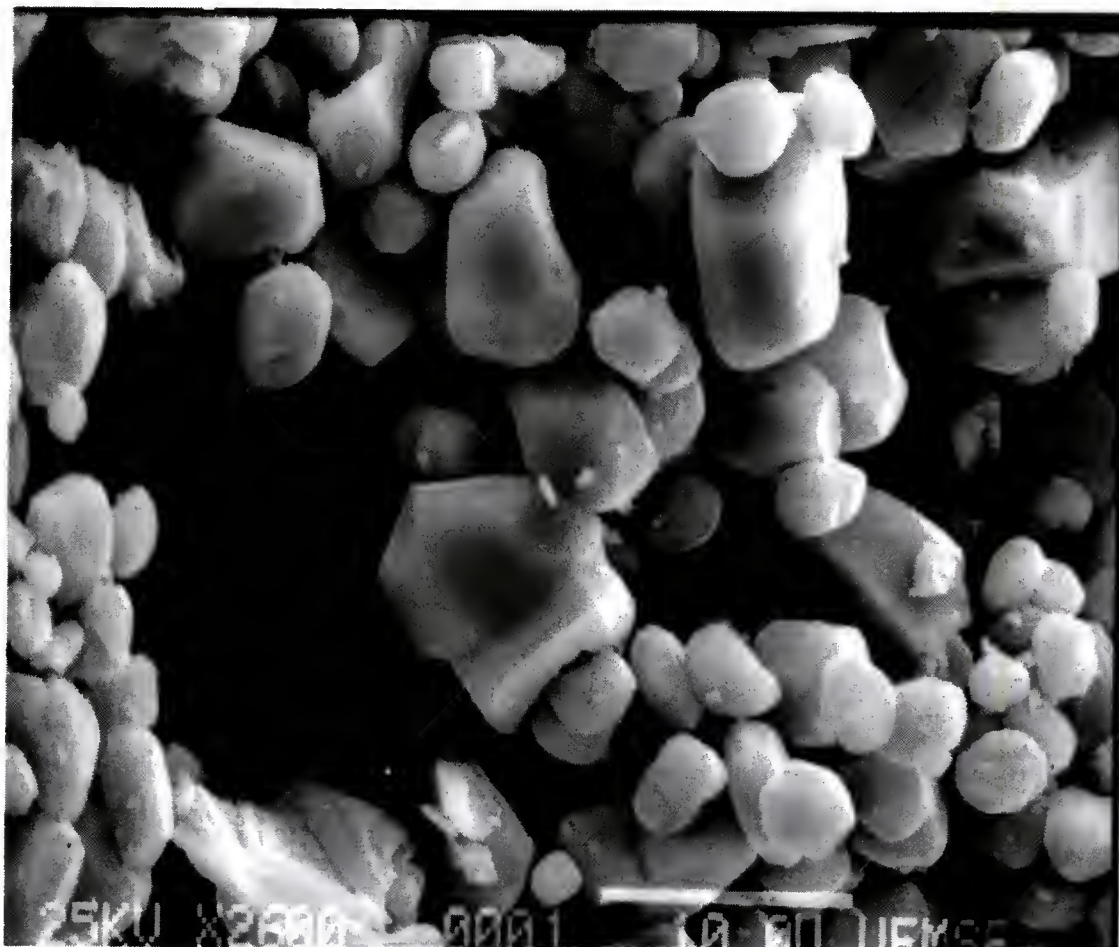
Figure 4-1   SEM image of $Y_2O_2S:Eu^{3+}$ particles. The photomicrograph was taken at 25kV and magnification of 2600X. The white bar at bottom right of image indicates a scale of 10 μm. Particles are faceted with an average diameter of 4.5 μm and a distribution from 1 to 10 μm.
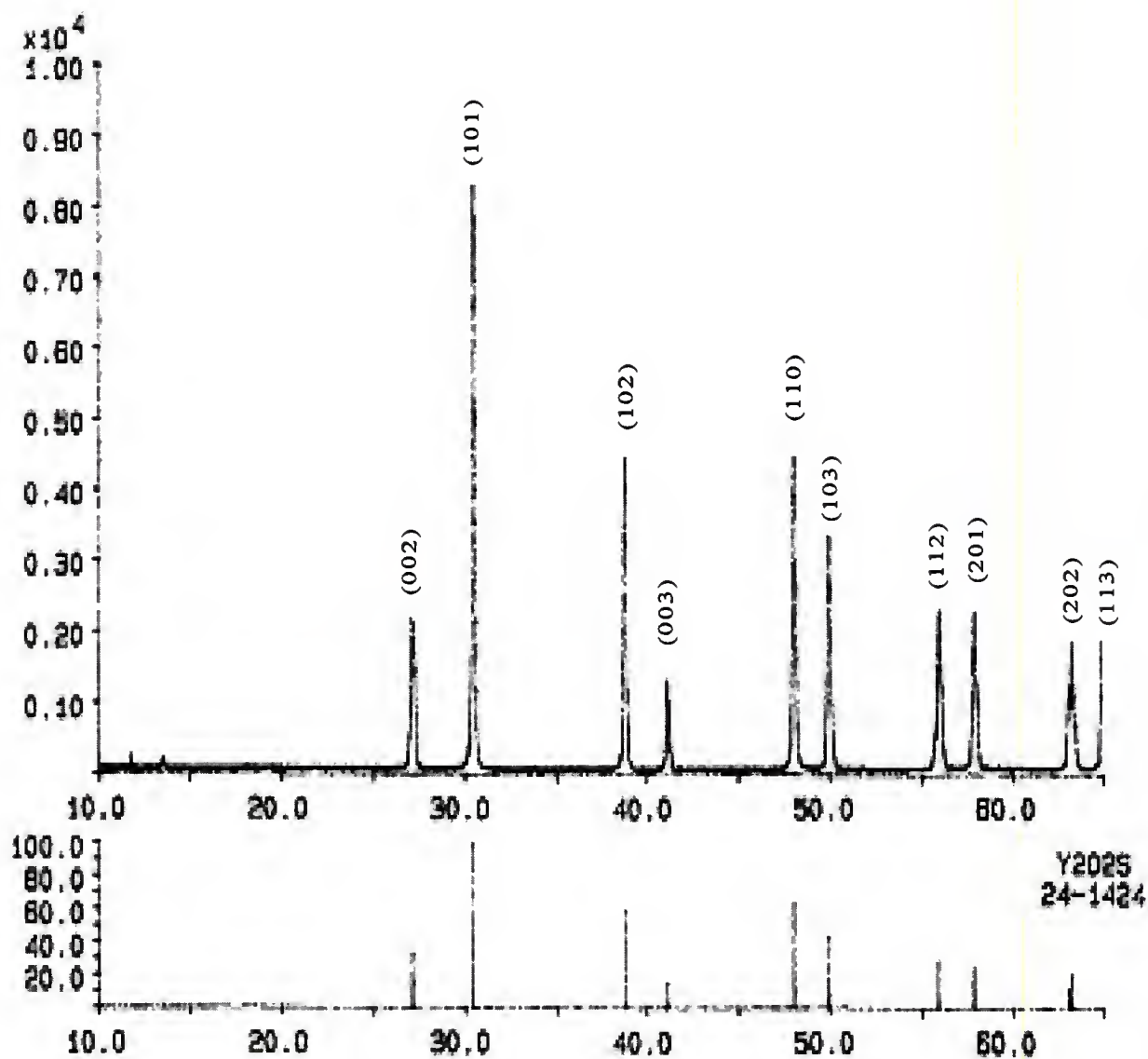
Figure 4-2   X-Ray powder diffraction spectra for
$Y_2O_2S:Eu^{3+}$ as a function of 2θ angle. The Miller Indices
of the crystallographic planes are indicated on the
upper graph. The lower graph is the matching JCPDS
(#24-1424) file displaying the expected relative
intensities for Y_2O_2S.
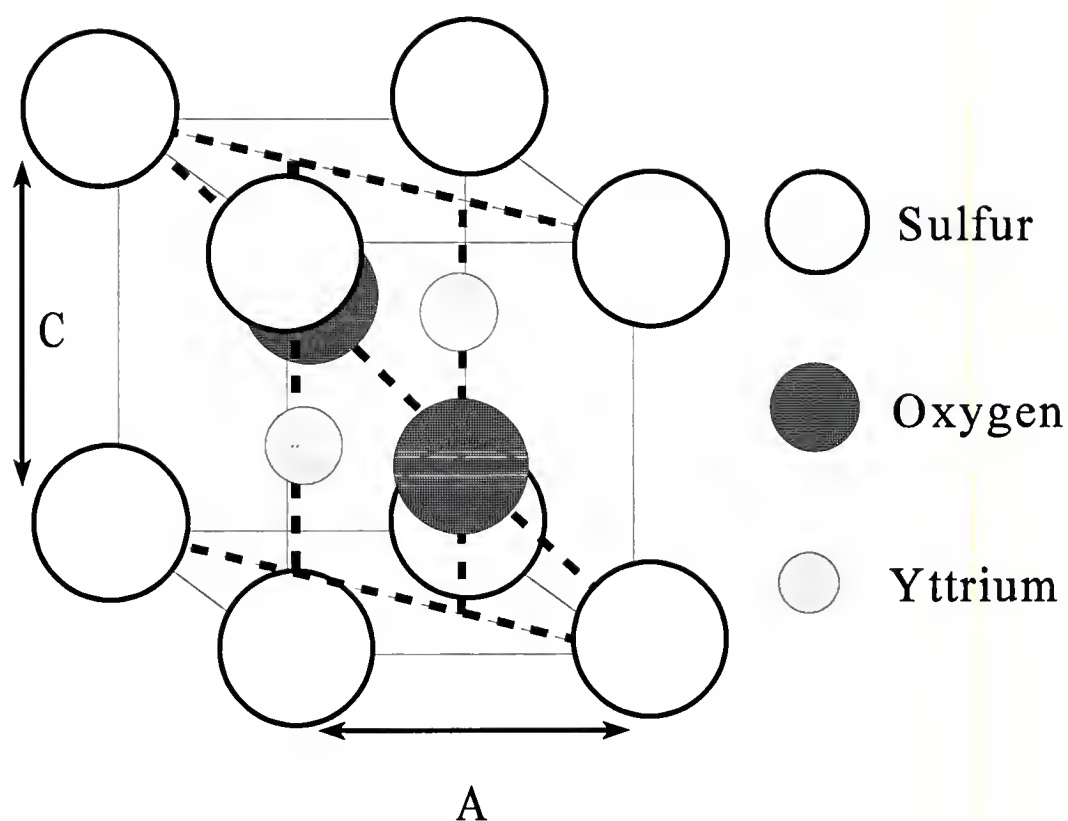
Figure 4-3   Schematic of the crystal structure of
$Y_2O_2S:Eu^{3+}$. 3 rhombehedral units make up the full
hexagonal structure for the material. Lattice
parameters are shown above with a=3.284Å and c=6.509Å.
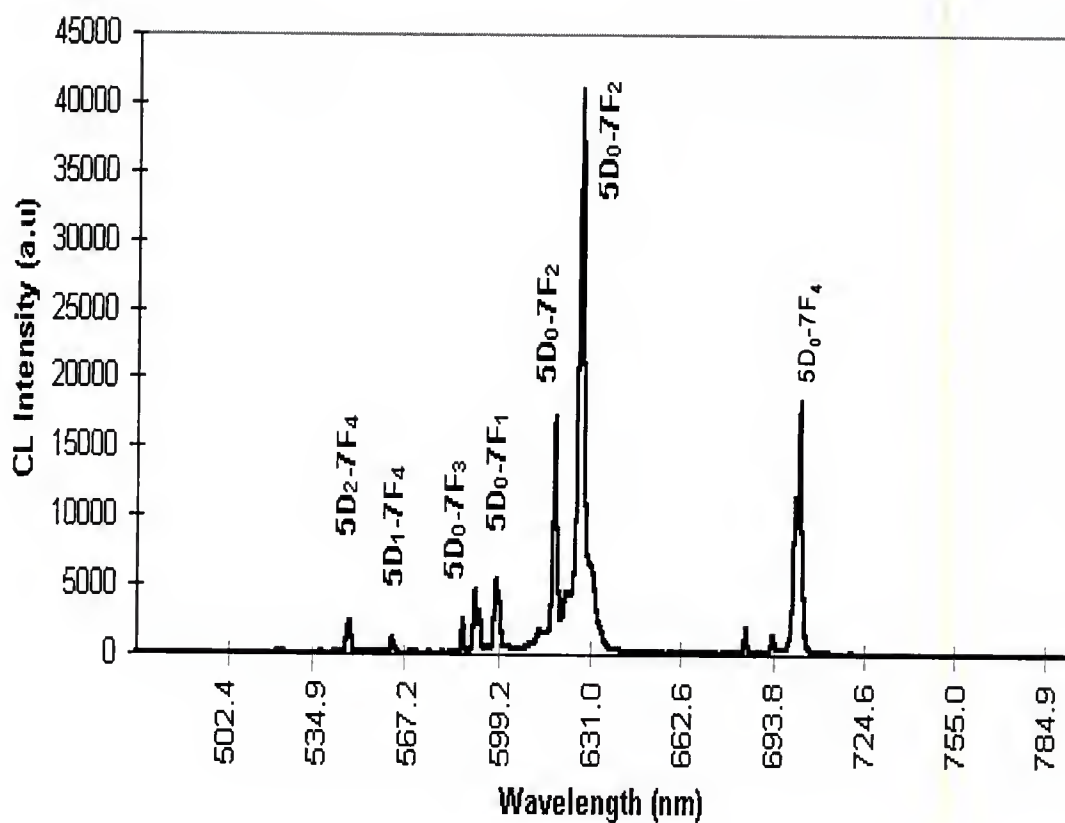
Figure 4-4   Cathodoluminescent intensity as a function of wavelength. The spectra was obtained with a 2kV accelerating voltage and $20\mu A/cm^2$ current density. The larger visible (red) transitions are indexed. The characteristic narrow line emission is due to the luminescent transition being localized on the Eu^{3+} ion.
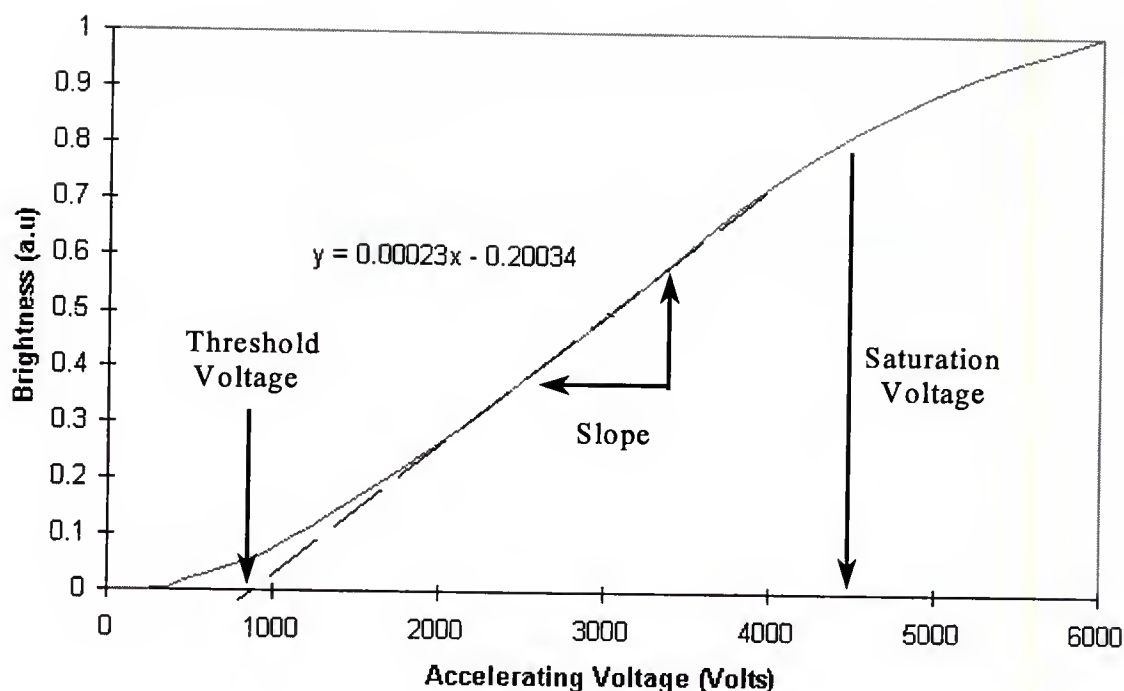
Figure 4-5   Representative curve of brightness (a.u) as a function of accelerating voltage for $Y_2O_2S:Eu^{3+}$ powder CRT phosphor. The beam current density was set at $20\mu A/cm^2$. The threshold voltage can be extrapolated from the linear portion of the curve as shown by the dashed line and equation and is found to be 871 volts. The slope of the linear portion of the curve represents relative luminous efficiency, and the saturation voltage (the voltage at which the CL response becomes sub-linear) is shown.
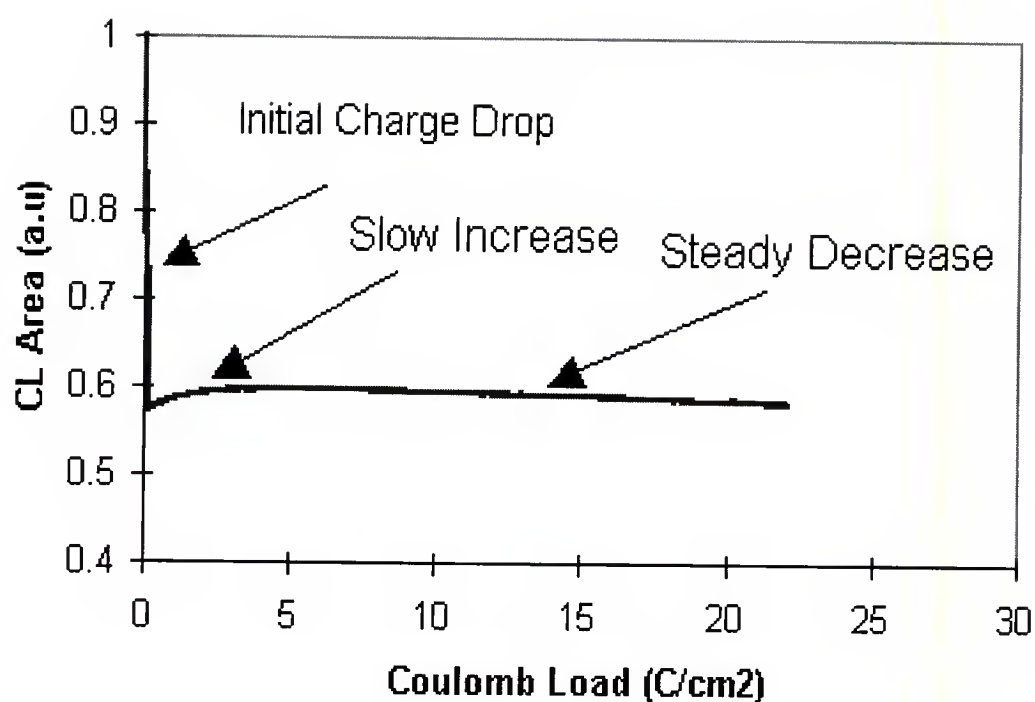
Figure 4-6   CL degradation observed for $Y_2O_2S:Eu^{3+}$ in background vacuum at 1.4×10^{-8} Torr. The electron beam was operated at 2keV and 272 $\mu A/cm^2$. Note the three regions of interest, the rapid intial charging loss (or thermal quenching), the slow increase in brightness to 5 C/cm^2 and the steady decrease until the end of the experiment (22 C/cm^2).
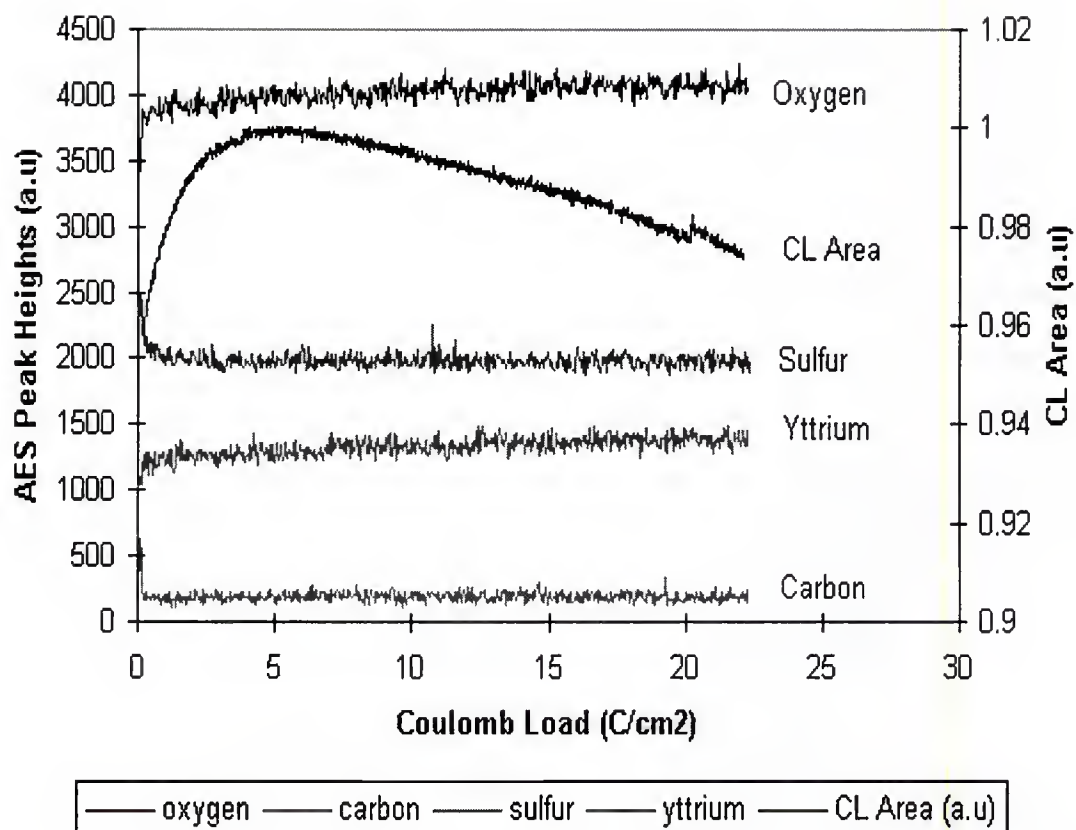
Figure 4-7   AES APPHs of O, C, S and Y monitored during coulombic aging of P22R powder phosphor. The CL brightness shows an intial increase while C and S AES signals decrease to approximately 5 C/cm². Once the C and S AES signals have stabilized, the CL brightness (CL Area) exhibits a steady decrease for the remainder of the experiment.
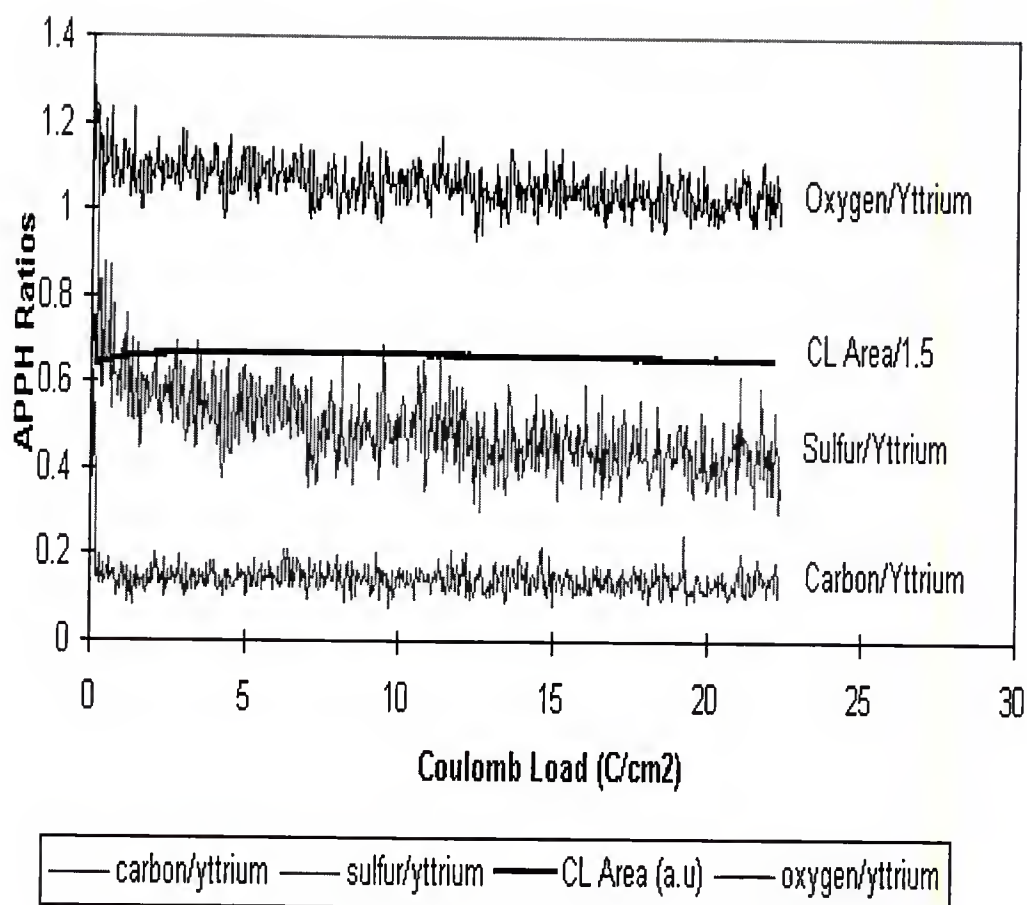
Figure 4-8   AES Peak-to-Peak Height Ratios and CL
Brightness(CL Area/1.5) as functions of Coulomb Load.
The normalized AES intensities show that C and S leave
the surface probe region and the O/Y remains constant.
The decrease of C/Y and S/Y ratios match the increase
in CL to approximately 5 C/cm². Once the C/Y and S/Y
ratios stabilize, the CL intensity steadily decreases.
Note that CL brightness has been reduced to fit to
scale.
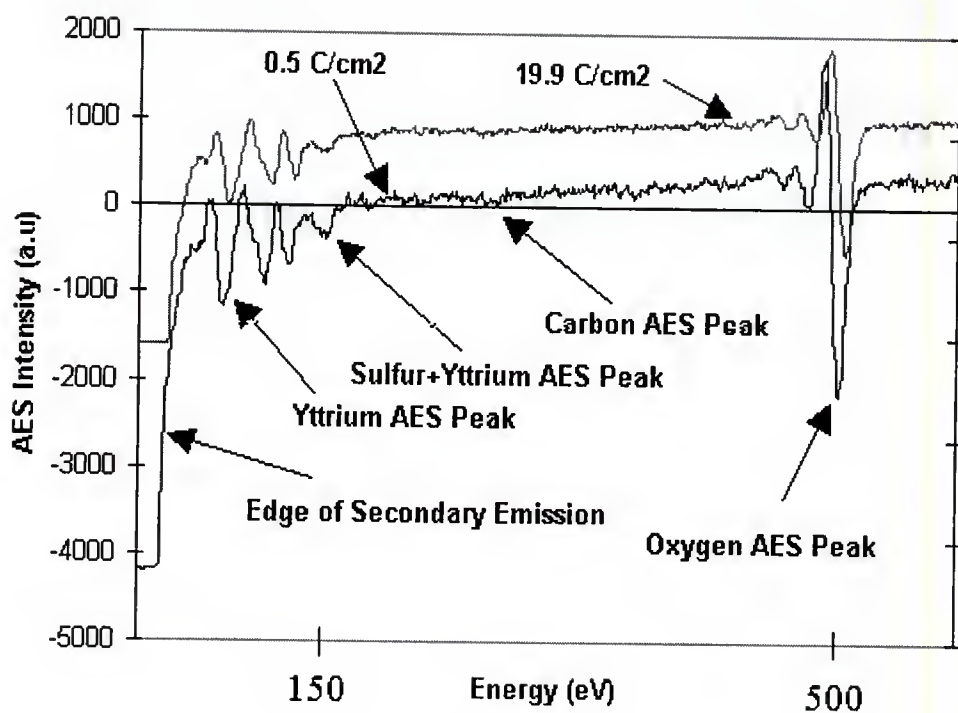
Figure 4-9   Initial (0.5 C/cm²) and final (19.9 C/cm²) AES survey scans. Increases in AES intensity are difficult to discern on this type of graph, thus ratios of peak heights normalized to Y AES are used to amplify the changes (Fig 4-8). Note the small positive shift in peak energy for O and Y AES peaks as noted. Also, a small positive energy shift can be seen on the tail of the secondary emission peak.
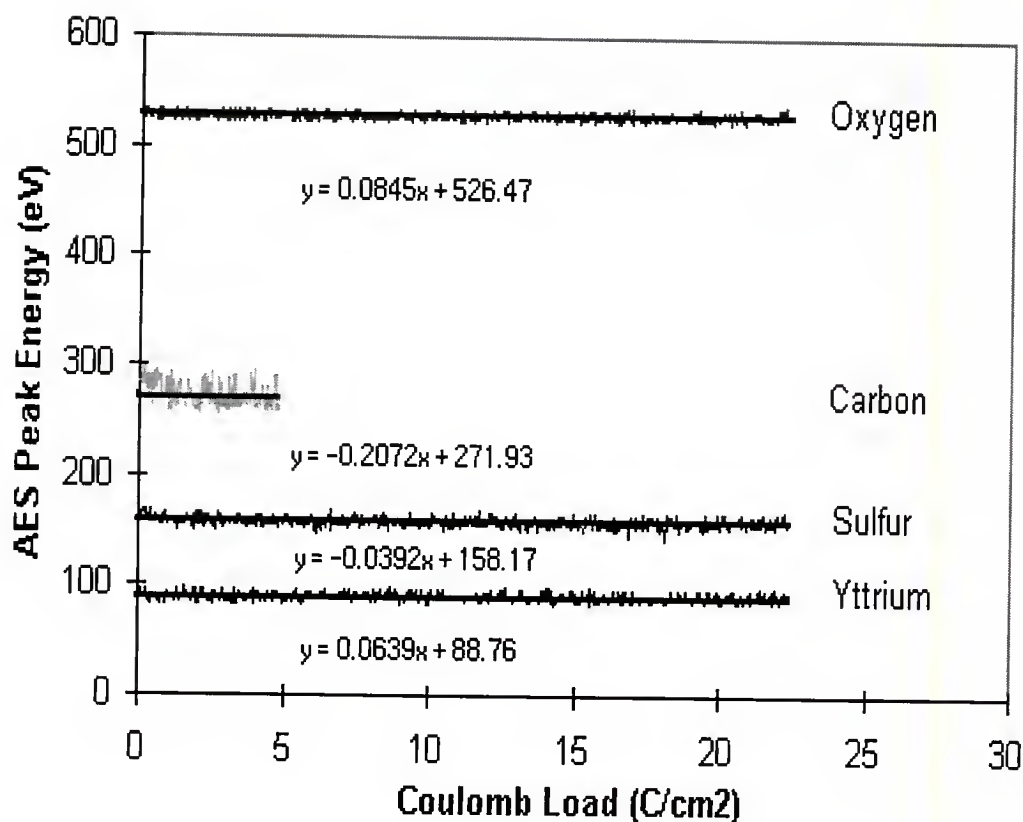
Figure 4-10   Examination of AES peak energy shifts during coulombic aging. AES energy data has been linearly fitted with equations displayed to determine the direction of energy shift for Y,O,C and S. The Y and O shift is slightly positive and amounts to approximately 1.5 eV from beginning to end of the experiment. C and S slopes are negative with sulfur energy shift of -.5 eV. The carbon AES energy cannot be determined with accuracy due to the total loss of the C AES peak at the end of the experiment. The C energy values after the total loss of C (~5 C/cm²) is an artifact of the software used to determine the AES peak energies.
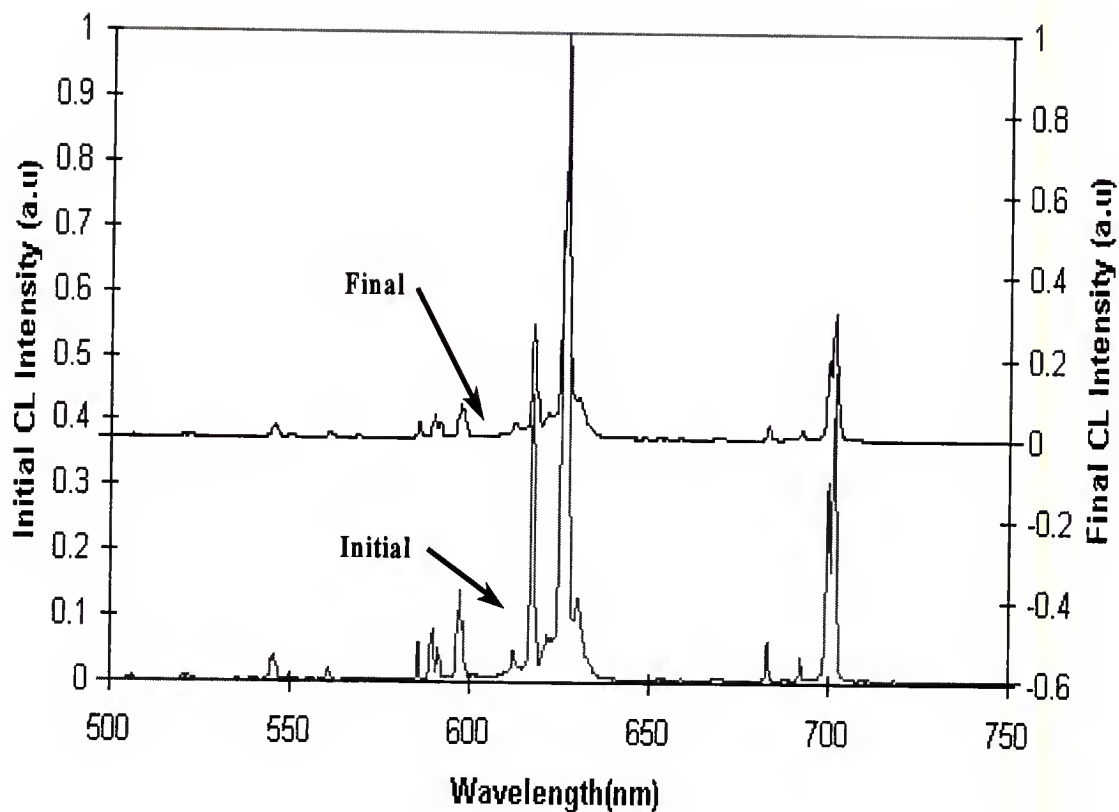
Figure 4-11   CL spectral intensity distribution as a
function of wavelength before and after 2keV
degradation. Small changes in peak heights are visible,
but very difficult to discern. Initial spectrum
intensities are denoted on the left hand y-axis scale,
final intensities on the right hand y-axis.

CL Spectral Intensity
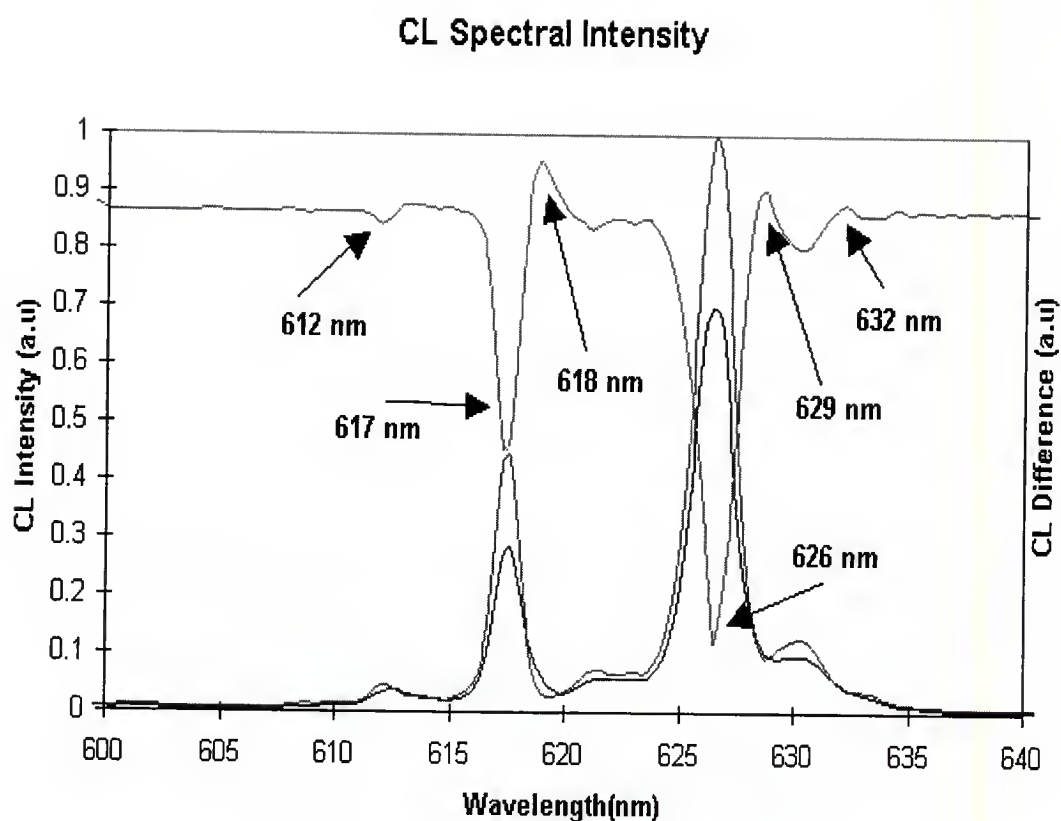
Figure 4-12   CL spectral intensity for the 600 to 640 nm region before and after 2keV degradation has occurred. The spectra are very similar to each other, so in order to understand what changes have occurred, the difference is plotted. Negative variations in the difference graph indicate CL peak height decreases (612, 617, 626 nm), and positive deflections indicate peak increases or appearances (618, 629, and 632nm).
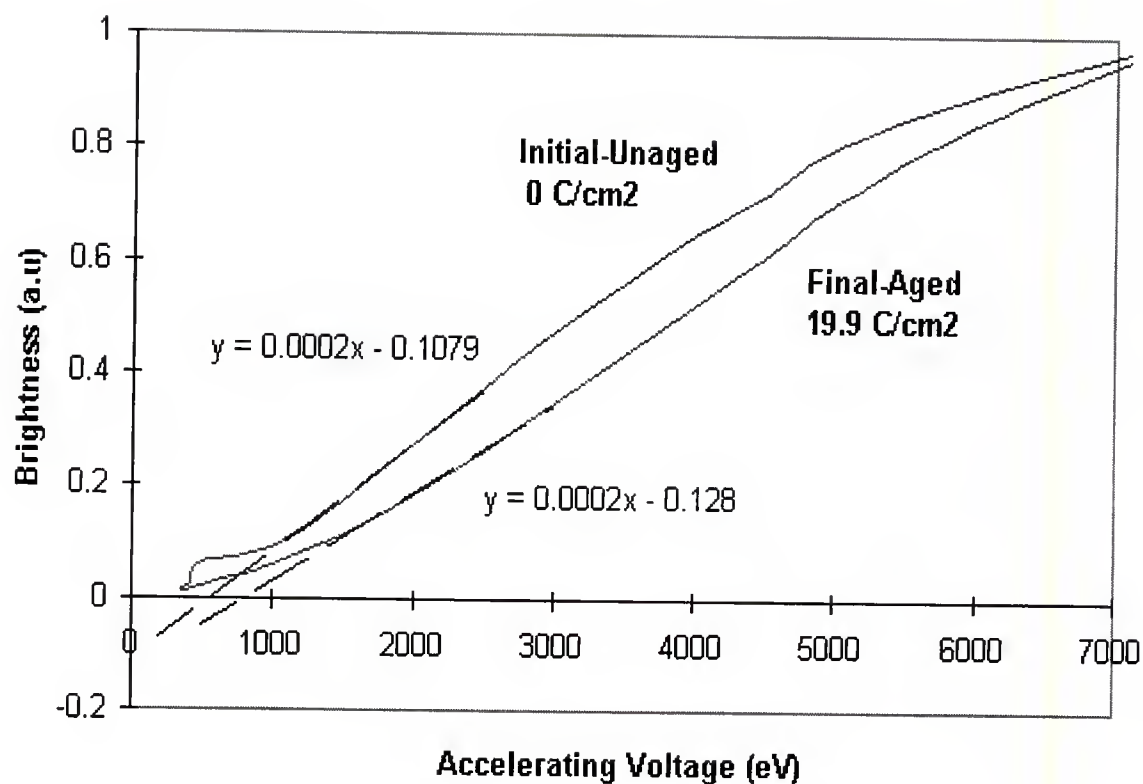
Figure 4-13   Threshold voltage experiment for
standard $Y_2O_2S:Eu^{3+}$. The unaged B-V curve was taken at
0 C/cm^2 and the aged B-V curve was taken at 19.9
C/cm^2. Note the increase in threshold voltage
for the degraded sample. Trendlines extrapolated from
the linear portion of the curves determine the turn-on
voltage. V_{th} (unaged)=539 volts, V_{th} (aged)=640 volts.

CHAPTER 5

EFFECTS OF OXYGEN AMBIENTS ON THE DEGRADATION OF $Y_2O_2S:Eu^{3+}$

Introduction

In this chapter, the CL degradation of $Y_2O_2S:Eu^{3+}$ powder phosphor will be examined in oxygen ambients. The results will be compared with the baseline experiment of chapter 4. A comparison of the results will show that $Y_2O_3:Eu^{3+}$ is formed at the surface of the phosphor in the oxygen ambient experiments. In the last chapter, it was shown that CL degradation may be caused by the formation of $Y_2O_3:Eu^{3+}$ near the surface and/or surface charging phenomena associated with the chemical changes. The evolution of these layers will be examined by time incremented threshold voltage experiments and CL spectroscopy conducted during an aging

study in oxygen and the surface layer formation will be correlated with the CL degradation of $Y_2O_2S:Eu^{3+}$. These experiments will provide insight into the growth of the surface layer and its effects on the luminescent properties of $Y_2O_2S:Eu^{3+}$.

Degradation of $Y_2O_2S:Eu^{3+}$ in an Oxygen Ambient

As stated in the previous chapter, CL degradation of $Y_2O_2S:Eu^{3+}$ has been found to be sensitive to oxygen and/or oxygen containing gases. The conversion of $Y_2O_2S:Eu^{3+}$ to $Y_2O_2SO_4:Eu^{3+}$ was indicated by AES analysis and CL spectroscopy. In order to better understand the gas-surface interaction induced by the electron beam, better control of the gas in the experiments is required. Oxygen of 99.9999% purity was leaked into the AES spectrometer during a CL degradation experiment to compare the degradation rate and surface changes induced by the electron beam in an oxygen ambient versus the baseline experimental data. Electron beam conditions were kept nearly the same (2keV beam energy and 274 $\mu A/cm^2$ current density). The base system pressure was

1.5x10^{-8} Torr before being backfilled to 1.1x10^{-6} Torr with oxygen gas.

Figure 5-1 shows the CL brightness decrease as a function of coulomb load for this experiment. The curve is very similar to the baseline CL degradation curve in figure 4-6, in that the brightness instantaneously dropped (not shown in figure 5-1), then recovered ~4% over ~5C/cm^2, and then fell again over the next 15 C/cm^2. The most noticeable differences in the two curves (figure 4-6 and figure 5-1) is the much smaller coulomb load to reach maximum brightness in the oxygen ambient (<1 C/cm^2) and the larger brightness loss (~35%) after 20 C/cm^2. These data dramatically demonstrate that the gas constituents and their partial pressures are important factors in determining the rate and extent of degradation of the $Y_2O_2S:Eu^{3+}$ phosphor. Presumably this is because the surface reaction and consequent CL degradation may be rate limited by the amount of reactive gas impinging on the surface and therefore available for reaction.

This effect is easily seen by comparing the rates of surface conversion as shown in figure 5-2. C and S are very quickly removed from the surface region (<1 C/cm^2) and the O and Y surface concentrations increase steadily throughout

the experiment. A small system fluctuation occurred at ~4 C/cm^2, and is noted in figure 5-2. Concurrently with the system fluctuation, the AES and CL signals intensities decreased. Both effects are consistent with a small decrease in current density at the sample. Another small decrease was noted at 15 C/cm^2 which is also indicative of a decrease in current density. In order to reduce the effects of these changes on the interpretation of the data, AES signals were normalized to the Y Auger peak-to-peak height (APPH). This normalization is shown in figure 5-3 as a function of coulomb load and the discontinuities at 4, 15 and 20 C/cm^2 are largely removed from the APPH ratios.

It is much easier to interpret the surface changes that have occurred using this type of graph. It can be seen that the initial increase in brightness occurs as the C and S are lost from the surface (<0.1 C/cm^2). This loss, in the baseline experiment, took nearly 5 C/cm^2 to complete. Therefore the presence of the oxygen gas increased the rate of C and S removal by about fifty times when compared with the baseline experiment. The O/Y APPH ratio drops throughout the experiment while the CL brightness steadily decreases.

Figure 5-4 shows the initial (0.1 C/cm^2) and final (19.5 C/cm2) AES spectra as a function of energy (eV). The C and S AES peak heights decreased throughout the experiment while the Y and O intensities increased. Positive Auger peak energy shifts to higher energies are observed on the Y and O peaks as well as on the secondary emission peak. The C and S Auger peak energies shift to lower energies.

Figure 5-5 depicts the AES peak energy shifts as a function of coulomb load for O, C, S and Y. Below 1 C/cm^2, C and S peak energies shift negatively (approximately 1eV) while the O and Y peak energies shift slightly positive (~1eV larger energy). These trends were also observed in the baseline experiment.

Figure 5-6 shows the initial and final CL spectra as a function of wavelength (nm). Both spectra are similar to one another after normalization, so the CL difference is determined from the two spectra and is shown in figure 5-7. The 600-640 nm region has been expanded to better display the differences between the two data sets in figure 5-6. The most notable feature is the large positive deflection in the CL difference curve at 611.9 and the large negative deflections at 617 and 626 nm. The large positive deflection

is indicative of the growth of a luminescent $Y_2O_3:Eu^{3+}$ during the degradation in oxygen. The initial CL spectra does have a small peak at 611.9nm, suggesting a small amount of $Y_2O_3:Eu^{3+}$ in the unaged powder. This small peak was also present in the baseline experiment. The small amount of $Y_2O_3:Eu^{3+}$ present in the powder may be a byproduct of the sulfide fusion production process which entails heating yttria (Y_2O_3) and europia (Eu_2O_3) in a sulfur atmosphere to produce yttrium oxysulfide (see Chapter 3). After degradation, smaller positive deflections are found at 616, 618 and 625 nm. Some spectral broadening of the two emission peaks of $Y_2O_2S:Eu^{3+}$ (626 and 617 nm) can be seen by comparing the initial and final CL spectra. This broadening produces positive deflections centered around the main peak. This broadening, may be caused by changes occurring in the local Eu^{3+} site symmetry, producing wider, less intense emission. Unfortunately, the broadening obscures any information about the presence of the $Y_2O_2SO_4:Eu^{3+}$, which would produce positive deflections at 616 and 618 nm.

Threshold voltage data before and after degradation are shown in figure 5-8. The conversion of $Y_2O_2S:Eu^{3+}$ to $Y_2O_3:Eu^{3+}$ has occurred to a sufficient extent to alter the low voltage

(1 kV to 2kV) brightness efficiency of the phosphor similar to the baseline data.

The threshold voltages were extrapolated from figure 5-8 and were found to be 765 V and 1290 V, respectively, for the unaged and aged spot. These electron energies correspond to penetration depths of ~0.087μm and 0.173μm, respectively, corresponding to a dead layer thickness is ~860Å. The dead layer thickness after CL degradation in oxygen is ~730Å thicker than that found for the baseline experiment. This suggests that the surface conversion and consequent CL degradation occur at a much higher rate in the oxygen ambient. In figure 5-8, a false cross-over in brightness of the unaged and aged phosphors can be seen at approximately 4500 volts, where the relative brightness of the aged phosphor is greater than the unaged phosphor. Each B-V curve in the figure is normalized to its maximum brightness value. This normalization process causes difficulties in interpretation of the data when the maximum brightness for the two threshold experiments does not occur at the same accelerating voltage. The brightness of the degraded spot in actual counts, is ~30% lower than the undegraded spot at all

voltages. Thus the crossover seen on the graph is a false crossover (4500 V) due to the normalization process.

It is clear that the presence of an oxygen ambient enhances the surface reactions and CL degradation rate when compared to the baseline ambient data. The increased amount of oxygen at the surface allows for faster reactions and removal rates of C and S from the surface, thus decreasing the coulomb load to maximum brightness. The CL degradation rate appears to depend at least in part on the removal rate of species from the surface. Thus, an increased impingement rate of reactive gas species will result in an increased removal rate. Therefore, the CL degradation rate and total degradation under equal coulomb loads, should be higher in the experiment which have a larger flux of reactive gas available at the surface. A comparison of the CL degradation curves as a function of coulomb load for the baseline and oxygen ambient experiment are shown in figure 5-9. In both curves, an increase to maximum brightness is followed by a steady decrease, but both the rate and extent to which these occur is enhanced in the oxygen ambient. Since the phosphor does not degrade while the electron beam is turned off, the surface reaction must be driven by the ionization of gas

and/or surface species with subsequent reaction and volatilization.

Time Dependent Threshold and CL Degradation Experiment

To this point, it has been shown that changes near the surface of the phosphor (within AES analysis limits) are correlated with CL degradation in the early stages of degradation. The threshold voltage studies have shown that this threshold voltage has increased after degradation. Since the data by Kingsley and Prener on ZnS powders [Kin72] show that threshold voltages can be correlated to the thickness of the dead layer, threshold voltage experiments during a CL degradation experiment could be used to study the increases in thickness of the "dead layer" during the CL degradation.

A CL degradation experiment was conducted under electron beam and vacuum ambient conditions similar to those used in the oxygen ambient experiment. A 2keV primary beam operated at a current density of 291 uA/cm^2 was used to bombard the phosphor in a backfilled oxygen ambient of 1x10^{-6} Torr. The initial system pressure was 1.3x10^{-8} Torr.

During the degradation experiment, threshold voltage experiments were performed at time intervals of 0, 15, 30, 45, 90, 180, 360, 720 and 1440 minutes. For the current density and spot sized used (0.011 cm^2) used, these times correlate to 0, 0.26, 0.46, 0.71, 1.42, 2.84, 11.3 and 22.6 C/cm^2 loads, respectively. Figure 5-10 shows a plot of the APPH ratios and CL brightness as a function of coulomb load for the experiment. Note that the C/Y APPH ratio is not plotted because no C peak was detected at the beginning of the experiment. It is interesting to note that in the absence of surface C contamination, the CL brightness curve did not exhibit an initial climb to maximum brightness. Only a steady decay of CL brightness is seen. This may be evidence that the initial loss of C is the cause of the increase to maximum brightness seen at the onset of all previous experiments.

Small spikes (labeled A-H) in the CL brightness curve occurred at the times when continuous electron bombardment was interrupted to collect the threshold voltage data (Figure 5-15 shows the series of B-V curves taken at the time intervals labeled A-H in figure 5-10 and will be discussed in greater detail). The spikes are simply the

large initial brightness recorded by the CL spectrometer which quickly decays to a steady state value due to charging or thermal quenching. The O/Y APPH ratio decreases slightly throughout this experiment, as was observed in the previous oxygen ambient experiment (figure 5-3). The S/Y APPH ratio decreases to below the AES detection limit in approximately 2-3 C/cm^2.

Figure 5-11 shows the AES peak energy shifts which occur throughout the experiment as a function of coulomb load for O, S and Y (no C AES signal was detected). The Y and O peak energies increase by approximately 1eV after a 2-3 C/cm^2 load while the S peak energy decreases during the same interval by approximately 2 eV. The data are consistent with that seen in the original oxygen experiment. The decrease at 3C/cm^2 followed by an increase at ~5C/cm^2 in the S AES peak energy is seen from 3-5 C/cm^2 was carefully investigated and concluded to be experimental error, since it precisely corresponds with the interval between point E and point F (figure 5-10).

Figure 5-12 shows the initial and final CL spectra as a function of wavelength (nm). The initial spectrum was taken prior to the degradation experiment and the final spectrum

was taken at point H shown in figure 5-10. A large increase

in the 612 nm $Y_2O_3:Eu^{3+}$ peak indicates an increase in the

amount of this phase sampled by the 2 keV electron beam. An

expanded view of the CL spectra (600-640nm) is shown in

figure 5-13. The CL difference (subtraction of initial and

final normalized spectra) is shown on the secondary y-axis.

Negative shifts (indicating losses in CL intensity) are

apparent at 617 and 626 nm due to decreased emission from

$Y_2O_2S:Eu^{3+}$. The largest positive deflection occurs at 612 nm.

This peak is the main emission peak of $Y_2O_3:Eu^{3+}$. Small

positive deflections are seen at 616 and 618 nm which may

correspond with the main emissions of $Y_2O_2SO_4:Eu^{3+}$. However,

similar deflections are seen around the 626 nm peak (625 and

627nm), thus, these peaks are attributed to spectral

broadening of the emission peaks of $Y_2O_2S:Eu^{3+}$.

Figure 5-14 depicts the brightness (a.u) as a function

of accelerating voltage (eV) for the an early (point B of

figure 5-10) and final (point H of figure 5-10) threshold

voltage experiments. Threshold voltages were extrapolated

for the linear regions of these curves volts. The threshold

voltages are found for the initial threshold voltage

experiment was calculated to be 166 volts and 866 volts for

final threshold experiments. These correspond to dead layer

thicknesses of 0.019 μm to 0.101 μm, respectively. The

difference between these thicknesses is found to be 820Å.

This calculated dead layer thickness is slightly smaller

(860Å) than that found in the original oxygen ambient

experiment. At 20 C/cm2, the total CL degradation is higher

than in the first oxygen experiment (~35% compared to 25%).

It is possible that the larger initial depth of the dead

layer in the first oxygen experiment (0.087μm compared to

0.019μm) caused the slower CL degradation rate under similar

experimental conditions.

Figure 5-15 shows the data from the entire series of

threshold voltage experiments conducted at different stages

of the CL degradation experiment. The slopes of the B-V

curves in the linear region are all very similar except for

the B-V curve at t=0 seconds, similar slopes indicate no

large net efficiency change during the experiment. The

threshold voltage increases with increasing coulomb load and

is easily visualized in figure 5-16. Linear trend lines were

used to obtain the threshold voltage values for each

successive experiment. The linear equations which fit the

curves of figure 5-16 are shown in figure 5-17. The threshold values are shown next to the respective equations. Figure 5-18 is a plot of the dead layer voltage and dead layer thickness versus coulomb load. Initially, the threshold voltage is small (166v) and correspondingly, the thickness of the dead layer is thin (0.015μm). As the phosphor is bombarded by electrons, the growth of the surface dead layer is fast, having increased to a thickness of 0.08 μm in the first 5 C/cm². Above this coulomb load, the growth rate slows dramatically and the dead layer approaches a thickness of 0.09 μm at 20 C/cm². Although this dead layer thickness seems small compared to the average particle size (4 μm), its importance becomes apparent in considering the penetration depth of an electron.

A 2keV electron has a penetration depth of ~0.3 μm. Thus a 0.09 μm dead layer (though not entirely non-luminescent) is 30% of the usable luminescent volume, presumably converted from $Y_2O_2S:Eu^{3+}$ (an efficient phosphor) to less efficient phosphors (either $Y_2O_3:Eu^{3+}$ or $Y_2O_2SO_4:Eu^{3+}$). If this layer was completely non-luminescent and the power dissipation and activator concentration (Eu^{3+}) were both

constant as a function of depth, a 30% loss in CL brightness would be expected for a dead layer of this thickness, similar to the value actually observed.

Figure 5-19 shows the relationship between the APPH ratios and the dead layer thickness.

<div align="center">

Summary

</div>

The sensitivity of CL degradation of $Y_2O_2S:Eu^{3+}$ to oxygen ambients has been shown. The data show that surface reactions involving surface C and S and impinging oxygen molecular gas dissociated to atomic species by the electron beam, reacted quickly and produced volatile compounds such as SO_2 and CO_2. The loss of C and S from the surface with subsequent formation of Y_2O_3 produced a dead (low luminescent) surface layer. Time dependant threshold voltage experiments have shown that the growth of this dead layer correlates with the decrease in CL. The dead layer thicknesses are much larger than those found in the baseline experiments where $Y_2O_2S:Eu^{3+}$ was exposed to an electron beam in good vacuum. The presence of oxygen gas increased the rate of removal of carbon and sulfur from the surface, and

increased the CL degradation rate. Since the ionization efficiency of gases are a function of the electrons kinetic energy, studies using different accelerating voltages may show different CL degradation rates; this will be reported next.
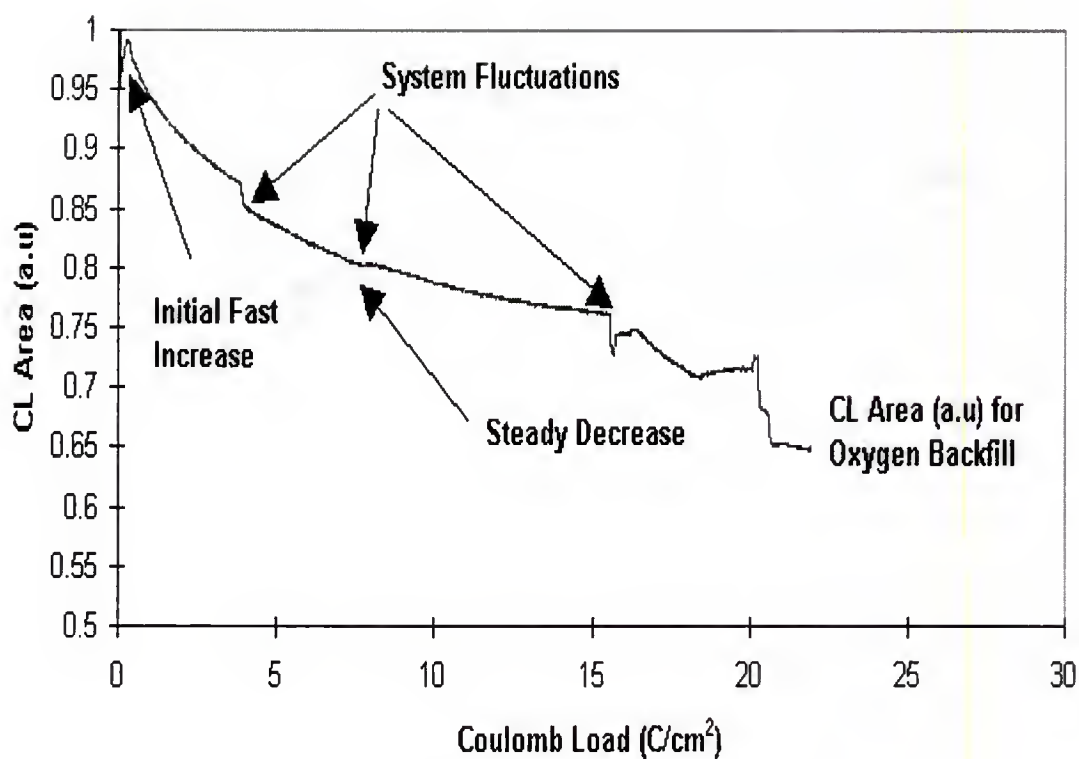
Figure 5-1   CL brightness as a function of coulomb load for the oxygen backfill experiment. System pressure was maintained at 1×10^{-6} Torr. Note the changes in CL brightness with various system fluctuations (typically current density changes). Also, note the very fast increase to maximum brightness (<1 C/cm^2), and the relatively fast decrease in CL for the duration of the experiment as compared to figure 4-6.
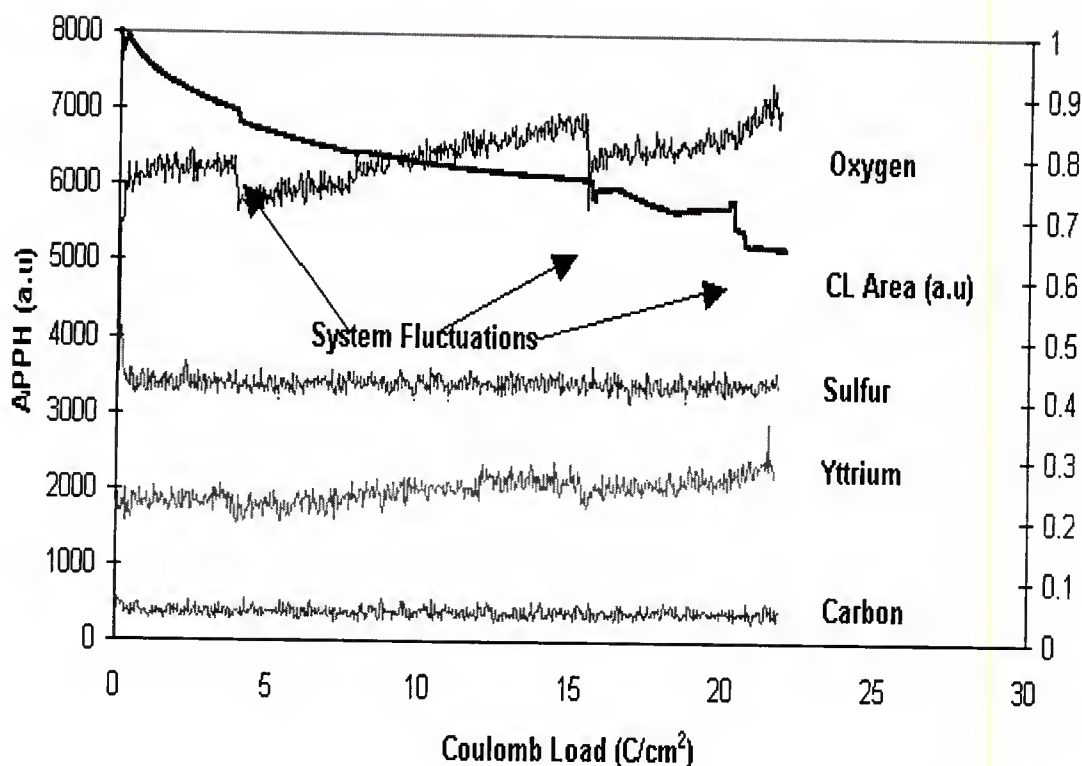
Figure 5-2   Auger Peak-to-Peak Height for O, C, S
and Y as a function of Coulomb Load. Note the system
fluctuations (current density changes) cause a decrease
in CL brightness as well as a decrease in APPHs. C and
S are quickly removed from the surface at a higher rate
than in the complimentary background experiment.
Loss of C and S occur before 1 C/cm2. The rate of
removal of these species is governed by the
availability of oxygen containing gas present at the
surface of the phosphor available for reaction.
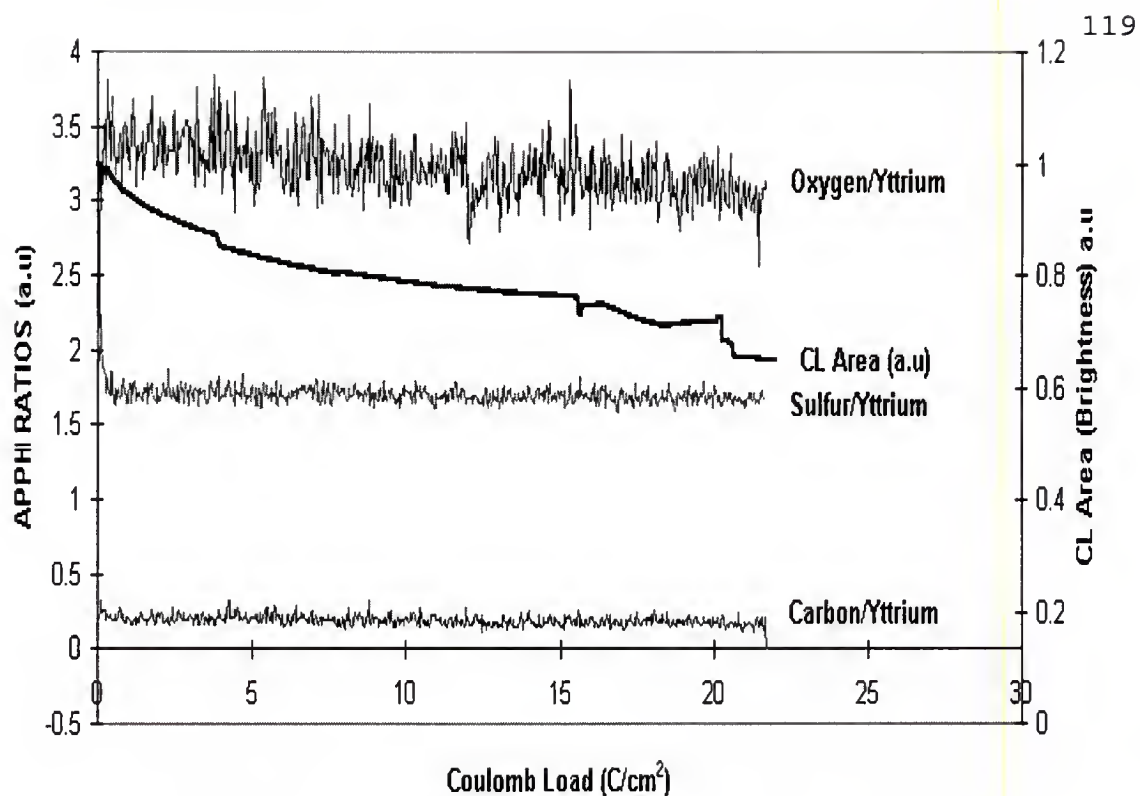
Figure 5-3   AES Peak-to-Peak Height ratios
normalized to the Yttrium Auger Peak-to-Peak Height.
Initial increase in CL brightness corresponds with the
removal of non-luminescent surface layer containing C
and S. CL Area (brightness) is depicted for comparison.
Note that although the AES ratios have stablized
after 2 C/cm2, the CL brightness continues to
decrease. This indicates that the degradation and
chemical modifications may be occurring below the
escape depth of the Auger electrons (5-10 atomic
layers).
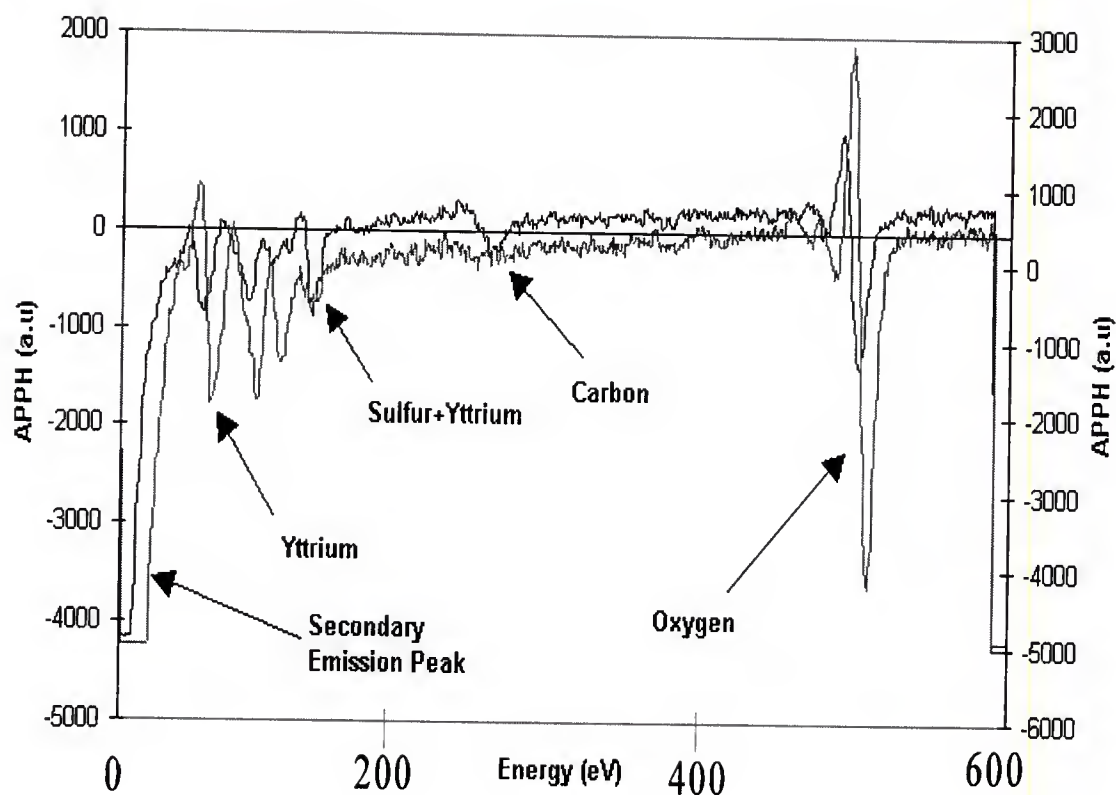
Figure 5-4   Comparison of Initial and Final AES
spectra taken at 0.1 C/cm² and 19.5 C/cm²,
respectively. Note the decrease in C and S APPH at the
end of the experiment. Also, note the positive energy
shift of the Y and O Auger peaks, as well as the
positive shift of the secondary emission peak. C and S
APPH's shift negatively in energy.
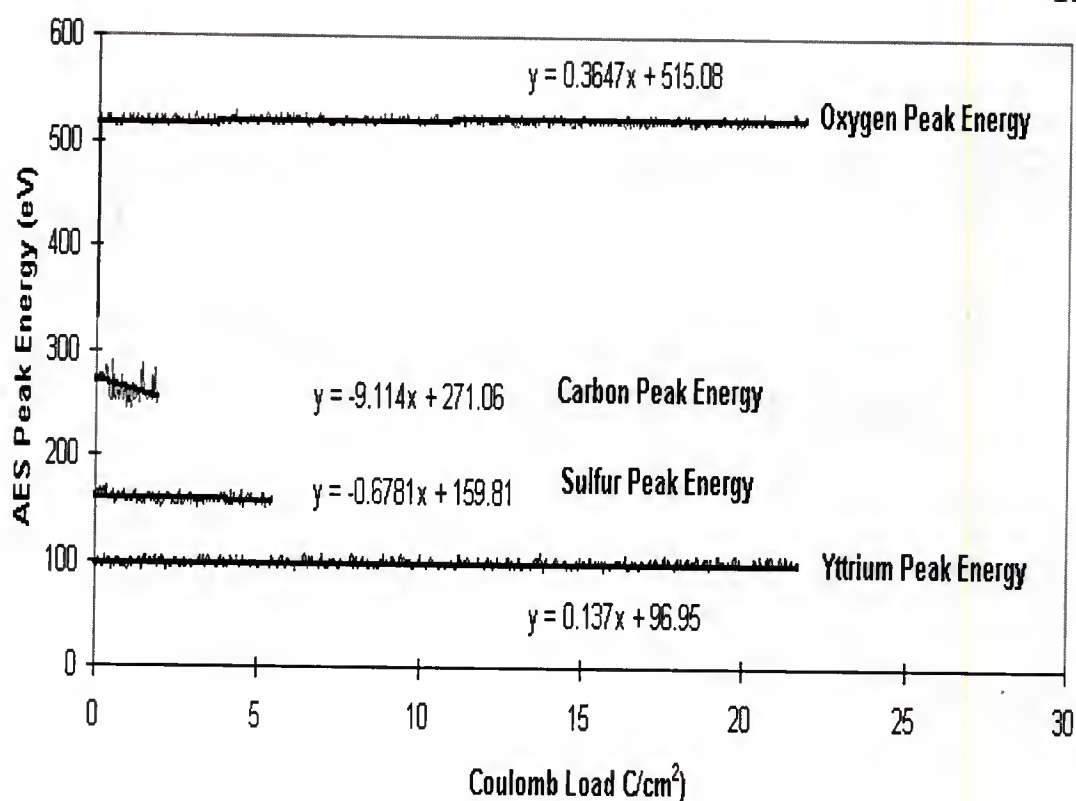
Figure 5-5   Auger Peak energy shifts as a function of coulomb load. Note the fast changes (as compared with the baseline experiment) that occur below 1 C/cm². O and Y shift to higher energies and C and S shift to lower energies. Equations are linear fits to the data presented.
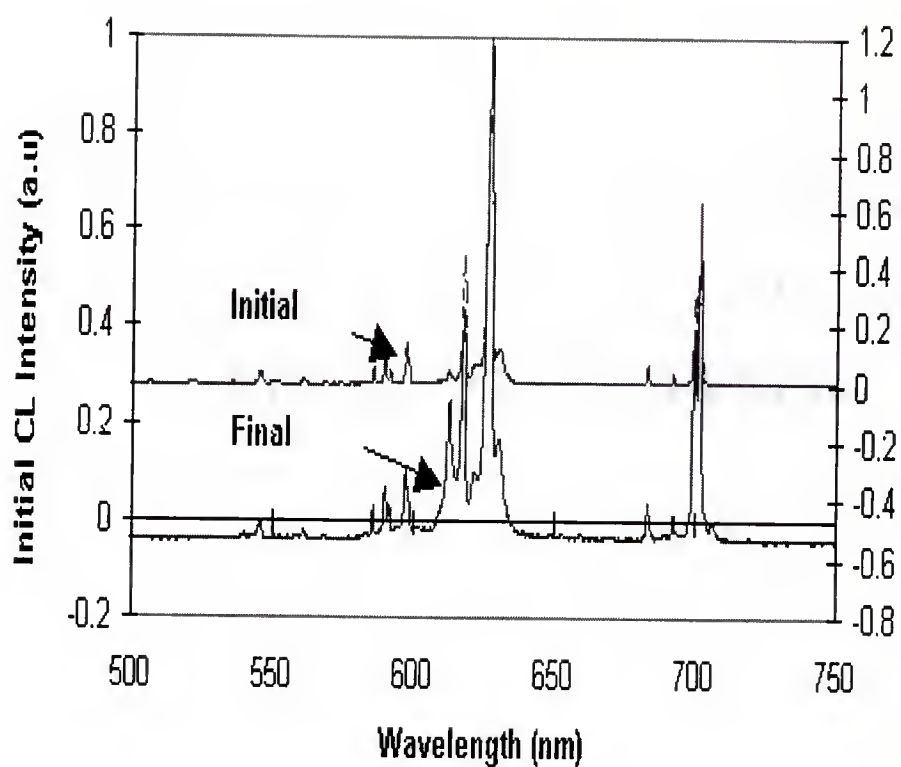
Figure 5-6   Initial and Final CL spectrum as a function of wavelength in nm. Large changes have occurred in the 600 to 640 nm region. The increase in the peak at 611 nm is indicative of $Y_2O_3:Eu^{3+}$ growth.
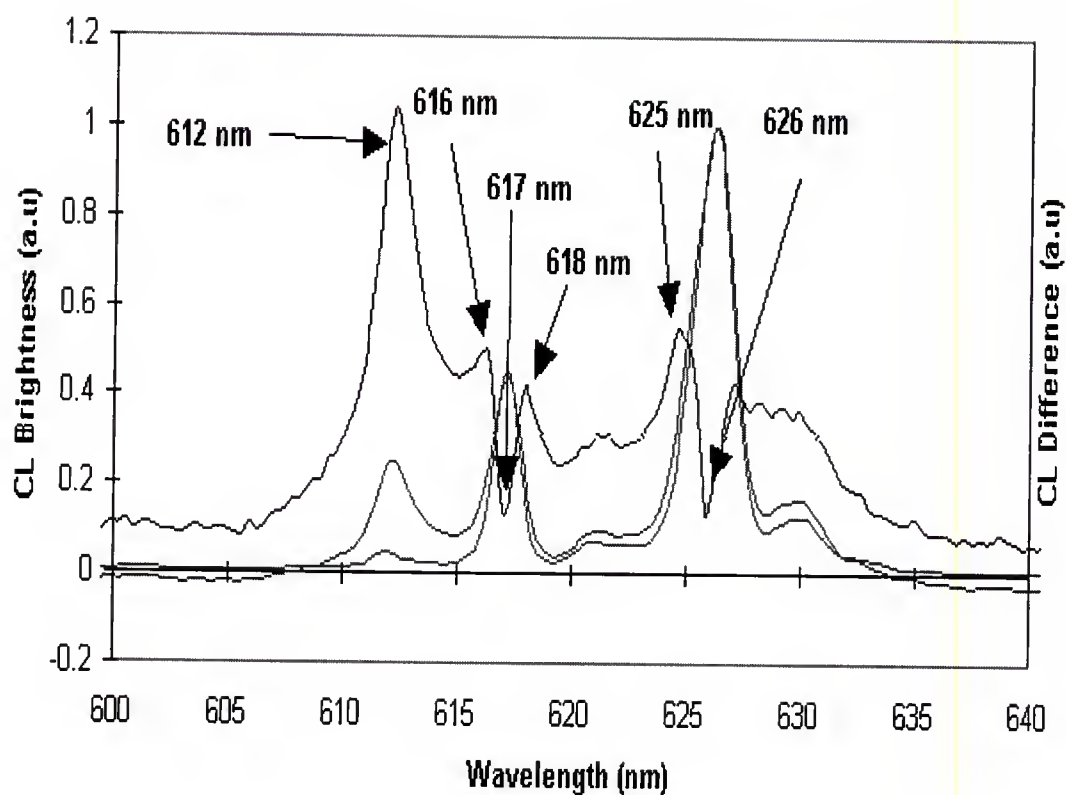
Figure 5-7   Initial and Final CL spectra as a
function of wavelength and the CL difference spectra.
Note the large negative deflection at 611.9 nm. This
large difference is indicative of the growth of
$Y_2O_3:Eu^{3+}$. Spectral broadening can be seen in the peaks
at 626 nm and 617 as shown by "wings" on the CL
difference spectra around the peaks.

The graph shows Brightness (a.u) on the y-axis versus Accelerating Voltage (eV) on the x-axis, with two fitted lines:

$y = 0.00033x - 0.25254$

$y = 0.00027x - 0.34847$
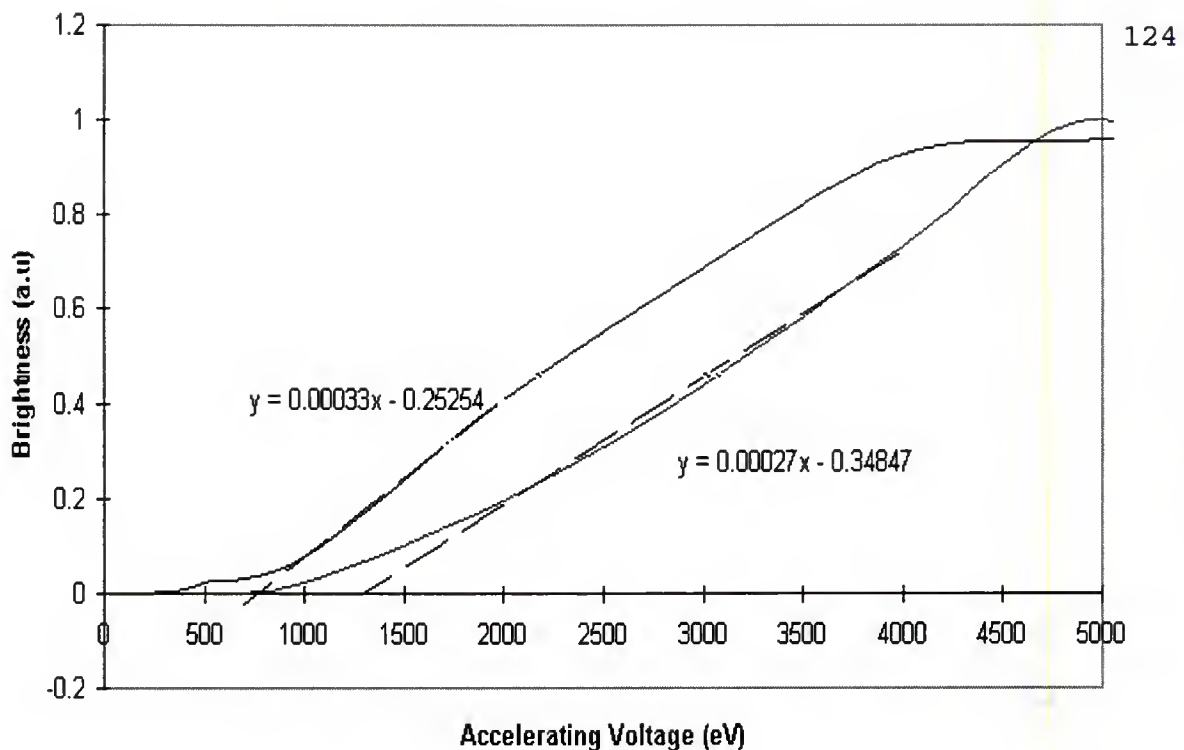
Figure 5-8   Threshold voltage experiment for phosphor prior to and after degradation experiment in oxygen gas. Note that the early portions of the curves (1kV-2kV) do not have the same slope, indicating a change in luminous efficiency. The threshold values have been calculated as 765 volts and 1290 volts. The difference in penetration depth is approximately 860Å. Note each line is normalized to itself, so the crossover at 4500 volts is not indicative of the aged spot brightness being higher than the un-aged spot.
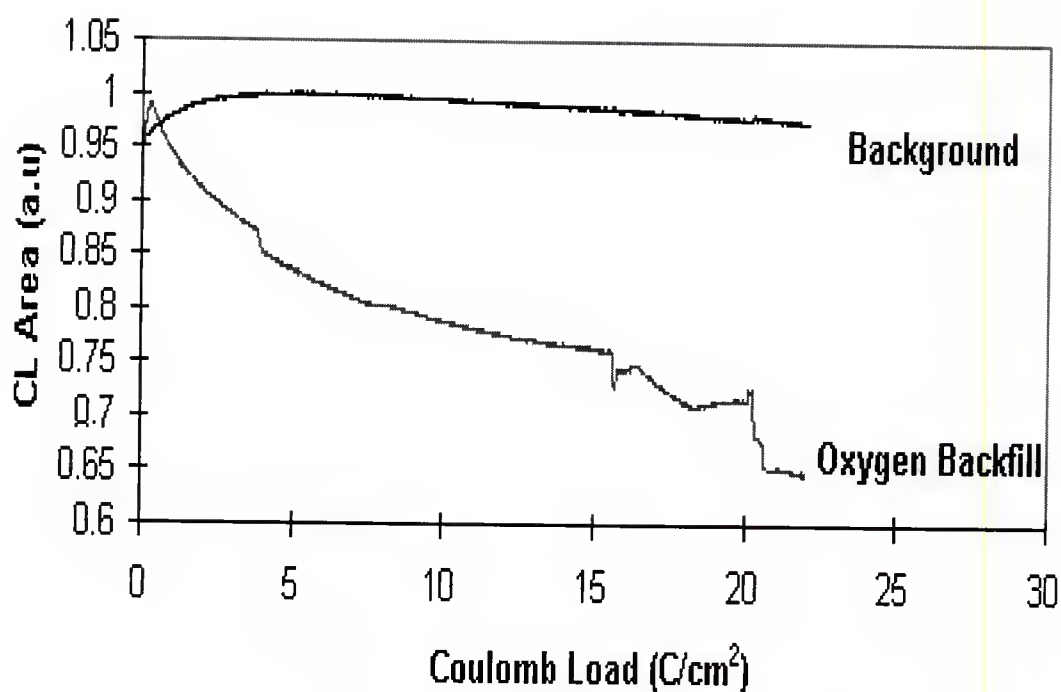
Figure 5-9   A comparison of the CL degradation rates
as a function of coulomb laod for the baseline
experiment and the oxygen ambient experiment. Note that
both curves show an initial increase in brightness (<1
C/cm^2 in oxygen and ~5 C/cm^2 in background), and a
steady decrease prior to maximum brightness. The rate
of degradation is much higher in oxygen, and is ~30% at
20 C/cm^2, whereas the baseline experiment has degraded
only 2-3%. The presence of oxygen in the system, allows
the surface reaction to occur at a faster rate, thus
the surface reaction and CL degradation occur at a
higher rate.
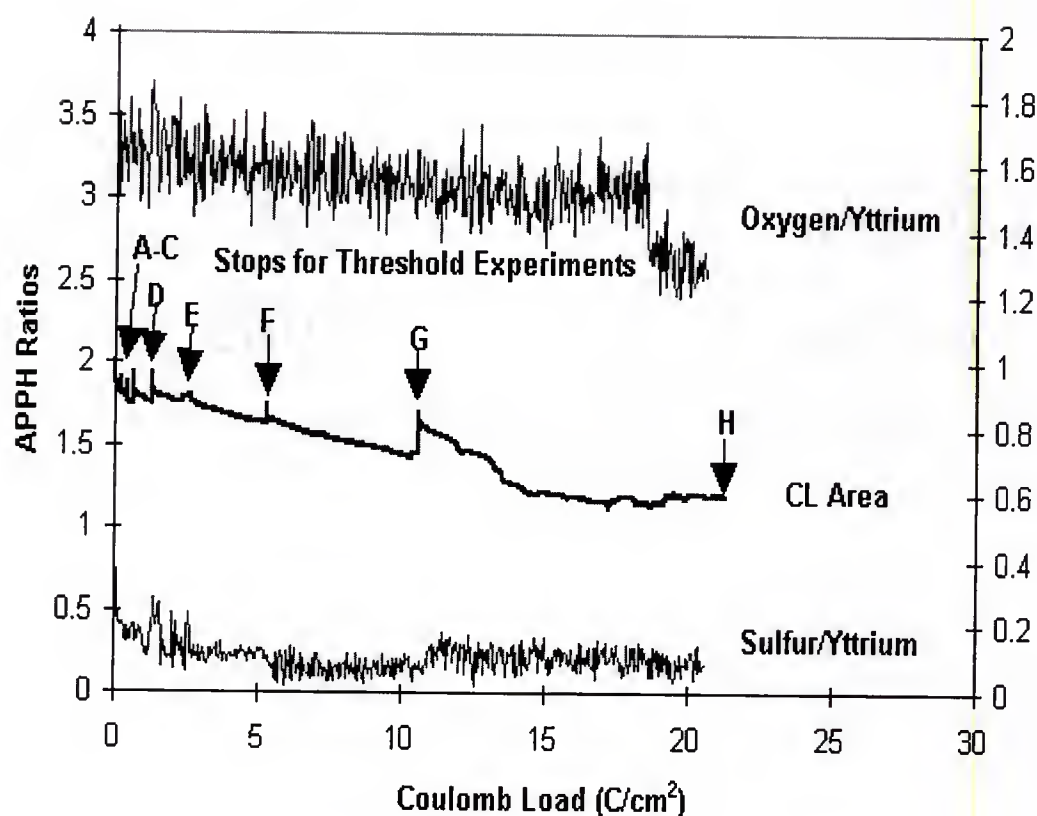
Figure 5-10   APPH ratios and CL degradation curve for the oxygen ambient experiment with threshold voltage experiments during the degradation. Points marked A through H are the points at which threshold voltage experiments were completed. No C/Y ratio is shown since no C was not present on the surface at the beginning of the experiment. Notice also that no initial climb to maximum brightness is exhibited.
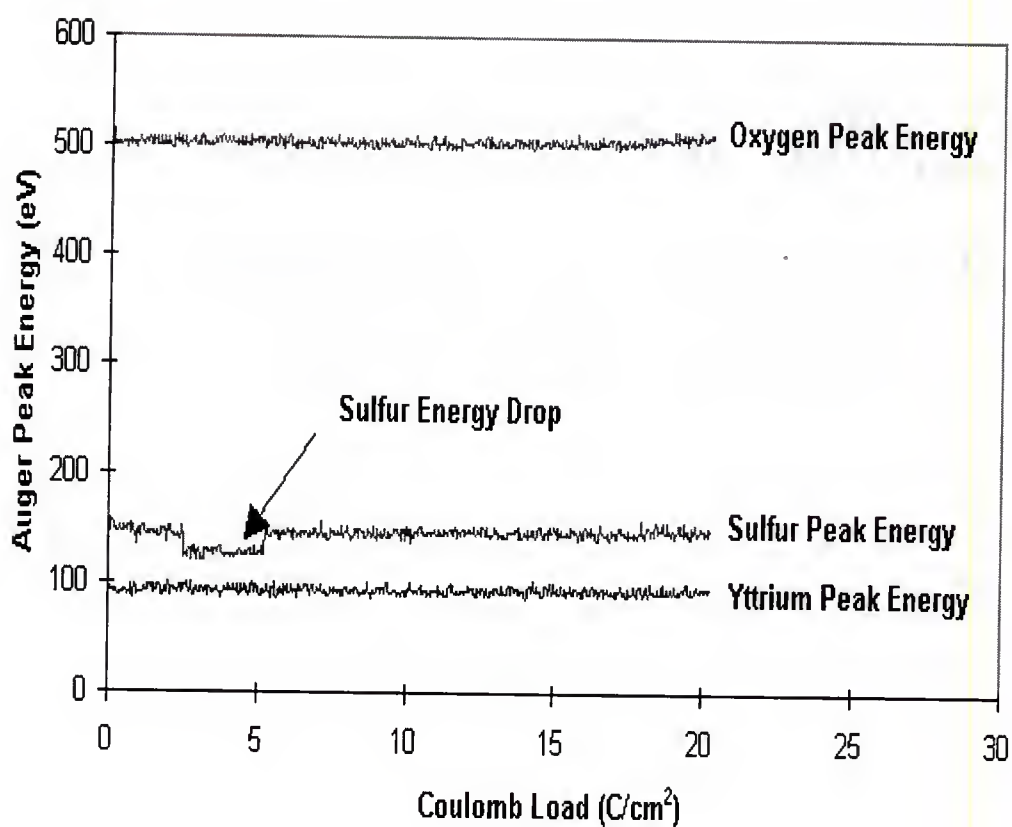
Figure 5-11   Auger peak energy shifts for the oxygen
ambient experiment with threshold experiments during
the degradation. O and Y peak energies increase
slightly prior to 3 C/cm², and S peak energy decreases
in the same load. Notice the drop in sulfur peak energy
between 3 and 5 C/cm².
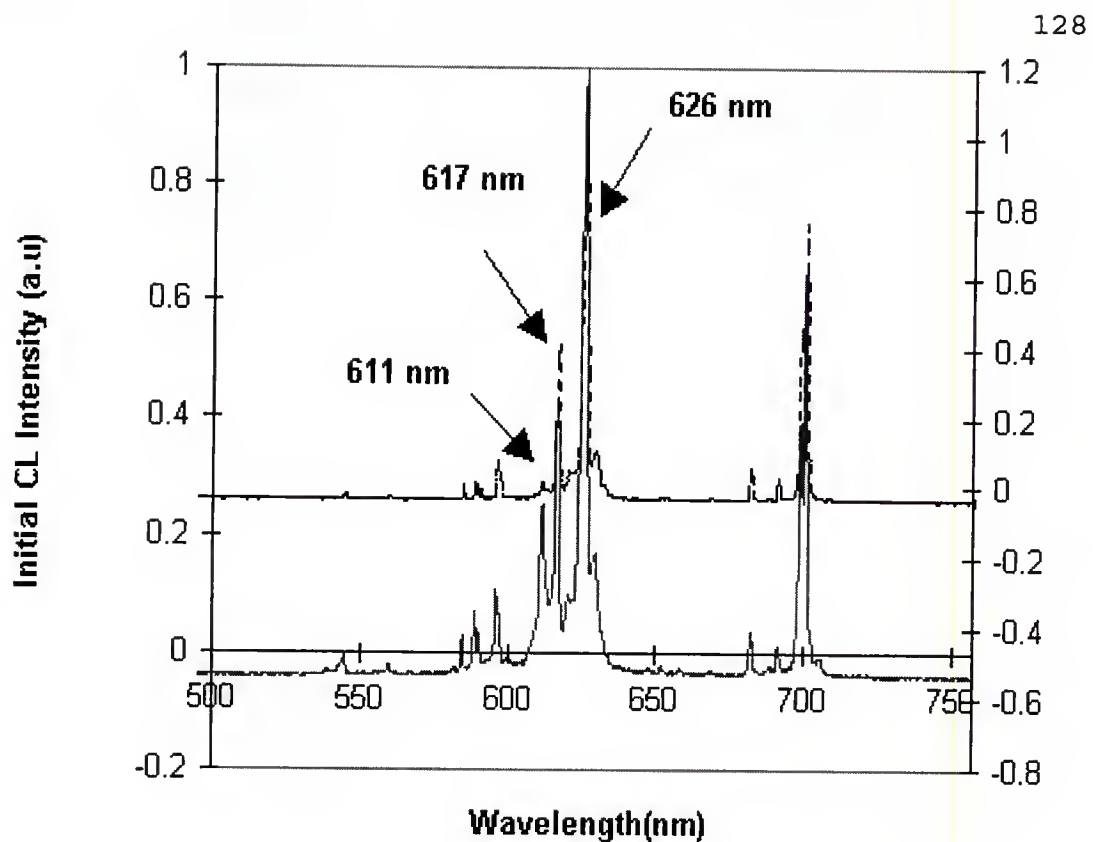
Figure 5-12   Initial and Final CL spectra as a function of wavelength in nm. Initial spectrum was taken prior to the beginning of the degradation experiment (0 C/cm²) and the final spectrum was taken at the end of the experiment (~22 C/cm²). Notice the large increase in the 611 nm peak, and decreases in the 626 nm and 617 nm peaks.
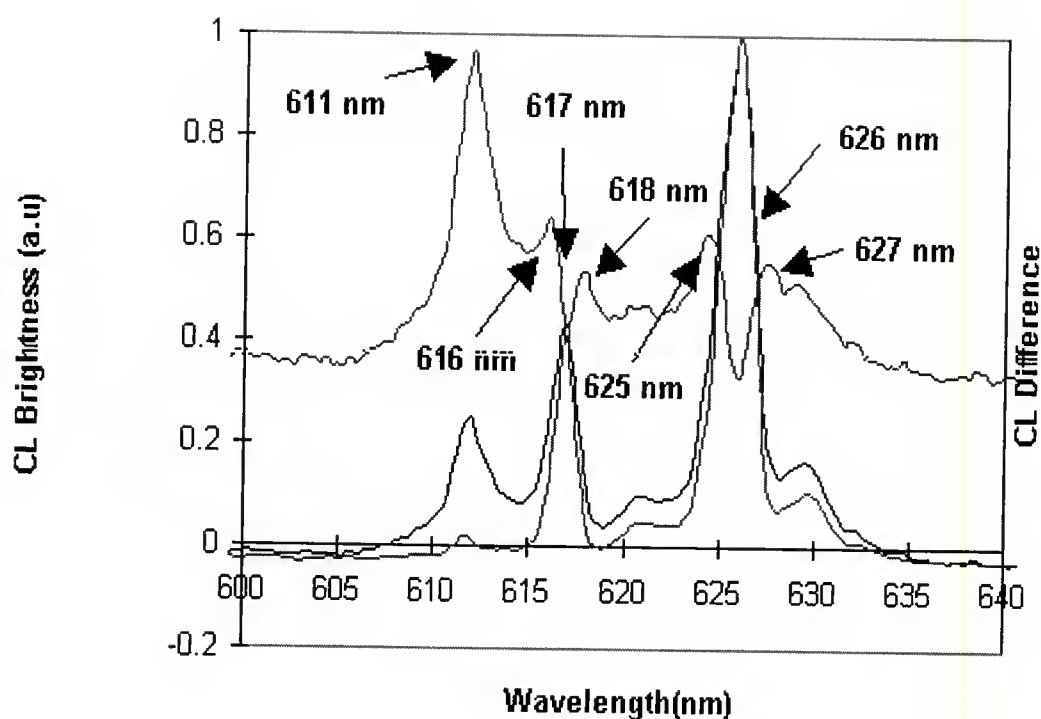
Figure 5-13   Expanded view of the initial and final
CL spectrum as a function of wavelength in nm. CL
difference is shown on the secondary y-axis. Notice the
loss in intensity (negative deflections on the CL
difference curve) for the $Y_2O_2S:Eu^{3+}$ peaks, 617 and 626
nm. A positive deflections are seen at 611 nm and 618
nm corresponding to $Y_2O_3:Eu^{3+}$.
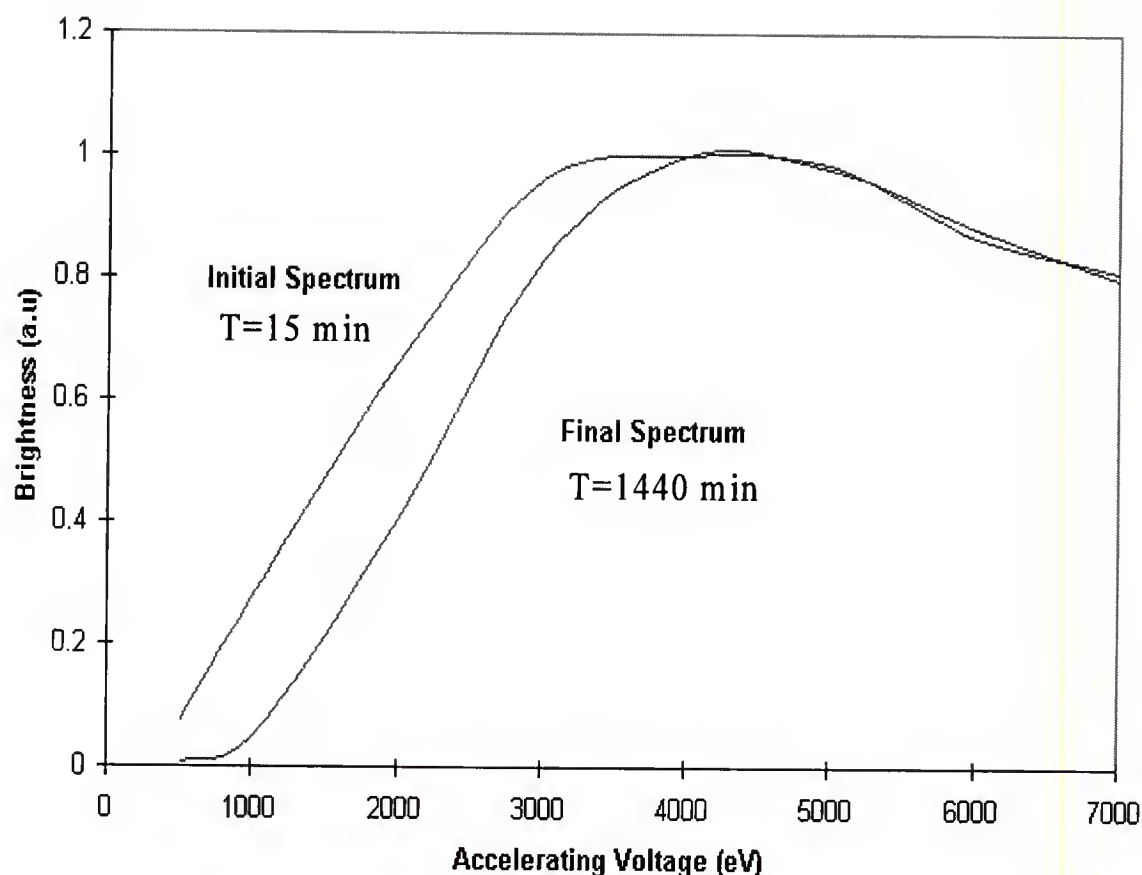
Figure 5-14   Initial and Final threshold voltage
experiment. Threshold voltages were found for the
curves and are 166 volts and 866 volts. These voltages
correspond to dead layer thicknesses of 0.019μm and
0.101μm, respectively. This suggests a dead layer
thickness of 820Å.
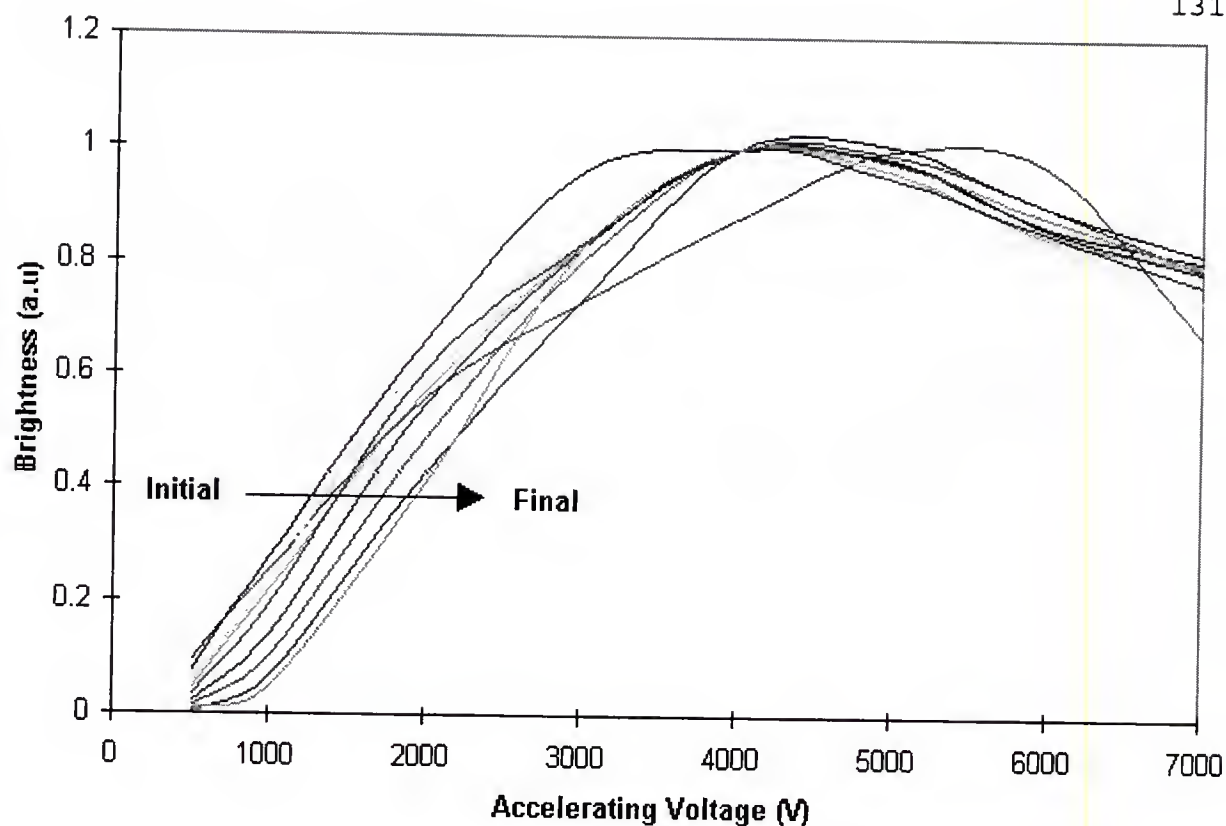
Figure 5-15   A Series of threshold curves taken
during the degradation of $Y_2O_2S:Eu^{3+}$ in an
oxygen ambient of $1.0x10^{-6}$ torr. Time intervals
are denoted in the legend. Notice the rightward shift
in threshold voltage as the CL degradation experiment
continued. No large changes in luminous efficiency are
seen in the linear portion of the curves, and no change
in saturation voltage is seen.
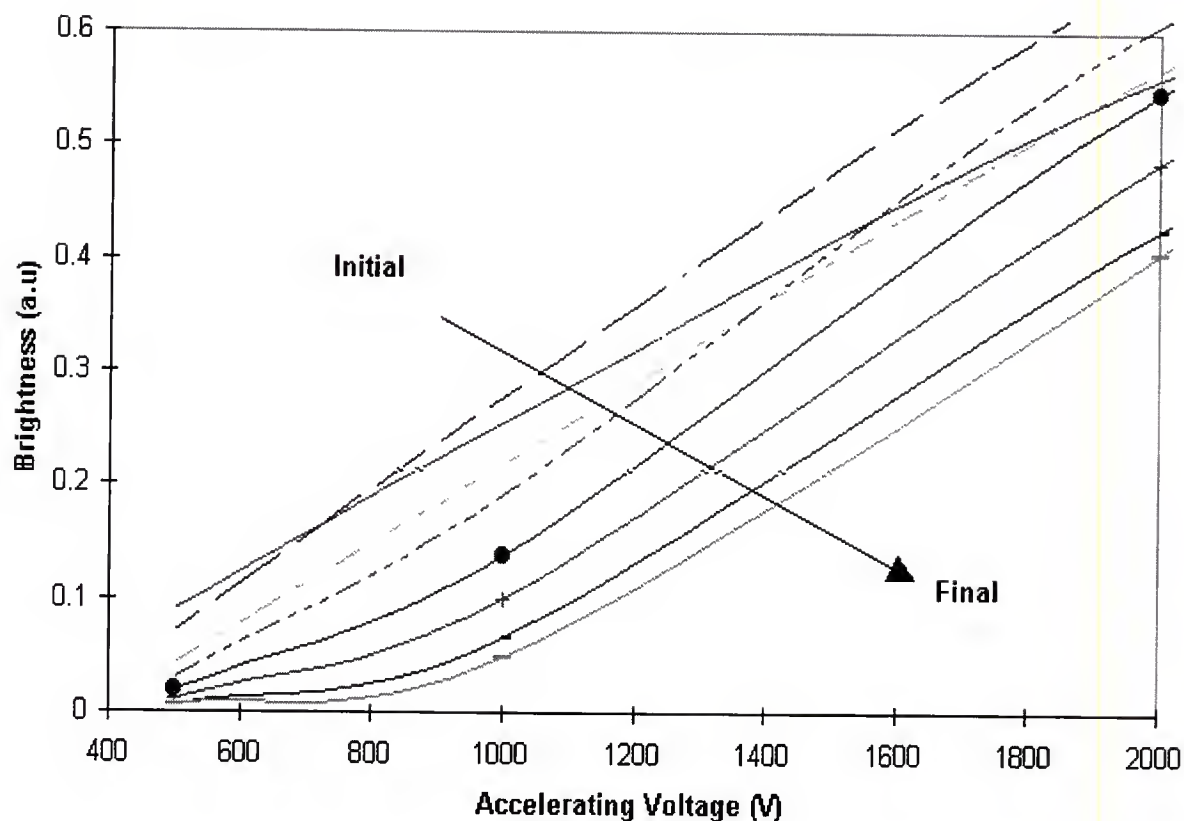
Figure 5-16   Expanded view of low voltage region of figure 5-15. Notice the smooth trend in increasing threshold voltage from the initial to final threshold experiment. This indicates continually increasing depth of dead layer through out the CL degradation experiment.
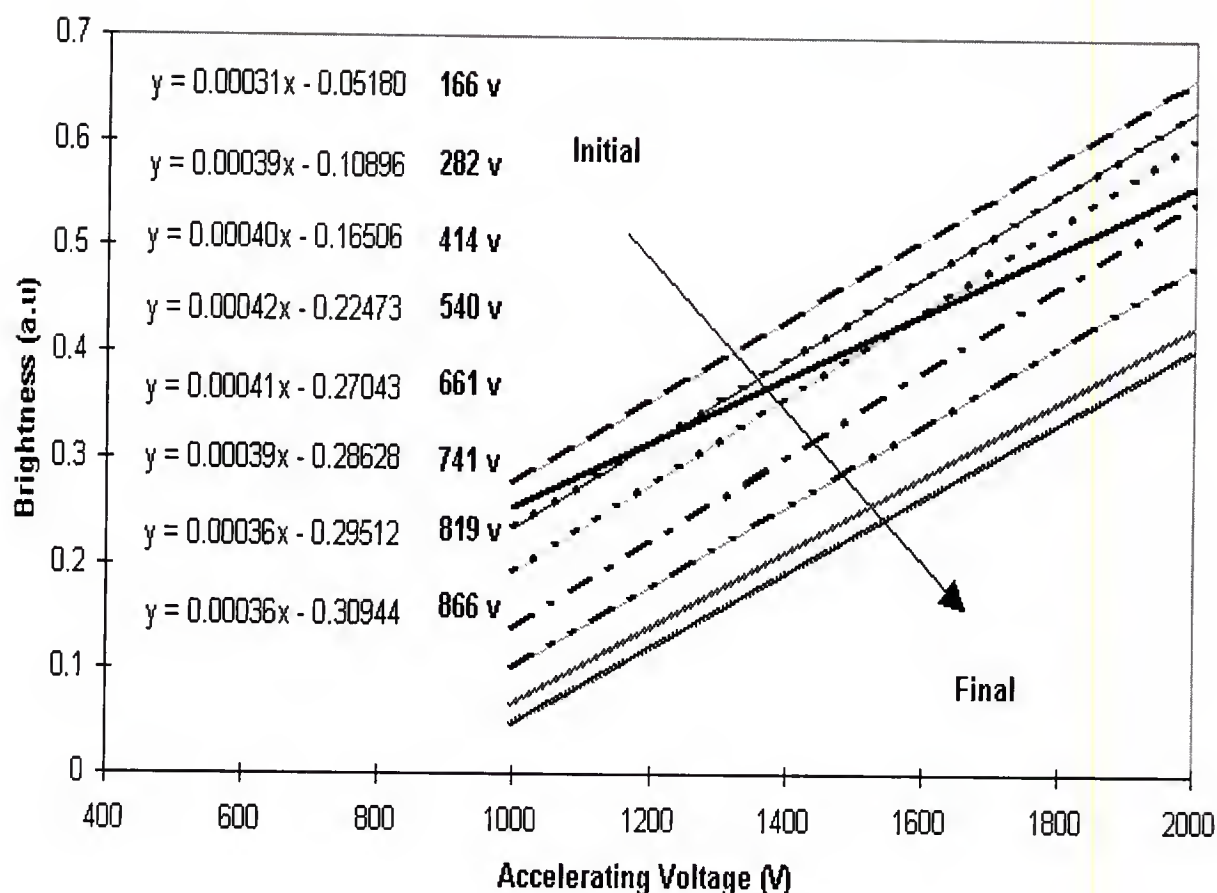
Figure 5-17   Trendline fits and equations for CL degradation experiment in oxygen ambient. The threshold voltages found from the linear portions of the curves are displayed next to their respective equations. Note the threshold voltage (indicative of dead layer thickness) increases rapidly then slows down.
This indicates a fast layer growth (possibly reaction limited) followed by a slow growth (diffusion limited).
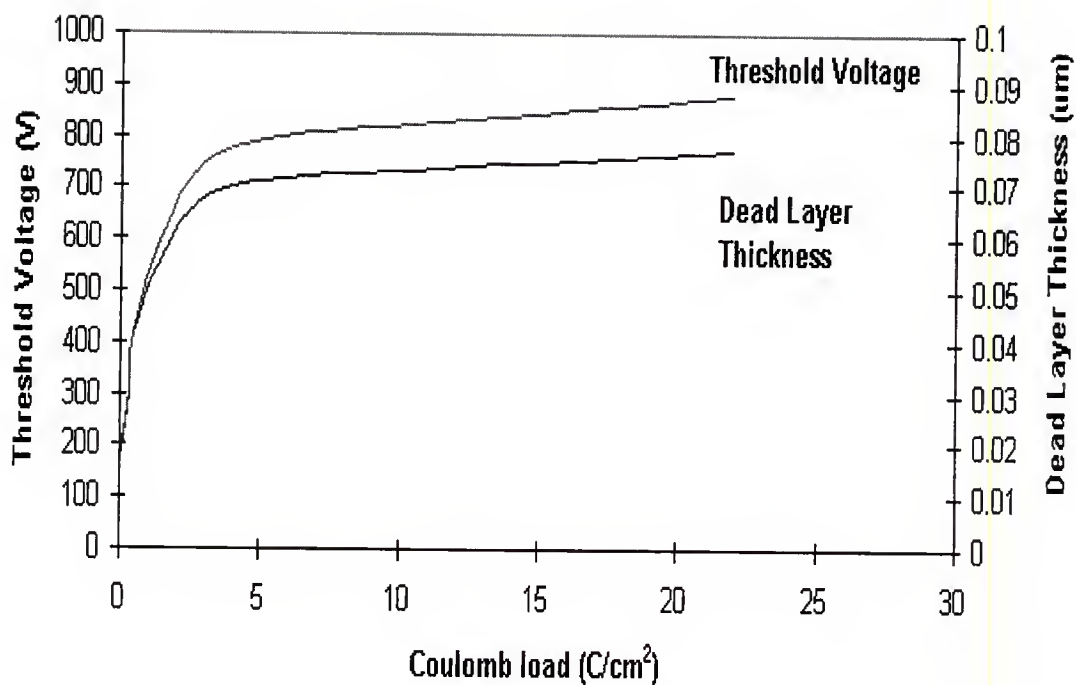
Figure 5-18   Threshold voltage and dead layer
thickness (calculated from figure 2-7). Note the fast
initial growth rate (<5 C/cm²) and the slow rate
afterwards. This type of growth is indicative of a
reaction limited growth followed by a diffusion limited
growth. The growth may become limited by the movement
of S through the dead layer as the CL degradation
continues past 5 C/cm².
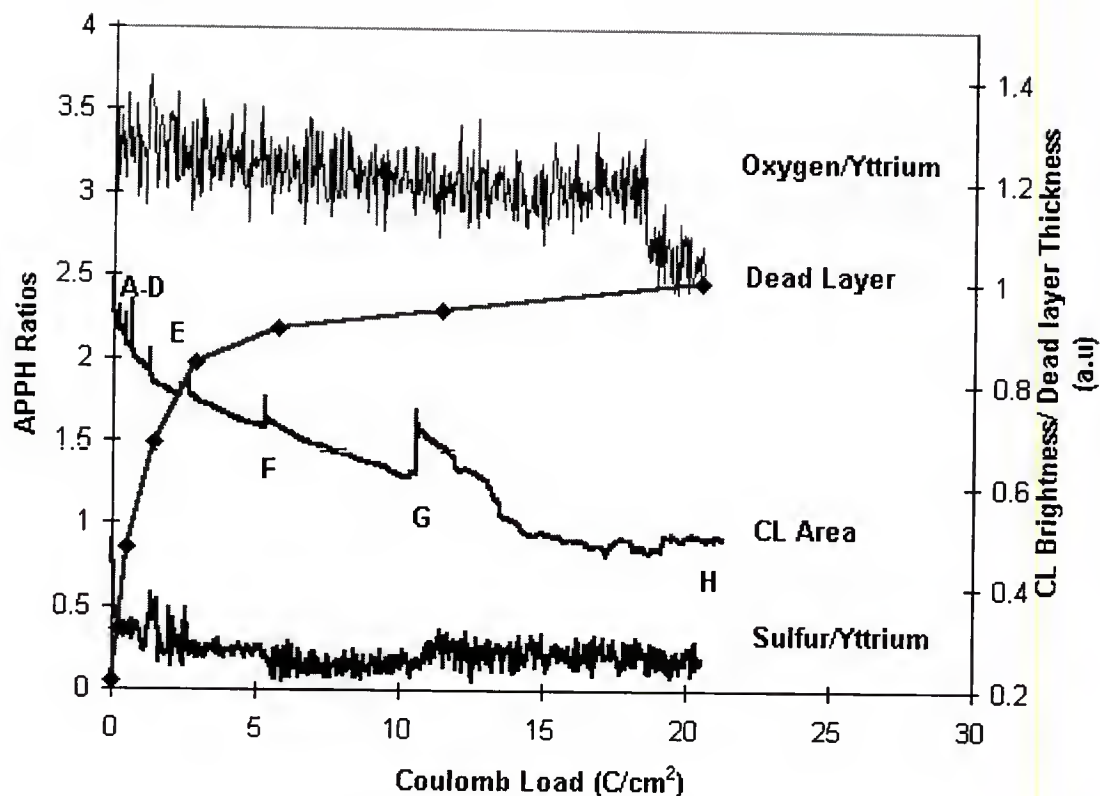
Figure 5-19   Correlation between AES APPH ratios and dead layer thickness as a function of coulomb load (C/cm²). O/Y and S/Y APPH ratios decrease and stabilize in 5 C/cm². Very good correlation between the dead layer thickness, the surface changes and the CL degradation are found. The generally smooth curve found for CL brightness is disrupted by the BV experiments conducted during the degradation. This indicates that the CL degradation is driven by the growth of surface phase.

CHAPTER 6

BEAM ENERGY DEPENDANCE ON DEGRADATION RATES OF $Y_2O_2S:Eu^{3+}$

Introduction

In the previous chapters, it has been shown that the CL degradation of $Y_2O_2S:Eu^{3+}$ is dependent on type and partial pressure of gas in the vacuum. It is postulated that impinging molecular gas, like O_2, striking the surface of the phosphor is dissassociated by the electron beam. Subsequently, the dissassociated gas molecule reacts with the surface of the phosphor. Initially C and S on the surface are reacted to volatile gas species which is carried away from the surface ($CO_{1,2}$, $SO_{1,2}$). The loss of C and S may initially be rate limited by the amount of reactive gas species available. Once a S depleted region exists near the

surface, further S removal should be slowed by S diffusion through the thickening S deficient layer. The diffusion of S may be driven by chemical potential gradients near the surface due to initial S depletion and/or may be driven by electric field enhanced diffusion induced by the presence of the electron beam and the charge induced near the surface.

An electron's ability to dissassociate gas is related to its kinetic energy [Eng94], assuming that the ionization cross-section is numerically equal to the disassociation cross-section. Classically, the ionization cross section decreases at energies greater than 200eV due to the reduction in interaction time with a gas molecule [Eng94]. As the electron's kinetic energy decreases, its velocity decreases and the amount of time the electron spends in the vicinity of a gas molecule increases. This allows for an increased probability of ionization of the gas molecule.

If CL degradation is limited by the amount of dissassociated gas available for reaction at the surface, it may be possible to observe a change in the rate of S loss from the surface at different accelerating voltages (different dissassociation efficiencies). It is suspected that lowering the accelerating voltage of the electron will

increase the amount of dissassociated gas available, thus increasing the rate of removal of S from the surface. Conversely, an increase in accelerating voltage will decrease the dissassociation efficiency, decreasing the amount of dissassociated gas at the surface, and decreasing the rate of S loss as seen by AES analysis.

This expectation may be simplistic due to other changes associated with lower accelerating voltage. The change in electron beam interaction volume will affect the CL degradation rate. Assuming that the conversion rate (Y_2O_2S to Y_2O_3) is constant for all electron beam energies, an increase in the CL generation volume will produce a slower rate of CL degradation. Thus the CL degradation rate may be higher for lower accelerating voltages due to a smaller electron beam interaction volume and also due to the higher dissassociation efficiency of gas molecules. The diffusion of S may be affected by a change in electric field strength near the surface and changes in surface temperature due to beam power, thus the effects of lower accelerating voltages on CL degradation are unclear.

Three experiments were conducted in vacuum ambients backfilled with oxygen gas to $1x10^{-6}$ Torr. A 1, 2 or 3keV,

electron beam will be used with nominal current densities between 100 and 400 $\mu A/cm^2$.

1 keV Experiment

A base pressure of 1.8×10^{-8} Torr was achieved initially and oxygen backfilling raised the system pressure to 1.0×10^{-6} Torr. Due to limitations of the electron gun, a sample current density of $150\mu a/cm^2$ was the maximum obtainable for the experiment. This limited the total coulomb load attainable in a 24 hour degradation experiment to ~16 C/cm^2. Figure 6-1 shows the APPH ratios for O/Y, S/Y, and C/Y and the CL brightness as functions of coulomb load (C/cm^2). The CL brightness decreased nearly 60% during this experiment. This decrease is larger than that observed in previous 2keV experiments (typically 30-40% decrease in brightness). The O/Y APPH ratio appears to decrease steadily while the S/Y and C/Y APPH ratios decrease rapidly initially and then stabilize after ~0.5C/cm^2. Note that the S/Y APPH ratio has been shifted up on the y-axis by 1 unit to separate it from the C/Y APPH ratio. Figure 6-2 shows the initial (0.06C/cm^2) and final AES spectra (14.1C/cm^2) as a function of energy. Both C and S have been removed from the

surface and both peaks have decreased below the sensitivity

of the AES spectrometer while the O and Y APPHs have

increased during the experiment. The AES peak energy shifts

of C and S can only be examined early in the experiment

(until ~3 C/cm^2). These results suggest a near-surface loss

of C and S as has been seen in the experiments reported in

Chapter 4 and 5. The near-surface is an oxygen-rich, S-

depleted material, most likely Y_2O_3 based on the conclusions

of Chapter 5. Figure 6-3 shows the AES peak energy shifts

(in eV) as a function of coulomb load (C/cm^2). The trend

line fits show that O and Y exhibit ~1.5eV positive shift in

energy during the experiment and the C and S energies shift

negatively by ~1eV, again consistent with the results of

Chapter 4 and 5. These shifts may be associated with changes

in surface charge changes induced by the chemical

modifications occurring at the surface. Figure 6-4 shows the

CL spectral intensity (a.u) as a function of wavelength (nm)

for the initial (0 C/cm^2) and the final CL spectra (16

C/cm^2). Only small changes can be seen on this graph

(specifically the increase in emission at 611nm). The

expanded spectra and the CL difference curves are shown in

figure 6-5 for the 600-640 nm wavelength regime. The largest

change is found at 611 nm, indicating an increase in the

emission from Y_2O_3:Eu^{3+}. Large peaks seen at 616, 618, 625

and 628nm, can be attributed to spectral broadening of the

main emission peaks of Y_2O_2S:Eu^{3+} at 617 and 626nm as

discussed in Chapter 5. This may be caused by the S removal

and densification to Y_2O_3:Eu^{3+}. Large negative deflections at

626 and 616 nm show the loss in intensity exhibited by the

Y_2O_2S:Eu^{3+} main emission peaks.

2keV Experiment

For this experiment, the vacuum pressure prior to

oxygen gas backfilling was 1.3×10^{-8} Torr. After backfilling,

the pressure was stable at 1.1×10^{-6} Torr. The electron beam

current density was $265\mu A/cm^2$. Figure 6-6 shows the APPH

ratios for O/Y, C/Y and S/Y as well as the CL brightness as

a function of coulomb load on the secondary y-axis.

Comparing the AES ratios to the 1kev ratios of figure 6-1,

the S/Y and C/Y APPH ratios decrease more with coulomb load

than the corresponding ratios at 1keV. The O/Y ratio

exhibits a fast decrease (<1 C/cm^2) and recovery (2C/cm^2)

and decreases slowly for the duration of the experiment. The

S/Y and C/Y ratios decrease quickly and stabilize after

~3C/cm^2. By comparing these decreases with figure 6-7, which

shows the initial and final AES spectra as a function of

energy, it is clear that C has dropped below the AES

sensitivity after 3 C/cm^2. Figure 6-7 shows relatively large

amounts of C and S on the surface in comparison to the 1keV

experiment. The C peak is very well defined, whereas in

figure 6-2 it is only slightly above the noise level. Total

CL degradation is estimated to be 45 percent at 15C/cm^2 in

figure 6-6 which compares to 60% degradation at 15 C/cm^2 for

the 1keV experiment (see figure 6-1). This indicates that CL

degradation is more severe at lower accelerating voltages.

This could be due to the smaller beam interaction volume

and/or due to the increase in dissassociation efficiency.

The initial and final AES spectra shown in figure 6-7 shows

that the O, Y and S peaks all exhibit a small negative

energy shift. The peak energy shifts and associated trend

lines and equations are shown in figure 6-8 as a function of

coulomb load (C/cm^2). Unlike previous experiments, which

showed positive Y and O peak shifts, Y and O peaks shifts

were negative during this experiment. This may be caused by

the loss of the relatively good conducting layer of C, which

initially was able to reduce surface charging induced by the

electron beam. Once the C is removed, the phosphor would charge and the energy of the AES electrons would be changed accordingly. A decrease in AES peak energy indicates a less negative charge near the surface since all peaks are shifted above the expected AES values initially. Figure 6-9 shows the initial and final CL spectra as a function of wavelength in nm. The spectra are very similar and the differences can only be seen in figure 6-10, where the expanded spectra and CL difference are shown. Peak intensity increases are found at 611, 616, 620, 625 and 630 nm. The 611 nm peak is attributed to the oxide growth. The (616,620) and (625,630) nm peaks may be caused by spectral broadening of the $Y_2O_2S:Eu^{3+}$ emission peaks, indicating local symmetry changes around the Eu3+ ions.

3keV Experiment

During this experiment, the current density was set at $371\mu A/cm^2$. The vacuum pressure was $1.8x10^{-8}$ Torr prior to backfilling with oxygen gas at $1x10^{-6}$ Torr. Figure 6-11 shows the APPH ratios for O/Y and S/Y. No C was present on the surface at the beginning of the experiment (within AES detection limits). As is typical for oxygen gas backfill

experiments, the O/Y ratio decreases in a non-linear fashion

(until ~5-10 C/cm²) then continues to decrease slowly for

the duration of the experiment. The S/Y ratio shows that S

leaves the surface by ~4 C/cm². The rate of removal of S is

slower than that observed in the 1keV experiment, but the

difference between the 2keV and 3keV rates are more subtle

(compare figure 6-1,6-6, and 6-11). The most drastic change,

in comparison with the previous two experiments, is seen in

the CL brightness plotted as a function of coulomb load. The

total CL decrease during the 3keV experiment is only ~10%.

Comparing the CL degradation at 15C/cm², the percent losses

are ~ 60%, 45% and 5% for 1keV, 2keV and 3keV, respectively.

As the accelerating voltage is increased, the excitation

volume is increased, and the dissassociation efficiency of

the electrons is decreased, thus the CL degradation is

slower. Figure 6-12 shows the initial (0.08 C/cm²) and final

(27C/cm²) AES spectra as a function of energy in eV for the

3keV experiment. Notice that the C signal is below the

detection limit of the AES spectrometer at the beginning of

the experiment. A significant S signal is present at the

onset but has fallen below the noise level by 27 C/cm². Y

and O APPHs increased slightly during the experiment. Auger

peak energy shifts in figure 6-12 are apparent on only the

Y, but the peak energies shown in figure 6-13 as a function

of coulomb load (C/cm²) show that both the O and Y peak

energies exhibited positive shifts (to higher energies)

while the S peak energy decreased. The shifts in energy are

7.2, -1.0 and 4.6 eV respectively for O, S and Y at 20

C/cm². This is consistent with a negative charge buildup on

the surface of the phosphor. The initial and final CL

spectra are shown in figure 6-14 as a function of wavelength

(nm). Large changes can be discerned without expanding the

graph and determining the differences between the two

spectra which are shown in figure 6-15. Peaks have increased

in intensity at 611 and 630nm (Y_2O_3:Eu^{3+}) and 618 and 627nm.

The 616,618 and 625,627nm peaks are attributed to broadening

of the main emission peaks of Y_2O_2S:Eu^{3+}. The 618nm peak

could also be the main emission peak of $Y_2O_2SO_4$:Eu^{3+} as was

seen in Chapter 4, but the similarity to the positive

deflections seen on the 627 nm peak coupled with the low

luminous efficiency of $Y_2O_2SO_4$:Eu^{3+} leads the author to

believe that both peaks are caused by spectral broadening

induced by local changes occurring at Eu^{3+} emission sites.

Peak decreases are noted at the emission wavelengths for

$Y_2O_2S:Eu^{3+}$ (616 and 626 nm).

Discussion and Comparison of 1,2 an 3 Kev Data

The CL degradation rates versus coulomb load (C/cm^2)

for the 1,2 and 3 keV experiments are shown in figure 6-16.

The CL degradation rate is higher at lower accelerating

voltages. At lower accelerating voltages, the degradation

curve takes on an exponential decay (1keV), whereas at

higher accelerating voltages (3keV) the CL degradation

appears nearly linear. The larger excitation volume at 3keV

seems less affected by the surface conversion of Y_2O_2S to

Y_2O_3. A comparison of the rate of removal of S can be seen

in figure 6-17 as a function of coulomb load. The S/Y ratios

are depicted for the 1, 2, and 3KeV experiments. Only the

very beginning of each experiment is shown (<$2C/cm^2$ load).

As expected, the rate of S loss is highest for the 1keV

experiment. The S/Y ratio has fallen to the noise level by

~0.2 C/cm^2, whereas the S/Y ratios for the 2keV and 3keV

experiment decrease and stabilize at ~0.8 C/cm^2. It is

interesting to see the effect of C on the removal rate of S

in the 2keV experiment. Note that the S loss rate is slower

at 2kev then it is at 3keV. This does not follow the

expected pattern for dissassociation efficiency, but upon

examining the initial conditions of the 2keV and 3keV

surface (figure 6-7,6-12) it is seen that a large amount of

C existed on the surface during the 2keV experiment, whereas

no C was seen on the 3keV surface. The volatilization

reactions for C are similar to those for S, and in the

presence of C, the S desorption rate would be lower due to

the competing process of C volatilization. This can actually

be seen where the initial loss of S at 2keV is slow (0-0.3

C/cm^2), but once the amount of C (as seen in Figure 6-6) has

decreased, the rate of S loss increases ($\sim$0.3 C/cm^2). Thus

the presence of C on the surface effectively slows the S

loss rate by acting as a competing process for reaction with

dissassociated gas species.

Depth Resolved CL Studies of Y_2O_3:Eu^{3+} Emission

Previously, it has been shown that the near surface

conversion of Y_2O_2S:Eu^{3+} to Y_2O_3:Eu^{3+} causes a spectral

redistribution in the CL spectra. In order to substantiate

further the existence of the Y_2O_3:Eu^{3+} surface after electron

beam aging, depth resolved CL studies were used after the

3keV experiment discussed previously in this chapter. By

varying the accelerating voltage of the electron gun, it is

possible to excite consecutively greater depths in the

phosphor. In order to be sure that the area examined was

within the aged spot, the beam was refocused within the aged

spot and then CL spectra were taken at energies of 300V to

5000V with the current density set at $176\mu A/cm^2$. The

refocusing of the electron beam alters the CL spectra

greatly. Since the beam energy exhibits a gaussian

dependance on distance from its center, the highest energy

density is found near its center. By narrowing the electron

beam, the CL spectra produced comes from the very center of

the larger degraded spot. Figure 6-18 shows the change in

the wide spot 3keV spectra and the narrow spot 3keV spectra.

The narrow spot is dominated by the 611 nm emission of

$Y_2O_3:Eu^{3+}$. This indicates that the conversion occurs at the highest rate where the beam energy density is highest (near the center of the wide spot). The use of the normalized intensity, coupled with the narrowing of the beam accentuates the oxide emission by reducing the amount of $Y_2O_2S:Eu^{3+}$ sampled in the narrow beam. Figures 6-19 through 6-26 show the evolution of CL spectra as a function of wavelength (nm) for increasing accelerating voltages. The lower voltage graphs (400,500 and 1000 V) in Figures 6-19, 6-20 and 6-21, respectively) are dominated by the oxide spectrum (main emission 612nm) with only a small contribution from $Y_2O_2S:Eu^{3+}$ (626nm). This indicates, a nearly complete surface conversion of $Y_2O_2S:Eu^{3+}$ to $Y_2O_3:Eu^{3+}$. As the accelerating voltage is increased from 1500 to 4000 V (figures 6-22 to 6-26), the $Y_2O_2S:Eu^{3+}$ emission peaks increased in intensity at a faster rate than the $Y_2O_3:Eu^{3+}$ peaks. Thus as the electron beam probes deeper, the relative contributions from $Y_2O_2S:Eu^{3+}$ versus $Y_2O_3:Eu^{3+}$ is increasing. This is consistent with a luminescent oxide layer at the surface. It is difficult to quantitate the depth to which the conversion took place because the phosphors efficiencies are different (8% for $Y_2O_3:Eu^{3+}$ and 13% for $Y_2O_2S:Eu^{3+}$). Also,

since the Y_2O_3 formed can only contain the Eu activator

concentration of the original Y_2O_2S (4 atomic %), the Y_2O_3

efficiency will be lowered further. The maximum CL

efficiency is observed with a Eu concentration of ~10 atomic

% for $Y_2O_3:Eu^{3+}$ [Oza90]. The low voltage spectra do verify

the presence of the $Y_2O_3:Eu^{3+}$ at the near surface and

confirms the presence of $Y_2O_2S:Eu^{3+}$ below the formed $Y_2O_3:Eu^{3+}$.

Figure 6-27 shows the complete evolution of $Y_2O_3:Eu^{3+}$ and

$Y_2O_2S:Eu^{3+}$ emissions in a single graph. Note the increase in

$Y_2O_2S:Eu^{3+}$ emission at the higher accelerating voltages (2keV

and above).

Summary

Degradation experiments with $E_p=1,2$ and 3 keV show that

the rate of CL degradation is faster at lower accelerating

voltages, but $Y_2O_3:Eu^{3+}$ dominates the CL spectra more at 3

keV. Higher dissassociation rates of gas molecules for lower

accelerating voltages increases the amount of available,

reactive gas at the surface which rapidly react to form

volatile C and S containing products. The sulfur desorption

rate is slowed by the high concentrations of C at the

surface of the phosphor. In the presence of oxygen gas, the conversion of $Y_2O_2S:Eu^{3+}$ to $Y_2O_2SO_4:Eu^{3+}$ could not be verified, but the presence of $Y_2O_3:Eu^{3+}$ CL emission peaks indicate that the surface has been chemically altered and a luminescent form of $Y_2O_3:Eu^{3+}$ is the product of the electron beam stimulated surface reactions. It is possible that the $Y_2O_2SO_4:Eu^{3+}$ emission intensity is too weak to measure, or that it is a metastable phase in the presence of oxygen gas. Confirmation of the oxide surface has been found by using depth resolved CL studies.
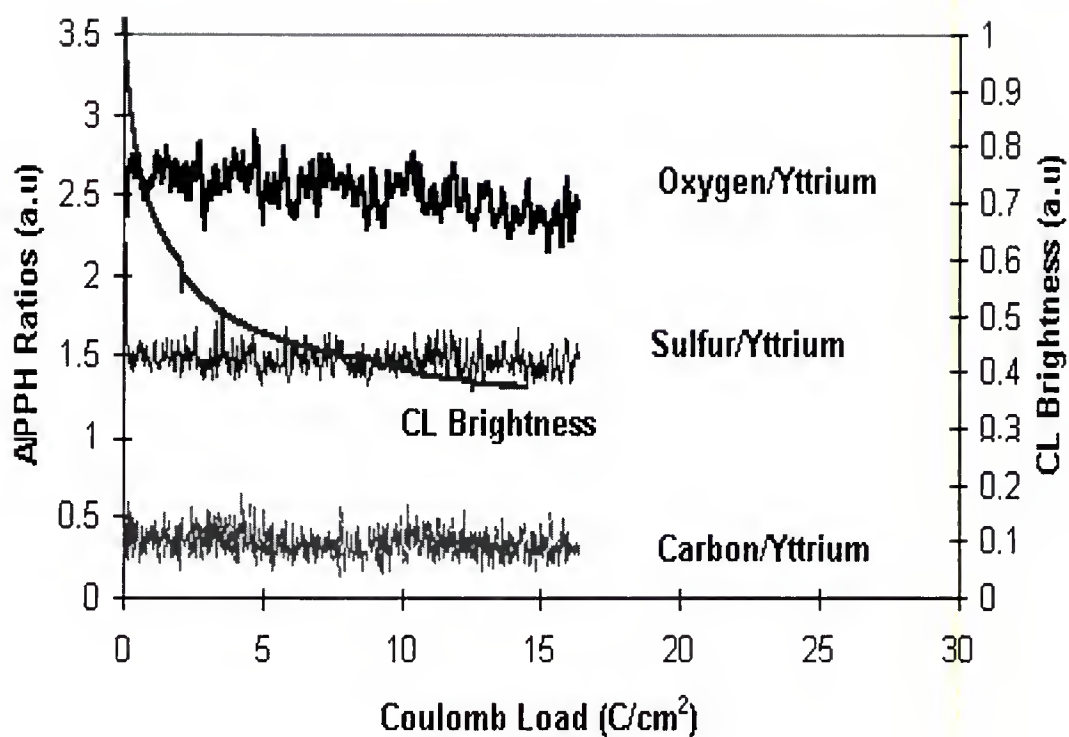
Figure 6-1   APPH Ratios and CL Brightness as functions of coulomb load (C/cm^2) for the 1kV accelerating voltage experiment. Note the fast removal of C and S. Also note the total loss in brightness of the 1keV experiment, nearly 60%. The S APPH ratio has been shifted up by 1 unit to separate it from the C/Y APPH ratio.
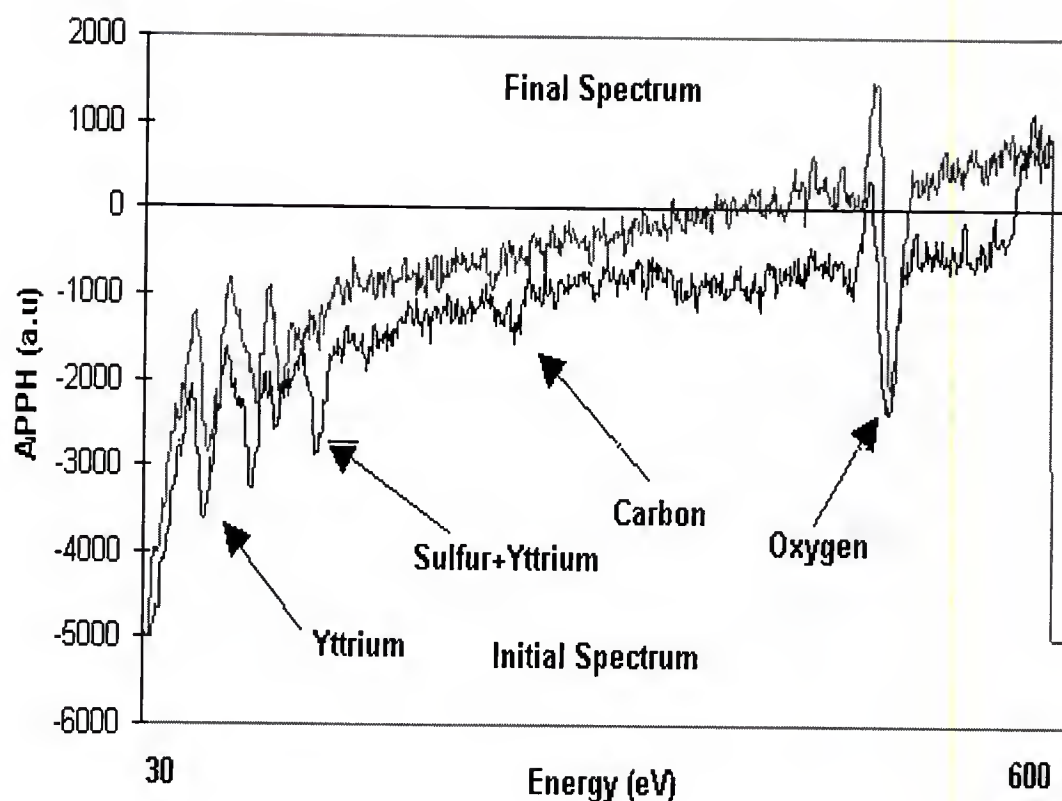
Figure 6-2   AES spectra taken at 0.06 C/cm² and 14.1
C/cm² for the 1keV accelerating voltage experiment.
Note the loss of S and C during degradation,
and the slight increases in O and Y peak
heights. A small, positive energy shift can be seen on
the oxygen peak.
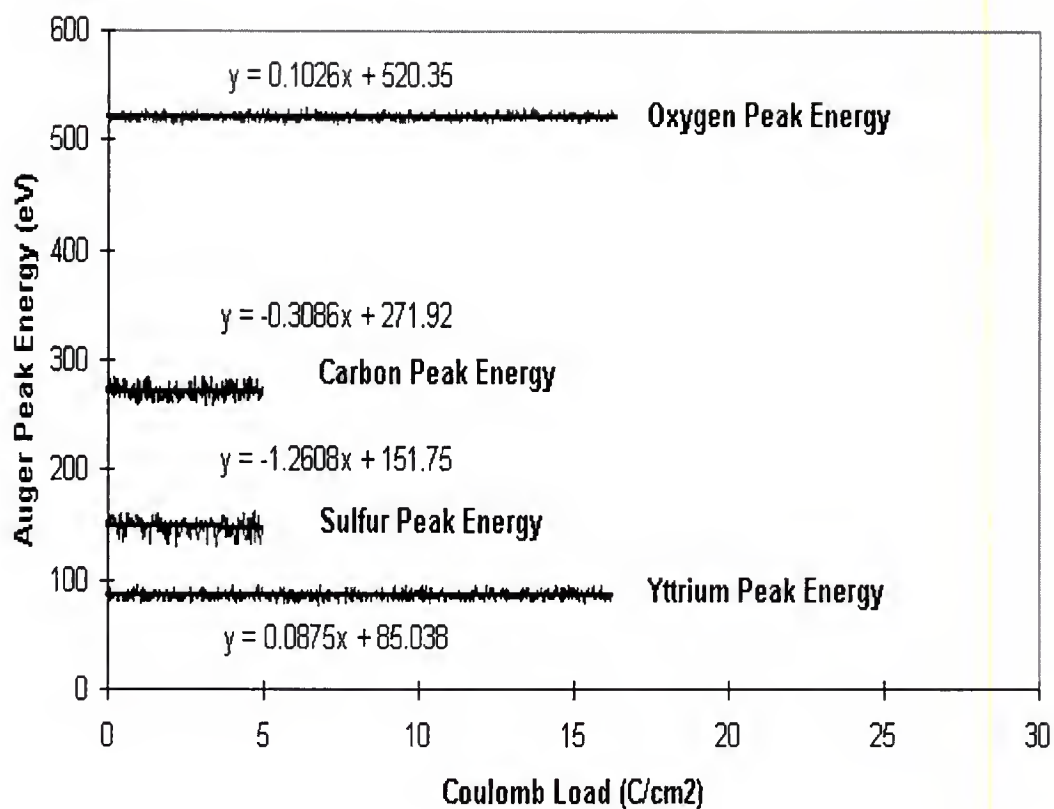
Figure 6-3   O, C, S, and Y peak energy shifts during coulomb aging with 1keV primary beam. Note that the Y and O slopes are positive, indicating an increase in peak energy during the experiment, while the S and C peak energies shift negatively (denoted by negative slope of trendline equation).
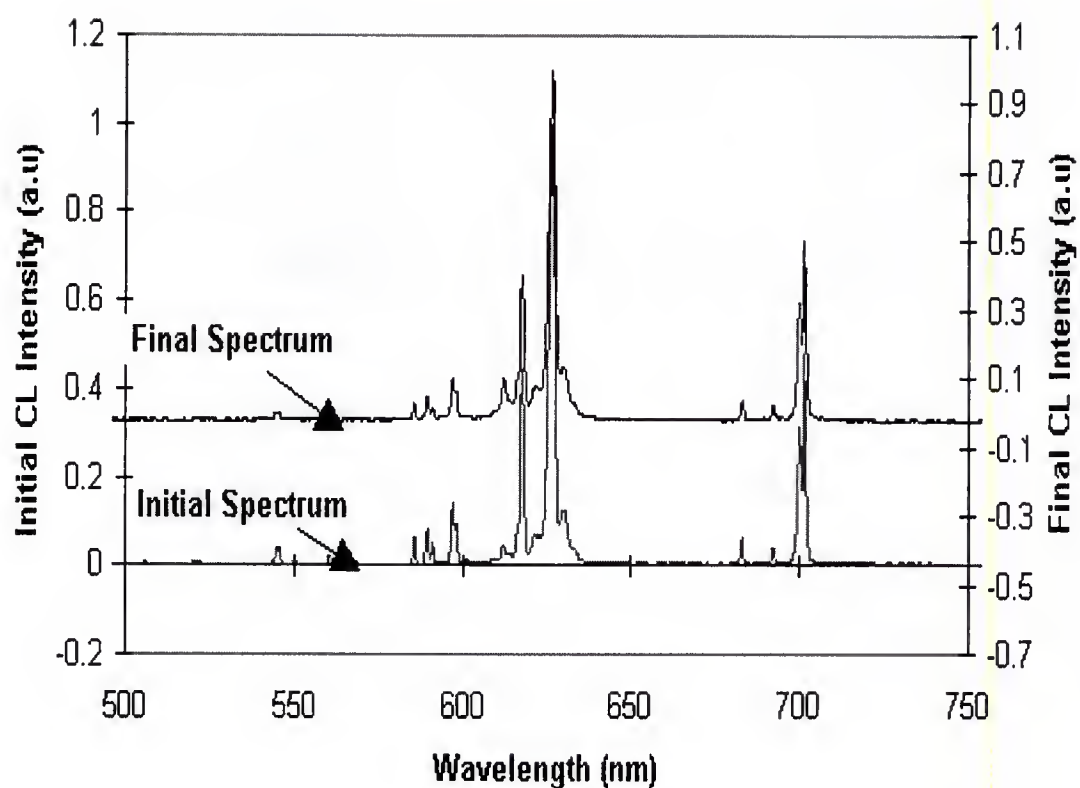
Figure 6-4   Initial (0 C/cm²)and final CL spectrum (16 C/cm²) for the 1keV degradation experiment in oxygen. The only noticeable difference is the slight increase in the 611 nm peak, suggesting the presence of $Y_2O_3:Eu^{3+}$ at the end of the experiment.
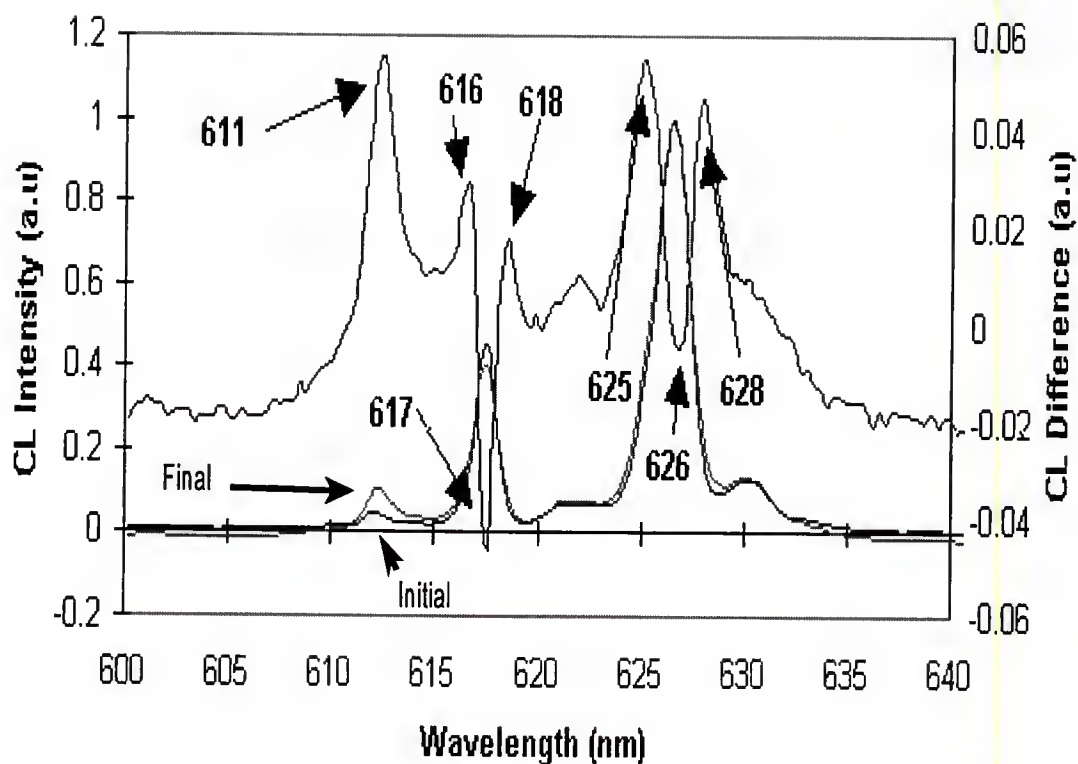
Figure 6-5   Expanded CL spectra (initial and final) and the CL difference spectra as function of wavelength. A large increase in the 611 nm peak indicates the presence of $Y_2O_3:Eu^{3+}$. Peaks at 616,618 and 625,628 are deflections associated with spectral broadening of the main emission peaks of $Y_2O_2S:Eu^{3+}$. Large negative deflections at 617 and 626 nm indicate loss in emssion intensity for $Y_2O_2S:Eu^{3+}$ caused by aging during the 1 keV experiment.
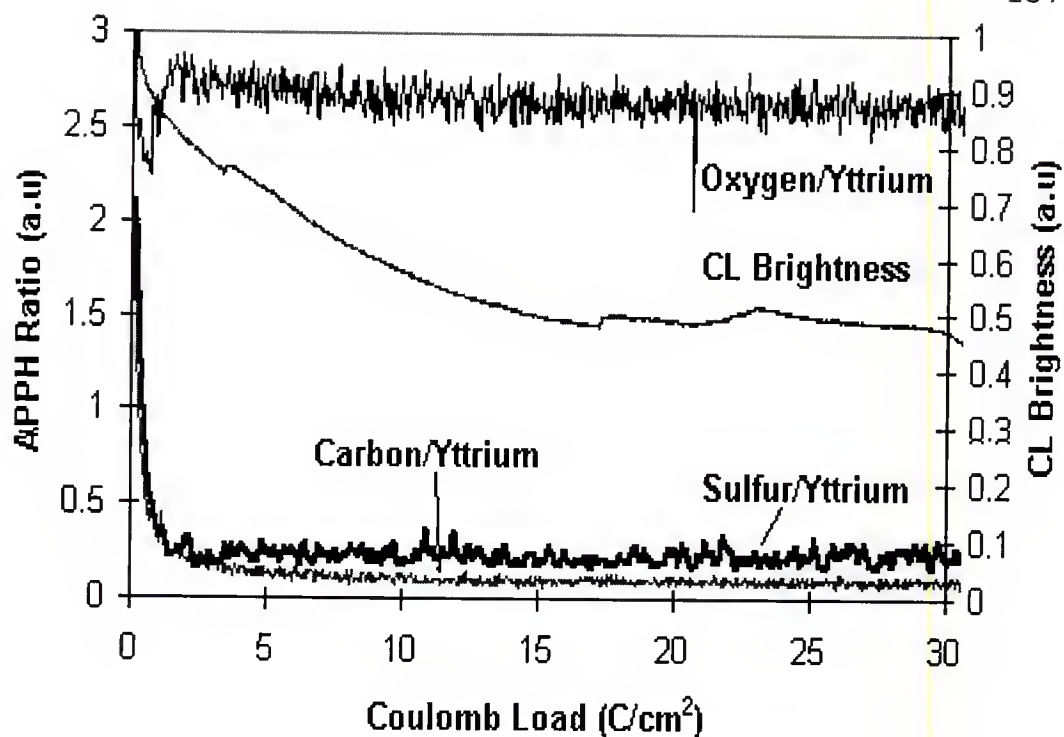
Figure 6-6   APPH ratios for O/Y, C/Y, and S/Y
as a function of coulomb load (C/cm²) for 2 keV,
$1.1x10^{-6}$ Torr O_2 experiment. Also shown is the CL
brightness as a function of coulomb load. The S/Y and
C/Y APPH ratios decrease slower than those in the 1keV
experiment (see figure 6-1). CL degradation is
approximately 45% at 15 C/cm², whereas, at 1 keV the
CL degradation was approximately 60%.
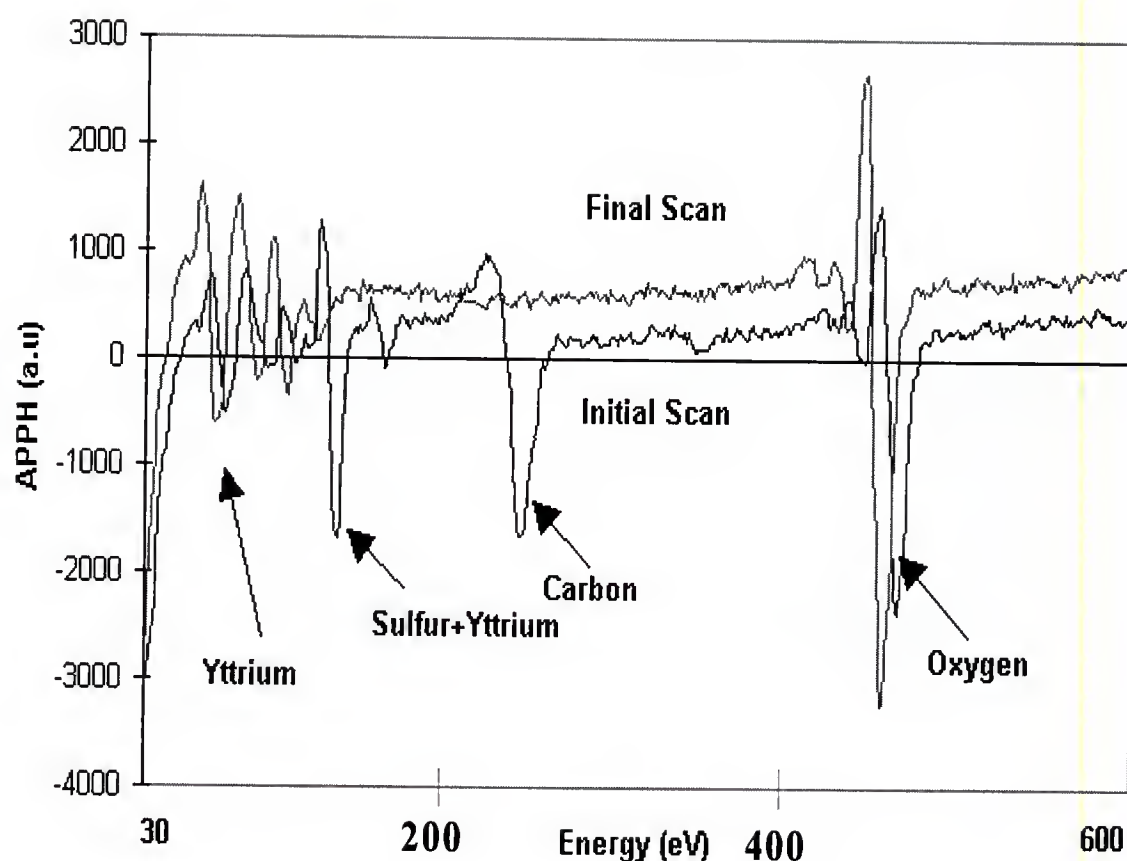
Figure 6-7   Initial and final AES spectra for the
2 keV degradation experiment. Notice the large amount
of C and S present on the surface prior to aging. It is
possible that the large amount of C initially present
on the surface protected the phosphor from degradation
up to 3 C/cm². Peak energy shifts are visible
on the O and Y peaks.
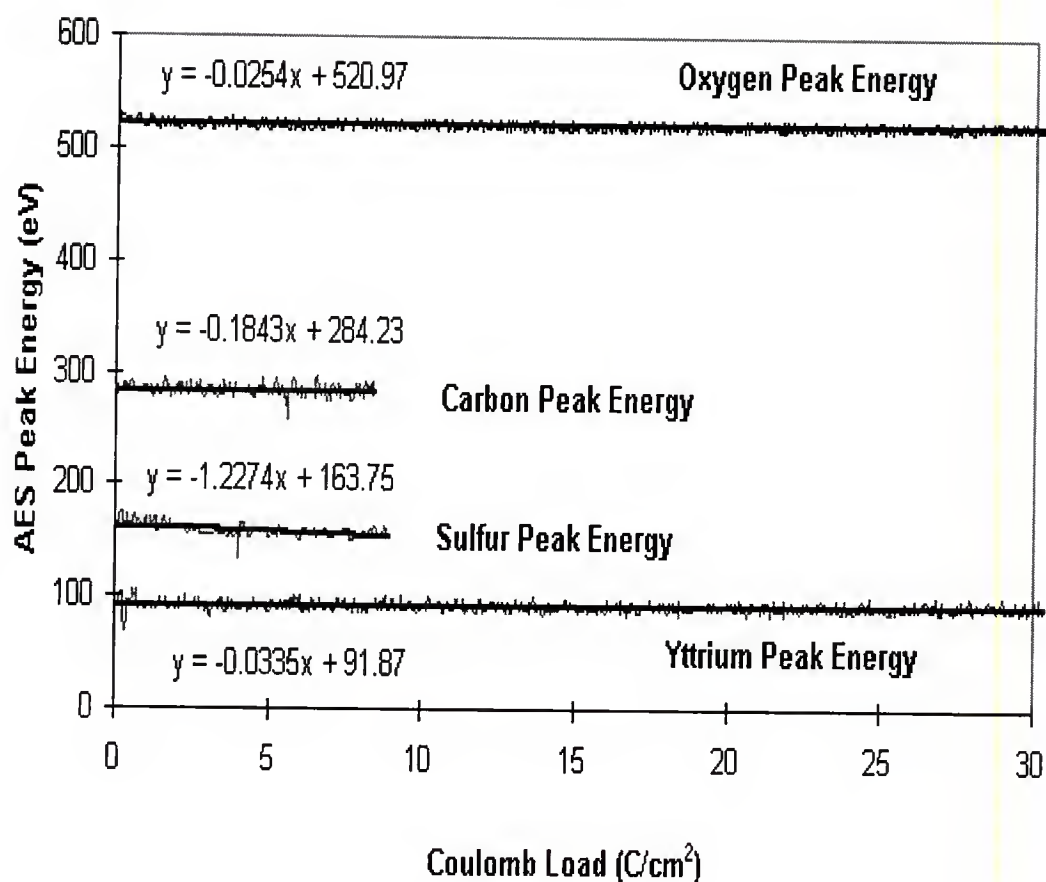
Figure 6-8   AES peak energy shifts exhibited during
the 2keV aging experiment. All peaks shift
negatively. This is unlike previous experiments where
the O and Y energies shifted positively.
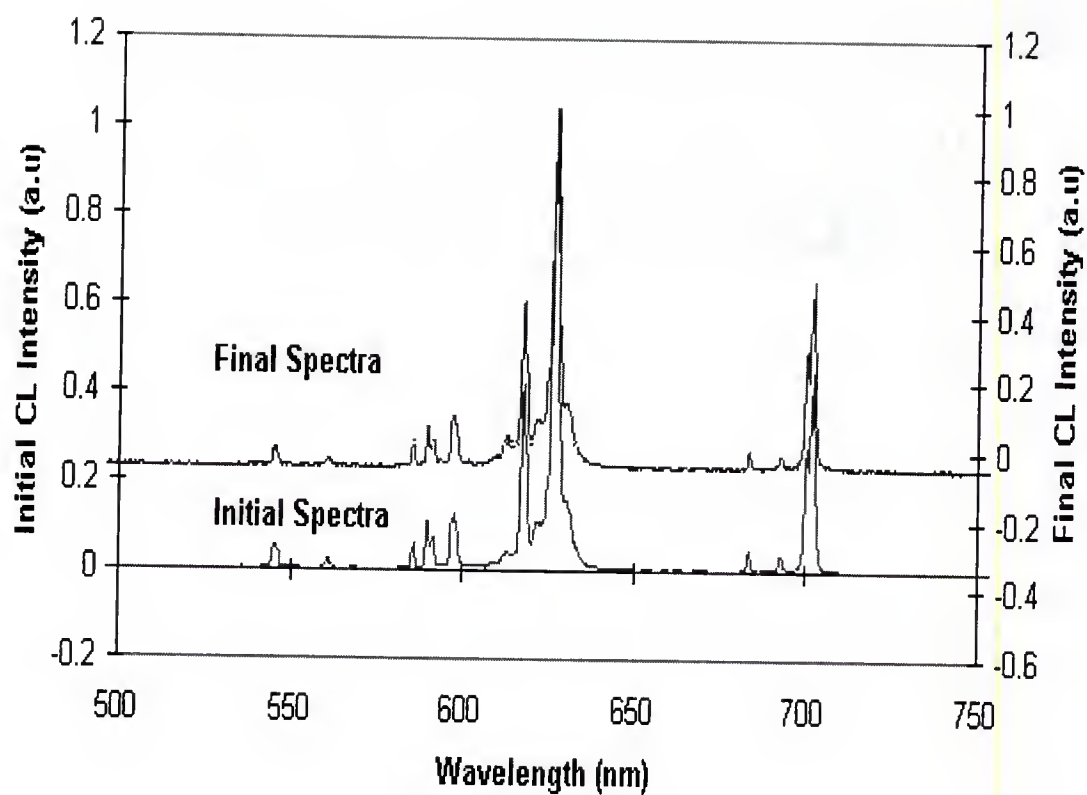
Figure 6-9   Initial and final CL spectra as a function of wavelength (nm) for the 2keV aging experiment. The spectra are very similar on full scale. Small changes exist near 611nm.
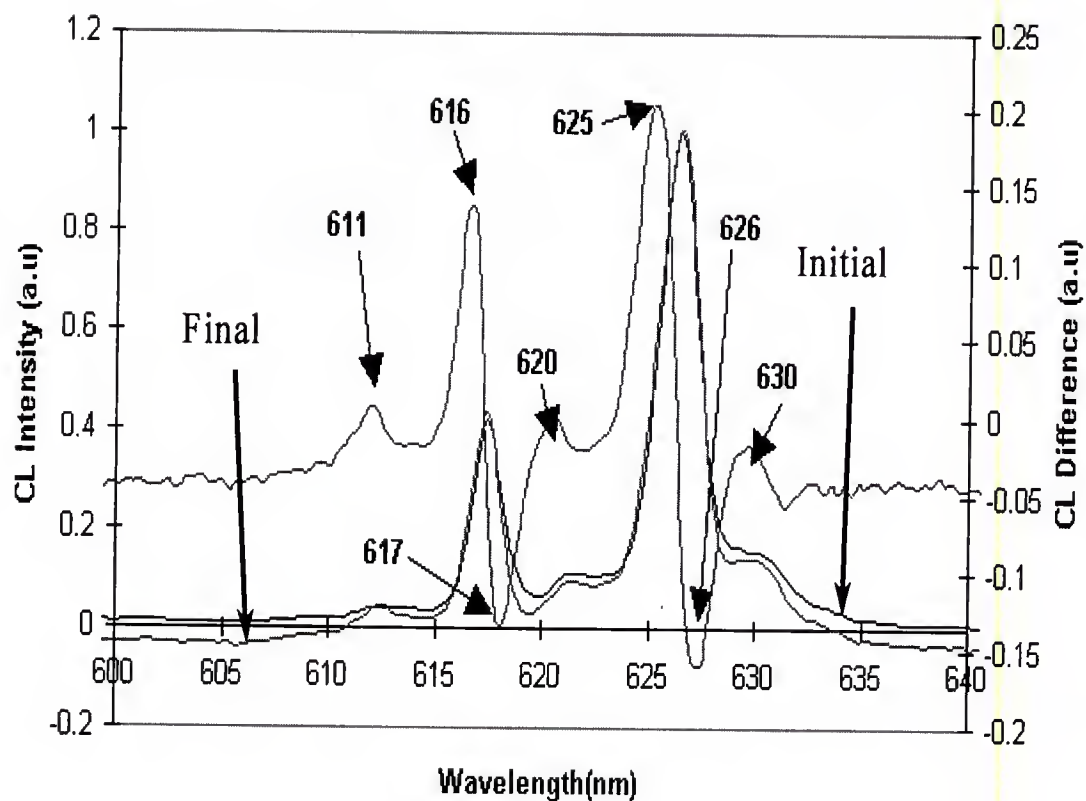
Figure 6-10   Initial and final expanded CL spectra and CL difference spectra as a function of wavelength (nm). Decreases on the CL difference spectra at 616,620 and 625,630 nm are attributed to spectral broadening of the main $Y_2O_2S:Eu^{3+}$ emission peaks which have decreased in intensity (617 and 626 nm). The 611 nm peak denotes the increase in emission from the $Y_2O_3:Eu^{3+}$ surface phase.
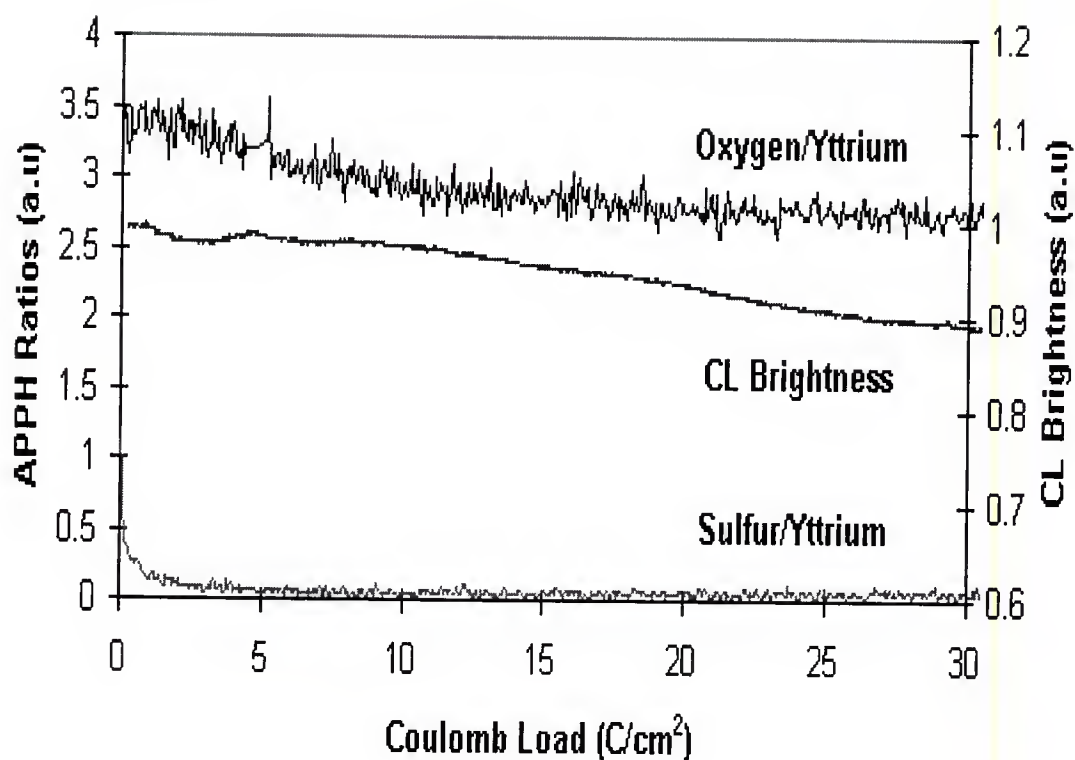
Figure 6-11   APPH ratios and CL brightness as a function of coulomb load (C/cm^2). Note that no C/Y ratio is present. No C was detectable on the surface of the phosphor at the beginning of the experiment. The O/Y APPH ratio decreases throughout the experiment. The S/Y ratio decreases to a level below AES detection in ~4 C/cm^2. The removal rate of S from the surface is slower than that found for the 1keV experiment. The CL brightness decrease at 3keV is very small (~10% loss).
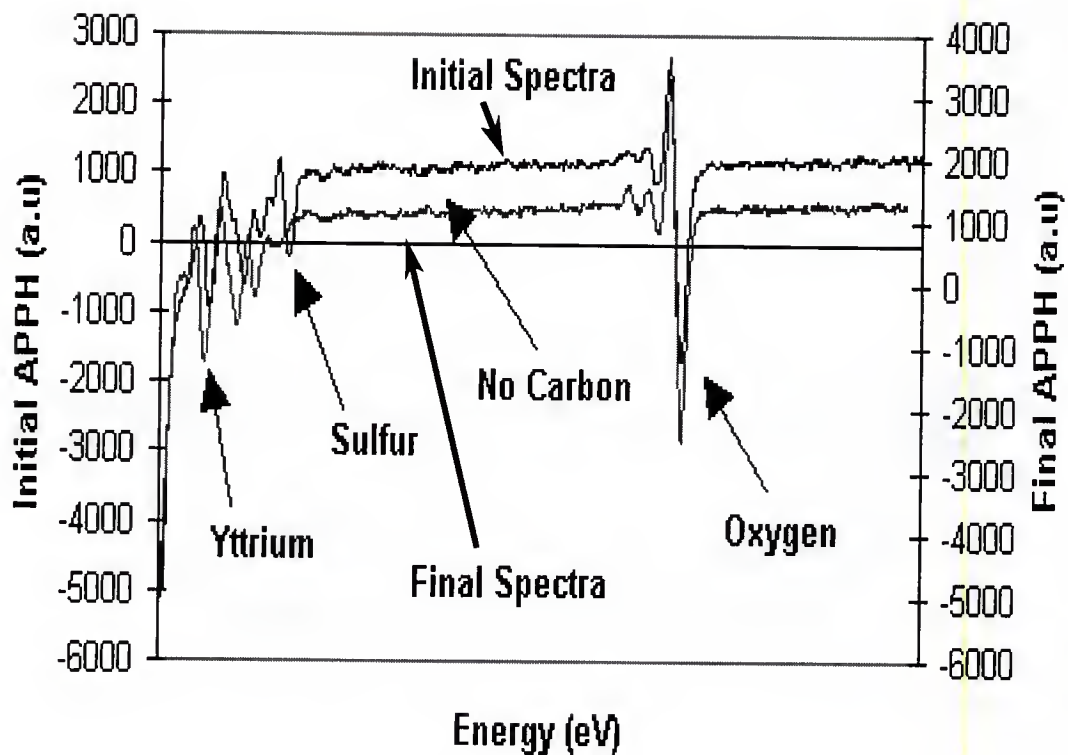
Figure 6-12   Initial and final CL spectra for the
3 keV degradation experiment. Note that no measurable
C existed on the surface of the phosphor at the
beginning of the experiment. The S APPH has fallen
below the AES detection limit by 27 C/cm2.
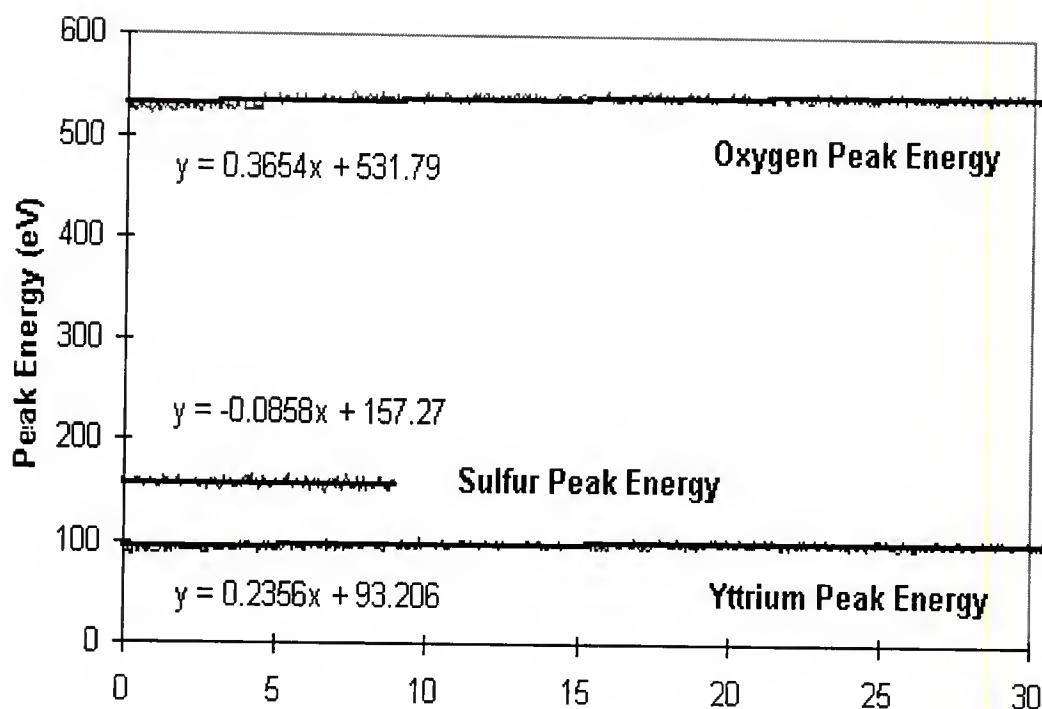
Figure 6-13   Auger peak energy shifts as a function of coulomb load for the 3 keV degradation experiment. O and Y peak energies increased by 7 eV and 4.6 eV respectively, at 20 C/cm^2. S peak energy shifted slightly negatively as denoted by the trend line equation ~ 1eV at the end of its measurability (~10 C/cm^2).
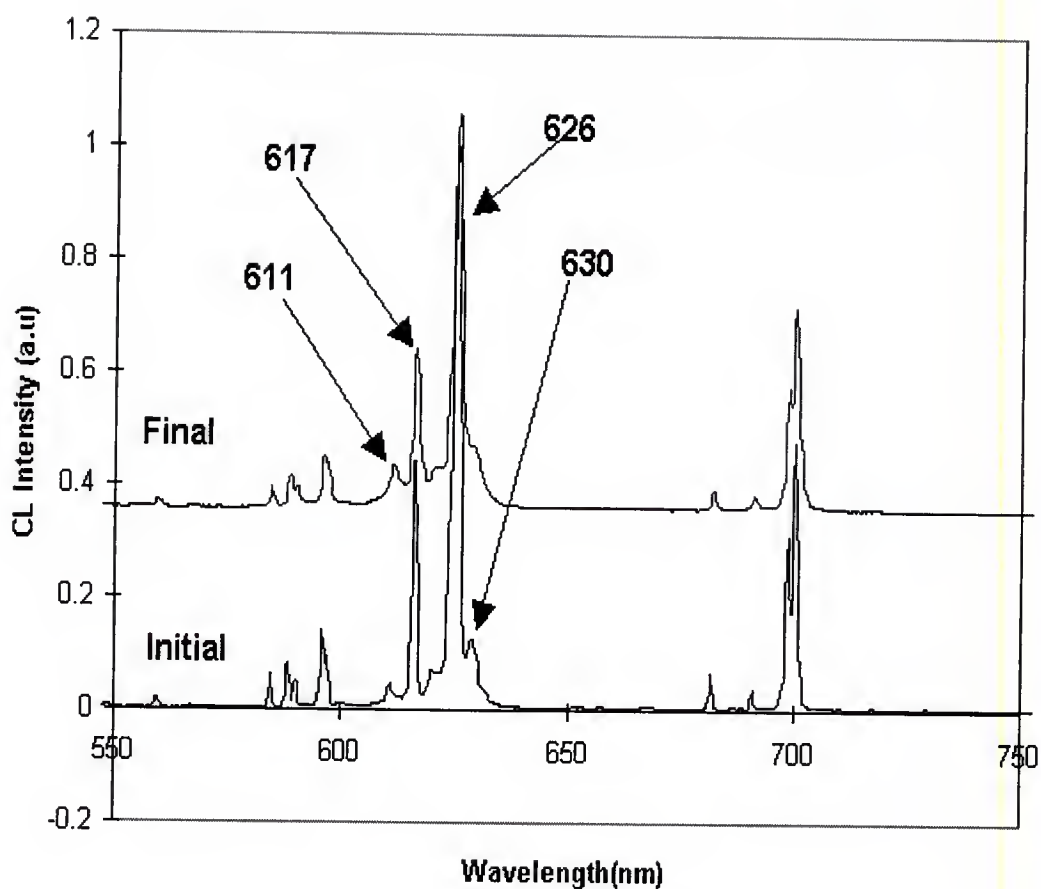
Figure 6-14   Initial and final CL Intensity distribution as a function of wavelength (nm) for the 3 keV degradation experiment. Only a small increase is seen at the 611 nm Y_2O_3:Eu^{3+} nm. The 617 and 626 nm emission is attributed to Y_2O_2S:Eu^{3+}.
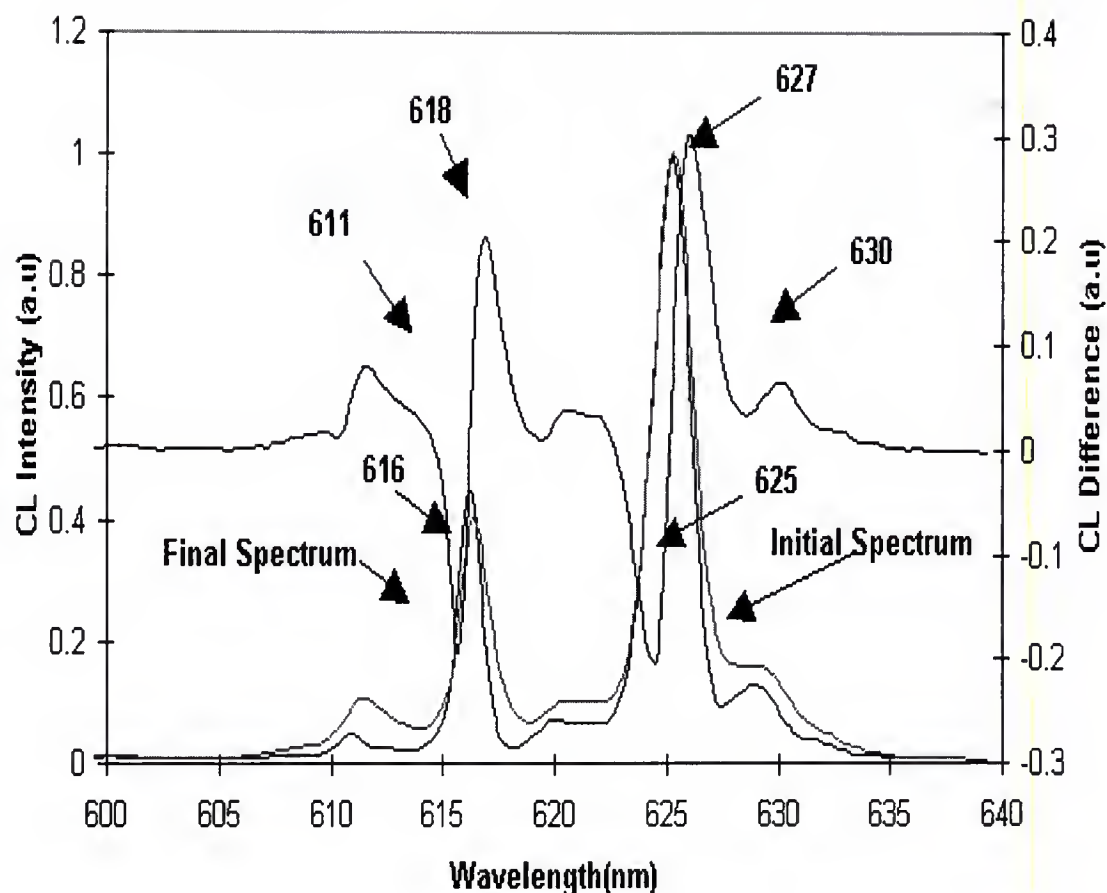
Figure 6-15   Expanded CL spectra for the 3keV degradation experiment. The CL difference is shown as well on the secondary y-axis (right). The 611 nm peak denotes the CL emission of $Y_2O_3:Eu^{3+}$. The 617nm and 626nm peaks are $Y_2O_2S:Eu^{3+}$ emission peaks that have decreased during degradation.
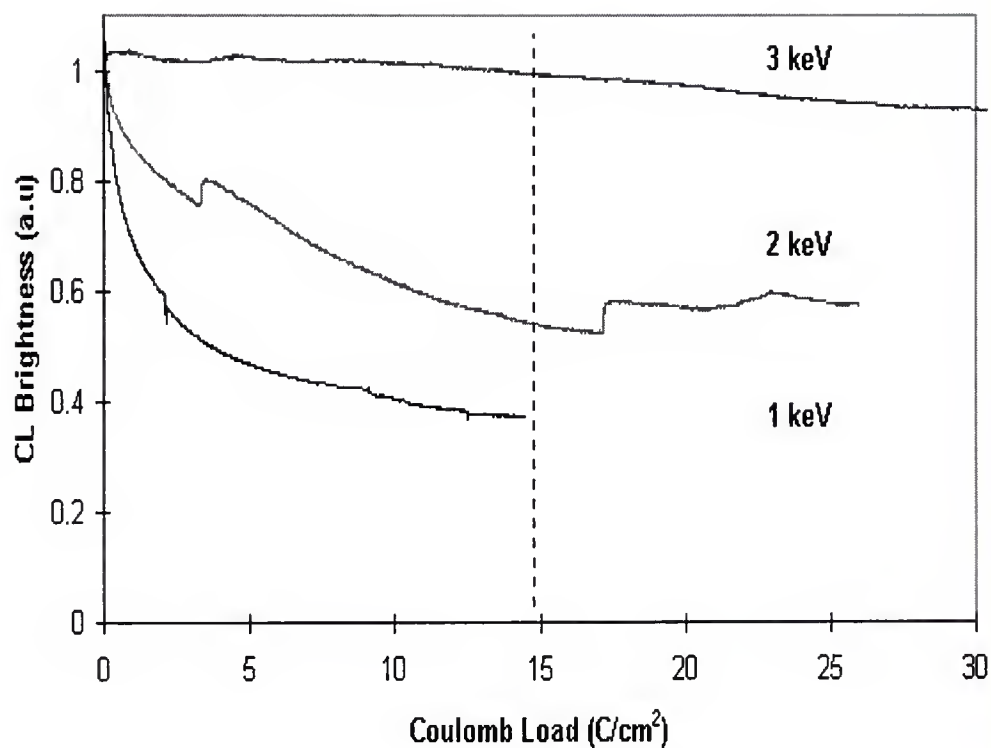
Figure 6-16   Comparison of CL degradation rates for
1, 2, and 3keV accelerating voltage experiments. The
The dashed line shows the 15 C/cm² comparison point.
As expected, lower accelerating voltages produce faster
degradation due to decreased excitation volume and
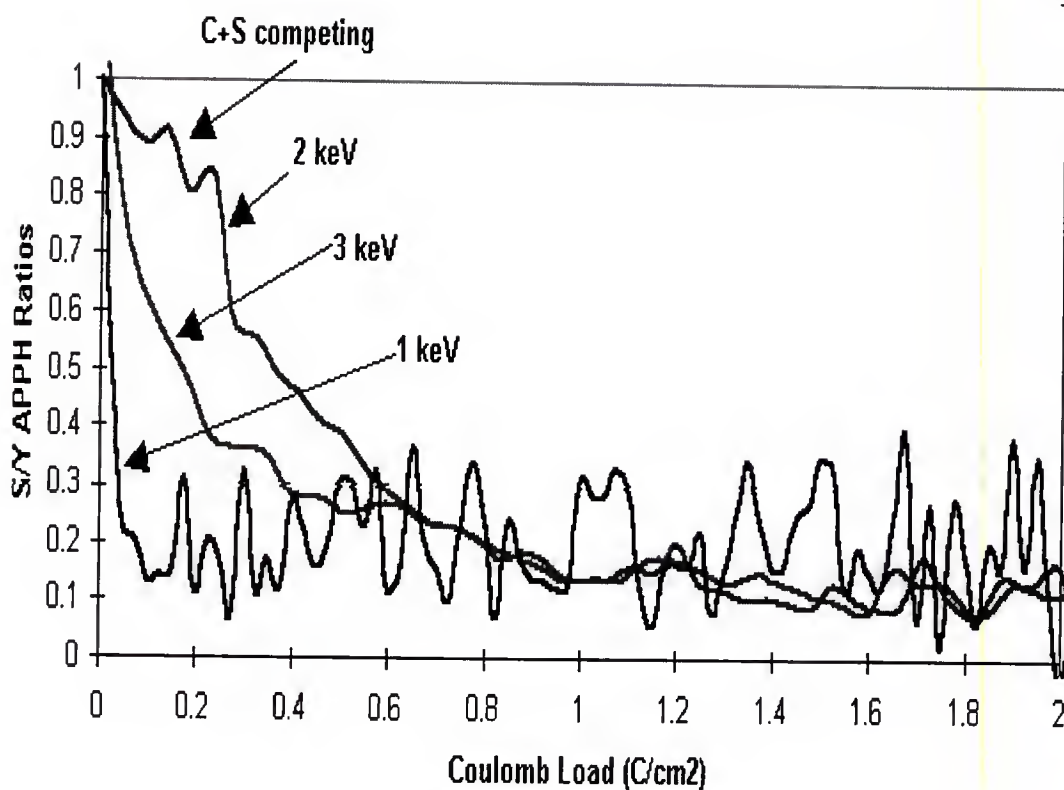increased disassociation efficiency for gases impinging
on the surface.

Figure 6-17 Removal rate of S comparison for the 1, 2, and 3keV degradation experiments. 1 keV S loss rate is the fastest, falling below detection limits in ~ 0.2 C/cm². The 2 keV and 3 keV S rates are not in the expected sequence. The 2 keV S loss rate is slowed due to the large amount of C competing with the S at the beginning of the experiment (C+S competing above). Once the C concentration is lowered, the S loss rate increases. The data suggest that the disassociation efficiency of the gas is an important factor in the CL Degradation rate of the phosphor.
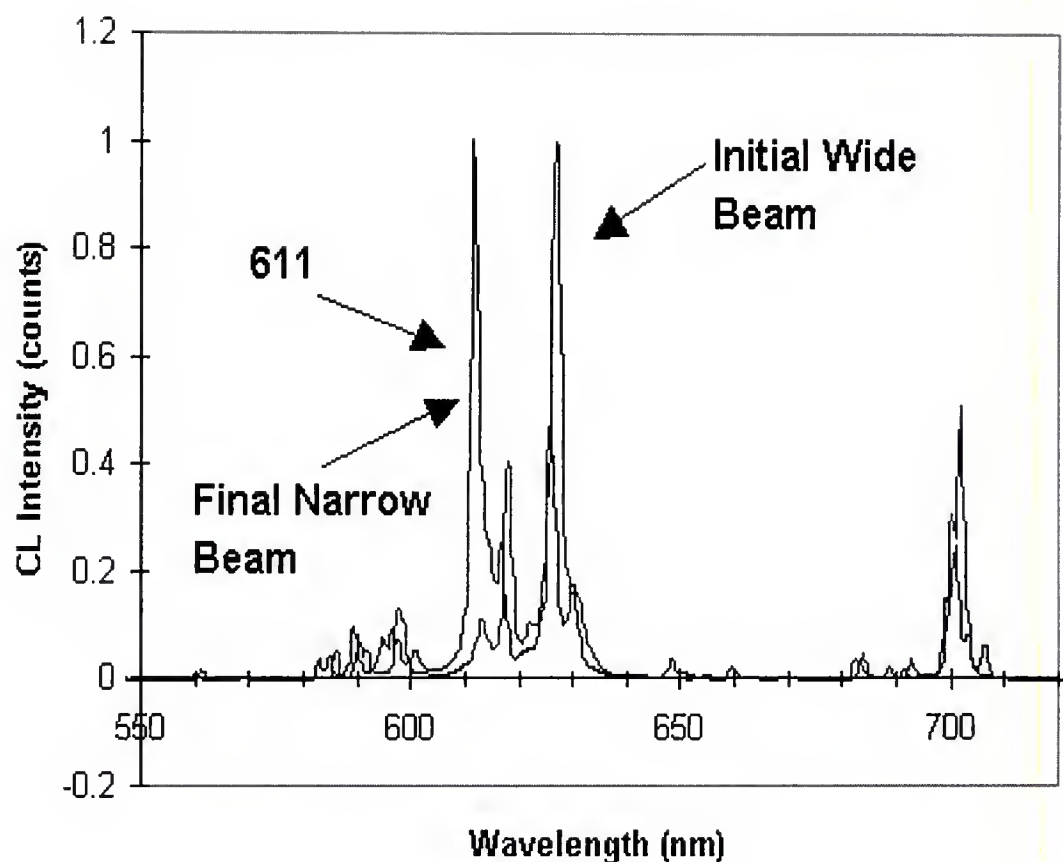
Figure 6-18   Comparison of 3keV Wide and narrow beam spectra. The narrow beam samples a small region within the degraded area. The dramatic difference in the two spectra indicate that the $Y_2O_3:Eu^{3+}$ formed is centered within the larger spot where the energy density of the electron beam is highest.
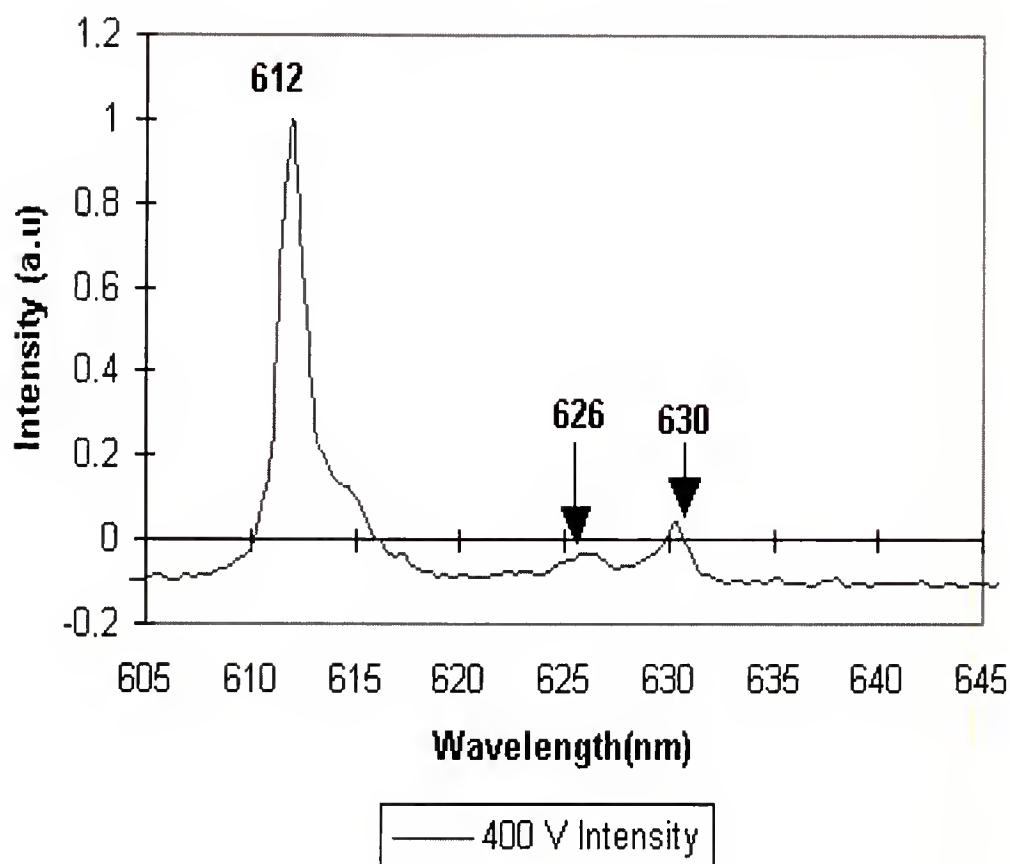
Figure 6-19   400 V CL Intensity spectra as a function
of wavelength (nm) after the 3 keV degradation
experiment. The spectra is dominated by the
Y_2O_3:Eu^{3+} spectra (612 and 630 nm). The 626 peak is
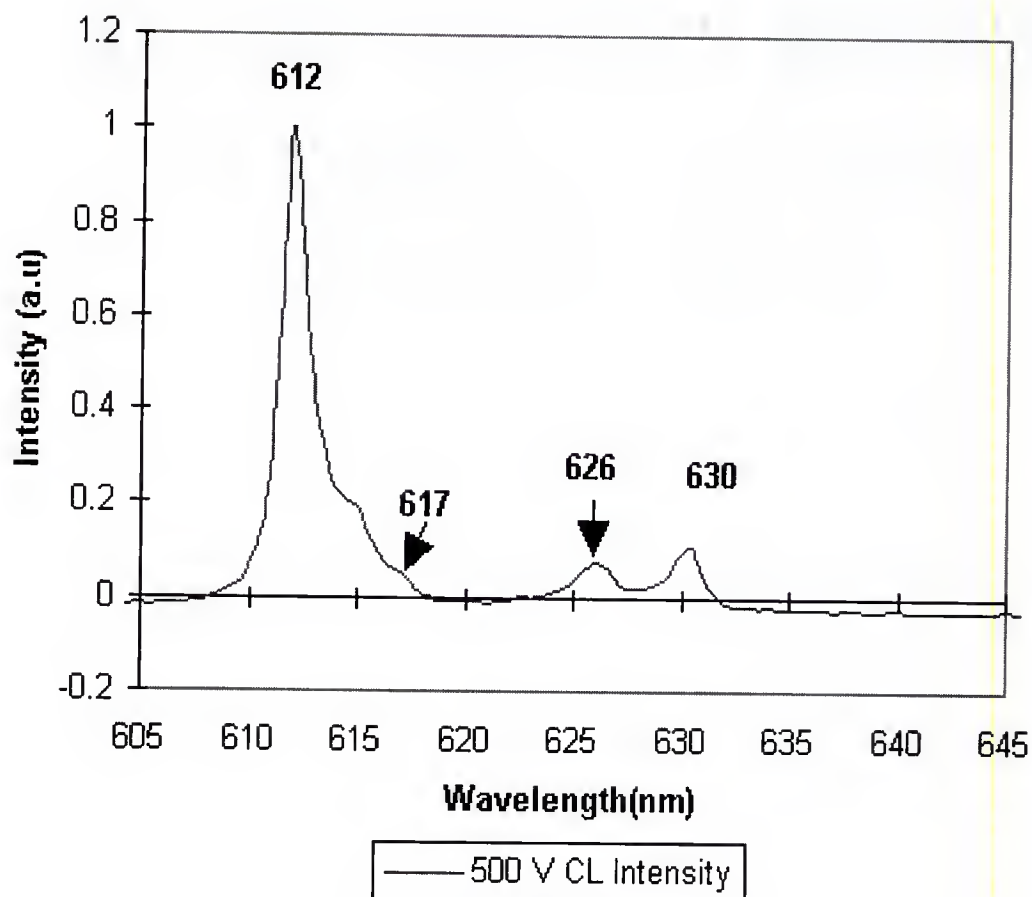the main emission peak of Y_2O_2S:Eu^{3+}, indicating only
a very small contribution.

Figure 6-20   500 V CL Intensity as a function of wavelength(nm) after 3keV degradation. The peaks 612 and 630 are associated with Y_2O_3:Eu^{3+} emission. The 626 and 617 peaks are the main emission peaks of Y_2O_2S:Eu^{3+}. Very little Y_2O_2S:Eu^{3+} is found from the surface to this depth (~500Å).
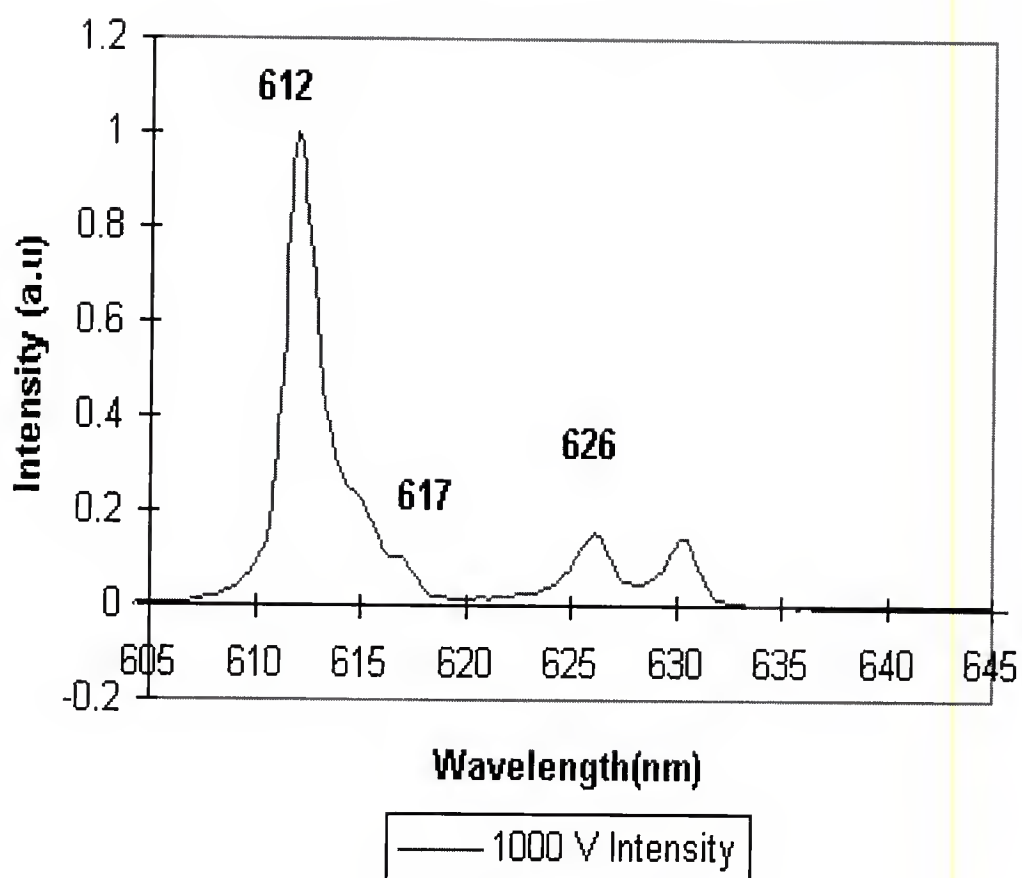
Figure 6-21   1000 V CL Intensity as a function of wavelength (nm) after the 3kev degradation experiment. Only small contributions are apparent from the 617 and 626 nm emissions of $Y_2O_2S:Eu^{3+}$. The spectra is dominated by the 612 nm emission of $Y_2O_3:Eu^{3+}$.
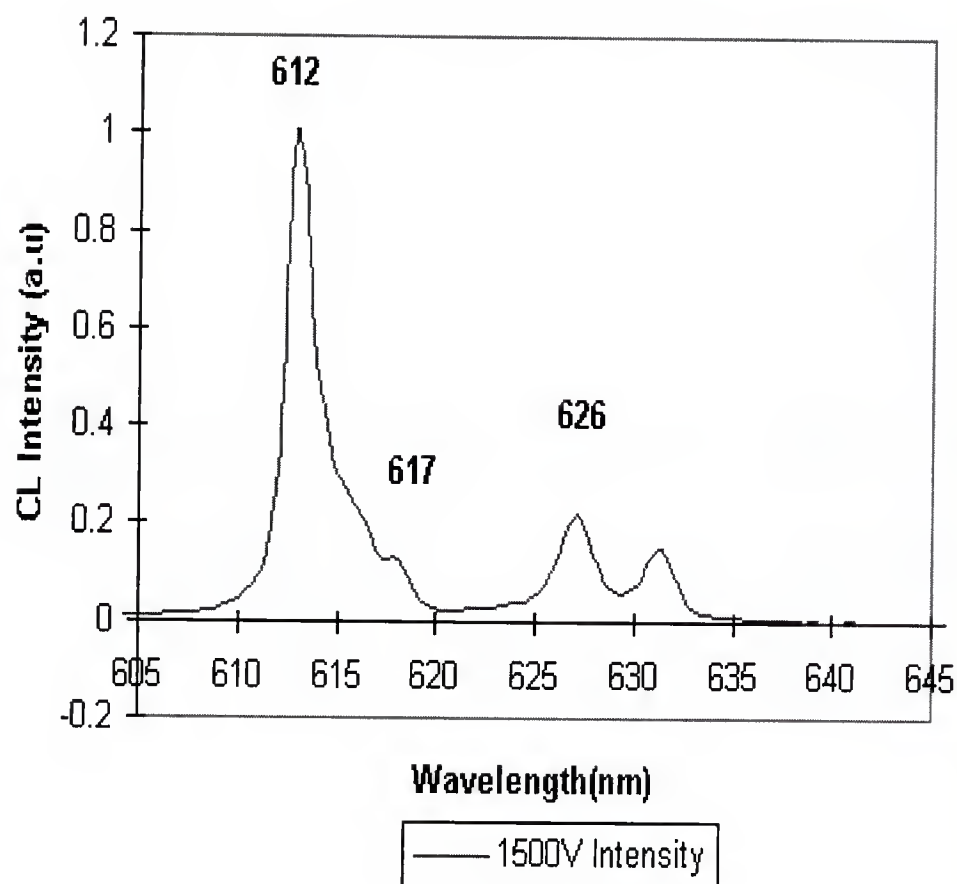
Figure 6-22   1500 V CL Intensity as a function of wavelength in nm for the 3 keV degradation experiment. Notice that the 626 nm emission of $Y_2O_2S:Eu^{3+}$ is beginning to increase in intensity.
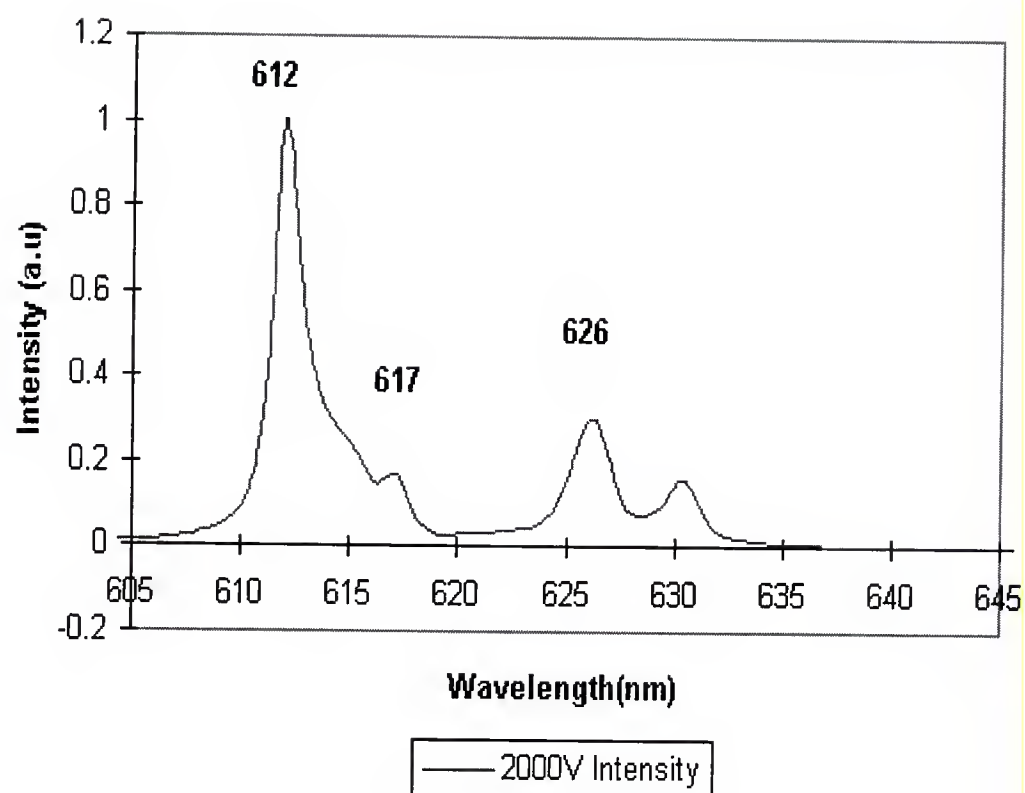
Figure 6-23   2000 V CL Intensity as a function of wavelength (nm) taken after the 3 keV degradation experiment.
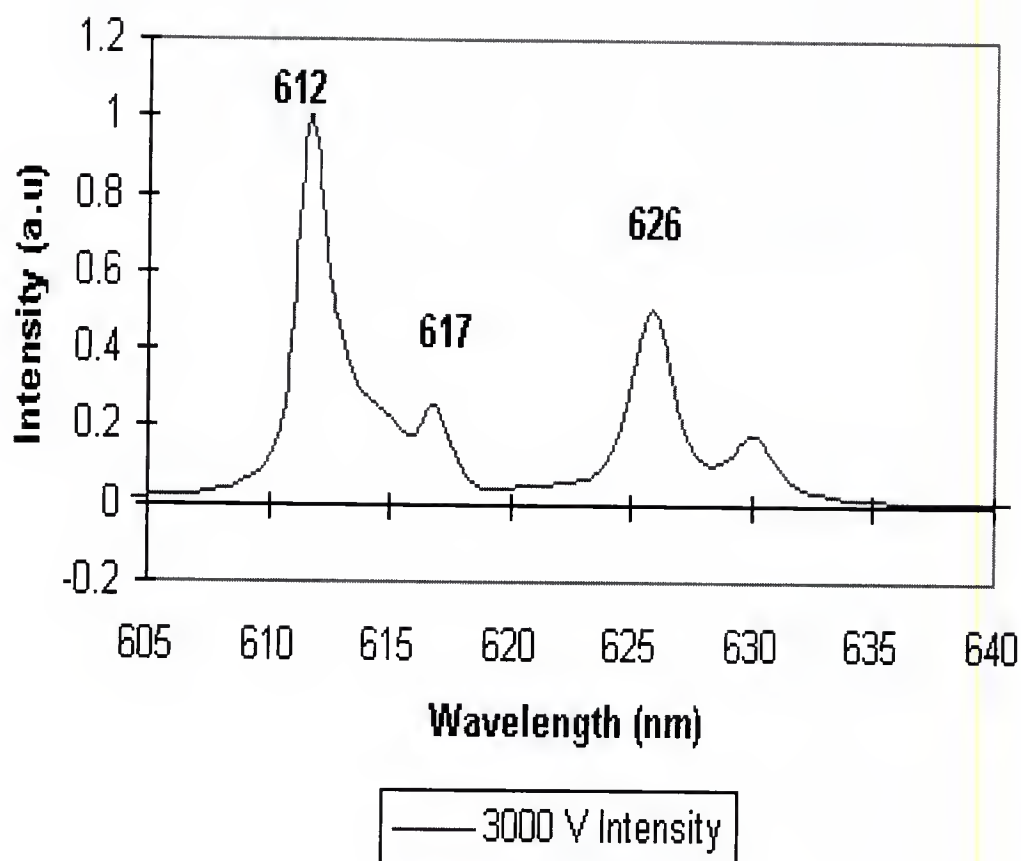
Figure 6-24   3000 V CL Intensity Spectra as a function of wavelength (nm). Note that the $Y_2O_2S:Eu^{3+}$ main emission peak is lower in intensity than is the 612 nm peak of $Y_2O_3:Eu^{3+}$. The spectra was taken after the 3keV degradation experiment in oxygen.
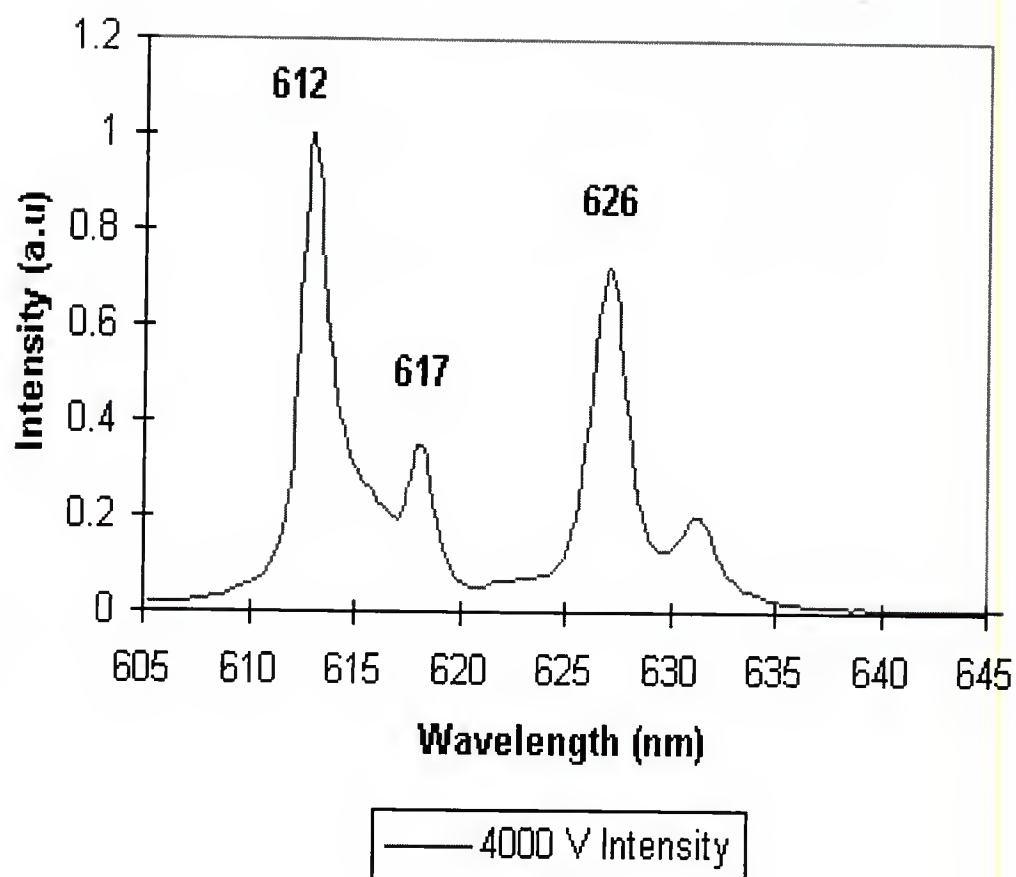
Figure 6-25   4000V CL intensity as a function of wavelength (nm). The oxysulfide emission (626nm) is nearly equal to the oxide emission (612nm). The spectra was taken after the 3keV degradation experiment.
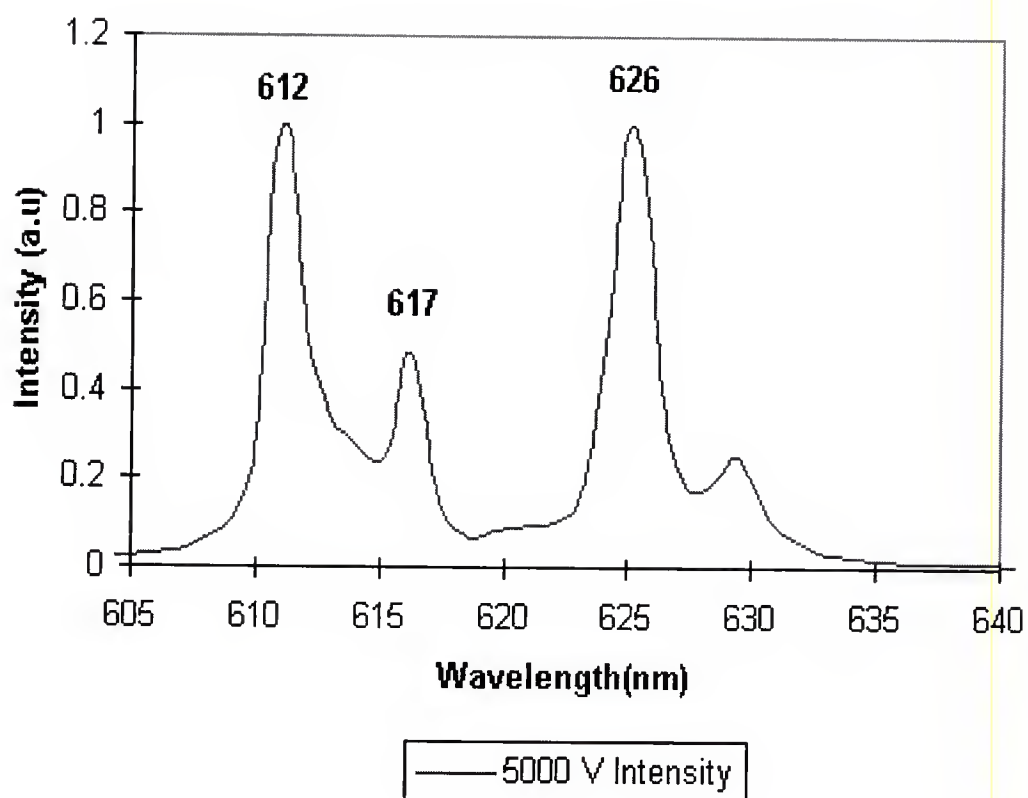
Figure 6-26   Normalized CL Intensity as a function of wavelength (nm) for the 3keV degradation experiment. Note that the Y_2O_3:Eu^{3+} peak (612nm) is equal in intensity to the 626 nm peak of Y_2O_2S:Eu^{3+}.
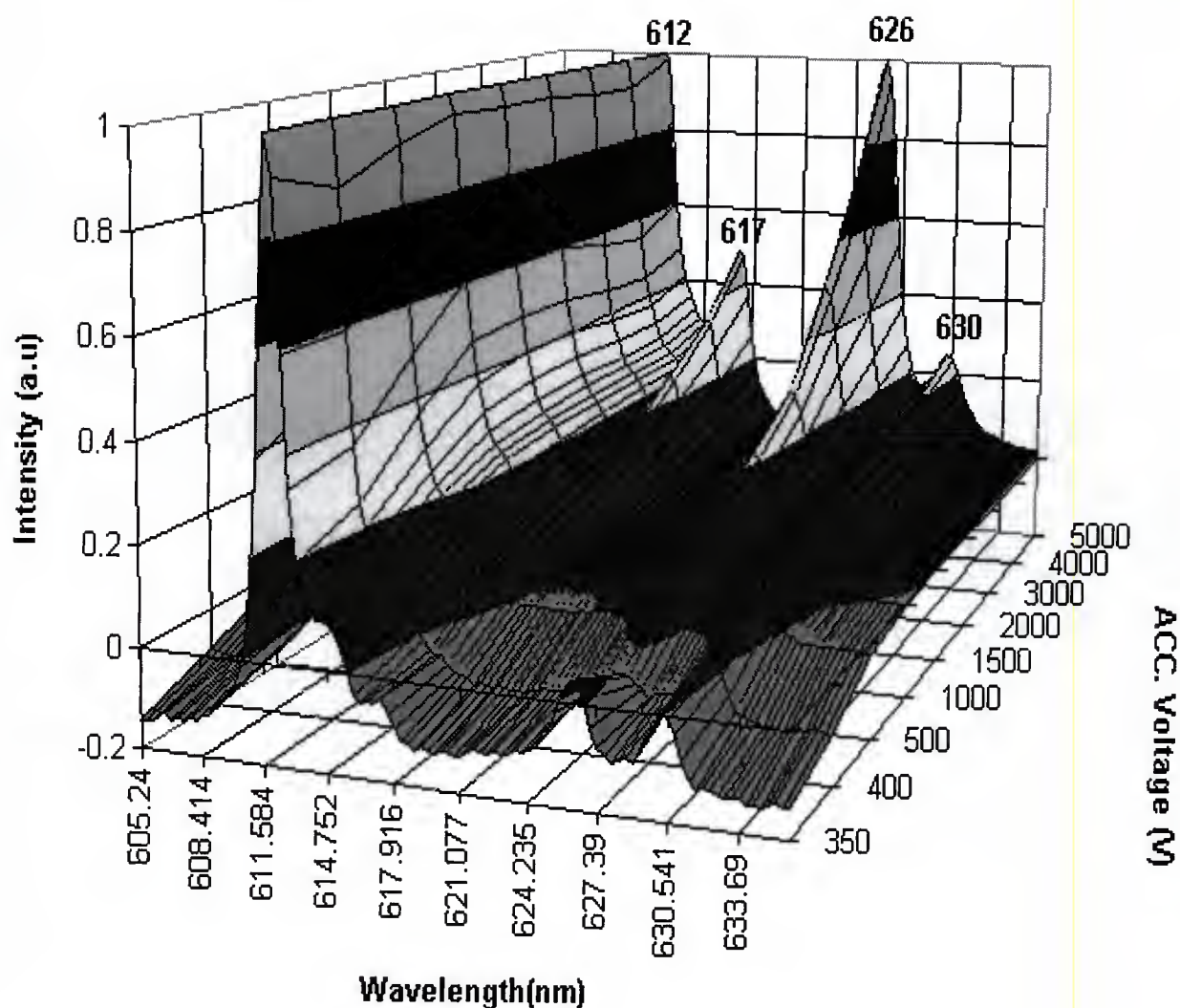
Figure 6-27   3-D surface representation of CL
intensity as a function of wavelength (nm) and
accelerating voltage (V).   It is
easy to see that the low accelerating voltage regime is
dominated by the oxide ($Y_2O_3:Eu^{3+}$) spectrum (611nm).
Only at higher accelerating voltages does the $Y_2O_2S:Eu^{3+}$
intensity (626nm) approach the oxide emmission
intensity (~4000V).

CHAPTER 7

MODELING OF THE CL DEGRADATION OF $Y_2O_2S:Eu^{3+}$

Introduction

In the preceding chapters, it has been shown that the CL degradation of $Y_2O_2S:Eu^{3+}$ is dependent upon many parameters such as electron beam energy, ambient gas pressure and type of gas. Each of these parameters was studied independently, and in each case, was found to be related to the CL degradation. In this chapter, some rudimentary models will be used to better understand the effects these parameters have on the CL degradation. In so doing, the calculations may indicate which of these factors is most important in understanding and semi-quantitatively predicting the degradation phenomena.

179

To better understand the CL degradation process, and knowing that the CL degradation is correlated with the growth of the dead layer during the aging process, modeling of the brightness as a function of depth for the phosphor may prove invaluable in understanding CL degradation. Since the dead layer growth is dependent on the pressure, type of gas and dissassociation efficiency of the gas at particular accelerating voltages, some kinetic modeling of gas-surface interactions is necessary.

Using Makhov's law (see Chapter 2), a relationship will be obtained between the brightness versus depth for the phosphor and the power dissipated by the electron beam as a function of depth. The brightness will be modified by a model for the CL efficiency as a function of depth for $Y_2O_2S:Eu^{3+}$ after taking into account the activator concentration distribution and concentration quenching phenomena. The model's accuracy will be determined by comparison to CL degradation rates reported in Chapters 4-6.

A second model will be used to estimate the amount of dissassociated gas available at the surface of the phosphor for reaction. This model will incorporate the dissassociation efficiency of the gas at a given

accelerating voltage, gas pressure, temperature, and the heat of adsorption of the gas on the surface. By varying the parameters in this model (accelerating voltage, temperature, pressure, and heat of adsorption), a better understanding of the surface kinetics associated with the electron beam stimulated reaction will be attained.

Both models together will be used as a guide to consider ways by which the CL degradation of $Y_2O_2S:Eu^{3+}$ can be slowed or stopped.

Modeling of Brightness as a function of Depth

In order to understand the relationship between CL degradation, electron kinetic energy and dead layer thickness, a model relating the brightness of the phosphor as a function of depth to these parameters is required. In Chapter 2, Makhov's Law was discussed which relates the CL brightness as a function of depth to the product of CL efficiency at a given depth and the power dissipated by the electron beam at that depth. Equation 2.6 was expressed as follows:

$$\frac{dB}{dx} = \rho(x) * \frac{dP}{dx} \qquad (7.1)$$

where dB/dx is the variation in brightness as a function of depth, x, from the surface of the phosphor, dP/dx is the power dissipated by an electron beam as a function of depth and $\rho(x)$ is the cathodoluminescent efficiency at depth x. Typically, $\rho(x)$ is assumed to be constant for all depths.

Thus, in order to obtain an expression for **dB/dx**, functions must be modeled for $\rho(x)$ and **dP/dx**. Makhov's Law does not take into account absorption of light, nor does it consider the effects of the diffusion of carriers on CL brightness.

CL Efficiency as a function of Depth

In most studies, $\rho(x)$ is assumed to be constant at all depths. In many cases, this is acceptable since the activator concentration is a constant as a function of depth, and all activators are equally efficient emitters. Both of these assumptions are incorrect for the industrially processed $Y_2O_2S:Eu^{3+}$ phosphor. Firstly, the activator concentration (Eu^{3+}) is not a constant as a function of

depth. Instead, it has been observed experimentally to have

a high surface concentration and a lower constant

concentration after some depth into the particle as reported

by Ozawa [Oza91]. Figure 7-1 shows the Eu concentration

normalized to the nominal concentration as a function of

depth. The Eu distribution as a function of depth was

determined by etching the phosphor particles, measuring the

weight loss to determine the thickness of the layer removed,

then using ICP to determine the amount of Eu in the etched

material. The bulk of the particle does have the expected Eu

concentration (equal to 1 on the y-axis), but in the near

surface region ($<0.5\mu$m), a concentration gradient leads to

higher surface concentrations. The importance of the high

surface concentration is easily understood when it is

correlated with the penetration depths of low energy

electrons that are of interest in FEDs ($.3\mu$m-1.5μm). It is

also important to the present study since a 2keV electron

beam was used for the AES and CL measurements. The maximum

range for these energies is only about 1μm which means that

up to 50% of the excited volume does not have the expected

activator concentration. Thus, the assumption that the

activator concentration is a constant as a function of depth

is generally not accurate for the energy regime of this study.

a mathematical fit of the normalized Eu concentration as a function of depth has been obtained using the data found in literature (shown in figure 7-1) and can be expressed as follows:

$$Eu(x) = 2(10^{-12})x^{-1.5672} + 1 \qquad (7.2)$$

where **Eu(x)** is the normalized Eu concentration at the chosen depth **x**.

With this expression, the fractional Eu concentration can be determined at any depth over the range of the primary electron. Since the Eu^{3+} concentration is not constant, the fractional distribution of Eu throughout the range of an electron will not be linear. The fractional distribution is the total amount of Eu contained within a fixed depth measured from the surface of the particle, normalized to the total Eu concentration contained within a chosen primary electrons range). This was examined for primary electron energies of 500, 1000, 2000 and 4000 eV and the fractional

Eu concentration as a function of depth for these energies is shown in Figure 7-2. The graph shows that there exists an initial sharp increase in the total fraction of Eu^{3+} and then tapers off. The fractional amount of Eu^{3+} contained in this region is larger for lower accelerating voltages.

If only the Eu^{3+} concentration determined the CL brightness emitted by the phosphor, the depths required to reduce the CL brightness by 50% would decrease with decreasing accelerating voltage. For instance, a phosphor with a dead layer of $0.017\mu m$ on the surface would exhibit about a 50% decrease in CL brightness using a 500eV primary electron beam, whereas the same dead layer would produce only a 12% CL brightness loss at 4keV.

Deriving the CL efficiency from the total Eu concentration curve is a rough first approximation. However, the phosphors brightness is known to depend on the amount of Eu^{3+} in the phosphor. For instance for $Y_2O_2S:Eu^{3+}$, the optimum Eu^{3+} concentration for CL is about 4 atomic %[Oza91]. If the activator concentration is too high, the Eu ions are too close and electron wave overlap which reduces the overall brightness (known as concentration quenching). If the concentration is too low, the CL brightness is linearly

reduced. It can be seen from figure 7-1 that the Eu

concentration is higher than the optimum concentration near

the surface (where $Eu/Eu_{inner}=1$, the Eu concentration is 4%).

This high concentration, coupled with the concentration

quenching effect, may actually reduce the near surface CL

brightness and lead to a "built-in" dead layer where the

brightness output of the phosphor is low due to

concentration quenching near the surface. The concentration

quenching curve for $Y_2O_2S:Eu^{3+}$ is shown in figure 7-3 [Oza90]

where the relative CL brightness is shown as a function of

Eu mole fraction.

In summary, the CL efficiency for $Y_2O_2S:Eu^{3+}$, typically

assumed to be a constant in previous studies, should

consider the Eu concentration as a function of depth as

modified by the concentration quenching factor. The value of

the concentration quenching factor at a given depth can be

obtained from the Eu concentration at that depth.

Power Dissipation as a function of Depth in $Y_2O_2S:Eu^{3+}$

The second term in Makhov's equation to be

consideration is the power dissipated as a function of

depth. Starting with the assumptions of chapter 2 (equation

2.1 modified by equation 2.4), the modified Bethe equation
proposed by Joy and Luo will be used to obtain the energy
dissipated by an electron as a function of depth. From this,
the power dissipated as a function of depth will be obtained
and is given by:

$$\frac{de}{ds} \approx \frac{-785\rho Z}{Ae} \ln\left(\frac{1.166e}{j'}\right).$$ (7.3)

The modified Bethe equation describes instantaneous
energy loss by an electron as a function of depth. a more
detailed look at the Bethe equation and the modified Bethe
equation is given in Chapter 2 (equation 2.1 and 2.4).
Makhov's law requires an expression for instantaneous power
as a function of depth. This can be obtained knowing the
electron's kinetic energy at a given depth and by
multiplying (eV/Å) by the electron velocity (Å/s) at that
depth (determined by its kinetic energy). Figure 7-4 shows a
plot of the power dissipated by an electron as a function of
depth for 1-5 keV initial primary electron energies. The
power dissipation curves are nearly flat, increasing

slightly towards the end of range and then tailing off to zero. These power calculations assume a single electron, which is inelastically scattered perpendicular to the surface after each scattering event, and that the electron has lost all its energy at the maximum range for a given initial kinetic energy. a better approximation in future work could be obtained using a Monte Carlo simulator.

Predictions of the Brightness Model

Combining the Eu concentration as a function of depth, concentration quenching (function of Eu concentration) effect, and the power dissipation curves allow the formulation of a model of the brightness emitted as a function of depth for $Y_2O_2S:Eu^{3+}$. The brightness at a given depth in this model is equal to the power dissipated at that depth, multiplied by the Eu concnetration at that depth, multiplied by the concentration quenching factor determined from the Eu concentration. The total brightness can be obtained by integrating over the entire range of the primary electron.

Figure 7-5 shows the brightness (a.u) as a function of depth for primary electron energies from 1 to 5kev. Three regions are observed on these curves. a large peak close to the surface (<0.1μm), which is attributed to the interplay between the high Eu concentration and concentration quenching curve at high concentrations, a flat mid-section (not observed at 1 or 2 keV) where the Eu concentration and power dissipation curves are essentially constant, and a tail off region at the end of electron range. The curves are very interesting because they suggest that the CL degradation rate should not be similar for different accelerating voltages. The 1 and 2keV curves exhibit no flat mid-section. If a growing surface dead layer grew at a rate versus coulomb load which was independent of $V_{p,}$ the CL degradation curves would look very different for 1 versus 5 keV electrons. Much of the brightness obtained at 1 or 2keV is from near the surface, and the CL degradation rates would be higher because of the smaller volume. The 3keV and higher primary energies have a larger fraction of brightness generated from depths below the initial brightness hump and thus would not be so strongly affected by the consumption of that region by a non-luminescent layer.

In order for a model to be useful, it must approximate
real events. Total CL degradations have been calculated by
the model using the experimentally measured threshold
voltages from previous chapters. The background experiment
of chapter 4 showed a 4% loss in CL brightness at 2keV. The
threshold voltage changed from 539V to 640V during the
experiment. The cumulative loss in brightness as a function
of depth has been calculated and is shown in Figure 7-6 for
1,2, and 3kev primary electron energies. By normalizing to
the brightness with a 539V dead layer and integrating to the
end of range, the % brightness loss can be calculated from
the model at 2keV. It is found to be 6%. The model is in
very good agreement with the experimentally determined
degradation value (~4%). The 1 and 3 keV cumulative
brightness fractions are meant for comparison. As expected,
the 1 keV degradation would be larger than the 2 keV with
the 3 keV loss the smallest. a second experiment, the time
dependent threshold voltage experiment of Chapter 5 (see
figure 5-17) was used to determine the validity of the model
for experiments in oxygen. The experimental threshold
voltage values found for the unaged and aged spot were 166V
and 866V ,respectively, and the total CL degradation was

about 40%. The theoretical loss calculated using the model,

shown in Figure 7-7 for a 2keV beam, is 45%. The theoretical

prediction may have overshot by 5% because it does not take

into account the fact that the converted surface layer can

actually be another luminescent material ($Y_2O_3:Eu^{3+}$). Thus in

both cases, the model is accurate for $Y_2O_2S:Eu^{3+}$ CL

degradation.

Modeling of Gas-Surface Interactions of $Y_2O_2S:Eu^{3+}$

Introduction

The results of chapters 4-6 have demonstrated that CL

degradation is dependant upon the gas pressure and the type

of gas which interacts with the surface of the phosphor. It

has been postulated that the CL degradation is initially

rate limited by the amount of reactive gas available at the

surface, and as the surface concentration of S decreases

(and the dead layer thickness increases), the reaction

becomes rate-limited by the diffusion of S and/or O through

the dead layer. It may be possible to confirm these

postulates by quantifying the amounts of reactive gas

available at the surface. It has also been suggested that the dissassociation efficiency of a gas by an electron is sensitive to the electrons kinetic energy. This also can be examined by a model which relates the gas pressure and kinetic energy of the electron to the amount of dissassociated gas found at the surface.

Gas Impingement On the Surface

As a first step, the determination of the amount of gas striking the surface needs to be examined. The impingement rate for an ideal gas is defined as the number of molecules striking a unit area in one second and is given as follows:

$$ImpingementRate(P,m,T) = 3.5(10^{22}) * [\frac{P}{(mT)^{.5}}] \qquad (7.4)$$

where **P** is the pressure of the gas of interest in Torr, **m** is the gram molecular weight of the gas molecule and **T** is the temperature of the gas.

In this case, the gas is O_2 (m=15.99 g/mole) and the pressure of the oxygen can be estimated knowing the initial system pressure and the oxygen backfilled pressure. Typically, the system pressure was near $1x10^{-8}$ Torr, and

backfilled oxygen experiments were conducted at 1×10^{-6} Torr.
The difference between these pressures is a good estimate of
the amount of oxygen in the system (neglecting the oxygen
present in the system at 1×10^{-8} Torr). Figure 7-8 shows the
calculated impingement rate as a function of partial
pressure of O_2 for temperatures of 100, 300, 500 and 700K.
At a partial pressure of 1×10^{-6} Torr and 300K, the
impingement rate approaches a monolayer of gas per second.
At 1×10^{-8} Torr, the impingement rate is only ~ 1% of a
monolayer per second. Also, as the temperature is increased,
the impingement rate decreases.

Dissassociation Efficiency of O_2 by Electron Impact

The impingement rates calculated above need to be
modified by the dissassociation efficiency of the gas by
electron impact to obtain the amount of dissassociated gas
available at the surface. Since no CL degradation occurs
while the electron beam is off, it is suspected that the
surface reaction is only possible when the gas at the
surface has been dissassociated by an incoming electron. a
curve relating the dissassociation efficiency to the
electron kinetic energy [Eng94] has been reported and is

shown in Figure 7-9. The fit to the curve is only valid for electron energies from 200-10,000 eV. The actual curve decreases below 200eV. Note that the units for dissassociation efficiency are given in #ion pairs/cm*mmHg. An ion pair was defined as an dissassociated gas molecule and the electron lost by dissassociation. Also note that the dissassociation efficiency is defined for a centimeter of travel for an electron. The dissassociation efficiencies will be much smaller for these calculations since the travel distance available is much shorter. It will be assumed that the only gas that will be available for reaction at the surface, must be on the surface physisorbed. The curve of figure 7-9 shows a smoothly increasing dissassociation efficiency as the accelerating voltage decreases. As the electron slows down (decreasing kinetic energy), its interaction time (cross-section) with a gas molecule increases, and the dissassociation efficiency increases.

There are two other considerations associated with the determination of the number of ions generated by the electron beam. The first is the mean stay time of the molecules at the surface which depends on the temperature and the heat of desorption of the gas and surface. The

average number of molecules found at the surface will vary

with the mean stay time which is defined as follows [Hud92]:

$$MeanStayTime(t_0, H_{des}, T) = t_0 \exp\left(\frac{h_{des}}{kT}\right) \qquad (7.5)$$

where t_0 is defined as the time between escape attempts by a

gas molecule (taken as 10^{-13} seconds), H_{des} is the heat of

desorption of the gas from the surface in cal/mol, k is

Boltzmanns constant and T is the temperature of the gas in °

Kelvin.

Figure 7-10 shows the mean stay time plotted as a

function of temperature for a constant heat of desorption

(5kcal/mol). The mean stay time increases with decreasing

temperature. Figure 7-11 shows the variation of mean stay

time with the heat of desorption. Typical values for O_2 weak

physisorption to weak chemisorption are from 1kcal/mol to 15

kcal/mol, respectively[Hud92]. As the heat of desorption

increases indicating stronger bonds between the gas and

surface, the mean stay time increases.

Knowing the partial pressure of the gas and the mean stay time (governed by T and H_{des}), the average number of molecules/cm² at the surface can be calculated as follows:

$$n_a = Impingement Rate * MeanStayTime \qquad (7.6)$$

where n_a is the average number of molecules/cm2 (assuming a unity sticking coefficient). Fig 7-12 shows the average number of O_2 molecules available for electron beam dissassociation as a function of partial pressure of O_2. Four curves are plotted for H_{des} values of 1, 5, 10 and 15 kcal/mol. It can be seen that the average number of molecules on the surface approaches the impingement rate at a given pressure with increasing heats of desorption.

The ionization efficiency curve show in figure 7-9 suggests that a single electron is capable of ionizing as many as 10 gas molecules at 1 mmHg in a centimeter of travel at 200eV.

Figure 7-13 is a plot of the number of electrons striking a 1 cm² area per second for electron beam currents from 0.1 to 10μa. The current densities were calculated using the experimentally determined beam spot size

(0.011cm^2). Typically, the sample current measured for this spot size is 3.0μa. This results in an electron density of ~10^{16} electrons/cm^2*second. Even with an H_{des} value of 15kcal/mol, at a partial pressure 1x10^{-6} Torr of O_2, there are only ~10^{14} mol/cm^2. Figure 7-14 shows the rate of generation at 2keV for H_{des} values of 1, 5, 10 and 15 kcal/mol with a sample current of 3.0μa. The system may be limited by the total amount of gas available for ionization at the surface.

Thus, within the constraints of the model, lower temperatures, higher H_{des} values and higher pressures would increase the CL degradation rate by increasing the amount of reactive gas at the surface. The experiments of chapters 4 and 5 made it clear that higher pressures increased the CL degradation rate. In future work, temperature control of the phosphor could be used to verify a change in CL degradation due to its effect on both H_{des} and mean stay time for a gas.

Discussion

This study has identified several important parameters related to the CL degradation of $Y_2O_2S:Eu^{3+}$ powder CRT phosphor. The surface reaction and volatility of C has been shown to correlate with small amounts of CL degradation (<5%). The effect of ambient pressure and constituents on the surface reaction rate with S has been shown to affect the CL degradation rate of the phosphor, especially in oxygen dominated ambient. Since the CL degradation is dependant on the surface reaction, the CL degradation rate is also affected by the initial surface condition of the phosphor. Surface charge effects observed may also contribute to the total CL degradation.

Since the surface conversion and CL degradation are inter-related, the brightness obtained from any given depth in the phosphor becomes extremely important in understanding the CL degradation phenomena. The concentration of Eu^{3+} light emitting centers versus depth is especially important at lower accelerating voltages and shallower penetration depths. This coupled with the concentration quenching effect and the power dissipated as a function of depth in the

material are all important factors in understanding the CL

degradation, as shown above.

The formation of $Y_2O_3:Eu^{3+}$ in oxygen ambient has been

shown to be the main cause of the CL degradation. Since the

temperatures achieved under the electron beam are not nearly

that required to form $Y_2O_3:Eu^{3+}$ from $Y_2O_2S:Eu^{3+}$ (1100 C), the

surface reaction must be stimulated by the electron beam.

This is consistent with the lack of degradation in O_2

without electron beam bombardment. Oxygen molecules

impinging on the surface are dissociated to atomic species

by the electron beam, which are very reactive. These atomic

species combine with surface C and S forming volatile gas

species (SO_x and CO_x) which may desorb from the surface. The

decreasing surface concentration of S relative to the bulk

increases the chemical potential and S continues to move

towards the surface where it can be desorbed. The diffusion

of sulfur may also be enhanced by the presence of strong

electric fields near the surface (which would be consistent

with the charge shifted AES peaks). The loss of S in

conjunction with the presence of O leads to the formation of

the $Y_2O_3:Eu^3$ phase near the surface. The presence of the

612nm CL emission peak demonstrates that this phase is

crystalline in nature with active Eu^{3+} occupying yttrium sites in the lattice. The formation of $Y_2O_3:Eu^3$ at the surface causes changes in the surface bonding and surface charging. The secondary emission ratio should change since this property is material dependant and from the experiments, an increase in secondary emission was observed after the formation of $Y_2O_3:Eu^3$. Surface bonding will change due to the phase growth and this could affect the adsorption of gas and the number of available sites for dissociation. Also, after formation of the first few monolayers of yttria, the rate at which S and/or O are transported to or away from the surface may change, which ultimately may limit the rate of degradation. Surface charging is related to the secondary emission ratio and the electrical conductivity of the material. Therefore, changes in surface charging may occur as well. The surface reaction is itself dependant on many system parameters. Since the surface reaction is electron beam stimulated, it depends on the ionization and dissociation of gas species at the surface, the electron beam energy, amount of gas available at the surface and current density must necessarily affect the CL degradation rate.

The modeling in this chapter has assumed that the "dead" layer region of the material contributed no brightness. In truth, some of this region does contribute to the total brightness since it was found to be a luminescent form of $Y_2O_3:Eu^{3+}$. This was briefly examined to determine the overall effect on the total brightness. The assumptions for the revised model were that the initial dead layer (that found prior to degradation) would contribute no brightness. The measured increase after CL degradation was then considered to consist entirely of $Y_2O_3:Eu^{3+}$. The threshold voltages were taken from an oxygen ambient experiment and were 166 and 866 volts. The modified model predicts a 43% loss in CL brightness, whereas the original model predicted a 46% loss. The modified model results are shown in Figure 7-15 as total brightness versus depth. The modified model does approximate the experimental loss slightly better, but the change is negligible (~3%). Basically, since the $Y_2O_3:Eu^{3+}$ is at best, half as efficient as the $Y_2O_2S:Eu^{3+}$, and the effieciency is further lowered by the low Eu^{3+} concentration in the dead layer (as far as efficient $Y_2O_3:Eu^{3+}$ is concerned), the treatement of the dead layer as a zero brightness layer was a good approximation.

Although the surface conversion of $Y_2O_2S:Eu^{3+}$ to $Y_2O_3:Eu^{3+}$ accounts for most of the CL degradation observed, other factors which were not studied may contribute to the overall degradation. Since the surface conversion requires the removal of S from the lattice with subsequent conversion to $Y_2O_3:Eu^{3+}$, point defects (even in an ionic crystal) may be created and presumably would increase with increasing conversion. If the production of point defects due to the power density of the electron beam or surface temperature was important, increased CL degradation should be observed for higher power densities. This was not observed.

Increased optical absorption of the surface of the phosphor has been found for many phosphors, but the formation of Y_2O_3 (which has a larger bad gap than Y_2O_2S) would not increase the optical absorption. Interface losses and a change in the critical angle of refraction might be expected from the surface conversion and index of refraction difference between the oxide and oxysulfide. However, rarely was a dark spot observed from degradation (only when a surface coating was present), therefore optical absorption was not a significant degradation mechanism.

In conclusion, removal of C led to small changes in CL brightness, while the removal and conversion of $Y_2O_2S:Eu^{3+}$ to $Y_2O_3:Eu^{3+}$ led to CL brightness losses of ~50%. The modification of the model to take into account the CL brightness contribution of $Y_2O_3:Eu^{3+}$ has shown that the layer does not contribute substantially to the total brightness of the phosphor after degradation. It is essentially a "dead" layer due to its low luminescent efficiency limited by the low Eu^{3+} concentration.

Summary

Two semi-quantitative models have been developed to aid in understanding the CL degradation phenomena. a model of the brightness as a function of depth has been developed specifically for $Y_2O_2S:Eu^{3+}$. The model takes into account the power dissipated by an electron as a function of depth, the Eu^{3+} concentration as a function of depth, and the concentration quenching curve found in the literature. Good correlation has been found between experimental and predicted CL brightness decreases.

The second model examined the availability of dissassociated gas species at the surface. Using gas kinetic equations, the average number of gas molecules residing on the surface was calculated. The number of dissassociated gas species at the surface was then calculated using the electrons kinetic energy and an ionization efficiency chart found in the literature. The average number of dissassociated gas molecules at the surface is dependant on temperature, heat of desorption and the partial pressure of the gas in question. The model suggests that the surface reaction is limited initially by the low surface concentration of dissassociated gas available for reaction.
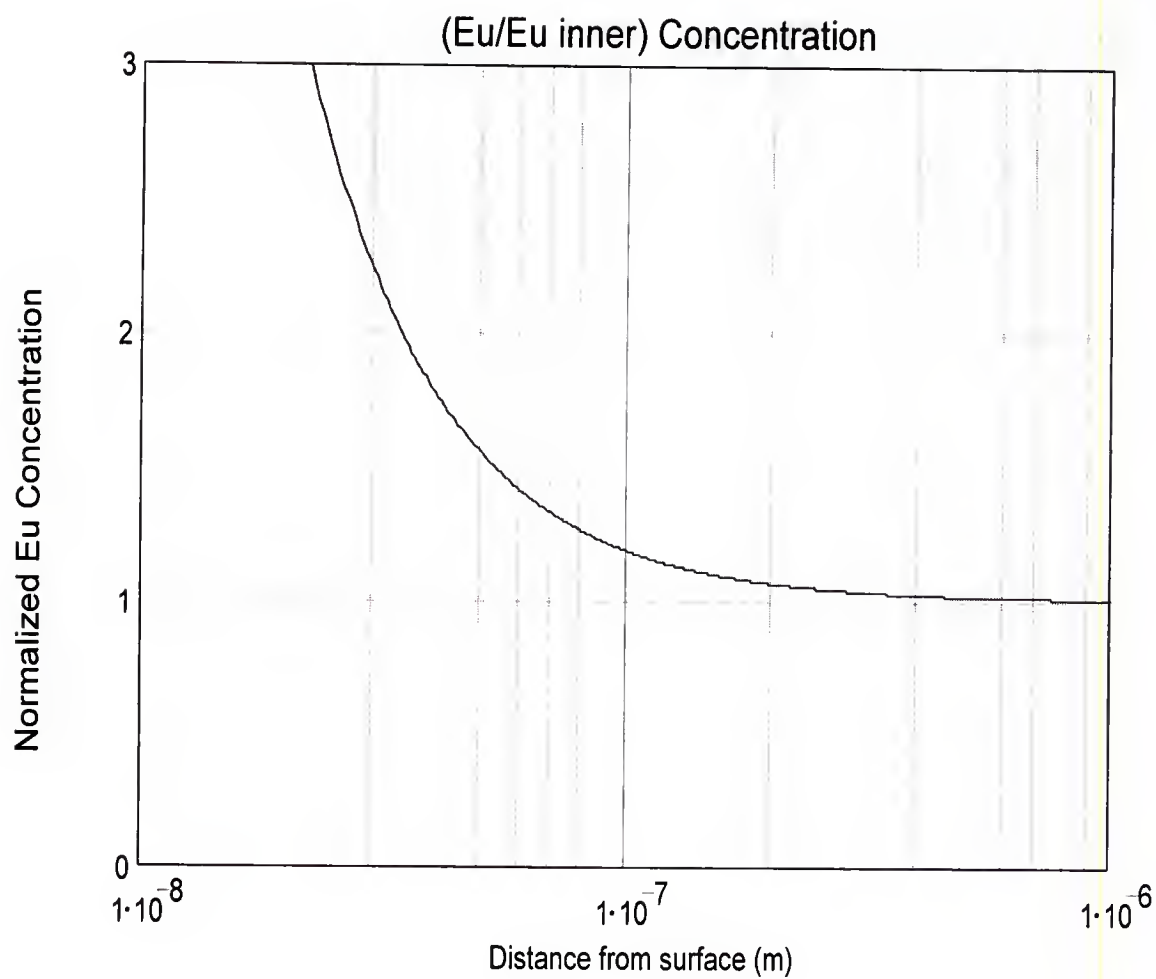
Figure 7-1 Normalized Eu concentration as a function of depth from the surface of the particle [OZA91]. Note the increasing concentration towards the surface.
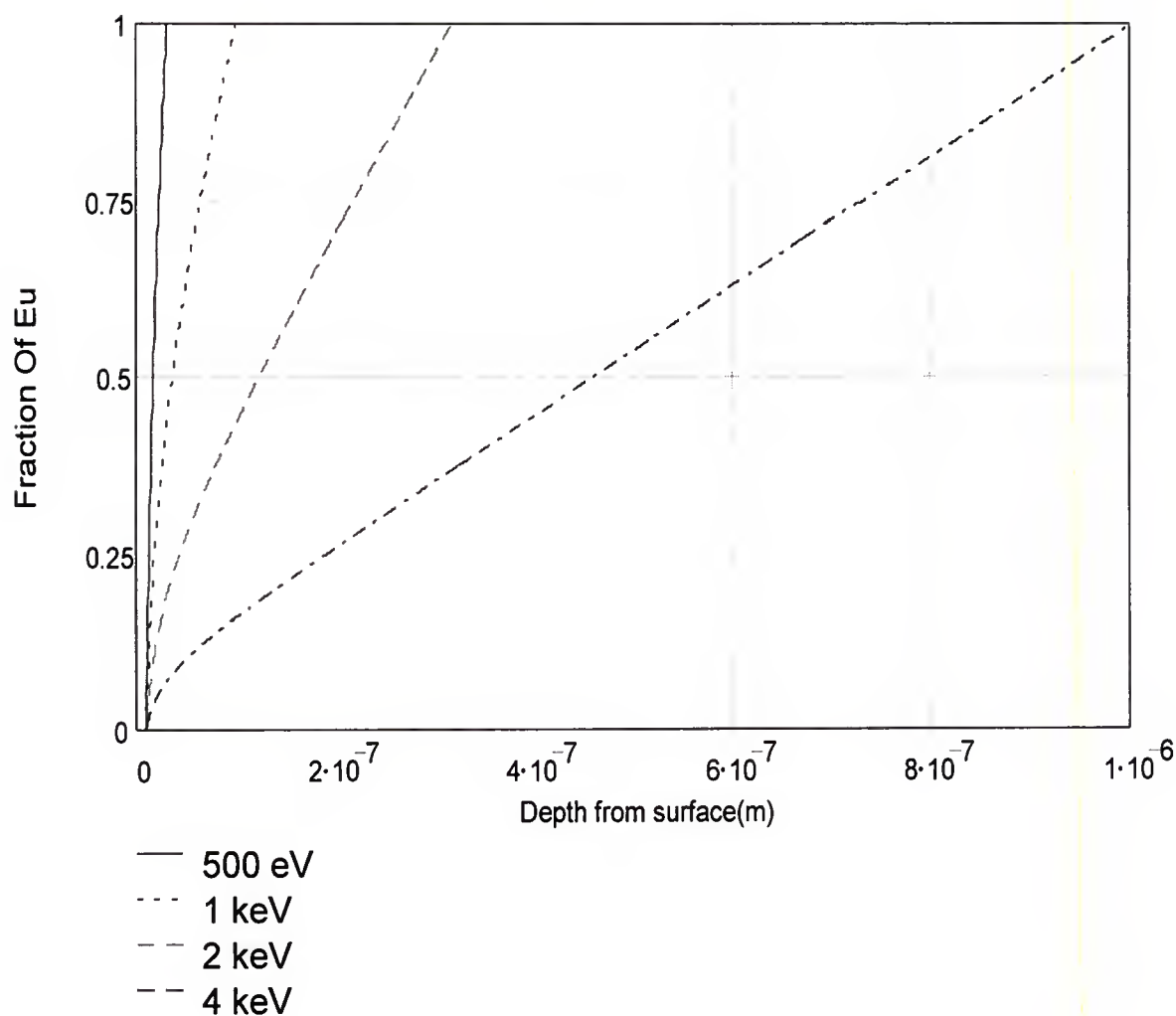
Figure 7-2   Fraction of Eu contained within a given primary electron's penetration range. The fractions were determined for a 500, 1000, 2000 and 4000 eV primary electrons range (from left to right). The higher slopes near the surface (near Depth=0) indicate the higher fractional contributions to the total by the Eu surface gradient shown in Figure 7-1.
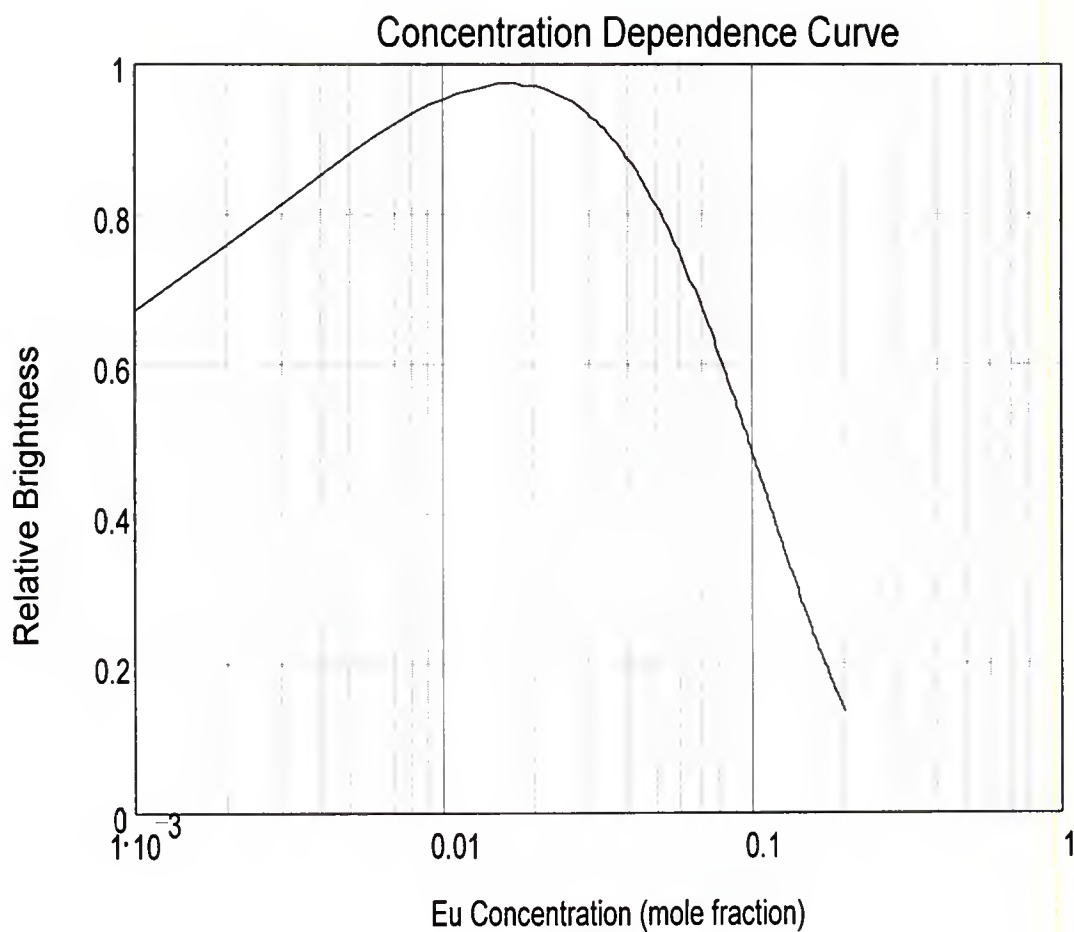
Figure 7-3   The concentration quenching curve for $Y_2O_2S:Eu^{3+}$ [OZA91]. The curve was fitted by an analytical expression and is used in conjunction with the Eu concentration as a function of depth to obtain a relative CL efficiency.
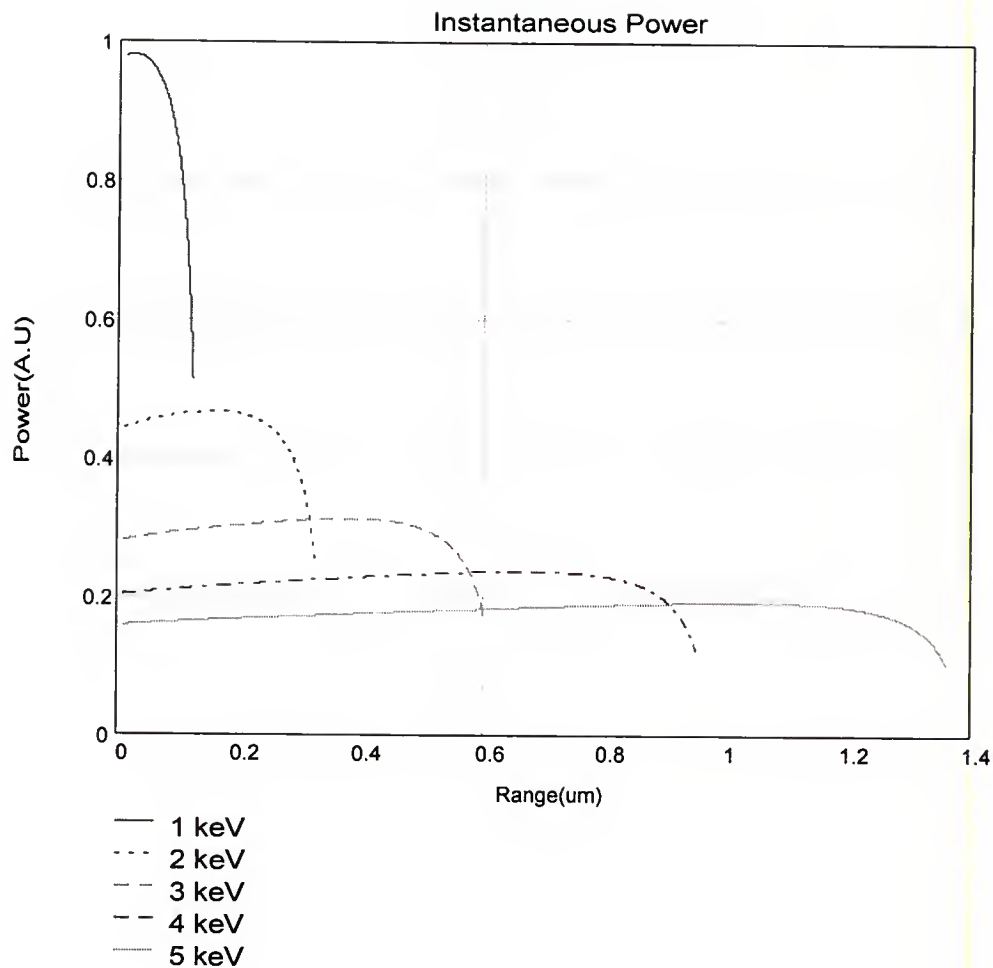
Figure 7-4   Power dissipation as a function of depth for 1-5keV primary electrons. The power curves are nearly flat, except at the end of range. Curves are for increasing primary energy (1-5keV) from left to right. A higher initial kinetic energy results in deeper electron penetration depths.
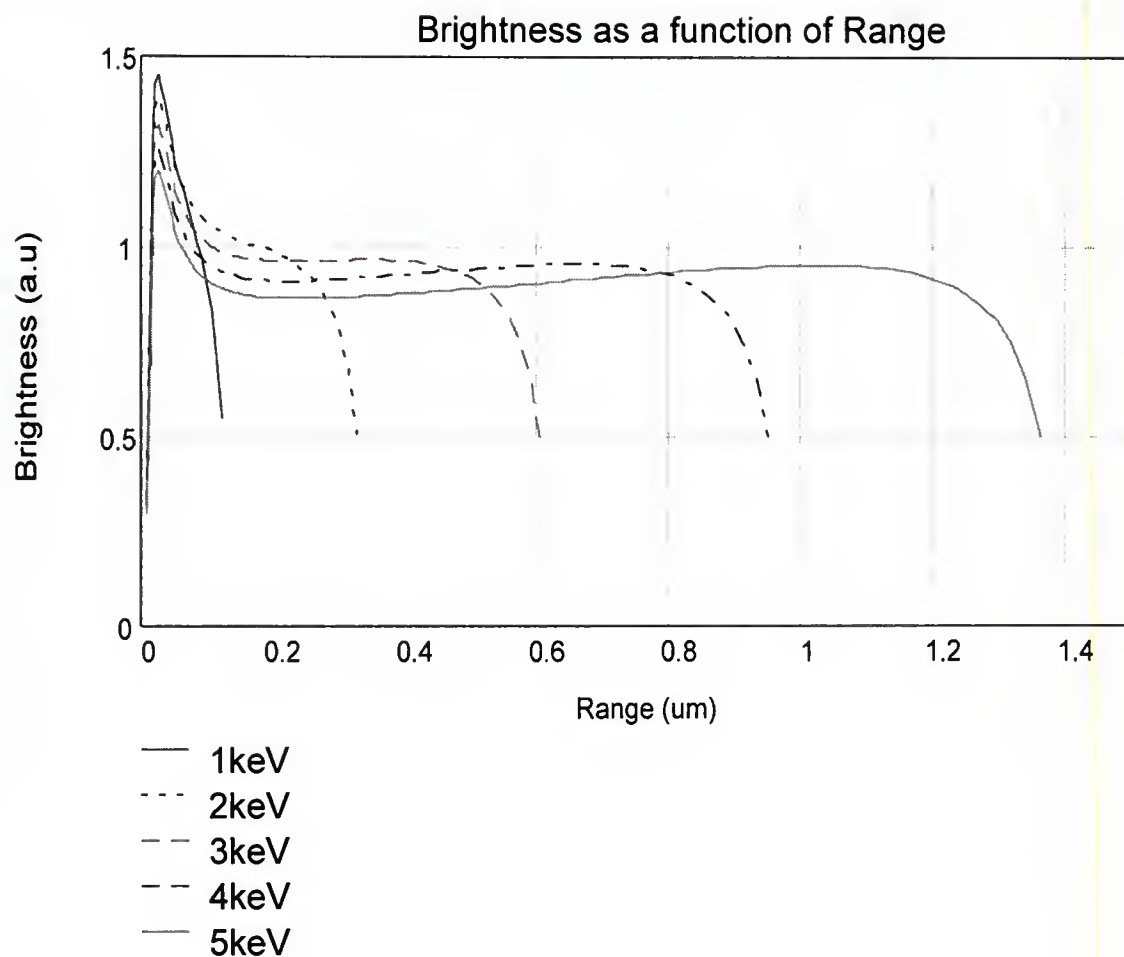
Figure 7-5   The brightness as a function of depth plotted for 1-5keV primary electron energies. Three regions are noted. A flat, nearly constant mid-section (not seen on the 1 or 2keV curve), a tail-off in brightness associated with the end of range, and a near surface brightness peak. Primary electron energies increase from left to right.

Brightness fraction for DLV 539to DLV640

Legend:
- ✕ 1keV
- ✕ 1keV aged
- — 2keV
- ···· 2kev aged
- + 3kev
- -+- 3kev aged
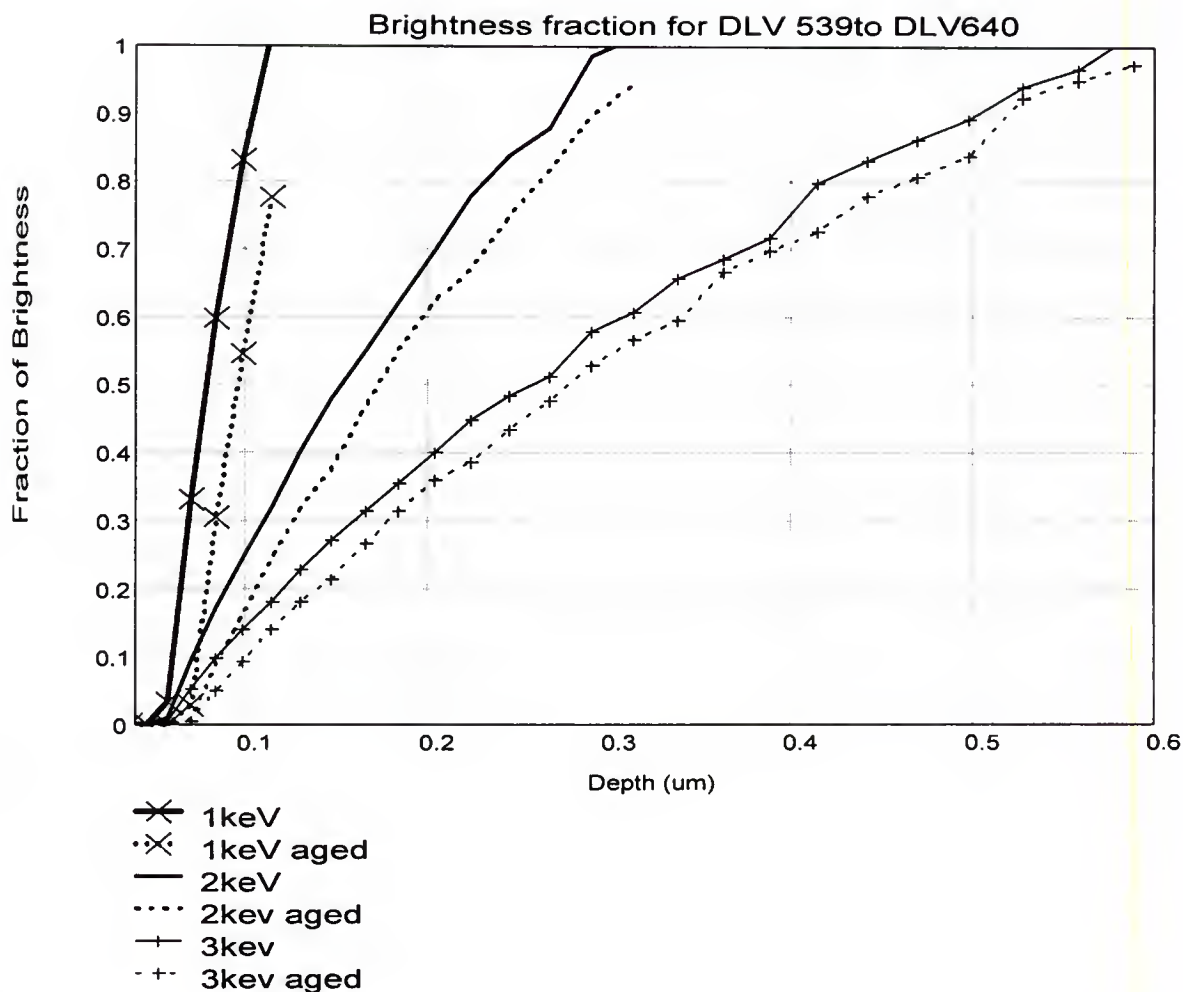
Figure 7-6   Modeling results for 1, 2 and 3kev brightness fraction as a function of depth (μm). Total CL degradation can be estimated at the end of range. All curves are for dead layer voltages of 539 and 640 volts. These are the experimental values from Chapter 4. Experimentally measured CL degradation was ~ 4% at 2keV. The calculated CL degradation (above) is ~6%. The model is in very good agreement with the experimentally determined values.
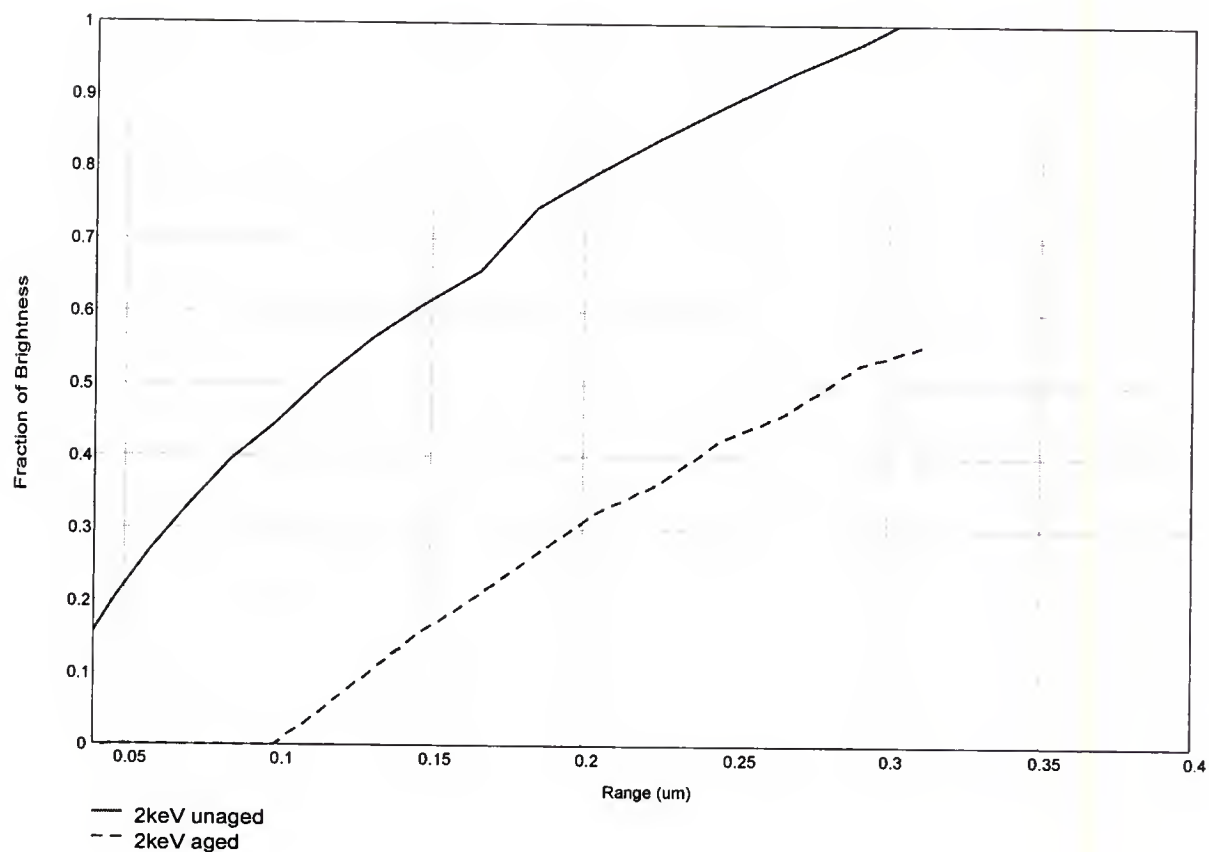
Figure 7-7   Theoretical change in brightness
calculated for an increase in Dead Layer Voltage
of 166V to 866V. The voltages were taken from
Chapter 5's Time Dependant Threshold experiment.
The observed CL degradation was ~40%. The
calculated loss in brightness was 44%.
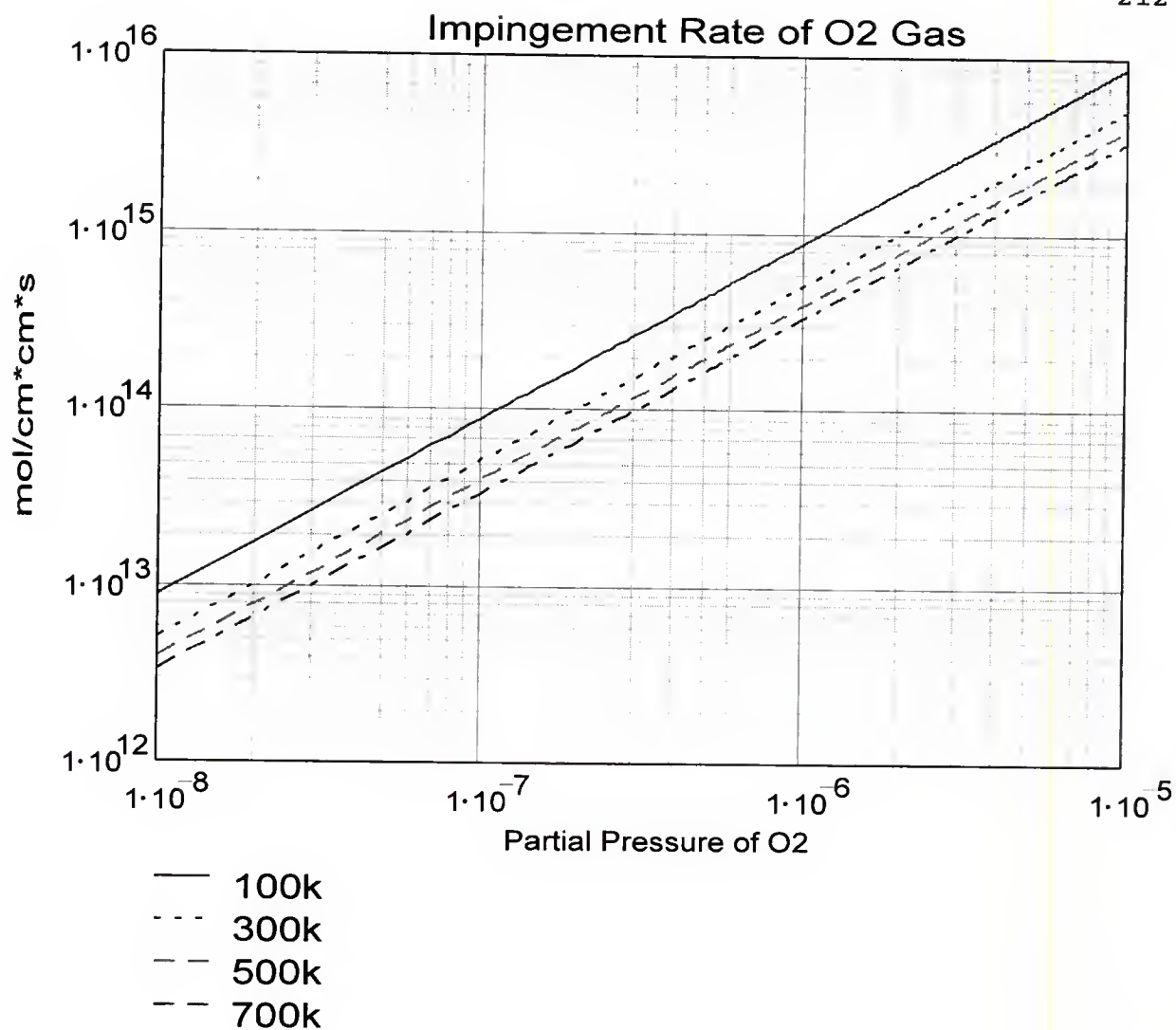
Figure 7-8   The impingement rate of O_2 gas on a surface as a function of the partial pressure of O_2 in the system. Curves are shown for temperatures of 100, 300, 500 and 700 °K. Lower temperatures increase the impingement rate.
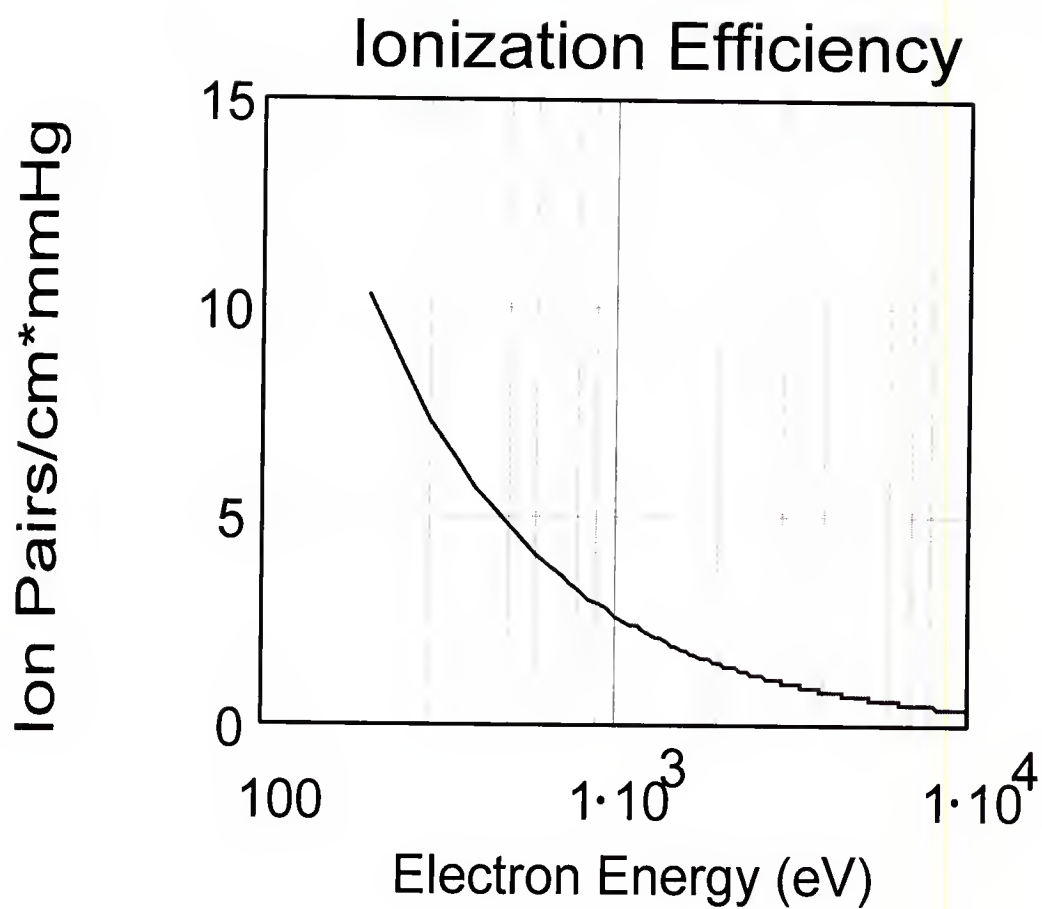
Figure 7-9   Curve fit of the ionization
efficiency data reported in literature [Eng94].
The ionization efficiency decreases with
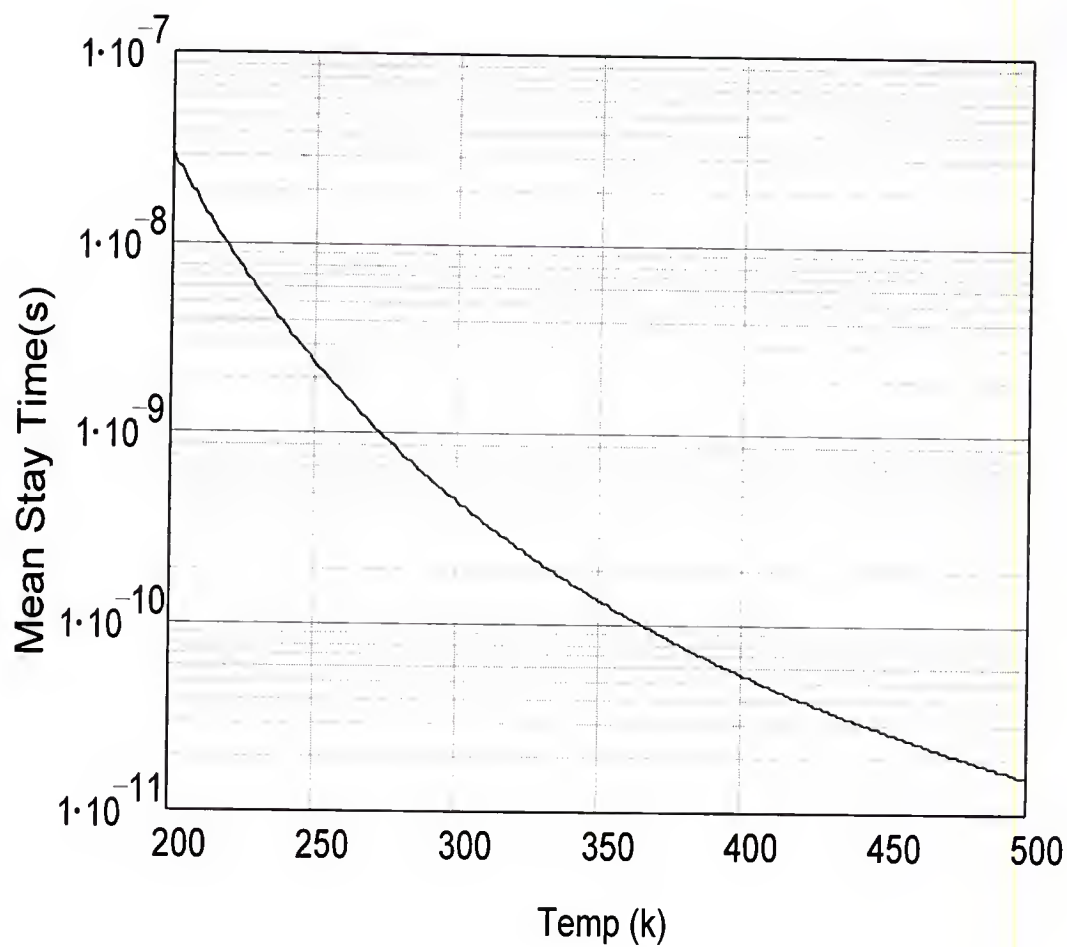increasing electron kinetic energy.

Figure 7-10   The decrease in mean stay time
with increasing temperature (°K) for an H_{des} value
of 5 kcal/mol. The mean stay time decreases with
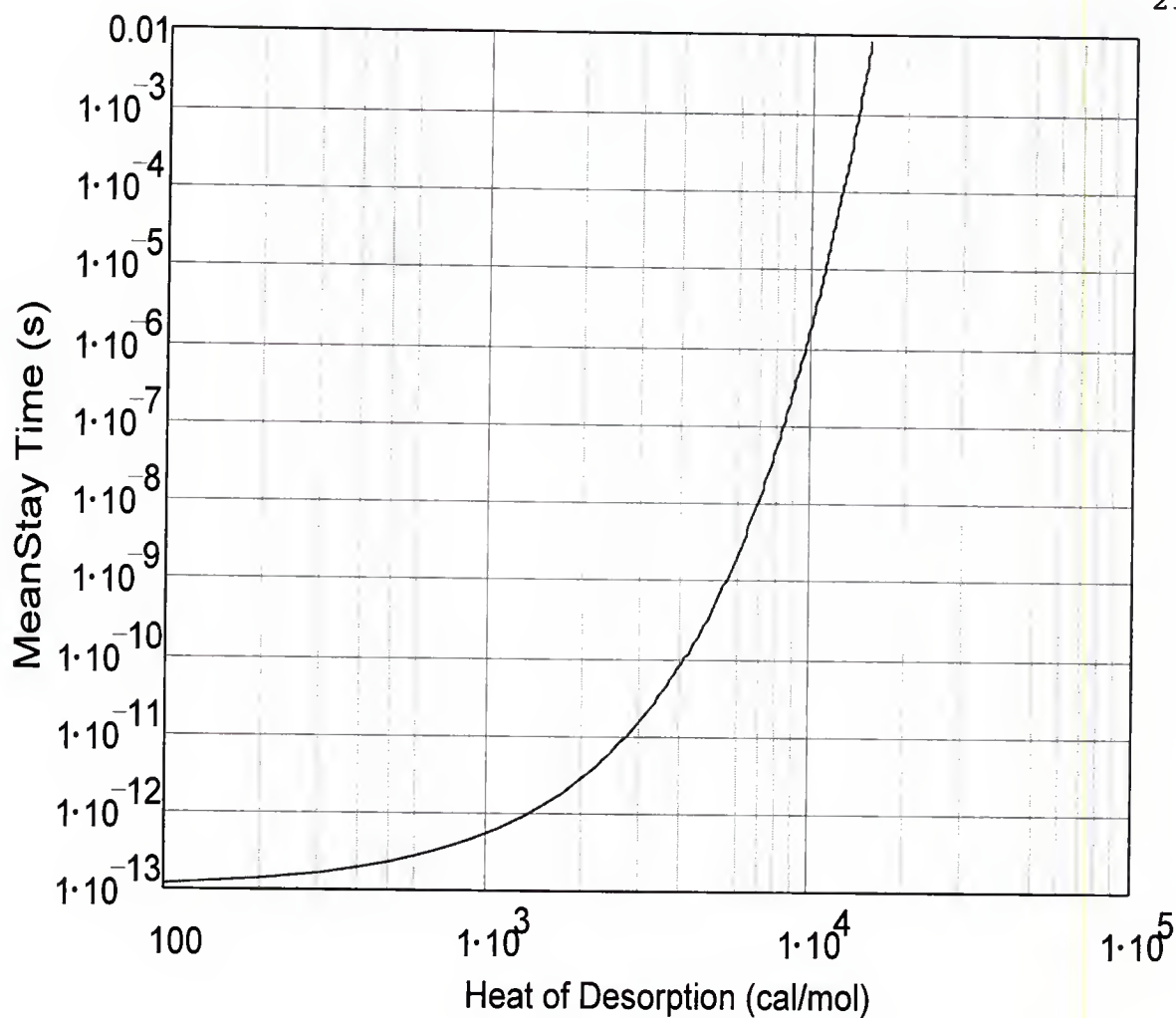increasing temperature. T_0 is assumed to be
1×10^{-13} sec.

Figure 7-11   The variation in mean stay time
with heat of desorption for T=300K. Typical values
for H_{des} for O_2 physisorption to weak chemisorption
are 1 to 15 kcal/mol. Higher H_{des} values induce
longer mean stay times, and increase the average
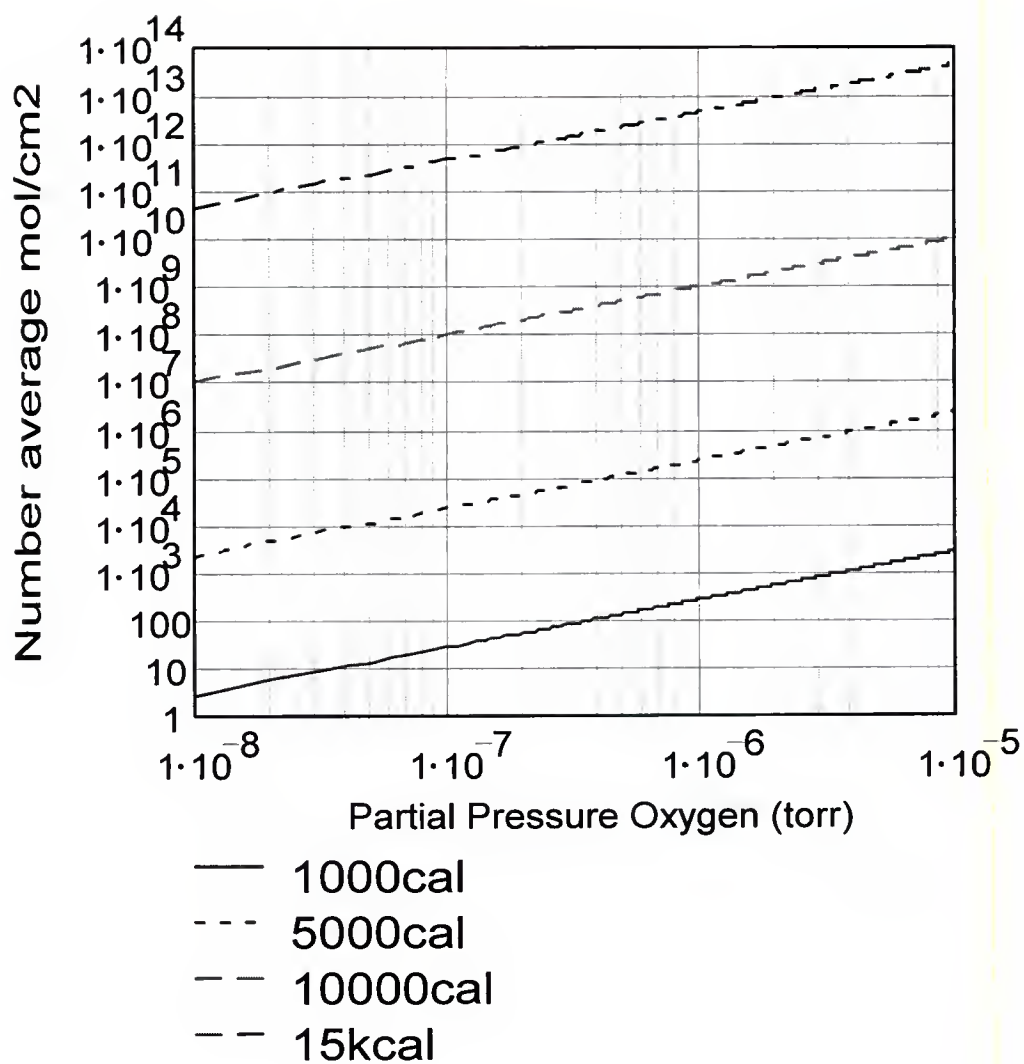number of molecules present on the surface at a
given temperature and pressure.

Figure 7-12   The average number of gas molecules found at the surface as a function of partial pressure of O_2. H_{des} values of 1,5,10, and 15 kcal/mol are shown for T=300k and a unity sticking coefficient. Increasing H_{des} values lead to increasing amounts of gas at the surface.
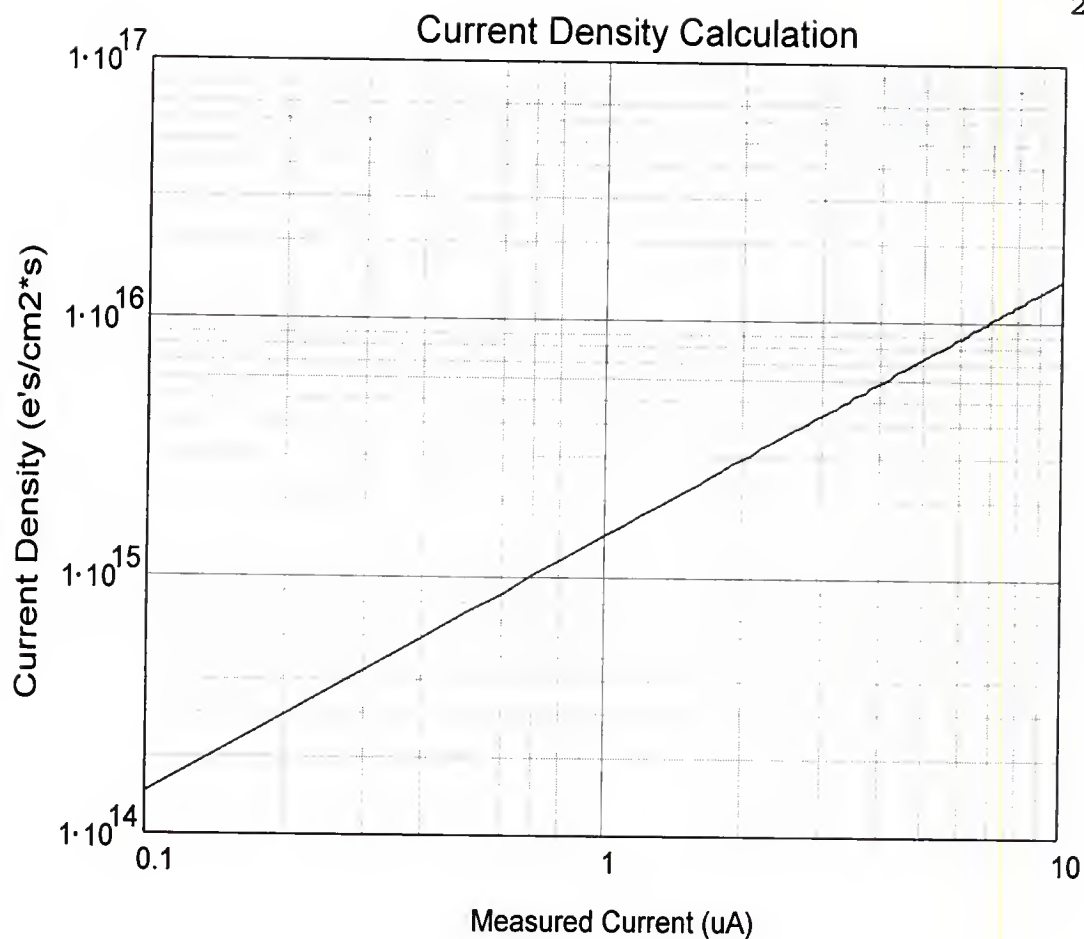
Current Density Calculation

Figure 7-13   Electron density for sample
currents from 0.1 to 10μA. The spot size was
experimentally measured and found to be 0.011 cm^2.
Note that the number of electrons is higher than
the number of gas molecules present on the
surface, even at a partial pressure of 1x10^{-6} Torr
and 15kcal/mol heat of desorption.

Number of Ions Generated at 2kev/ 3uA

y-axis: #Ions/cm2*s

x-axis: Oxygen Partial Pressure (torr)

Legend:
- —— 1kcal
- - - - 5kcal
- – – 10kcal
- – – 15kcal
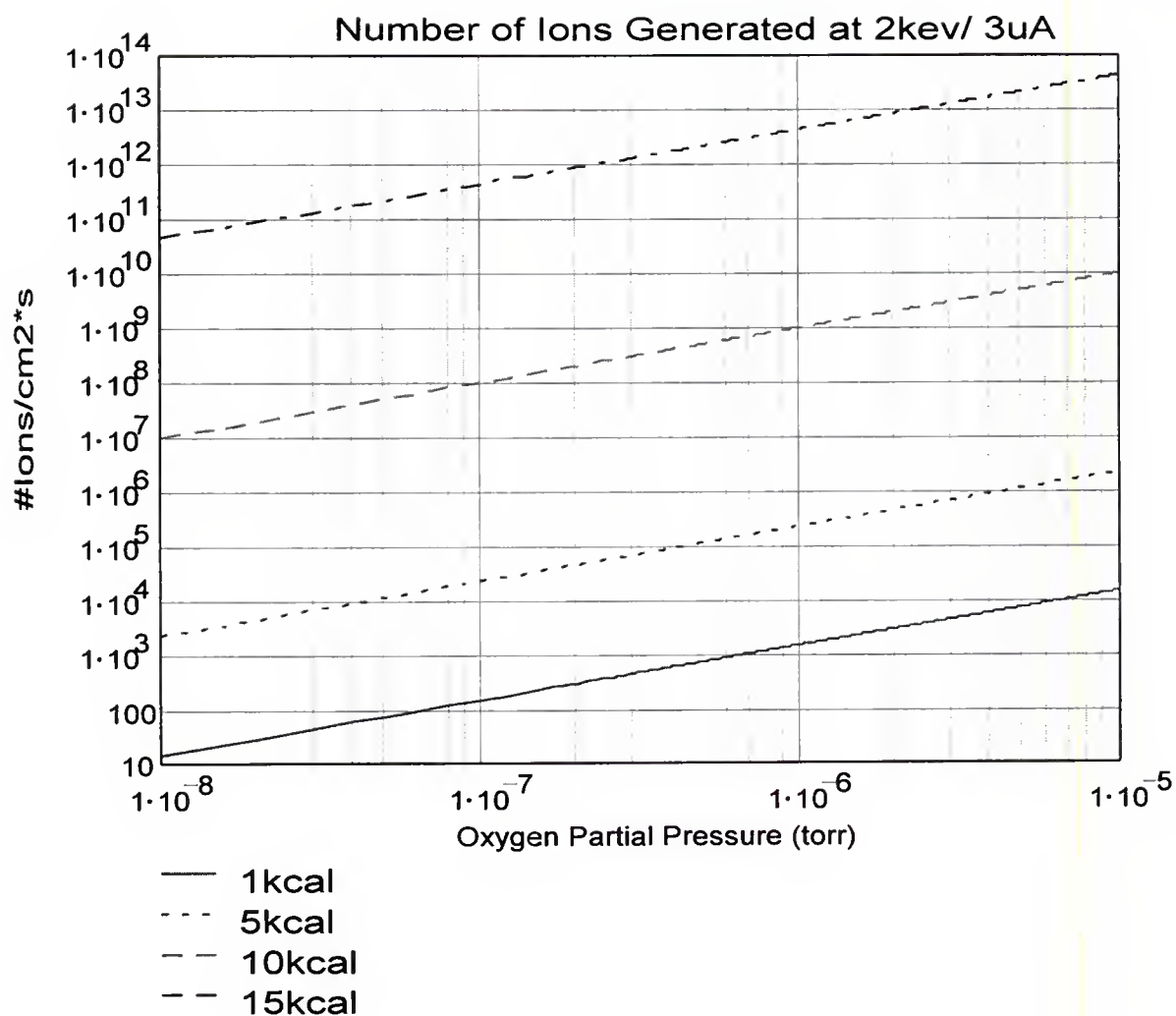
Figure 7-14   Rate of generation Total of ions for O_2 gas at 300°K with a 2keV electron beam and $265\mu A/cm^2$ sample current. The total number is limited by the number of gas molecules present. As the average number of molecules increases (increasing H_{des} 1,5,10 and 15 kcal/mol are shown), the rate of atomic species production increases.
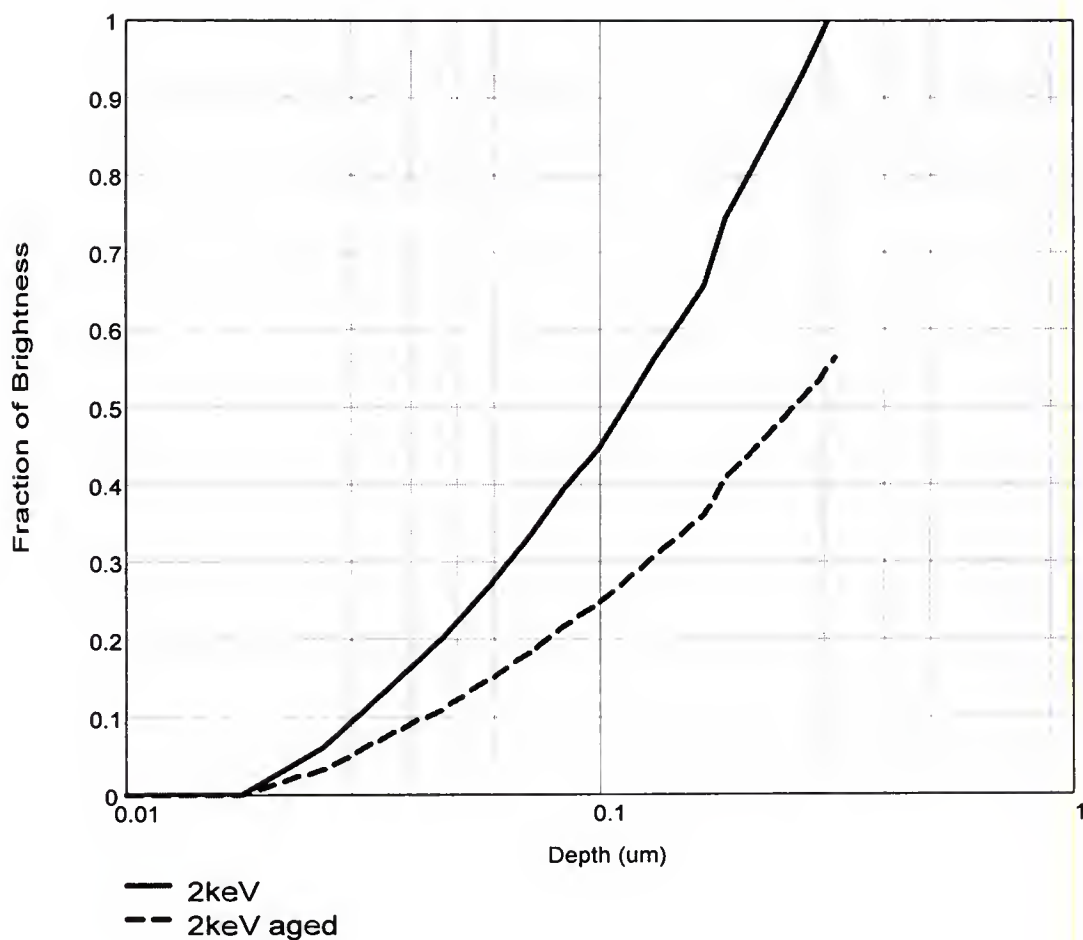
Figure 7-15   Model calculations of brightness loss
when the dead layer (0 brightness contribution) is
replaced with an $Y_2O_3:Eu^{3+}$ layer of the same thickness.
The $Y_2O_3:Eu^{3+}$ contribution is modified by the
concentration quenching curve found in the literature
[Oza91]. The threshold voltages used correspond to the
oxygen ambient experiment of chapter 5. Threshold
values of $V_{initial}$=765 volts and V_{final}=1290 volts. The
brightness loss is calculated for a 2keV primary beam.
The model predicts ~43 % loss in brightness. The
experimentally measured loss was ~35%. Without the
incorporation of the oxide layer, the theoretical loss
was 46%. The calculation is closer to the
experimentally observed loss, but the contribution from
the oxide is small (~3%).

CHAPTER 8

DEGRADATION RESISTANT COATINGS FOR $Y_2O_2S:Eu^{3+}$

Introduction

It has been shown that the CL degradation phenomena of
$Y_2O_2S:Eu^{3+}$ is related to chemical reactions of some phosphor
surface species (namely C and S) in the presence of electron
beam and is sensitive to the overall pressure and gas
species. In particular, oxygen ambients have been shown to
enhance the degradation rate of the $Y_2O_2S:Eu^{3+}$ phosphor.
Modeling of the gas-surface interaction has shown that the
surface reactions are limited by the amount of gas available
at the surface (see Chapter 7 for details). The model
indicates that the average number of gas molecules present
on the surface is a strong function of gas pressure,

temperature and heat of desorption. Experimentally, the gas pressure and temperature are easy to modify and study, but in a finished flat panel display neither of these will be controllable. Thus, for industrial relevance, the only factor which is available for minimizing the CL degradation rate of the phosphor is the heat of desorption. Since the gas cannot easily be altered, a new surface material could be used to change the heat of desorption of the gas-surface, thereby reducing the number of molecules present on the surface available for volatilization reactions and/or reducing the diffusion of S to the surface.

Since O is reacting with the surface S to form volatile reaction products, protective coatings can be applied to the phosphors effectively separating the gas phase from the phosphor surface and hence reducing the rate of CL degradation. a good coating must provide effective protection from degradation and must not reduce the brightness efficiency of the phosphor below acceptable performance levels. Coatings have been chosen based on ease of preparation and availability. No attempts were made to optimize the coatings and only the viability of protective coatings was studied.

Phosphate and silica wet chemistry coatings were studied since they were readily available and easy to produce in the laboratory. Also, TaSi and Ag coatings were deposited by a novel pulsed laser ablation technique, and Al was deposited on a screened phosphor by electron beam evaporation (see Chapter 3 for details). CL degradation experiments on all coated materials mentioned in this chapter were performed at 1×10^{-6} Torr backfilled with oxygen gas as in Chapter 6. a primary beam energy of 2keV and current densities ranging from 200 to $300\mu a/cm^2$ were used. In this chapter, the results of the CL degradation experiments for the coated phosphors will be discussed and compared.

Comparison of CL Degradation Rates

Figure 8-1 shows the CL degradation rates as a function of coulomb load for all the coated materials. a baseline $Y_2O_2S:Eu^{3+}$ oxygen experiment with no coating is shown for comparison (marked original). All coated materials exhibited less CL degradation at 20 C/cm^2 then the original powder with the exception of the phosphate coated material.

Comparing the phosphate coated powder to the uncoated

powder, the initial CL degradation rate (<5 C/cm²) is

faster, the steady rate loss after 5 C/cm² is lower than the

uncoated material but at 20 C/cm² the total degradation is

approximately equal.

By far, the best CL maintenance was demonstrated by the

TaSi and Ag coated materials. Both coatings were deposited

by pulsed laser ablation. The TaSi coated material degraded

only 15% and the Ag coated material degraded only 25% after

20 C/cm². These were followed by the SiO₂ wet chemistry

coated material which exhibited a 45% loss in brightness and

finally the phosphate coated material which degraded 52%.

TaSi Coated material

The TaSi coating exhibited the smallest amount of CL

degradation. Figure 8-2 shows the APPH ratios for O/Y and

S/Y as a function of coulomb load as well as the CL

brightness (right hand axis). At ~1 C/cm², the sulfur within

the AES detection limit has been reacted and desorbed,

correlating with the small CL brightness increase at very

low dose. For the duration of the experiment the S/Y ratio

increases while the O/Y ratio drifts down. The S/Y ratio

seen may increase due to the overlap with a Y peak. This is, however, unlikely since the Auger sensitivity of the Y peak is about 5 times smaller than the S peak. The AES signal of Ta and Si were verified separately and are not shown. The Ta AES signal is relatively high in energy and a 4keV primary energy was required to excite it. It was found that the TaSi coating is not continuous and the phosphors constituents(O, Y and S) are always detected.

Figure 8-3 shows the initial (0.07 C/cm^2) and final (15 C/cm^2) AES survey for the TaSi coated material. No C was present initially on the surface. The main Si AES peaks are at 92 and 107 eV. If Si is present, its signal is masked by the low energy Y peaks. All peaks have shifted to higher energies by the end of the experiment. This indicates a more negative surface charge present. These peak energy shifts are shown in figure 8-4. Using the trend line equations shown, the energy shifts were calculated and found to be 1.2, 1.3 and 1.8 eV for O, S and Y, respectively.

The initial and final CL spectra as functions of wavelength (nm) are shown in figure 8-5. Immediately apparent is the large increase in the 612 nm $Y_2O_3:Eu^{3+}$ peak. Other changes can be seen in figure 8-6 where the wavelength

scale is smaller and the CL difference curve is shown. Peak increases are found at 612, 618, 628 and 632nm. The 612 and 632 nm peaks are attributed to the oxide formation at the surface. The 618 and 628, along with the peak decreases at 617 and 626 nm are attributed to spectral broadening of the $Y_2O_2S:Eu^{3+}$.

Since the coating is discontinuous, it is possible that the TaSi coating reduced the available number of S for reaction and slowed the degradation process. Surface sites with no coating, reacted with the ambient and formed $Y_2O_3:Eu^{3+}$. TaSi may provide a diffusion barrier limiting the migration of S to the surface. Thus only a fractional amount of the surface would be available for the volatilization and conversion reactions. Unprotected areas would be converted to $Y_2O_3:Eu^{3+}$. After the aging experiment, the presence of Ta on the surface was reverified. Thus the surface coating was still present after degradation and was not volatilized.

Ag Coated $Y_2O_2S:Eu^{3+}$

The Ag coated material performed well exhibiting about half the total CL degradation observed in the uncoated baseline experiment at 15 C/cm². Figure 8-7 shows the APPH

ratios and the CL brightness as functions of coulomb load. Only O/Y, S/Y and Ag/Y APPH ratios are shown since no C was present on the surface at the beginning of the experiment. The S/Y APPH ratio decreased quickly (~1 C/cm²) and became undetectable for the remainder of the experiment. The O/Y APPH ratio climbed slightly until about 4 C/cm², while the Ag/Y APPH ratio decreased. During this time, the CL brightness increased slightly (~4%). It is suspected that the Ag migrated along the surface during electron beam aging away from the center of the electron beam. After the experiment, a dark ring was observed with a lightened center region where the electron beam had impacted. As the Ag migrated, the phosphor underneath became more exposed to the electron beam and oxygen ambient and the CL degradation occurred at near normal rates. Figure 8-8 shows the initial (0 C/cm²) and final (15 C/cm²) AES spectra. Initially, a significant Ag peak is present, but has been nearly removed by 15 C/cm². The Ag may have volatalized or it moved away from the area sampled by the electron beam. A small Cl peak is shown, which may be the result of a light HCL etch done prior to coating. The S APPH has fallen below the AES spectrometer sensitivity at the end of the experiment. The

AES peaks exhibit smaller energy shifts then did the TaSi coated material.

Figure 8-9 shows the FED's peak energy shifts and trend lines for O, Ag, S and Y. The relative shifts are 0.2, 0.3, 1.2 and 0.5 eV, respectively, to higher energies. These shifts are relatively small which may result from the high conductivity of Ag reducing the charge buildup at the surface.

Similar to the TaSi CL spectrum, the Ag coated phosphor exhibited a large increase in the 612 nm $Y_2O_3:Eu^{3+}$ peak after a 15 C/cm² load as shown in figure 8-10. The expanded scale spectra and CL difference curves are shown in figure 8-11, and the appearance of the oxide peak is more apparent. New peaks are found at 612 and 630nm, both associated with the oxide phase. The spectral broadening of the 626 and 617 nm peaks of $Y_2O_2S:Eu^{3+}$ are seen at 616,618 and 625, 627 nm.

The Ag coating provides some protection against CL degradation, but migrates away from the electron beam, exposing the phosphor underneath. Another possibility is the formation of a volatile Ag_2S or Ag_2O species. Comparing the rate of degradation of the Ag coated material to the baseline experiment in figure 8-1, it is seen that the rate

of degradation after 10 C/cm^2 is very similar to the

baseline rate of degradation.

SiO_2 Coated $Y_2O_2S:Eu^{3+}$

Figure 8-12 shows the APPH ratios and CL brightness as

functions of coulomb load for the silica coated phosphor. No

evidence of the silica coating was found by AES or SEM

analysis. This phosphor was obtained from Kasei Optronics of

Japan. The method used for coating the phosphor is described

in Chapter 3. a nano-particle sol of SiO_2 is slurried with

the phosphor particles. The SiO_2 nano-particles adhere to

the phosphor due to coulomb attraction. These types of

coatings are typically very thin (<100Å) because once the

surface charge of the particles has been reduced, no more

SiO_2 deposits on the surface.

The AES ratios look very similar to the baseline oxygen

experiments in Chapter 6, and S leaves the surface by 2

C/cm^2 and the O/Y ratio increases. The SiO_2 coating has not

slowed the rates of removal of C or S.

Figure 8-13 shows the initial (0 C/cm^2) and final (15

C/cm^2) CL spectra for the SiO_2 coated material. No

discernible differences are seen. Figure 8-14 shows the

expanded CL spectra and CL difference curves as functions of wavelength from 600 to 640 nm. Spectral broadening of the 626 and 617 nm $Y_2O_2S:Eu^{3+}$ peaks is visible at 616,618 and 625, 627 nm. a small $Y_2O_3:Eu^{3+}$ peak is visible at 612nm.

The SiO_2 coating did not slow the CL degradation enough to stand out from the baseline oxygen experiments. The data examined shows that its surface reactions and CL changes are very similar to the baseline experiments.

Phosphate coated $Y_2O_2S:Eu^{3+}$

The wet chemical process used to produce this coating left large nodules on the surface of the particles. Figure 8-15 shows the surface of the phosphate coated particles as seen in an SEM. The CL degradation was very close to the baseline oxygen experiment (as seen in figure 8-1). However, the changes which occurred on the surface of the phosphate coated particles were very different than the baseline experiments. Figure 8-16 shows the APPH ratios for O/Y, S/Y, P/Y and C/Y as well as the CL brightness as functions of coulomb load (C/cm^2). C is lost quickly (~2 C/cm^2), possibly volatilized by surface oxygen bonded in a phosphate configuration. The O/Y ratio drops over the same load,

supporting this postulate. Once the C is removed, the S/Y
ratio begins increasing suggesting the arrival of sulfur to
the surface. The O/Y APPH ratio follows the loss of C, and
then follows the loss in P until ~10 C/cm². It is possible
that initially the C is most readily reacted and
volatilized, and once it is depleted phosphate containing
species are next to be consumed. As the P is volatilized, S
may replace it at the surface. Probably in a similar
configuration, such as $Y_2O_2SO_4$.

The initial (0 C/cm²) and final (15 C/cm²) CL spectra
are shown in figure 8-17 and the expanded spectra and CL
difference curves are shown in figure 8-18. In figure 8-18,
no oxide peak is visible (612 nm), only peaks associated
with spectral broadening of the main $Y_2O_2S:Eu^{3+}$ peaks are
seen.

The degradation of the phosphate coated material does
not produce the $Y_2O_3:Eu^{3+}$ phase observed previously. When
$Y_2O_3:Eu^{3+}$ is produced at the surface (as is the case for TaSi
and Ag coatings) the CL degradation was slower. The
combination of the coating limiting S sites for reaction and
the early production of $Y_2O_3:Eu^{3+}$ in uncoated areas may slow
the CL degradation rate.

The phosphate coating does not appear to impede the CL degradation. S readily replaces P, possibly by forming $Y_2O_2SO_4$. The CL brightness loss of the phosphate coated material occurs at a higher rate than does the baseline experiment. This system may not be gas limited because a large amount of oxygen has been placed on the surface on purpose (as phosphate groups). Thus the surface conversion and reaction occurs faster for the phosphate coated sample as seen in figure 8-1.

Summary

Coatings have been applied to $Y_2O_2S:Eu^{3+}$ by various deposition techniques. These coated material's CL performance has been compared with the baseline oxygen experiments of Chapter 6. It has been shown that a tenacious coating, which does not migrate or volatilize during aging provides the best protection against CL degradation. Of the coatings tested, the TaSi pulsed laser ablation coating demonstrated the best ability to protect the phosphor and to remain on the surface. After 15 C/cm^2, the TaSi coated

material had degraded 3 times less then the baseline $Y_2O_2S:Eu^{3+}$.

The formation of $Y_2O_3:Eu^{3+}$ on the surface slows the rate of CL degradation in oxygen as well. It is suspected of providing a diffusion barrier to S. The silica and phosphate coatings did little to slow the degradation rate. Both provide an extra source of oxygen which may have enhanced the surface reactions removing C, S and P.
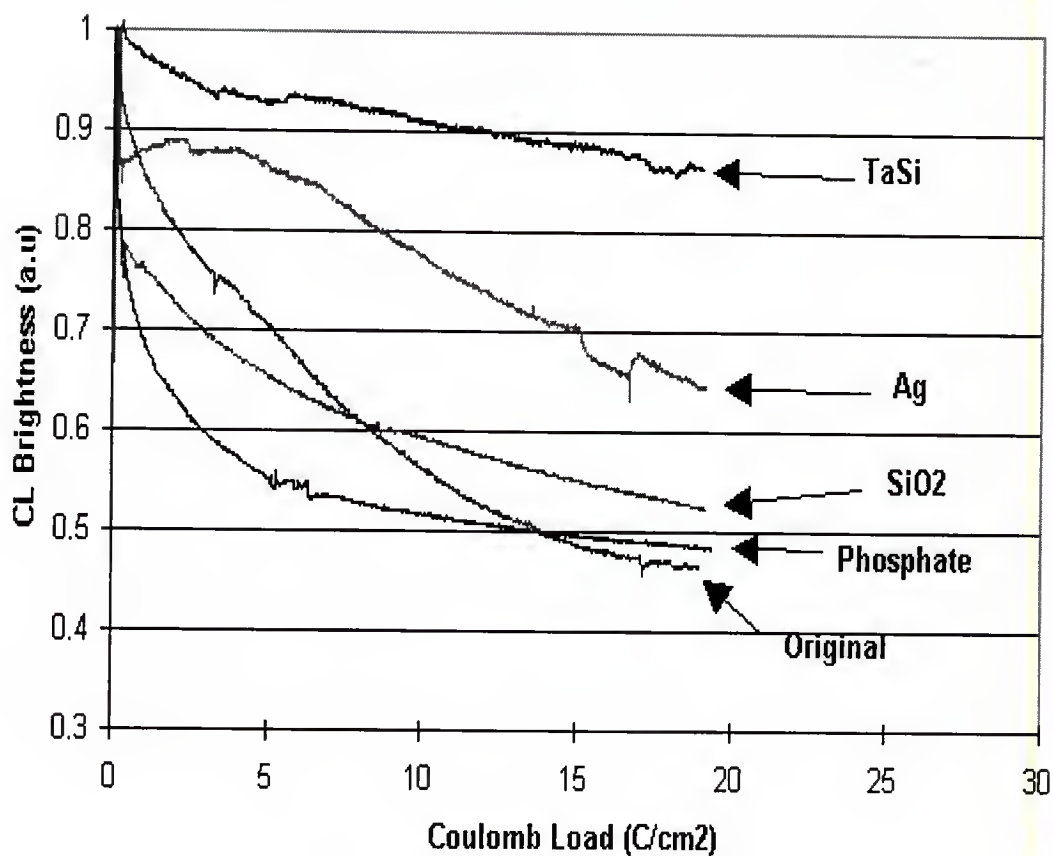
Figure 8-1   Comparison of CL degradation
for the coated phosphors. An uncoated powder is
shown for comparison and is marked "Original". The
silica and phosphate wet chemistry coatings faired
little better than the original powder. The Ag and
TaSi coated powders degraded slower than the
original powder.
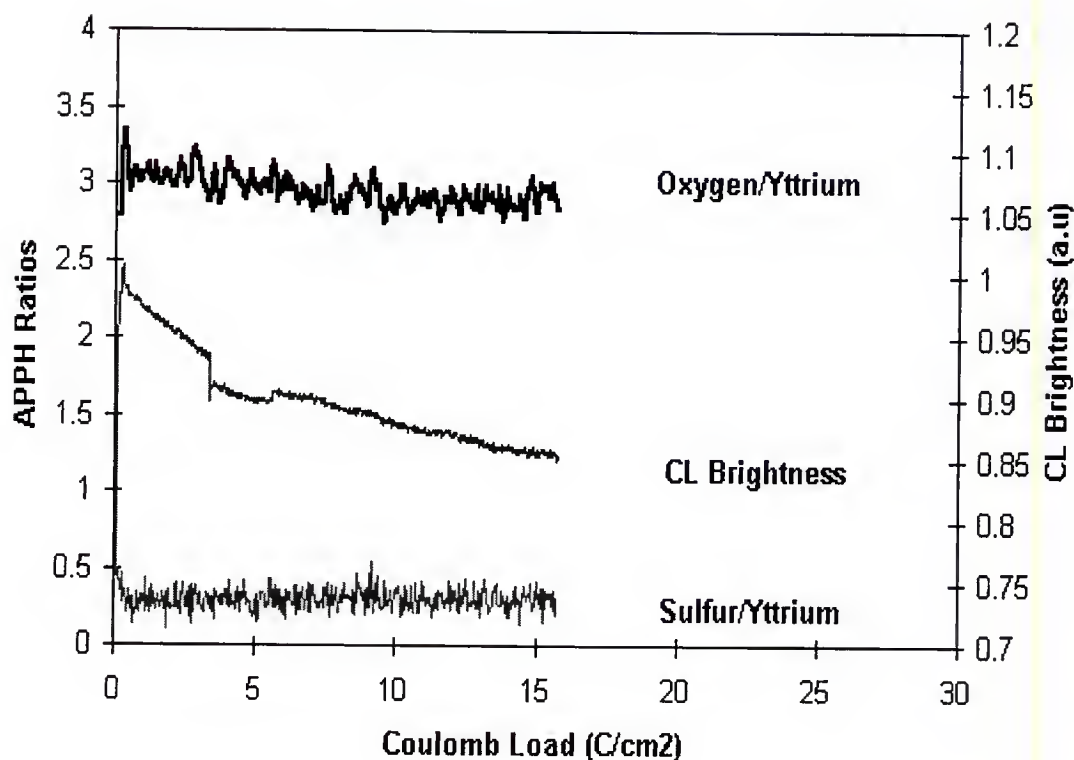
Figure 8-2   APPH ratios for O/Y and S/Y as well as CL brightness as functions of coulomb load for the TaSi coated powder. Note the very fast decay of the S/Y ratio, and the stable O/Y ratio through-out the experiment.
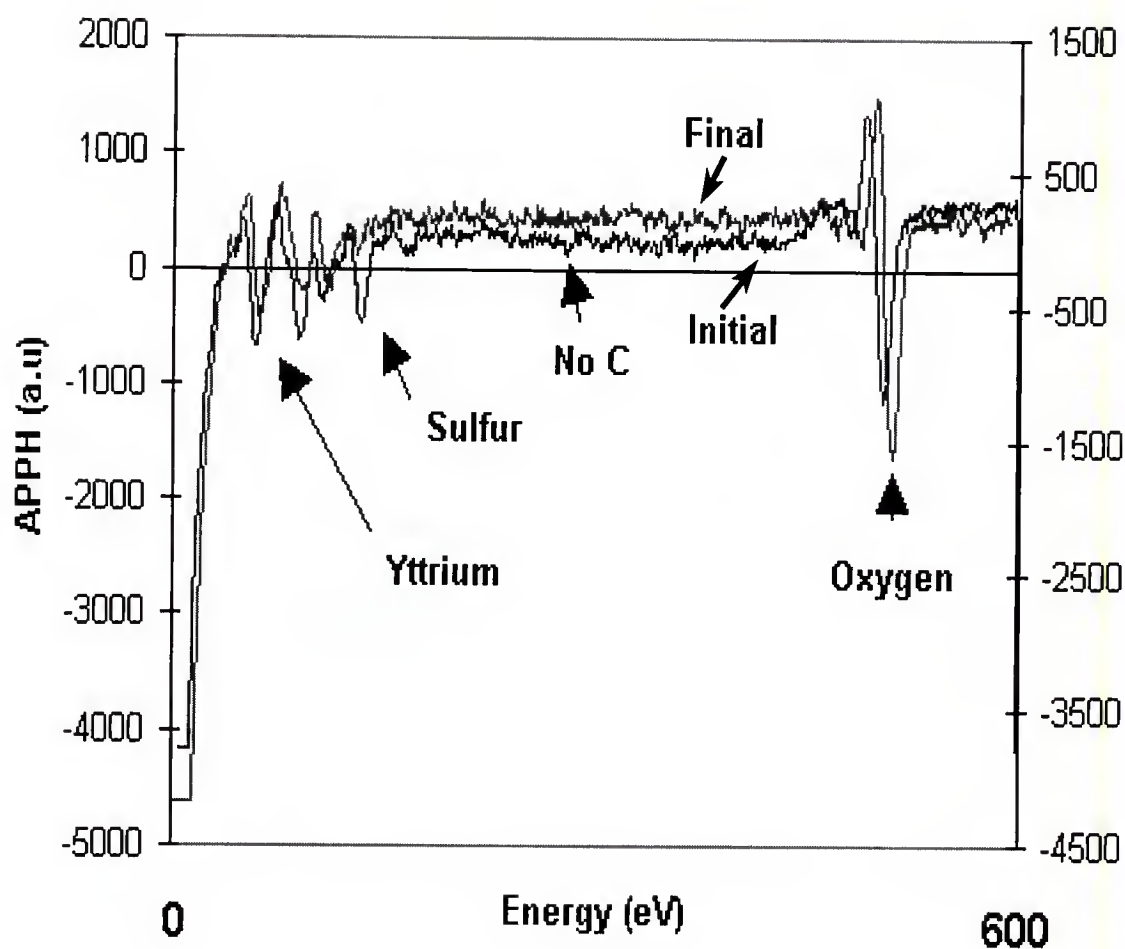
Figure 8-3   Initial and final AES scan for the TaSi coated $Y_2O_2S:Eu^{3+}$, taken at 0.07 C/cm² and 15 C/cm². No C was present initially on the surface. Small peak energy shifts are visible on all three peaks.
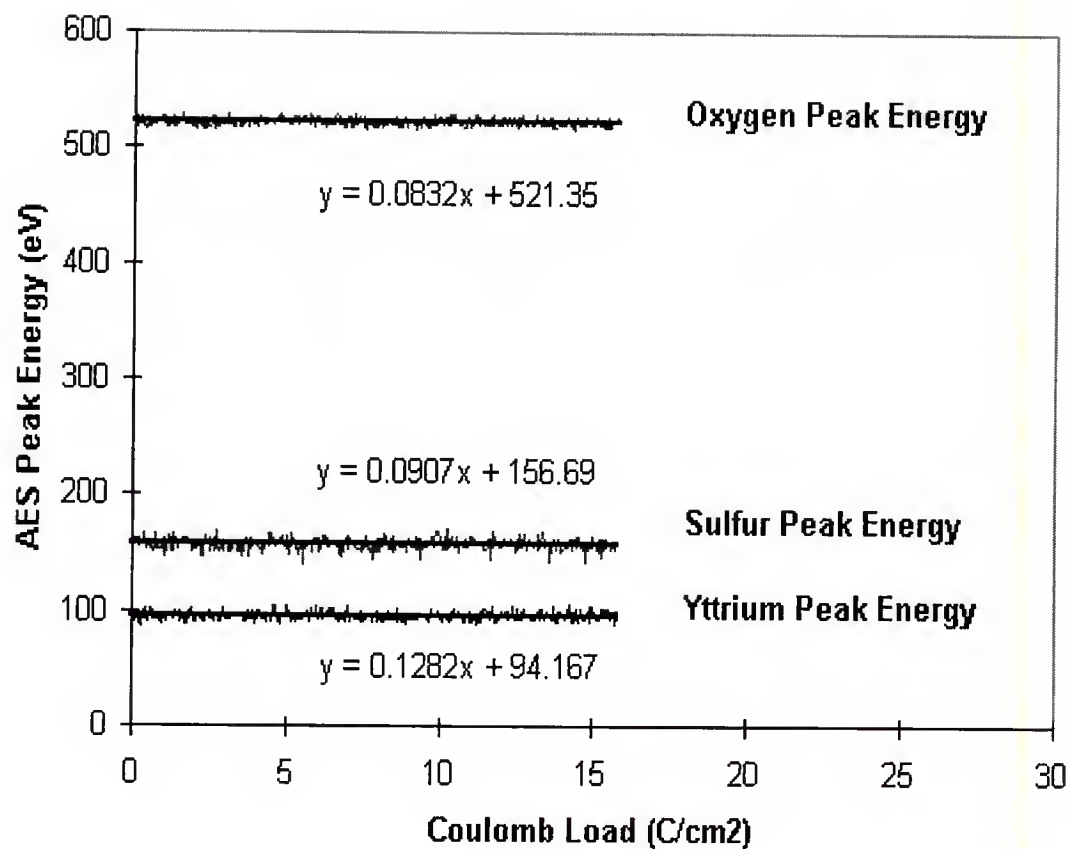
Figure 8-4   AES peak energy shifts for the TaSi coated powder. Peaks shifts at 15 C/cm² on the O, S and Y are 1.2, 1.3, and 1.8 eV, respectively.
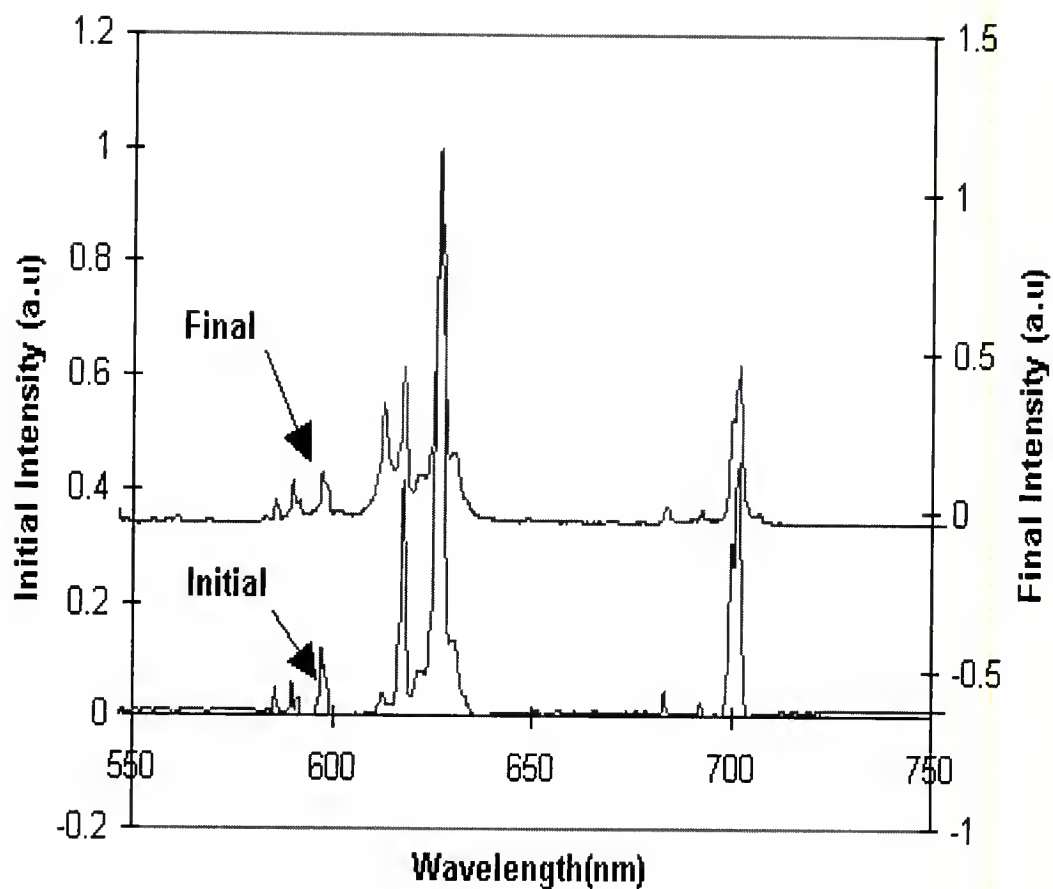
Figure 8-5   Initial (0 c/cm²) and Final (15 C/cm²) CL Intensity spectra for the TaSi coated material degraded at 2keV and ~1x10^{-6} Torr O_2. Note the large increase in the oxide emission peak at 612 nm.
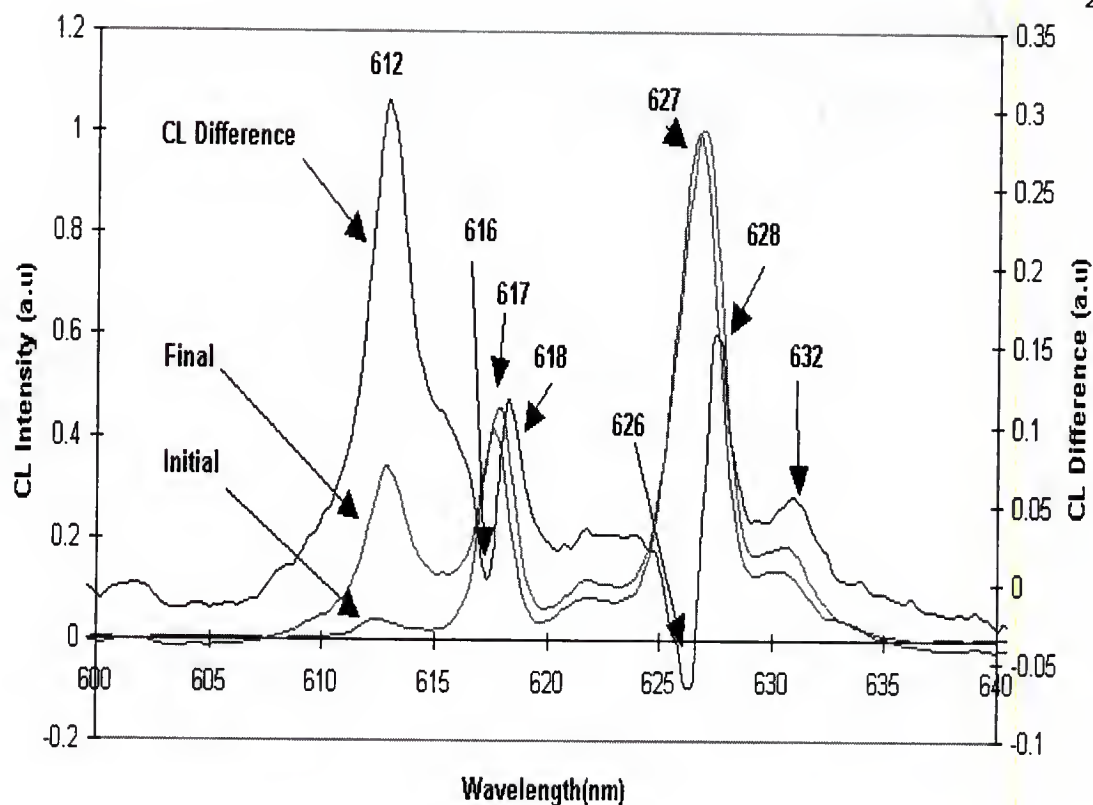
Figure 8-6   Enhanced CL spectra and CL difference curves as functions of wavelength(nm) for TaSi coated phosphor. Note the large increase in the 612, 632 nm emission indicating the growth of the oxide phase. Spectral broadening peak pairs are found around the 617 and 627 nm oxysulfide emission peaks at 616, 618 and 626, 628 nm.
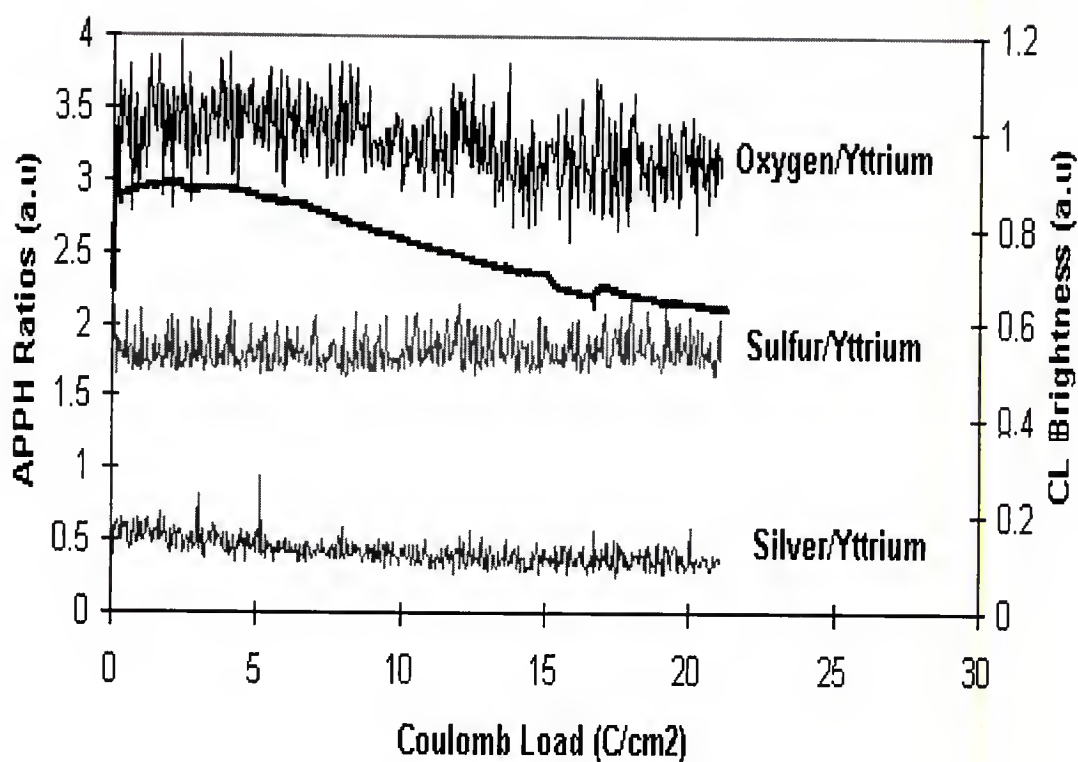
Figure 8-7   APPH ratios for Ag coated sample.
Note the slow loss of Ag and the comparable
increase in S. This indicates that the Ag is
moving away from the electron beam (possibly due
to heat gradients), exposing the phosphor beneath
the coating. The CL degradation curve is shown on
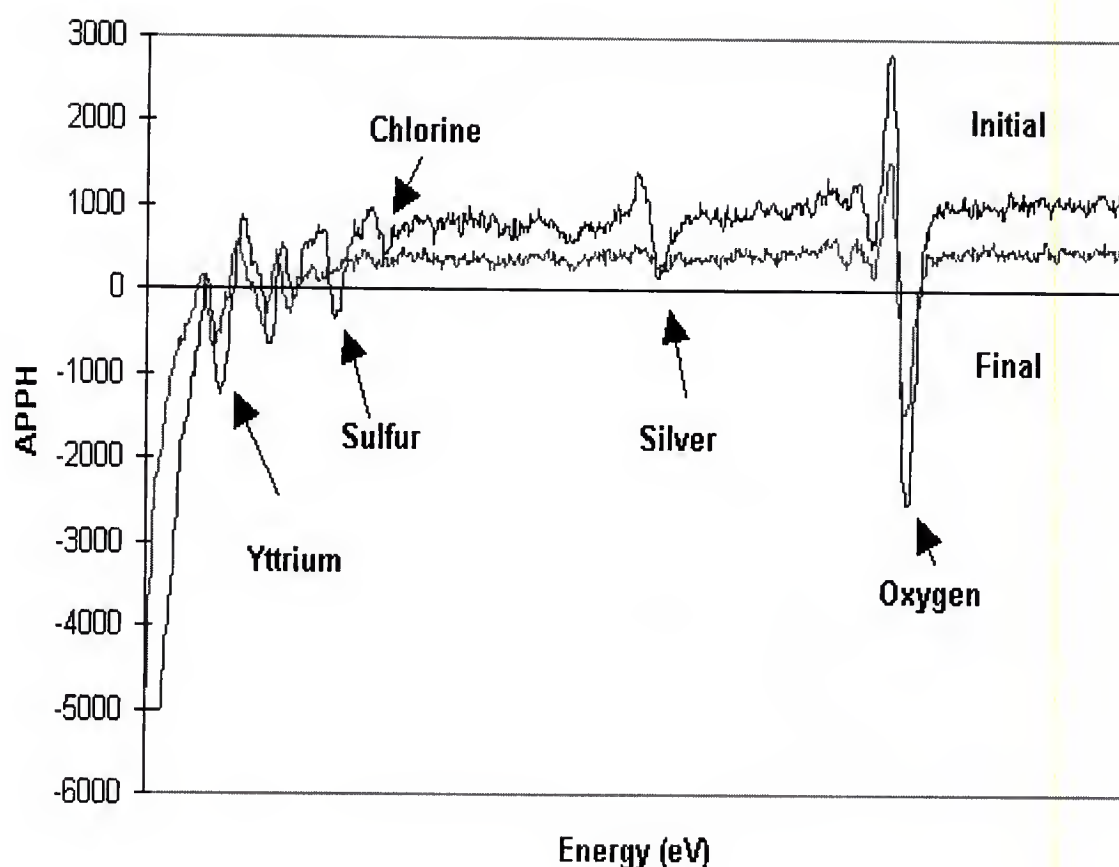the right y-axis.

Figure 8-8 Initial (0 C/cm²) and Final (15 C/cm²) AES spectra for 2keV degradation in ~1x10⁻⁶ Torr O₂. Note the large Ag peak initially, which is almost immeasurable at 15 C/cm². This may indicate the migration of Ag from beneath the electron beam or desorption of volatile Ag species.
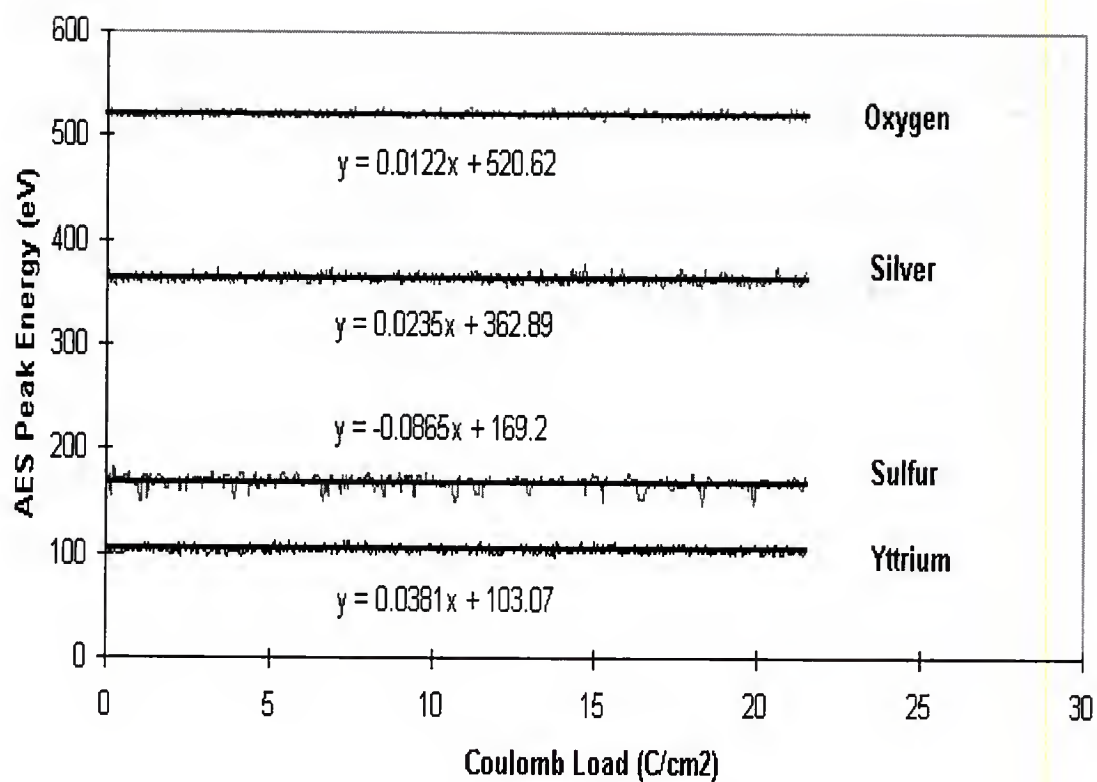
Figure 8-9   AES peak energy shifts for the Ag coated phosphor. The peak shifts are small, possibly due to the conducting nature of the coating.
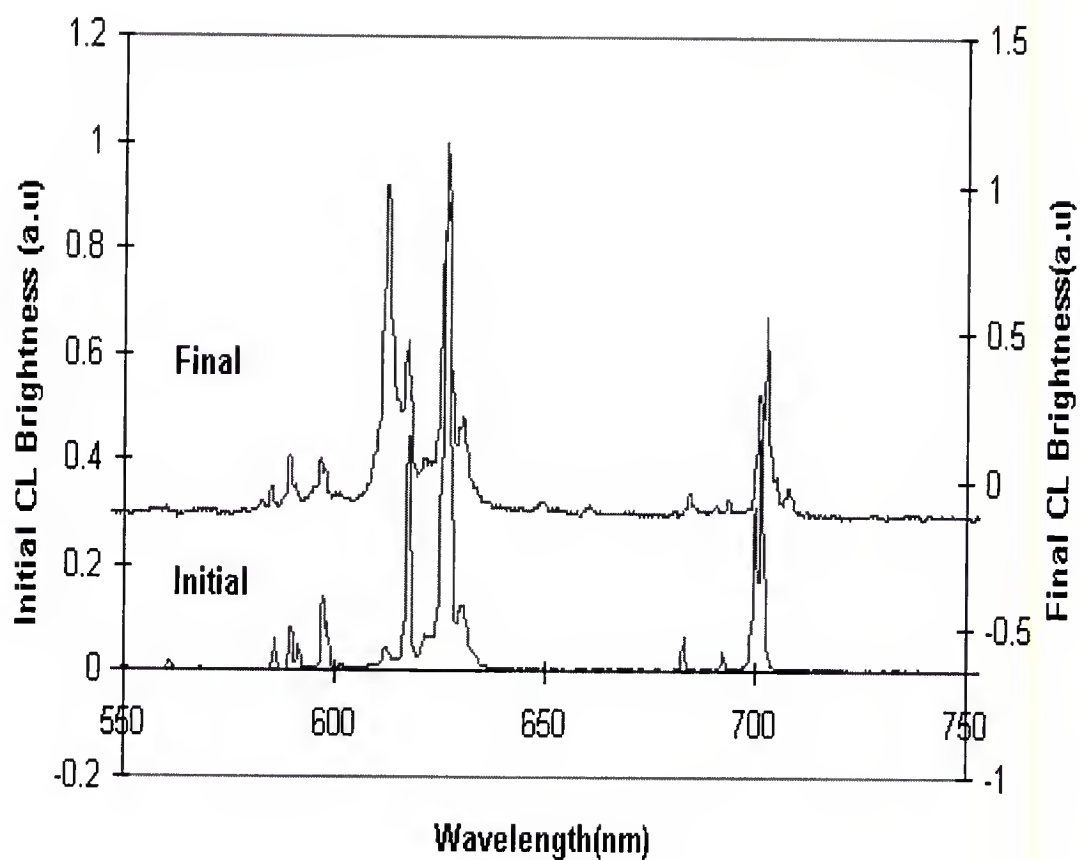
Figure 8-10   Initial and final CL Intensity
spectra as a function of wavelength (nm). Note the
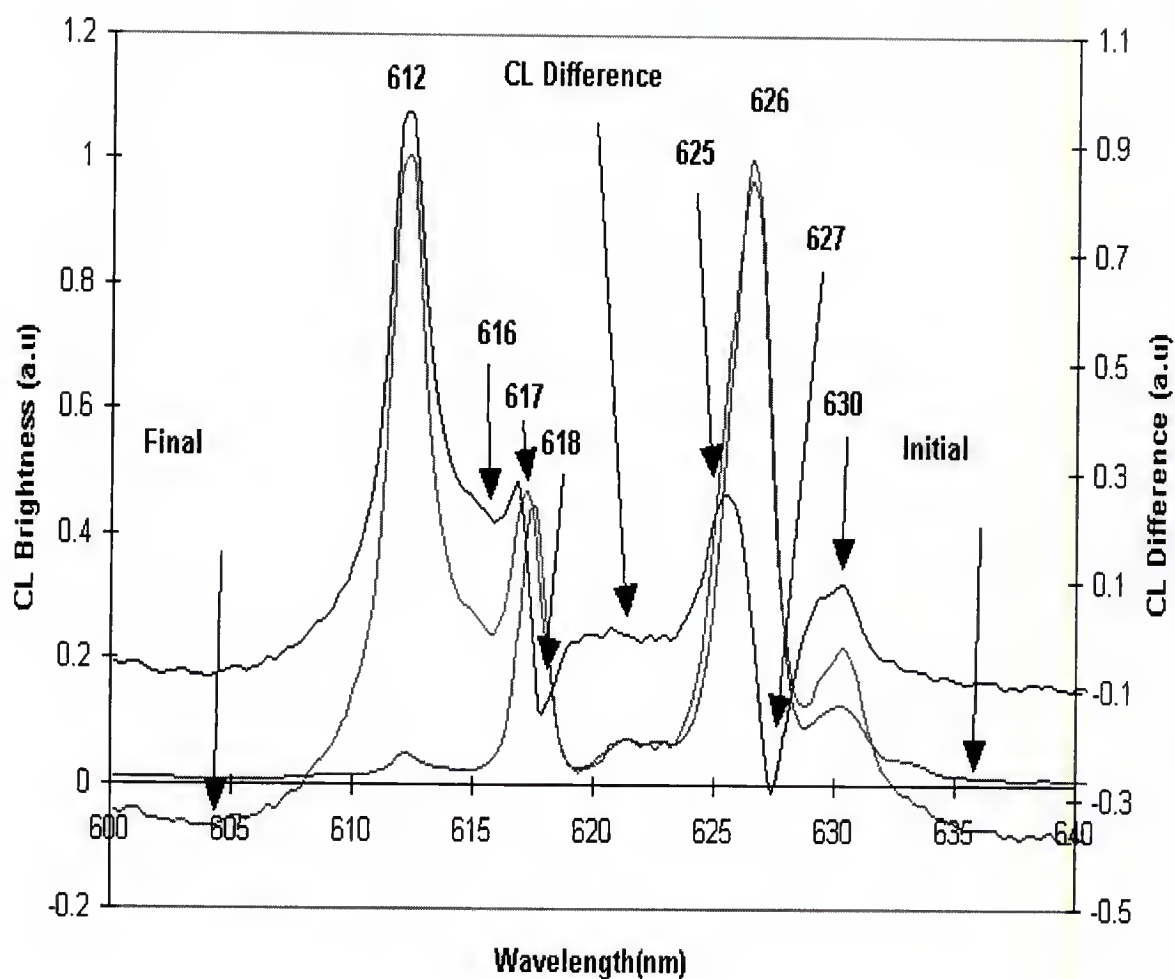large increase in the oxide peak at ~612 nm.

Figure 8-11   Ag coated oxysulfide expanded CL
and CL difference spectra. Spectral broadening of
the oxysulfide main peaks at 626 and 617 nm occurs
at 616, 618nm and 625, 627 nm. Note the emissive
increases at 612 and 630 nm. The 612 nm peak is
the oxide peak emission. The 630 nm may be the
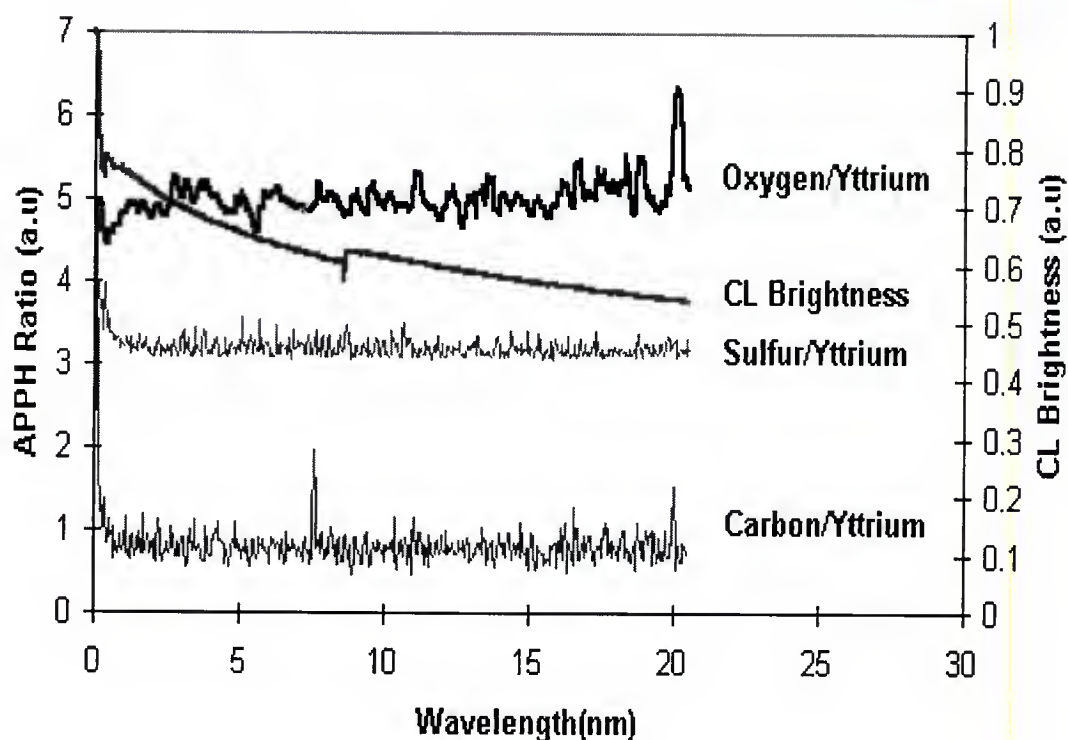second strongest emission of the oxide, but is
difficult to discern.

Figure 8-12   APPH ratios and CL brightness curve as functions of coulomb load (C/cm²) for the silica coated phosphor. No silicon signal could be distinguished because of overlap with low energy Y peaks. The curves are very similar to the baseline oxysulfide oxygen experiments of chapter 6.
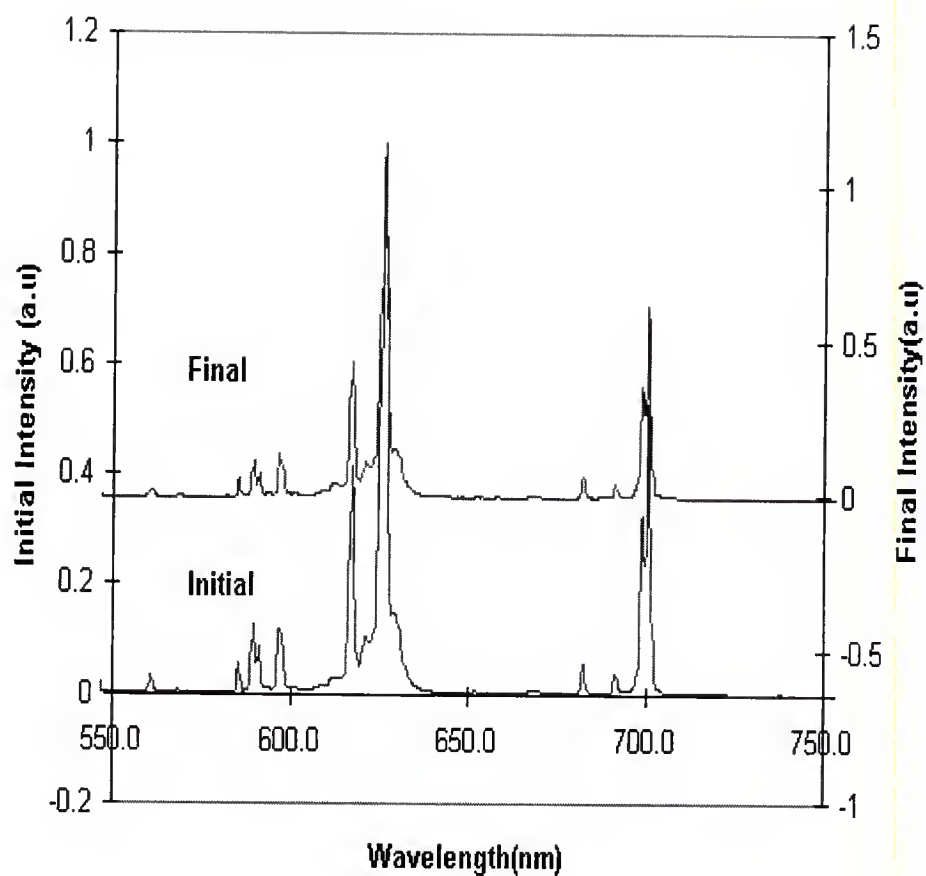
Figure 8-13   Initial and Final CL spectra as a function of wavelength (nm) for the Silica coated oxysulfide powder. No differences can be discerned.
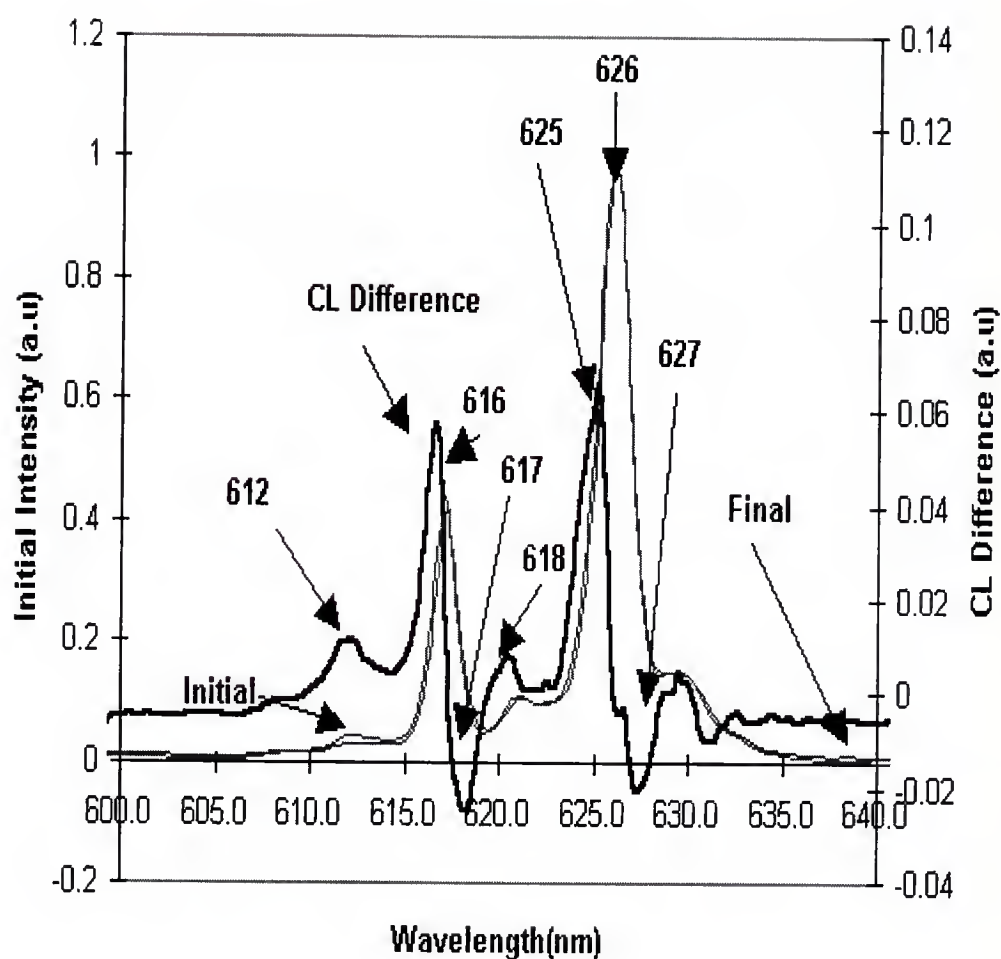
Figure 8-14   Silica coated oxysulfide enhanced CL spectra and CL difference spectra. Some spectral broadening is observed on the oxysulfide main emission peaks (617 and 626 nm) and a small oxide peak is visible at 611 nm but not nearly to the extent seen in the TaSi and Ag coated materials.
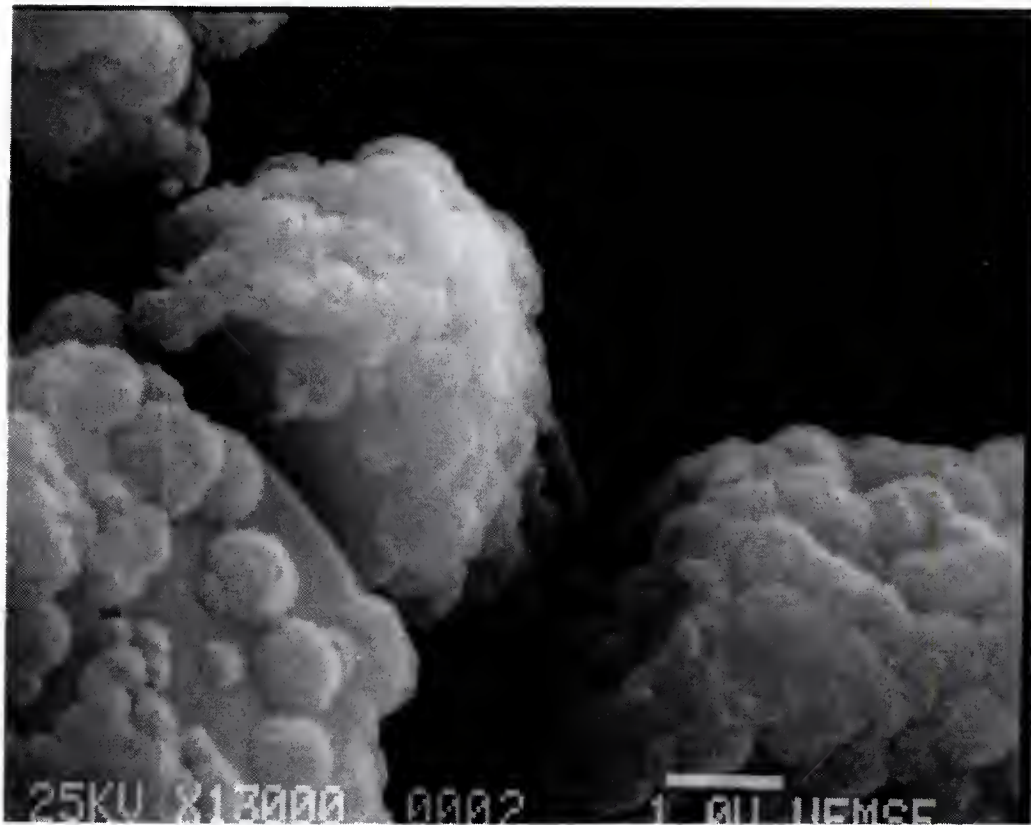
Figure 8-15   SEM of phosphate coated oxysulfide powder. The scale at bottom right is 1μm. Note the large nodular outcropppings on the particles.
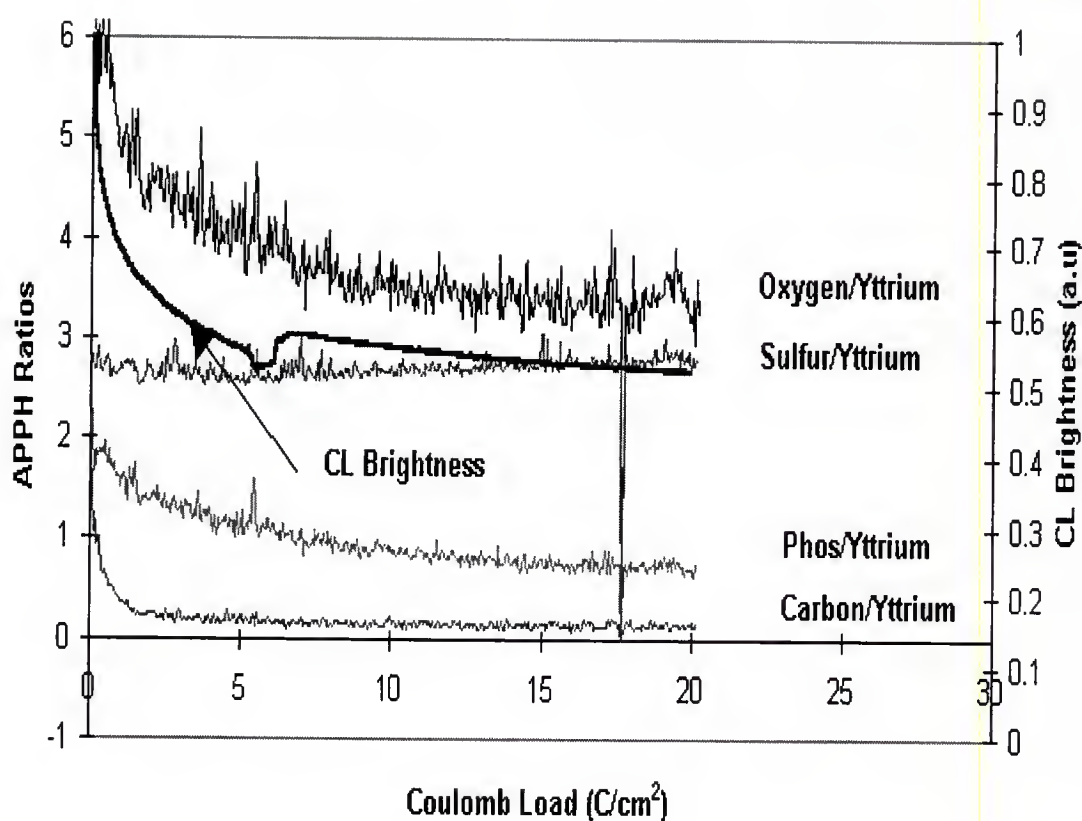
Figure 8-16   APPH ratios and CL brightness as functions of coulomb load for the phosphate coated phosphor. Note that the O/Y ratio first follows the C/Y and then the slope changes and follows the P/Y ratio. C may be more easily volatilized than the P. Surface oxygen may be enhancing the degradation.

Figure 8-17   Initial (0 C/cm²) and final (15 C/cm²) CL spectra for the phosphate coated oxysulfide powder degraded at 2keV and ~1x10⁻⁶ Torr O₂.

Figure 8-18   Enhanced CL spectral distribution and Cl difference curves for the phosphate coated powder. Note the absence of the 612 nm oxide emission. Only spectral broadening of the oxysulfide emission peaks at 617 and 626 nm are observed.

CHAPTER 9

SUMMARY AND CONCLUSIONS

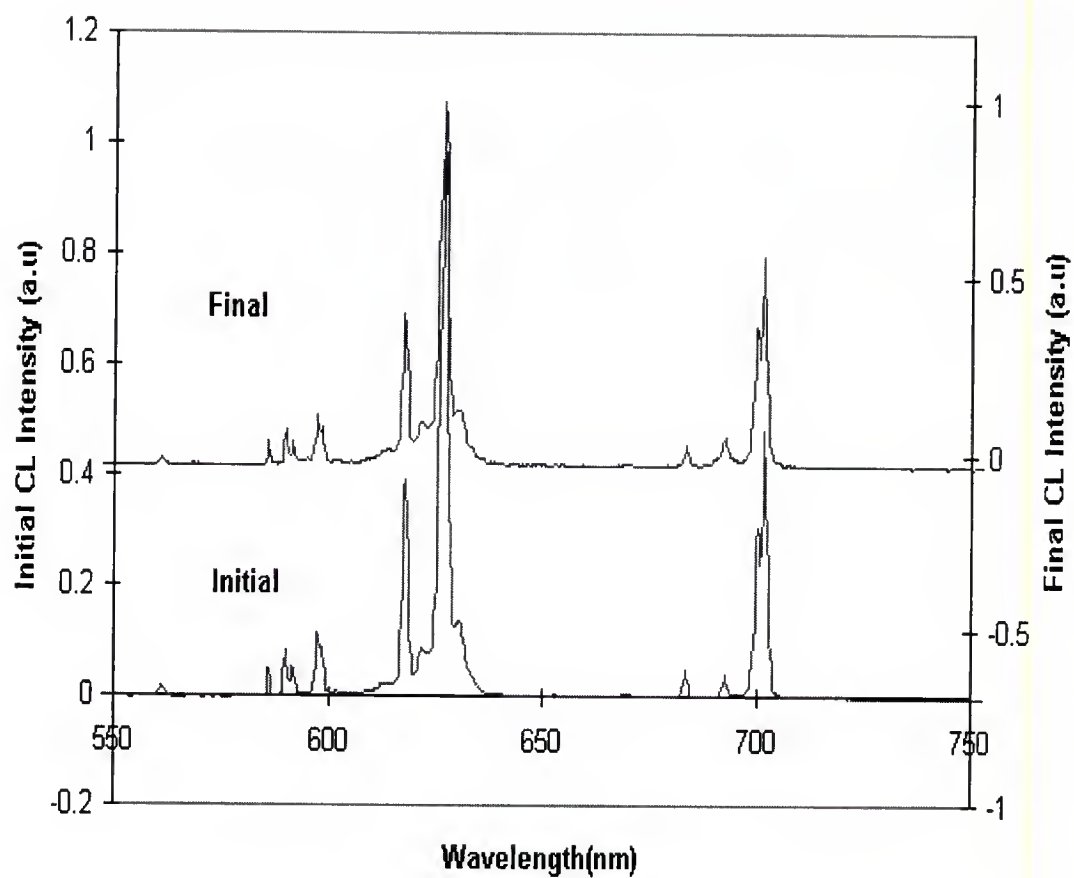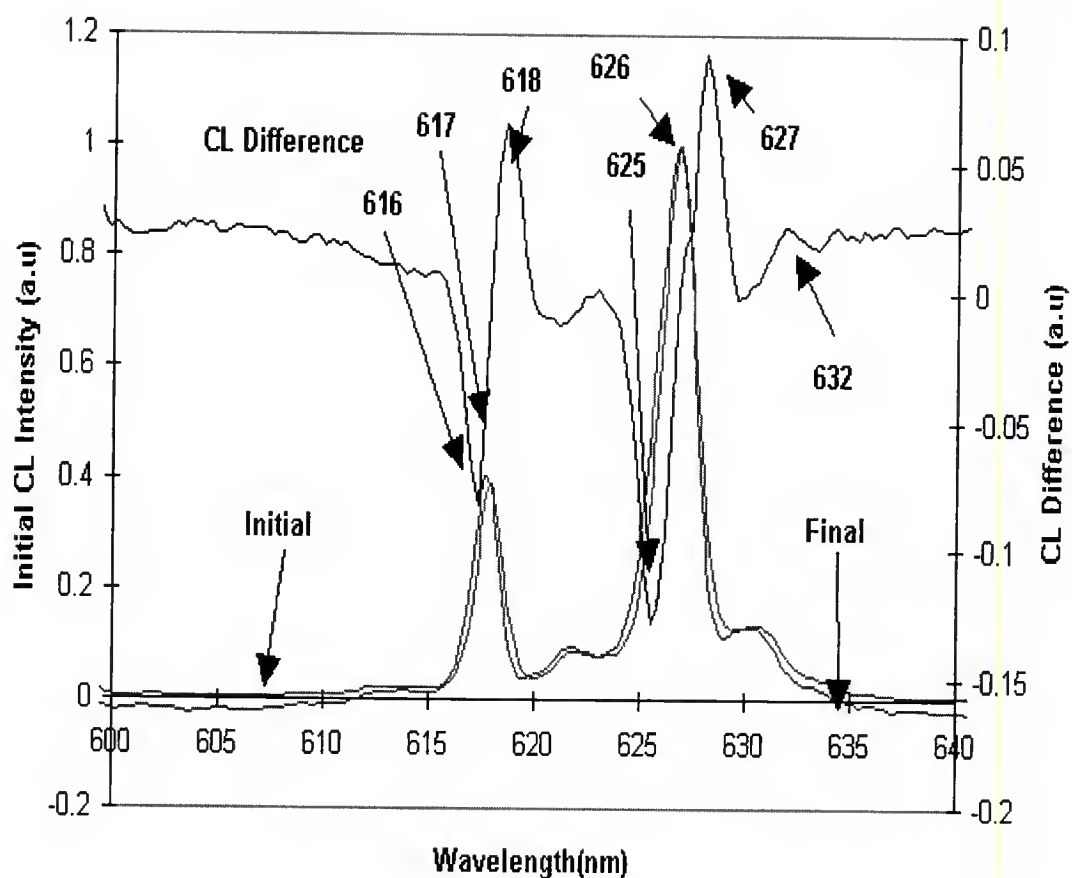The CL degradation of $Y_2O_2S:Eu^{3+}$ powder phosphors was studied by Auger electron spectroscopy (AES) and cathodoluminescence (CL) spectroscopy. Electron beams of 1, 2 and 3 keV energies were used to induce cathodoluminescence, as well as generate auger electron signals. DC current densities ranged from 100 to 400 $\mu a/cm^2$ for CL and AES. Vacuum pressures during the CL degradation studies ranged from a base pressure of $1x10^{-8}$ Torr to $1x10^{-6}$ Torr of backfilled oxygen gas.

CL degradation occurred slowly at $1x10^{-8}$ Torr and the AES and CL data indicated the loss of S and adventitious contaminant C from the surface of the phosphor. The CL degradation observed only occurred while the electron beam was turned on. The reactions involved O containing gases,

the electron beam and the surface C and S and created a thin non-luminescent layer (~130Å). This layer growth, which for modeling purposes was taken to be a continuous layer, decreased the total brightness of the phosphor. The dead layer thickness increase was determined from threshold voltage curves obtained before and after the CL degradation experiment. The increased threshold voltage and CL degradation may have been caused by the conversion of $Y_2O_2S:Eu^{3+}$ to $Y_2O_2SO_4:Eu^{3+}$ or due to increased non-radiative recombination near the phosphor surface due to charging.

Further experiments examined the effects of gas pressure and type of gas on the rate of surface change and CL degradation rate, and both were much higher in the presence of oxygen gas. a conversion of $Y_2O_2S:Eu^{3+}$ to $Y_2O_3:Eu^3$ occurred in the presence of oxygen. The growth of this layer was studied by time dependant threshold voltage experiments, and was found to correlate well with both the AES changes observed and the CL degradation. The complete layer thickness was calculated to be ~600 Å from threshold experiments. The growth of the dead layer was initially fast (corresponding to the S and C loss), then slowed for the remainder of the CL degradation.

The dependance of CL degradation rate on the electrons primary energy was also investigated for 1, 2 and 3 keV energies. It was found that the CL degradation was faster for lower accelerating voltages primarily due to the decrease in excitation volume. It was also shown that the presence of large amounts of C at the surface affected the S loss rate.

The CL brightness loss as a function of the growth in dead layer was modeled using Makhov's Law to predict the total brightness loss of the $Y_2O_2S:Eu^{3+}$. The model assumed that the effects on CL brightness due to carrier diffusion was negligible, and the range predicted by the modified Bethe equation was equal to the excitation volume. The absorption of light by the material was assumed to be negligible. The CL efficiency term in Makhov's equation, was modified using experimental data relating the Eu^{3+} concentration to depth and the concentration quenching curve (which defines the brightness of a phosphor as a function of the molar concentration of Eu^{3+} present). Very good correlation was found between all experiments and the brightness loss predictions of the model. The observed CL degradation in the baseline experiments was 4%, the model

predicted a 6% loss. The observed degradation in the oxygen experiments was 40% and the predicted degradation was 45%. a more refined model would take into account that some of the degraded material is converted to $Y_2O_3:Eu^{3+}$, a luminescent solid. The model used in this study considers the entire dead layer non-luminescent.

The ionization rate of gas at the surface was modeled using the assumptions of kinetic theory of gases to obtain impingement rates for oxygen gas on the surface of the phosphor. The determination of the number of gas molecules available for ionization at the surface assumed a unity sticking coefficient. a modified ionization efficiency for electrons of varying kinetic energies was used to determine the number average of dissassociated oxygen molecules residing at the surface of the phosphor. This model showed that the CL degradation rate is initially limited by the amount of dissassociated gas available for surface reaction. The amount of electrons available to dissassociate gas near the surface exceeds the amount of gas at the surface for all the experimental conditions (pressure, temperature, heat of desorption) examined in this study. Based on these models,

protective surface coatings were applied to the phosphor particles in an attempt to slow the CL degradation.

Non-uniform coatings of TaSi and Ag were deposited by a pulsed laser ablation technique and were found to reduce the CL degradation by 60% and 40%, respectively. The TaSi coating was still present on the surface after the CL degradation experiment, and may have acted as a diffusion barrier to S, preventing the surface formation of Y_2O_3:Eu3+ where it was present on the surface. The TaSi coating was tenacious and was not desorbed or dispersed by the electron beam. The Ag coating delayed the CL degradation. Under the influence of the electron beam, the Ag may have migrated away from the beam spot during bombardment, slowly exposing the Y_2O_2S:Eu^{3+} phosphor. It is also possible that the Ag was volatilized as Ag_2S during the experiment. Once the amount of Ag had decreased under the electron beam, CL degradation occurred at rates nearly equal to the uncoated phosphor.

Wet chemistry coatings of SiO_2 and phosphate were applied as well, and were found to not slow the CL degradation rate. The CL degradation rate of the phosphate coating was enhanced initially possibly due to the presence of O on the surface of the phosphor in the coating. The

surface reaction sequence observed by AES was altered

(compared to the uncoated powder), but the CL degradation

rate was not inhibited. The SiO_2 coated material exhibited

AES surface changes similar to those of the uncoated

phosphor and the presence of Si could not be verified by

AES. Thus, it was not studied in as much detail as were the

other coatings.

LIST OF REFERENCES

Bec96   Bechtel, H., Czarnojan, W., Haase, M., Wadow, D., <u>J.Soc.Inf.Display.</u>, <u>4(3)</u>, 219 (1996)

Bet53   Bethe, H., Ashkin, J., <u>Passage of Radiations through Matter</u>, *Experimental Nuclear Physics* (Wiley, New York, 1953)

Bla94   Blasse, G., Grabmaier, B., *Luminescent Materials* (Springer-Verlag, New York, 1994)

Bli57   Bliss, W.H., Juong, C.J., *Facsimile Scanning by Cathode Ray Tubes*, <u>R.C.A.Rev.</u>, <u>15</u>, 275 (1957)

Bru92   Brundle, C.R., Evan C.A, Wilson, S., *Encyclopedia of Material Characterization*, (Manning Publications Incorporated, Greenwich, CT, 1992)

Der94   Derbyshire, K., <u>J.Solid.State.Tecnology</u>, <u>Nov.</u>, 1994

Don78   Donalato, C., <u>J. Optics</u>, <u>52</u>, 19 (1971)

Eve71   Everhart, T.E, Hoff, P.H., <u>J.Appl.Phys.</u>, <u>42</u>, 5837 (1971)

Fit97   Fitzgerald, J., Singh, R.K, *Nano-particle Flux Based Dry Coatings*, Patent Disclosure, University of Florida, Gainesville, FL 1997

Gil56   Gilfrich, H.P., <u>Z.Phys.</u>, <u>145</u>, 241 (1956)

Han52   Hanle, W., Rau, K.H., <u>Z.Phys.</u>, <u>133</u>, 297 (1952)

Has90   Hase, T., Kano, T., Nakozawa, E., Yamamoto, H., Advances in Electronics and Electron Physics, 79, 273 (1990)

Hay69   Haynes, J.W., U.S Patent # 3,607,371

Hol97   Holloway, P.,Sebastian, J., Trottier, T., Jones, S., Swart, H., Petersen, R., *Degradation Mechanisms and Vacuum Requirements for FED Phosphors*, Flat Panel Display Materials II, <u>MRS Proceedings</u>, <u>424</u>, 1997

Hud92   Hudson, J.B., *Surface Science*, (Butterworth-Heinemann, Stonehame, MA, 1992)

Ito89   Itoh, S., Kimizuka, T., Tanegawa, T., <u>J.Electrochem.Soc.</u>, <u>136</u>, 1819 (1989)

Jac95   Jacobsen, S., Yang, S., Zhang, F., Summers, C., *SID Display Manufacturing Conference*, Late News Paper, 1995

Joy89   Joy, D.C., Luo, S., <u>J.Scanning</u>, <u>11</u>, 177 (1989)

Kad92   Abdel-Lader, a., Elkholy, M.M., <u>J.Mat.Sci</u>, <u>27</u>, 2887 (1992)

Kan71   Kanaya, K., Okayama, S., <u>J.Appl.Phys.</u>, <u>5</u>, 46 (1971)

Kin72   Kingsley, J.D., Prener, <u>J.S., J.Appl.Phys.</u>, <u>43</u>, 3073 (1972)

Kla87   Klaassen, D., de Leeuw, D., <u>J. Luminescence</u>, <u>37</u>, 21 (1987)

Kom96   Kominami, H., Horikawa, K., Auki, T., Nakamura, T., Nakanishi, Y., Hatanaka, Y., Proc. 15th Int. Display Res. Conf., 867 (1996)

Kot95   Kottaisamy, M., Jaguannathan, R., Rao R.P., Auudaithai, M., Srinivason, L.K., Sunfaram, V., <u>J.Electrochem. Soc.</u>, <u>142</u>, 3205 (1995)

Lav85   LaVerne, J.A., Mozumber, a., <u>J.Phys.Chem.</u>, <u>89</u>, 4219 (1985)

Lev91   Levy, F., Meyer, R., International Display Research Conference, San Diego, CA , Oct. (1991)

Lum78   Lumb, M., *Luminescence Spectroscopy* (Academic Press, London, 1978)

Mak60   Makhov, A.F., <u>Fiz.Tverd.Tela.</u>, <u>2</u>, 2161 (1960)

Mar57   Martin, W., <u>Z.Phys.</u>, <u>147</u>, 583 (1957)

Myk76   Myklebust, R.L., Newbury, D.E., Yakowitz, H., <u>J.Scan.Electron.Mic.</u>, <u>460</u>, 15 (1976)

New76   Newbury, D.E., Yakowitz, H., <u>J.Scan.Electron.Mic.</u>, <u>2</u>, 1917 (1988)

Nie88   Nieminen, R.M., <u>J.Scan.Electron.Mic.</u>, <u>2</u>, 1924 (1988)

Oza90   Ozawa, L., *Cathodoluminescence* (VCH Publishers, New York, NY, 1990)

Pat94   Patel, M., Pu, C.J., Sharpe, L., <u>Langmuir</u>, <u>11</u>, 2003 (1995)

Pet97   Petersen, R., <u>J.Soc.Info.Dis.</u>, <u>13(3)</u>, 22
         (1997)

Pfa61   Pfahnl, a, *Advances in Electron Tube
         Techniques* (Pergamon, New York, 1961)

Pha91   Pham-Ti, M. and Morell, a., <u>J.
         Electrochem.Soc.</u>, <u>138</u>,1100 (1991)

Rao74   Rao-Sahib, T.S., Wittry, D.B., <u>J.Appl.Phys</u>,
         <u>45</u>, 5060 (1974)

Ron94   Ronda, C., Bechtel, H., Welker, T.,
         <u>J.Appl.Phys</u>, <u>75</u> (1994)

Rot54   Rottgart, K.J., Berthold, W., <u>Z.Agnew.Phys.</u>,
         <u>6</u>, 160 (1954)

Rot55   Rottgart, K.J., Berthold, W., <u>Z.Naturef.</u>,
         <u>10A</u>, 736 (1955)

Sch93   Schwoebel, P., <u>J.Electrochem.Soc.</u>, <u>140</u>, L34
         (1993)

Sch96   Schwoebel, P., *Short Course on Vacuum Package
         Technology*, (SRI International, Menlo Park,
         CA, 1996)

Sea79   Seah, M.P., Dench, W.A, <u>J.Surf.Int.Anal.</u>, <u>1</u>,
         12 (1979)

Sea83   Seah, M.P, *Practical Surface Analysis by AES
         and XPS* (Wiley, New York, 1983)

Sil83   Silverberg, S., U.S Patent # 4,393,118

Swa96   Swart, H., Sebastian, J., Trottier, T.,
         Jones, S., Holloway, P., <u>J.Vac.Sci.Technol.</u>,
         <u>14</u>, 1697 (1996)

Tan85   Tannas Jr. L., *Flat Panel Displays and CRT's*
         (Van Nostrand Reinhold Company, New York,
         1985)

Tro96   Trottier, T.A., Swart, H.C., Jones, S.L.,
         Holloway, P.H., J.Soc.Inf.Display, 4, 354
         (1996)

Tun79   Tung, C.J., Ashley, J.C., Ritchie, R.H.,
         J.Surf.Sci., 81, 427 (1979)

Yac90   Yacobi, B.G., Holf, D.B., *Cathodoluminescence
         Microscopy of Inorganic Solids* (Plenum Press,
         New York, 1990)

BIOGRAPHICAL SKETCH

Troy Anthony Trottier was born on April 3rd, 1969, in
Westfield, MA. He spent much of his childhood attempting to
burn and/or blow up things. At Westfield High School, he
graduated with honors. Upon graduation, he enrolled at
Western New England College in electrical engineering and
spent the next 4 years learning how to burn and/or blow
things up electrically. Upon graduating, he got a job. After
years of traveling around North America, he realized the job
did not allow him to follow his dream (seldom did he get to
burn or blow things up). He learned of the UF Department of
Materials Science and a man by the name of Holloway who
would be sympathetic. After being accepted for PhD research,
he was given the job of burning and/or blowing up computers,
lab equipment and phosphor particles. He has spent the last
4 years, following his dream, doing just that.

I certify that I have read this study and that in my opinion it conforms to acceptable standards of scholarly presentation and is fully adequate, in scope and quality, as a dissertation for the degree of Doctor of Philosophy.

Paul H. Holloway, Chair
Professor of Materials
    Science and Engineering

I certify that I have read this study and that in my opinion it conforms to acceptable standards of scholarly presentation and is fully adequate, in scope and quality, as a dissertation for the degree of Doctor of Philosophy.

Kevin S. Jones
Associate Professor of
    Materials Science and
    Engineering

I certify that I have read this study and that in my opinion it conforms to acceptable standards of scholarly presentation and is fully adequate, in scope and quality, as a dissertation for the degree of Doctor of Philosophy.

Rolf E. Hummel
Professor of Materials
    Science and Engineering

I certify that I have read this study and that in my opinion it conforms to acceptable standards of scholarly presentation and is fully adequate, in scope and quality, as a dissertation for the degree of Doctor of Philosophy.

Rajiv K. Singh
Associate Professor of
    Materials Science and
    Engineering

I certify that I have read this study and that in my opinion it conforms to acceptable standards of scholarly presentation and is fully adequate, in scope and quality, as a dissertation for the degree of Doctor of Philosophy.
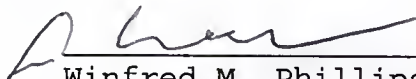
David B. Tanner
Professor of Physics

This dissertation was submitted to the Graduate Faculty of the College of Engineering and to the Graduate School and was accepted as partial fulfillment of the requirements for the degree of Doctor of Philosophy.

August, 1997

Winfred M. Phillips
Dean, College of
Engineering

Karen A. Holbrook
Dean, Graduate School